Understanding Welding and Machining Properties of High- and Medium Entropy Alloys: A Study on CoCrFeMnNi and CoCrNi Systems

Dissertation
zur Erlangung des akademischen Grades

Doktoringenieur
(Dr.-Ing.)

von M.Sc. Tim Richter
geb. am 26.11.1992 in Magdeburg
genehmigt durch die Fakultät Maschinenbau der Otto-von-Guericke-Universität Magdeburg

Gutachter/innen:
Prof. Dr.-Ing. habil. Thomas Kannengießer
Prof. Dr.-Ing. Jonas Hensel
Dr.-Ing. Dirk Schröpfer

Promotionskolloquium am 07.04.2025

Ehrenerklärung

Ich versichere hiermit, dass ich die vorliegende Arbeit vollständig ohne unzulässige Hilfe Dritter und ohne Benutzung anderer als der angegebenen Hilfsmittel angefertigt habe. Alle verwendeten fremden und eigenen Quellen sind als solche kenntlich gemacht und im Falle einer Ko-Autorenschaft ist der Eigenanteil richtig und vollständig ausgewiesen. Insbesondere habe ich nicht die Hilfe einer kommerziellen Promotionsberaterin/eines kommerziellen Promotionsberaters in Anspruch genommen. Dritte haben von mir weder unmittelbar noch mittelbar geldwerte Leistungen für Arbeiten erhalten, die im Zusammenhang mit dem Inhalt der vorgelegten Dissertation stehen.

Ich habe insbesondere nicht wissentlich:

- Ergebnisse erfunden oder widersprüchliche Ergebnisse verschwiegen,
- statistische Verfahren absichtlich missbraucht, um Daten in ungerechtfertigter Weise zu interpretieren,
- fremde Ergebnisse oder Veröffentlichungen plagiiert,
- fremde Forschungsergebnisse verzerrt wiedergegeben.

Mir ist bekannt, dass Verstöße gegen das Urheberrecht Unterlassungs- und Schadensersatzansprüche der Urheberin/des Urhebers sowie eine strafrechtliche Ahndung durch die Strafverfolgungsbehörden begründen können.

Ich erkläre mich damit einverstanden, dass die Dissertation ggf. mit Mitteln der elektronischen Datenverarbeitung auf Plagiate überprüft werden kann.

Die Arbeit wurde bisher weder im Inland noch im Ausland in gleicher oder ähnlicher Form als Dissertation eingereicht und ist als Ganzes auch noch nicht veröffentlicht.

(Ort, Datum bei Eröffnung des Promotionsverfahrens)

(Vorname, Name und Unterschrift)

Abstract

The constant drive in production engineering to optimize component properties has led to an exploration of various variables, including material composition and processing techniques. High Entropy Alloys (HEAs), introduced in 2004, represent a new class of materials with complex compositions and promising properties. Unlike conventional alloys, HEAs consist of at least five alloying elements (Medium Entropy Allys- MEA with 2 to 4 alloying elements) with nearly equal proportions, leading to unique crystalline structures and potentially improved properties. While much research has focused on synthesizing HEAs with specific properties, the manufacturing and processing aspects, particularly weldability and machinability, are gaining increasing importance.

This doctoral thesis focuses on investigating the weldability and machinability of CoCrFeMnNi-HEA and CoCrNi-MEA, using Tungsten Inert Gas (TIG) and Friction Stir Welding (FSW) processes. Welding experiments were conducted to assess joint integrity, microstructure evolution, mechanical properties, and residual stresses. Results show that both HEA and MEA exhibit good weldability under TIG welding, with welds free from defects and mechanical properties comparable to the base material. Additionally, dissimilar metal welds (DMWs) with conventional austenitic steel (AISI 304) were successfully produced, indicating the potential for multi-material applications.

Machinability studies were carried out through conventional and Ultrasonic-Assisted Milling (USAM) processes, focusing on cutting forces, surface integrity, and residual stresses. Both alloys demonstrated good machinability, with USAM showing improved surface integrity by reducing defects and residual stresses. The findings suggest potential applications of HEAs and MEAs in functional surfaces and coatings.

In conclusion, this research provides comprehensive insights into the weldability and machinability of HEAs and MEAs, laying a foundation for their integration into real components. Further investigations are recommended to explore the impact of welding and machining parameters, as well as the application of these alloys in specialized areas, to fully exploit their potential.

Kurzfassung

Das ständige Bestreben in der Produktionstechnik, die Eigenschaften von Bauteilen zu optimieren, hat dazu geführt, dass verschiedene Variablen, einschließlich der Materialzusammensetzung und der Verarbeitungstechniken, überdacht werden. High Entropy Alloys (HEAs), die 2004 eingeführt wurden, stellen eine neue Klasse von Werkstoffen mit komplexer Zusammensetzung und vielversprechenden Eigenschaften dar. Im Gegensatz zu herkömmlichen Legierungen bestehen HEAs aus mindestens fünf Legierungselementen (Medium Entropy Alloy -MEA mit 2 bis 4 Legierungselementen) mit nahezu gleichen Anteilen, was zu einzigartigen kristallinen Strukturen und potenziell verbesserten Eigenschaften führt. Während sich ein Großteil der Forschung auf die Synthese von HEAs mit spezifischen Eigenschaften konzentriert hat, gewinnen die Herstellungs- und Verarbeitungsaspekte, insbesondere die Schweißbarkeit und Zerspanbarkeit, zunehmend an Bedeutung.

In dieser Dissertation wird die Schweißbarkeit und Zerspanbarkeit von CoCrFeMnNi-HEA und CoCrNi-MEA unter Verwendung von Wolfram-Inertgas- (WIG) und Friction Stir Welding (FSW) Verfahren untersucht. Es wurden Schweißexperimente durchgeführt, um die Integrität der Verbindung, die Entwicklung des Mikrogefüges, die mechanischen Eigenschaften und die Eigenspannungen zu bewerten. Die Ergebnisse zeigen, dass sowohl HEA als auch MEA beim WIG-Schweißen eine gute Schweißbarkeit aufweisen, wobei die Schweißnähte frei von Fehlern sind und die mechanischen Eigenschaften mit denen des Grundmaterials vergleichbar sind. Darüber hinaus wurden erfolgreich Mischschweißnähte mit herkömmlichem austenitischem Stahl (AISI 304) hergestellt, was auf das Potenzial für Multi-Material-Anwendungen hinweist.

Studien zur Zerspanbarkeit wurden mit konventionellen und ultraschallunterstützten Fräsverfahren (USAM) durchgeführt, wobei der Schwerpunkt auf Schnittkräften, Oberflächenintegrität und Eigenspannungen liegt. Beide Legierungen erwiesen sich als gut zerspanbar, wobei USAM die Oberflächenintegrität durch die Reduzierung von Defekten und Eigenspannungen verbesserte. Die Ergebnisse deuten auf mögliche Anwendungen von HEAs und MEAs in funktionalen Oberflächen und Beschichtungen hin.

Zusammenfassend lässt sich festhalten, dass diese Forschungsarbeit einen umfassenden Einblick in die Schweißbarkeit und Zerspanbarkeit von HEAs und MEAs bietet und damit eine Grundlage für deren Integration in reale Bauteile schafft. Weitere Untersuchungen werden empfohlen, um die Auswirkungen von Schweiß- und Zerspanungsparametern sowie die Anwendung dieser Legierungen in speziellen Bereichen zu erforschen, um ihr Potenzial voll auszuschöpfen.

Table of Content

1. Introduction

The general objective of research in production engineering is to optimize the properties of components. The number of variables (e.g., material composition, material processing, manufacturing processes) that can be changed in component manufacturing is very large.

In this context, a new class of materials known as high entropy alloys (HEA) introduced in 2004 (see Figure 1) has once again significantly increased the number of possible variables relating to alloy composition. Conventional approaches to materials development focus on alloy systems with a crystalline structure and one or two main alloying elements, like Fe in the case of steels or Al and Ni with their respective alloys. Small amounts of further elements are added to improve the material properties like the C-addition to Fe, described in the very well-known Fe-C-diagram. However, these approaches have their limits. Therefore, material research into alternative development strategies is gaining importance. Whereby HEAs are a promising alternative, consisting of at least five alloying elements with nearly equal proportions and having a crystalline structure. HEAs have complex compositions but form solid solutions with face-centered cubic or body-centered cubic lattice structures, which can lead to improved properties compared to conventional alloys. Due to the high number of possible alloy combinations, this new class of alloys shows great potential for improved material and thus component properties. For a long time, the focus of research was on material synthesis and property testing in order to obtain possible alloys with specific properties. This resulted in further concepts such as medium entropy alloys (MEA) and compositionally complex alloys (CCA) were derived from the HEA concept. These new concepts are summarized under the name multi-principal element alloys (MPEA).

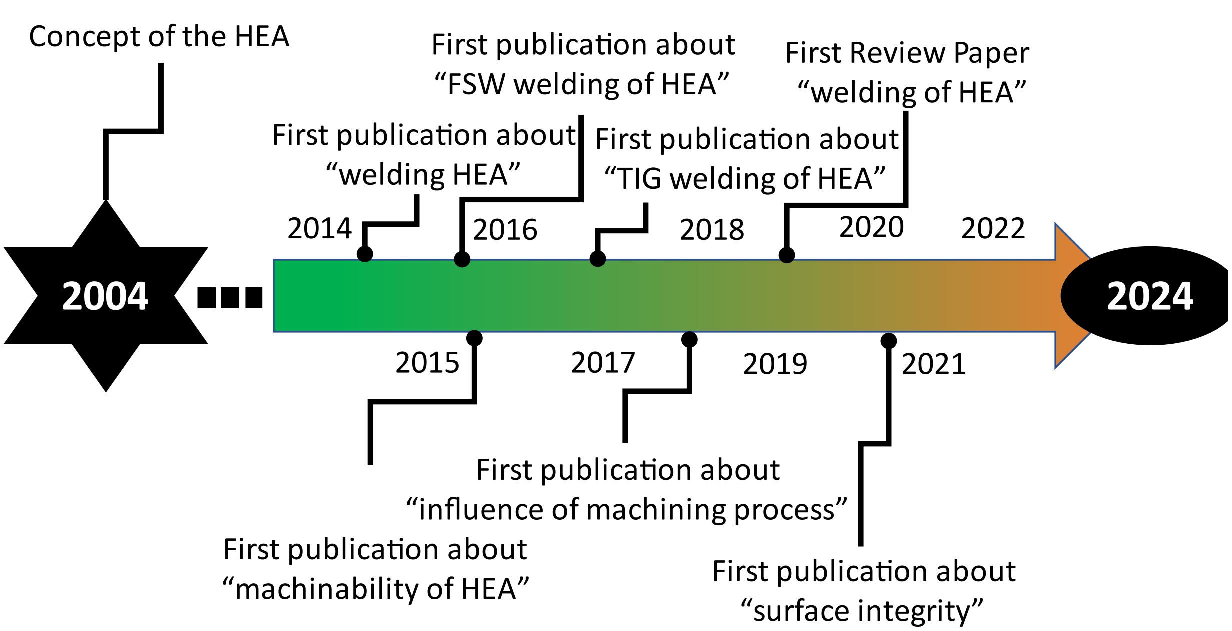

Figure 1: Timeline from the discovery of the HEA concept through the milestones of weldability and machinability of HEAs

However, even the best materials cannot be used for structural or functional applications if they are hardly or nearly impossible to process. Thus, research into the manufacturing and processing of HEAs has gained considerable importance in recent years. Critical stages in this process are the welding and machining of HEAs. Some important first milestones in the weldability and machinability of HEAs are dated in Figure 1. It is important to develop optimized processes to maintain or improve the properties of these materials, e.g. in terms of mechanical performance, corrosion resistance or other physical properties like thermal, or electrical conductivity.

In that scope, for modern component manufacturing welding is crucial as a most important joining process for metallic materials. In order to manufacture components such as turbines, engines, and pressure vessels even more efficiently, the focus is on optimizing their properties. This can only be achieved through close coordination between the material and the joining process, which is why the two aspects are inextricably linked. Therefore, the investigation of the weldability of a novel alloy system is of extraordinary importance for technological progress. In that connection, the weldability is described by interactions of the material and its processing for a desired design. For that reason, an essential factor for weldability is whether the material can be successfully joined by a respective process under consideration of the given technological requirements.

For that reason, the present work is intended to contribute to the important field of the weldability of MPEAs by tungsten inert gas welding (TIG) and friction stir welding (FSW). Two MPEA types were comprehensively investigated, the CoCrFeMnNi-HEA and CoCrNi-MEA by joining HEA-to-HEA and MEA-to-MEA, so-called joints of similar materials. In addition, dissimilar metal welds (DMWs) of HEA and MEA with conventional austenitic AISI-304 steel are investigated to answer the important question of the suitability of MEPAs for multi-material mixes. The aim is to show that these alloys can be welded without defects. In addition, the effect of welding on the microstructure formation and the mechanical properties (local and global) will be analyzed. All this forms the basis for the further use of these materials in real, welded components.

Machining also plays a crucial role in the fabrication of various components. This is because various manufacturing processes such as casting, forming, and welding often require additional machining steps to achieve the final product. Machining processes change the geometry of the manufactured parts by removing material, which enables the production of complex contours, small holes, and special surface finishes. Research into the processability of HEAs is necessary for their use in industrial applications. The goals are cost-effective processes that produce functional surfaces to meet the potential requirements for future components made from these alloys.

Next to welding this work focuses on the analysis of process conditions during finish milling of CoCrFeMnNi-HEA and CoCrNi-MEA. Ultrasonic-assisted milling (USAM), in addition to conventional ball end milling, and their effects on the milling process and resulting surface integrity are investigated. These results will be used to characterize the machinability, which is important for the use of these materials. Surface integrity in particular has a major influence on the usability of the alloys when functional surfaces are required in safety-relevant components.

2. State of the art

2.1 High and medium entropy alloys (HEA)

High entropy alloys (HEA) are a new class of materials that were described in the first publications in 2004 [1-3]. Basically, it is assumed that the control of the configuration entropy influences the phase stability of these alloys. Furthermore, this concept opens up new alloys and phenomena to be explored.

2.1.1 Definitions and special properties of high and medium entropy alloys

Since the first publications, some new insights into HEAs have emerged. An important step was the definition and classification of alloys within this alloy class. Two main definitions have emerged [4] [1, 5]. One definition is based on the composition [1, 4] of the alloys, and another on the entropy [4, 5].

Definition according to the alloy composition

Accordingly, HEAs are defined as "those consisting of five or more major elements in equimolar ratios" [1]. For MEA consequently, equimolar concentrations are restrictive. The definition is expanded by the following phrase in the same paper "major elements with a concentration of each element between 35 and 5 atomic %." Accordingly, HEAs need not be equimolar, which greatly increases the number of possible alloys. In addition, HEAs may also contain subordinate elements to modify the properties of the base HEA, further increasing the number [5]. This composition-based definition only prescribes the element concentrations and places no limits on the magnitude of the entropy. Furthermore, this definition does not prescribe the presence of a single-phase solid solution [4].

Definition according to the entropy

The term "high entropy" conditions a definition based on entropy magnitude. An alternative definition therefore distinguishes between alloys with low ($S_{conf} < 0.69\ R$, where S_{conf} is the total molar configuration entropy and R is the gas constant), medium ($0.69\ R < S < 1.61\ R$; MEA for medium entropy alloy), and high ($S > 1.61\ R$) entropy [5], which is illustrated in Figure 2. This definition implies that an alloy has a single value of configurational entropy [4]. However, the entropy of an alloy can change with temperature. The temperature effect can be minor, leading to small changes in near-atomic order, or it can be drastic, leading to a first-order phase transformation. Addressing these issues, the entropy-based definition assumes that the alloy can be represented by the "liquid solution and high-temperature solid solution" conditions, where the thermal energy is sufficiently high to cause the various elements to assume random positions within the structure [5]. This characterizes an alloy by the maximum possible entropy.

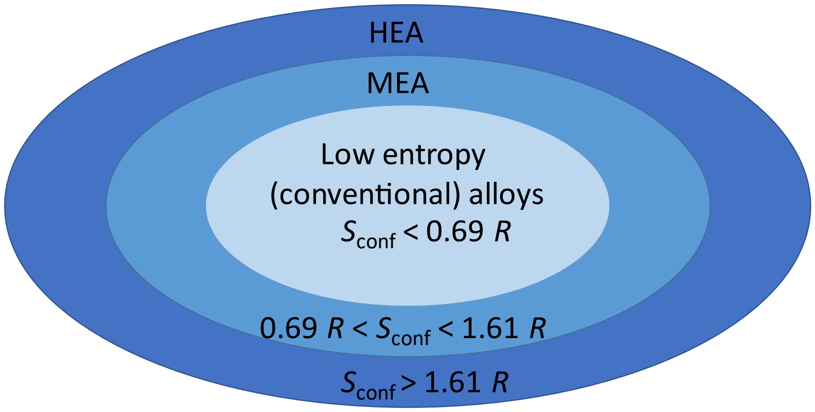

Figure 2: Classification of alloys depending on the configuration entropy S_{conf} according to [5]

The DFG special priority program “SPP 2006: Legierungen mit komplexer Zusammensetzung - Hochentropielegierungen (CCA - HEA)”[6] is used the nomenclature:

- “High entropy alloys, HEA, which are defined single solid solution phases, preferably with simple crystal structures.”
- “Compositionally complex alloys, CCA, consisting of multiphase microstructures with two or more phases, which may include a solid solution phase.”

It can be stated that there is no unambiguous definition in the international research community. For this reason, the following definitions apply in this work:

A HEA has:
- Single-phase soiled solution
- At least five different main elements
- Main element amounts in a range between 5 and 35 at.-%

A MEA has:
- Single-phase soiled solution
- Two to four different main elements
- Main element amounts in a range between 5 and 50 at.-%

A CCA has:
- Multiphase microstructure
- At least two different elements
- Main element amounts in a range between 5 and 35 at.-%

In addition, to avoid the problem of exact classification, the term multi-principal element alloys (MPEA) [4] is defined as a generic term that includes all alloys of HEA, MEA, and CCA.

<u>Four HEA “core effects”</u>

The special composition of HEA, which differs from that of conventional alloys, also gives rise to special properties. These are called the four core effects. These are the high entropy effect, the sluggish diffusion, the server lattice distortion effect, and the cocktail effect. Three of these effects are hypotheses and the cocktail effect is rather a separate description of the HEAs. These effects have been described extensively in the literature [4, 5, 7, 8] and are therefore only briefly explained here.

High entropy effect
Here it is assumed that an increased configuration entropy stabilizes a solid solution phase instead of, for example, intermetallic phases. Reference is made to the second law of thermodynamics, according to which the state is stable at a certain temperature if it leads to the minimization of the free enthalpy *G*. Therefore, for alloys of elementary compounds is valid [9]:

$$\Delta G_{mix} = \Delta H_{mix} - T\Delta S_{mix} \qquad \text{Equation 1}$$

Where ΔG_{mix} is the free enthalpy of mixing, ΔH_{mix} is the enthalpy of mixing, T is the temperature and ΔS_{mix} the mixing entropy. Alloys with high binding energies between elements show low negative ΔH_{mix} and low ΔS_{mix} for the formation of an elemental phase. Intermetallic phases exhibit large negative ΔH_{mix} as well as low ΔS_{mix}. In disordered solid solutions, a low negative ΔH_{mix} and high ΔS_{mix} occur. For simplicity, only the dominant part of the configurational entropy ΔS_{conf} is considered in the mixing entropy [9, 10]. The mixing entropy for the formation of a disordered solid solution of n elements is calculated as follows:

$$\Delta S_{mix} = \Delta S_{conf} = -R\sum_{i=1}^{n} x_i \, ln x_i \qquad \text{Equation 2}$$

With R = 8.314 J/mol*K as the ideal gas constant and x_i as the molar fraction of component i. For equimolar alloys, the configuration entropy ΔS_{conf} for the formation of a disordered solid solution can be calculated according to:

$$\Delta S_{conf} = -R\left(\frac{1}{n}ln\frac{1}{n} + \frac{1}{n}ln\frac{1}{n} + \ldots + \frac{1}{n}ln\frac{1}{n}\right) = -R\,ln\frac{1}{n} = R\,ln\,n \qquad \text{Equation 3}$$

Alloys with one main element show a low ΔS_{conf}. An equal-ranking mixture of different elements causes a significant increase in ΔS_{conf}. The mixing entropy for the formation of disordered solid solutions leads to a reduction in the free enthalpy, especially with an increasing number of components and simultaneously high temperatures. Thus, a stabilization of these phases occurs compared to the formation of elemental and intermetallic phases [1, 4, 10].

Sluggish diffusion effect
Sluggish diffusion [11, 12] refers to the fact that diffusion-controlled processes, such as oxidation [13], phase transformations [14], high-temperature diffusion, particle growth [15], or creep [16], occur at a slower rate. The theoretical basis is the random arrangement of elements and the associated constantly changing atomic configurations and binding energies. This increases the activation energy of elemental diffusion in the matrix, and the diffusion process proceeds at a sluggish rate due to the slowed diffusion kinetics.

To date, only a few results of diffusion experiments in HEA and MEA have been published, and no significant differences in diffusion kinetics were found compared to conventional alloys [4, 8]. Therefore, this effect is currently in the materials science community critically discussed but mostly regarded as an unproven hypothesis.

Severe lattice distortion effect

As a hypothesis, it was assumed that the effect of severe lattice distortion is caused by different elements forming the crystal lattice with different atomic radii. As a result, local displacements of atoms compared to their positions in dilute alloys are assumed. This should lead to enhanced solid solution hardening compared to conventional alloys. Systematic studies on the effect of lattice distortion are rare so far [16]. It is reasonable that this effect does not apply to all HEA compositions.

Cocktail effect

The cocktail effect states that the properties of a mixture of different elements do not necessarily produce the averaged properties of these. Rather, unpredictable properties or even microstructures can arise that may completely deviate from or even exceed those of the pure elements. So, the phrase “[…] the result is unpredictable and greater than the sum of the parts […]" [4] became accepted for this effect. For example, the addition of Al to the CoCrFeMnNi-HEA results in a BCC lattice structure although both Al and the HEA have FCC lattice [17]. This has resulted in a research trend for HEA and MEA to investigate element combinations that were not considered in the past [18, 19].

2.1.2 CoCrFeMnNi-HEA, CoCrNi-MEA, and its derivates

The CoCrFeMnNi-HEA, or "Cantor alloy" since it was first described by Brian Cantor et al. [2], is considered as a model alloy among HEAs. The reason for this, apart from its early introduction in 2004, is the very stable FCC solid solution. Furthermore, it does not contain any exotic components. All these are the reasons why it is the most researched HEA [8]. Nevertheless, this alloy has a very high chemical complexity, especially for basic studies of metal physics and its simulation [20]. Therefore, the MEA sub-alloys, i.e. ternary and quaternary systems, have also become the focus of research [21, 22]. Especially the ternary CoCrNi-MEA is in the focus [20, 23] due to a very stable FCC solid solution and good properties. The most highlighted properties of CoCrFeMnNi-HEA and CoCrNi-MEA are the mechanical properties at cryogenic temperatures [23-25]. For illustration purposes, the engineering stress-strain curves of the alloys at room temperature (RT) are compared in Figure 3 with those in liquid N_2 (77 K). This clearly shows that the strength and ductility of both alloys increase at cryogenic temperatures. The low stacking fault energy is described as the reason for the good mechanical properties at room and cryogenic temperatures. The stacking fault energy of the CoCrNi-MEA is approximately 25 % lower than the CoCrFeMnNi-HEA [23], which is why the MEA exhibits the better mechanical properties (higher strength and ductility) of the two pure FCC materials. The dominant forming mechanism is twinning, but nano-twinning is also described by the authors. The additional grain boundaries form dislocation barriers. Therefore, during deformation, in addition to work hardening, a "dynamic Hall-Petch effect" acts which increases the ductility of these alloys [23].

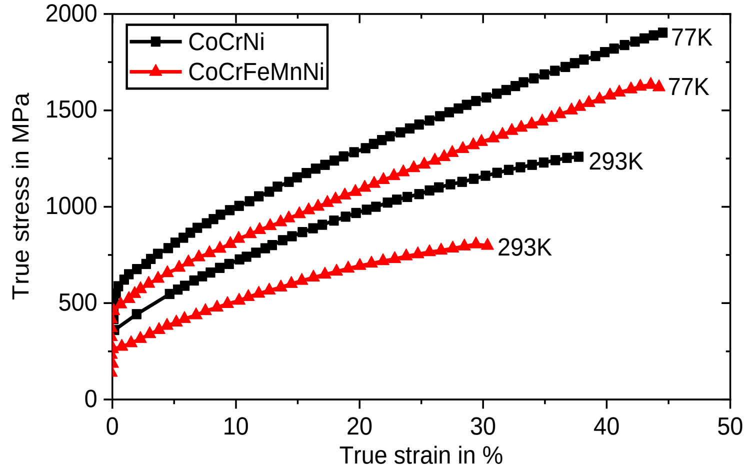

Figure 3: True stress – true strain curves of CoCrFeMnNi-HEA and CoCrNi-MEA at RT (293 K) and in liquid N_2 (77 K), according to [23]

In addition to the mechanical properties, research focuses primarily on the formation of the microstructure. It is shown that both alloys in equiatomic composition form a very stable single-phase FCC phase [25-27]. Only the CoCrFeMnNi-HEA shows the transformation of the FCC phase into an HCP up to an amorphous phase at very strong deformation directly micrometers before a crack tip [28]. However, the alloy composition has an influence on the phase composition, so an increase of the Cr-content with a decrease of the Ni-content shows the formation of an intermetallic sigma phase [14, 15], which leads to hardening and embrittlement. Sigma phase formation could have an influence especially for dissimilar metal welding with high alloyed CrNi steels, following a change in chemical composition. During the welding of CrNi steels, for example, it is known that the sigma phase in the heat-affected zone (HAZ) precipitates at temperatures between 600 and 900°C [29]. In general, an attempt should be made to avoid precipitation of the sigma phase, as in addition to embrittlement, this also results in a reduction in corrosion resistance, as Cr is locally removed from the metal matrix to form a passive layer. Furthermore, the addition of more than 8 % Al to the CoCrFeMnNi-HEA shows with increasing Al-content a transformation of the FCC into a BCC phase [17]. As the proportion of the BCC phase increases, the tensile strength and hardness increase while ductility decreases. At more than 16 % Al-content, a single-phase BCC solid solution appears.

In addition to microstructural formation and mechanical properties at room and cryogenic temperatures, many other properties of CoCrFeMnNi-HEA and CoCrNi-MEA have been investigated. For example the electrochemical corrosion properties [30-32], high-temperature oxidation resistance [13, 33], creep properties [25, 34], fatigue behavior [35], hydrogen embrittlement [36-38], and hydrogen diffusion characteristics [39, 40]. Some selected properties are discussed in detail in the following section with reference to the respective applications. Furthermore, the thermophysical properties are particularly important for (fusion) welding processing. This is because the temperature distribution and the heat conduction into the sheet metal have a major influence on the welding process and the resulting welded joint. Therefore, the thermophysical properties of MPEAs are compared in Table 1 with those of conventional FCC alloys (like AISI 304/ X5CrNi18-10 and Inconel 718/ NiCr19Fe19NbMo3). This shows comparable heat dissipations and thus comparable temperature gradients in the HAZ are to be expected. Due to the comparable specific heat capacity c_p, comparable heat input is required to heat the materials. Therefore, comparable heat input should also be usable for the HEA and MEA welds as for the conventional FCC materials. There is already a big difference in the melting temperatures between both MPEAs. The MEA is in the range of the AISI 304 steel, whereas the HEA is significantly lower. Problems could arise here, especially for dissimilar metal welding (DMW), due to different melting volumes. In conclusion, however, the thermophysical properties of HEA and MEA are very similar to conventional FCC materials and weldability can therefore be expected to be similar, ignoring effects such as phase changes or precipitation.

Table 1: λ - thermal conductivity; α – thermal expansion coefficient; c_p – specific heat capacity and T_s melting temperature of the CoCrFeMnNi-HEA and CoCrNi-MEA compared with conventional FCC matrix alloys (here AISI 304 and Inconel 718). Except Ts are all values for RT

Alloy	**λ in W/mK**	**α in 10^{-6}/K**	**c_p in J/(kg*K)**	**T_s in °C**
CoCrFeMnNi-HEA	13.7 [41]	15.0 [42]	450 [43]	1289 [44]
CoCrNi-MEA	11.4 [41]	16.4 [22]	-	1417 [45]
AISI 304 [46]	16.2	17.8	500	1455
Inconel 718 [46]	9.94	13.4	425	1336

2.1.3 Potential applications for CoCrFeMnNi-HEA, CoCrNi-MEA, and their derivates

HEAs and MEAs offer great potential to replace conventional materials in some areas. In the following, some possible HEA and MEA which are close in composition to the CoCrFeMnNi alloy are presented. The application under cryogenic temperature is not presented (see Section 2.1.2.).

<u>Hydrogen</u>

HEA systems have been investigated with respect to potential applications in the hydrogen economy. Hydrogen is known to cause embrittlement in metals [47, 48], which presents a difficulty for applications under hydrogen exposure with simultaneous mechanical loading. Diffusion of hydrogen has already been studied in several HEA systems that are candidates for hydrogen applications, such as the CoCrFeMnNi-HEA by Rhode et al. [39] or Kim et al. [49]. As a major outcome, a significantly increased hydrogen absorption capacity is shown in the CoCrFeMnNi-HEA compared to austenitic steels such as the AISI 316L [50]. It is also shown that hydrogen desorbs at higher temperatures than in 316L. Furthermore, it is described that the loading method, as for steels, has a great influence on the amount and distribution of absorbed hydrogen [50]. Lee et al. [51] show an increased diffusion coefficient in the CoCrFeMnNi-HEA ($1.75*10^{-11}$ m²/s) compared to the AISI 304 ($0.58*10^{-11}$ m²/s) by permeation studies, which does not make much difference in real terms with a potency of 10^{-11}. In [52] improvements in ultimate tensile strength (UTS) and total elongation were reported for CoCrFeMnNi-HEA after hydrogen loading. These initial studies show that alloys of the CoCrFeMnNi-HEA group show great potential for applications under hydrogen and additional mechanical loading.

High-temperature applications

Perhaps the largest area of research in materials engineering in recent decades has been the development of new materials for high-temperature applications. High-temperature applications require materials that can withstand those extreme conditions in combination with superimposed loads like oxidation or other high-temperature corrosive loads. As a result, there is also great potential for improved high-temperature materials in the field of HEAs. In this context, besides the obvious use of HEAs made of refractory metals, such as an alloy HfMoNbTaTiZr [53] there are also investigations on CoCrNi-based alloys. The problem with HEAs is that they are single-phase by definition, as shown in Section 2.1.1. However, at elevated temperatures particle and solid solution hardening are the main strain hardening mechanism. At high temperatures, most of the alloys studied are multi-phase and some are called high entropy superalloys due to their γ/γ' microstructure, in reference to Ni-based superalloys. These are, for example, $Al_{10}Co_{25}Cr_8Fe_{15}Ni_{36}Ti_6$ alloys with a CoCrNi γ and an AlNiTi γ' phase [53, 54]. With this alloy concept, yield strength at 800°C is comparable to Inconel 617. One way to maintain the definition of HEA/MEA-like MPEA after a single phase and still achieve good mechanical properties at high temperatures is to introduce hard thermally resistant particles. Smith et al. [55] added Y_2O_3 particles to a CoCrNi alloy. They achieved significantly better creep properties at 1093 °C than the commonly used Ni-base alloys Inconel 617 or Haynes 230 alloy, as shown in Figure 4. In addition, this alloy is a laser powder bed fusion additive manufactured and thus can be assumed to have a certain weldability.

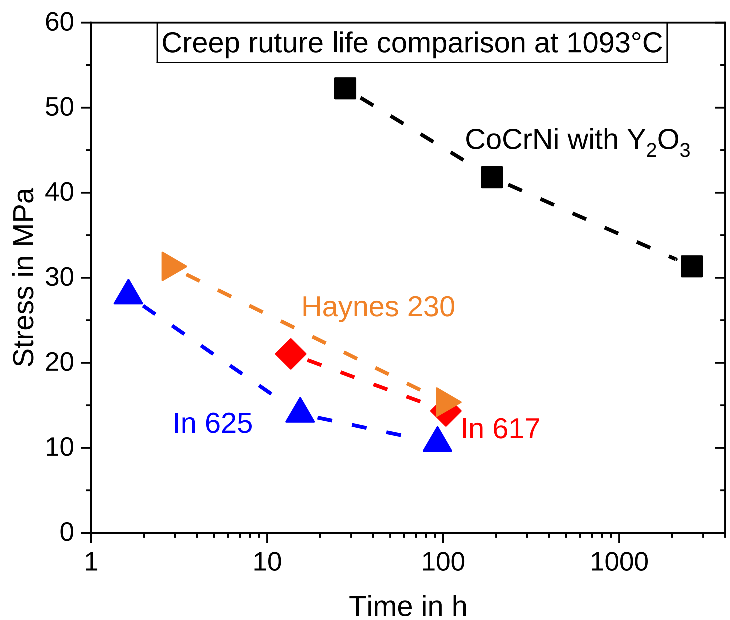

Figure 4: Creep rupture life of as-built CoCrNi-MEA with Y_2O_3 particles compared with current state-of-the-art additive-manufactured superalloys (according to [55])

In addition to the mechanical properties at high temperatures, high temperature corrosion or oxidation is also an important property for high-temperature applications. Here, both in 2 % O_2 and in 10 % H_2O at 800°C, CoCrNi-MEA shows significantly better resistance to oxidation than CoCrFeMnNi-HEA [33]. The main reason is the Mn in the HEA, which causes Mn_3O_4 formation and, above all, porously on the surface, thus preventing the formation of a protective layer. The HEA also shows this at 600°C [56]. The CoCrNi-MEA forms a closed protective passive Cr_2O_3 layer, increasing the resistance to high-temperature oxidation. Bürckner et al. [57] showed that the CoCrFeMnNi-HEA, especially the substitution of Mn, e.g. with Al or Cu, leads to a significantly improved oxidation resistance, as no Mn_3O_4 will form. Pang et al. [56] presented that the initial material condition of the CoCrFeMnNi HEA has a major influence on oxidation. Thus, the oxidation resistance increases significantly with annealing the material for one hour between 700°C and 900°C. This is attributed to the increasing grain size and number of tempering twins.

2.2 Weldability

Definition of weldability

Joint welding involves the creation of an indissoluble material connection between a minimum of two distinct components through the application of an appropriate welding procedure. Welding is one of the most common joining processes for metallic materials. Weldability results from the complex interaction of the (metallic) material with a certain welding process and the construction (design) (see Figure 5). It provides information on whether a metallic material can be joined by means of a welding process for a given design.

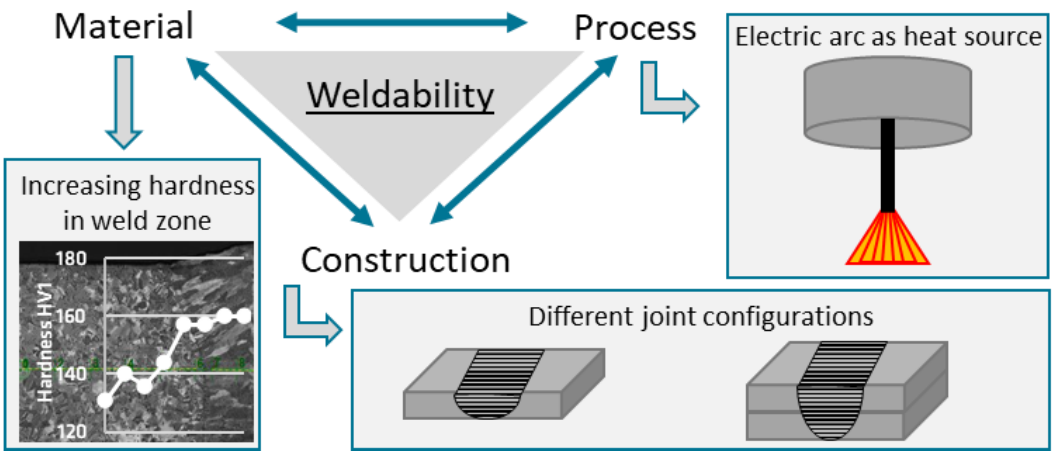

Figure 5: Weldability triangle as a complex interaction between material, construction, and process according to DIN ISO/TR 581 [58] for arc welding processes

Material
The material properties are of fundamental importance for the use of components. In addition to the chemical composition, the material condition (heat treatment condition) also has a major influence on the properties. Here, the mostly unavoidable change in the mechanical-technological properties of the base metals (BM) during welding is considered. This is based on heat input and/or plastic deformation. These can lead to microstructural transformations. This can result, for example, in changes in local tensile strength, ductility, or corrosion resistance. Based on this, welding should not change the mechanical-technological properties of the material significantly or within a tolerable range and in accordance with the requirements for the joint. For simplification, there are three subcategories. These are the changes in metallurgical properties (e.g. grain size), physical properties (e.g. strength), and chemical composition (e.g. aging tendency) [59].

Construction
Constructive weldability indicates whether the constructive design of the welded joints ensures the safe operating behavior of the structure under the existing operating conditions. In particular, the factors of the design (e.g. material thickness or the arrangement of the welds) and the load condition (stresses in the component, loading rate) must be taken into account. The construction-related weldability is only influenced to a small extent by the weldability of the material, which is why it will not be discussed further here [59].

Process
The process-related weldability describes the selection of the best possible welding process. This must be considered the material to be welded and the design. The accessibility of the area to be welded plays a particularly important role here so that the required weld preparation (e.g. preheat-ing), execution (e.g. welding sequence), and post-weld heat-treatment (PWHT) are ensured [59].

<u>Classification of welding processes</u>

For a dedicated assessment of weldability, it is divided into subgroups according to DIN ISO/TR 581 [58]. A classification of welding processes is shown in Figure 6. Welding processes can be primarily divided into fusion welding and solid-state welding, i.e. according to the condition of the weld metal (WM) during the welding process. In the case of fusion welding, processes are as-signed which are carried out by means of local melt flow and without the application of force, with or without filler metal. Solid-state welding is welding with the application of force and relative move-ments or increased temperature, with or without filler metal, in which case local heating can enable or facilitate joining. The welding processes can be subdivided further according to the type of energy transfer, e.g. via an electric arc (electrical discharge of an ionized gas) in arc welding [60].

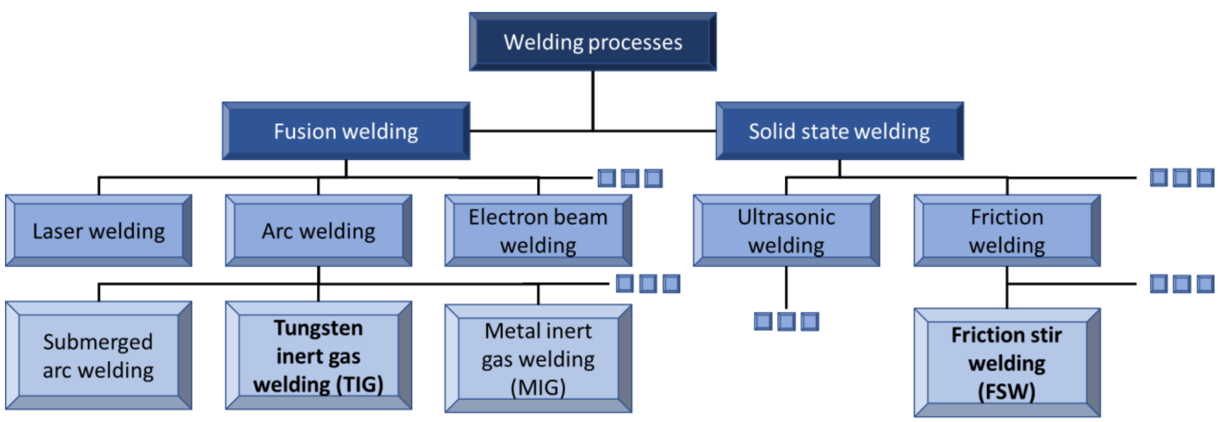

Figure 6: Classification of welding processes (according to [60])

In the following, two welding processes will be discussed in more detail, as these are of crucial importance for this work. These are TIG- and FSW-welding, i.e. a fusion welding process and a solid-state welding process.

2.2.1 Tungsten inert gas (TIG) welding

In the case of TIG welding, the welding arc burns between a non-consumable tungsten electrode and the melting BM. Figure 7a shows the process schematically. Welding is performed under protective shielding gas (e.g. Ar, He, or gas mixtures) to prevent the weld metal (WM) from reacting with the surrounding medium. The shielding gas is ionized between the electrode and the workpiece to generate the electric arc. This requires a voltage to be applied between the electrode and the workpiece [61].

Figure 7b shows the formation of different weld zones by TIG welding based on the local maximum temperatures and the heating and cooling curves. In addition to the temperature-time history, the formation of the zones depends on the material or initial condition. First, a partially melted zone may occur at the fusion line (FL), i.e. the phase boundary to the WM. This zone can be susceptible to segregation of chemical elements e.g. at occurring dendrites and hot cracking due to the short heating and cooling time [59, 62]. In the coarse-grain heat-affected zone (CGHAZ), grain growth and the dissolution of particles such as carbides and nitrides can take place. This is followed by the fine-grain heat-affected zone (FGHAZ), which causes grain refinement by recrystallization. This zone thus exhibits increased strength and toughness. In the intercritical zone, strength and hardness often decrease due to stress relief, recrystallization, and precipitation coarsening [59].

In the area of the arc, the BM melts, creating a molten pool between the BMs. The subsequent solidification, which depends on the energy introduced as well as the heat dissipation, largely determines the resulting microstructure (grain structure, grain size, segregation, or defect formation). In arc welding processes, epitaxial solidification occurs predominantly, in which a dendritic morphology is formed in the direction of the solidification front due to heat dissipation [59].

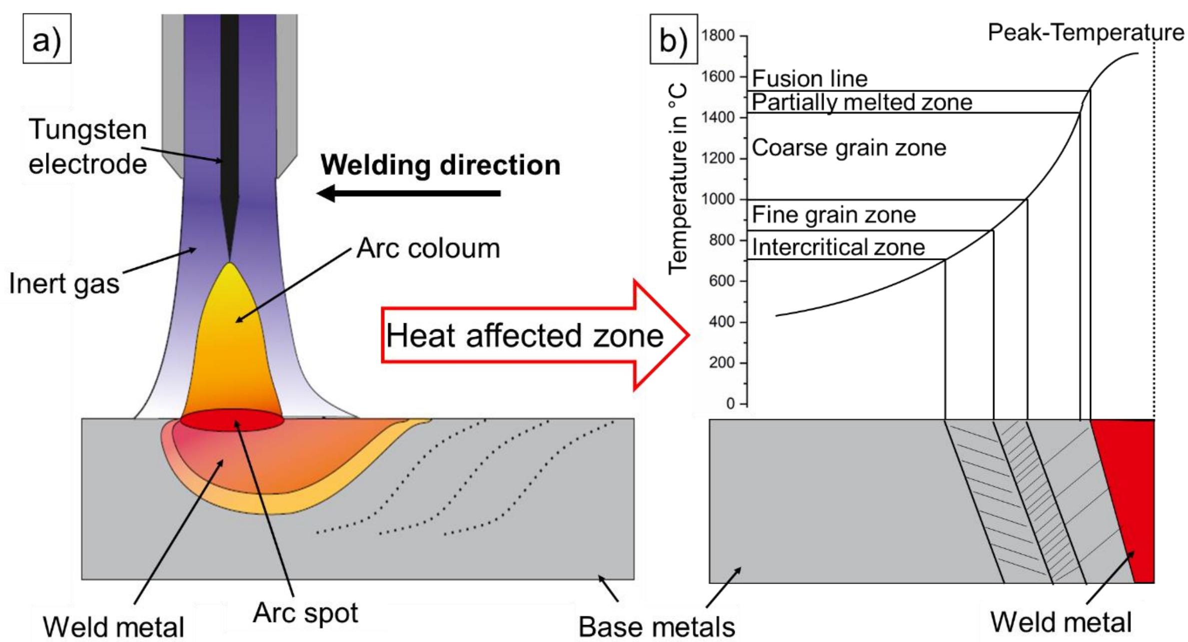

Figure 7: Schematic representation of (a) the TIG-welding process and (b) the forming HAZ, according to [59, 61]) for materials with steel-similar melting temperature

The process presented so far refers to a single-pass weld. Due to multiple heating and cooling cycles, the shaping of the HAZ can become significantly more complex in multilayer welds, but this will not be discussed in this work, as only single-pass welds are examined.

2.2.2 Friction stir welding (FSW)

FSW is considered as a solid-state welding process because the process temperatures are below the melting temperature and materials are thus joined in a solid state. Basically, in the FSW process, the material to be joined is stirred into each other by means of a rotating tool, as shown in Figure 8. The rotating tool consists of a pin and a shoulder, with the stirring pin diving into the joining zone and the shoulder resting on the surface [63]. The basis for the material mixing is the plasticization of the BMs. The plasticization of the BMs is supported by heat, which is generated by the occurring friction between the BMs and the tool as well as by the material deformation. The maximum process temperature is about 80 - 90 % (below the melting point) of the respective BM melting temperature [64]. The explanation for this is the sharp drop in torque with increasing rotation speed [65, 66], which is justified in terms of material mechanics by decreasing yield strength with increasing temperature. Consequently, for a given deformation rate, the power, that can be converted into heat in the material, decreases as it heats up. The softening of the material facilitates the strong plastic deformation, in which the BMs are bonded under elevated temperatures [67]. The rotating tool moves along the weld seam in the welding direction, pressing the tool shoulders against the BM surface. The process can be path or force-controlled. In addition, the BMs are mixed between the welding partners by the pin of the tool in the welding seam.

An asymmetry of the process follows from the relation of the rotary and advanced movements. On one side, the shoulder of the tool moves in the feed direction (labeled as advancing side - AS), and on the other, it moves against the feed direction (retreating side - RS). Thereby, on the AS, due to, a higher relative speed between the workpiece and the tool, more friction and a greater deformation are generated. Consequently, there is a greater heat input on the AS compared to the
RS [63, 64, 68].

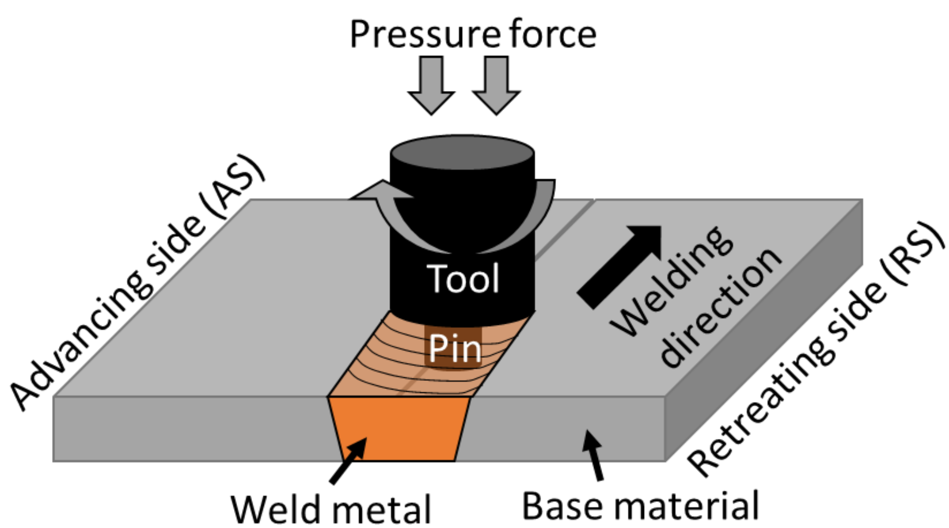

Figure 8: Schematic illustration of the FSW (according to [63])

FSW produces characteristic weld zones, which differ significantly from fusion welds due to the mechanical action of the tool. For this reason, the individual zones, and their cases in terms of material technology are briefly described below, using the schematic example of a FSW seam, as shown in Figure 9.

The zone in the center of the weld, which is characterized by the stirring of the material, is called the stir zone (SZ) or "weld nugget" [64, 69, 70]. The material is severely deformed and sheared around the pin. At the same time, the SZ material is heated by friction and deformation-induced heat. Therefore, it is now assumed in the literature that the resulting fine-grained structure is formed by dynamic recrystallization [64, 71, 72]. Values in the single-digit µm range are given for the grain size in the nugget [64]. Next to the SZ is the thermomechanical affected zone (TMAZ), which also exhibits severe plastic deformation. As controversy discussed in the literature, dynamic recrystallization is assumed as predominant mechanism for material formation [64]. However, a combination of deformation and temporal heat development in the TMAZ is discussed to be insufficient for the recrystallization of the microstructure during FSW [73]. Similar to fusion welding, a HAZ is present. In the HAZ, the material condition is influenced by the process heat, but not by plastic deformation [63, 64, 74]. Compared to fusion welding FSW HAZs indicate lower maximum temperatures (process-related).

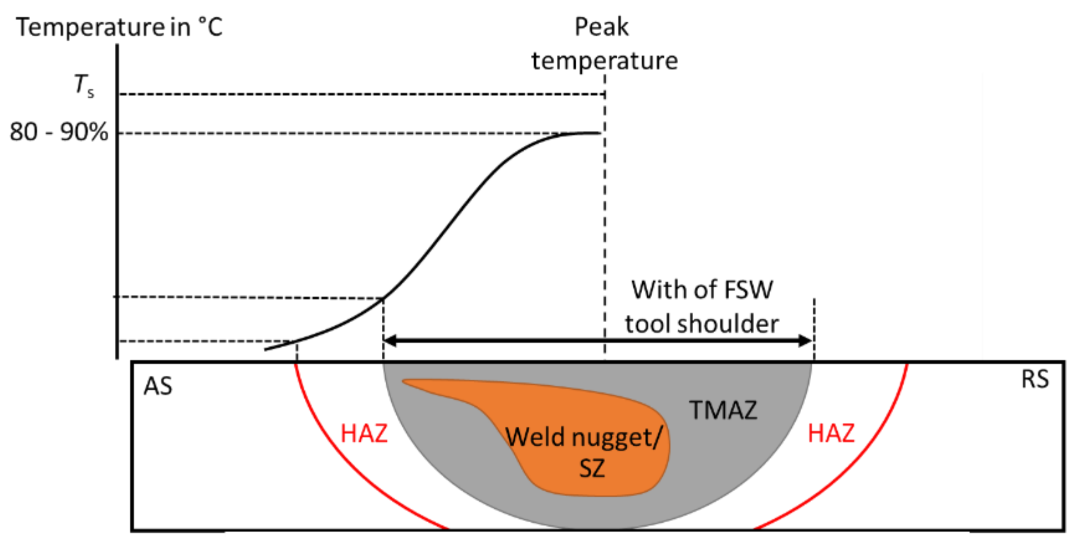

Figure 9: Characteristic weld zones of an FSW-joint and local maximal temperature (with SZ - stire zone, TMAZ - thermomechanical affected zone, and HAZ - heat affected zone)

As mentioned, dynamic recrystallization is the dominant mechanism of microstructural evolution in the SZ and TMAZ. Mechanisms involved in dynamic recrystallization are different from those involved in recrystallization, such as annealing of a deformed material. [72, 75]. The applied strain and deformation temperature determine the homogeneity of the resulting structure. Decreasing the strain rate and/or increasing the deformation temperature results in an increased homogeneity of the recrystallized microstructure. Thus, the homogeneity of the recrystallized microstructure is independent of the dynamic recrystallization. Hence, it results in a uniform microstructure in the SZ, which usually appears as small equiaxed grains. However, in the TMAZ, due to the different strain rates and temperature distribution, only a partially recrystallized structure occurs [76, 77] with a gradient in grain size in-between the BM and SZ. The main influence on the mechanical properties that cause dynamic recrystallization is fine grain strengthening resulting in increased tensile strength and hardness compared to materials in the tempered state.

There are two types of dynamic recrystallization, discontinuous and continuous. Discontinuous dynamic recrystallization is a two-step recrystallization phenomenon. In that case, different steps of nucleation and subsequent grain growth are included [72, 75]. It occurs in materials with low to moderate stacking fault energy, in which dynamic recovery proceeds slowly after reaching a critical strain at temperatures above > 50 % x T_s [72, 75]. On the other hand, continuous dynamic recrystallization is a one-step process that occurs in all materials < 50 % x T_s [72, 75] and also in materials with medium to high stacking fault energy at > 50 % x T_s. New grains are formed by the increase in sub-boundary misorientation. Here, the cause is the continuous accumulation of dislocations introduced by plastic deformation [72, 75]. The 3D network of small-angle grain boundaries develops due to the previous dynamic recovery. The occurrence of discontinuous dynamic recrystallization needs high temperatures and low strains, while continuous dynamic recrystallization occurs at medium temperatures and high strains [78, 79].

2.2.3 Weldability of conventionally FCC alloys

Conventional FCC materials that have a primary FCC matrix are, for example, austenitic stainless steels or Ni-based materials. These materials are widely used and have a broad range of applications. For example, austenitic CrNi steels are mainly used in areas with corrosive loads. Ni-based materials are mainly used for high-temperature applications. In steels, Ni is considered a typical austenite former, so these steels usually contain an increased proportion of Ni. In addition to forming the FCC structure, Ni primarily contributes to improving corrosion resistance but also helps to increase high-temperature strength [80]. As shown in the previous Section 2.1.2 and Table 1, these materials exhibit similar thermophysical properties compared to the FCC HEAs of the Cantor family.

Austenitic steels

Due to their low thermal conductivity (see Table 1), austenitic steels can exhibit a strong temperature gradient in the HAZ, which can lead to possible overheating. Nevertheless, good weldability is observed in practice, due to the weldability without preheating or PWHT [81, 82]. This is true for both TIG and FSW welding [82, 83]. Kurt et al. [82] report the formation of a distinct HAZ with an intergranular ferrite portion between the austenite matrix and the CGHAZ during TIG welding of AISI-304 steel. This leads to reduced hardness in the HAZ and at the same time shows a susceptibility to intergranular cracking in this region [82]. In contrast, during friction welding, Sahin et al. [84] found no significant change in hardness in the weld zone of the AISI-304 steel. Moreover, an ultimate tensile strength (UTS) in the range of the AISI-304 BM is achieved by friction welding [83, 84]. Compared to most HEAs, steels contain some carbon as an alloying element. This carbon stabilizes the FCC phase and improves the mechanical properties. However, carbon has a negative effect on corrosion resistance, as it can lead to the formation of Cr-carbides. This, in turn, deprives the matrix of alloying elements such as Cr, which are beneficial for corrosion resistance. The formation of carbides is temperature-dependent and can occur during welding in the HAZ [59].

Ni-base materials

The weldability of Ni-base alloys has been the subject of intensive research for many years [85]. It has been shown that they exhibit outstanding weldability for a wide range of processes [86], including TIG welding, laser beam (LB) welding, electron beam (EB) welding, and friction welding [87]. Despite these positive properties, however, there are known challenges with Ni-based alloys, such as the formation of hot cracks in the HAZ [85, 86]. These can take the form of ductility dip cracks or liquation cracks. Since these mechanisms can potentially also occur in the FCC-HEA and MEA, they are briefly discussed below.

Typical crack formation mechanisms in welding FCC materials

Ductility dip cracks (DDC)
Ductility dip cracks are hot cracks (occur during or shortly after the welding process at elevated temperatures) that occur when a solid phase is present. These cracks form in materials that exhibit reduced ductility at elevated temperatures in the solid phase condition [88-90]. Occurring welding residual stresses (residual stresses) cause local strains that (are combined with the reduced ductility in the HAZ due to temperature exposure) responsible for the DDCs [88]. They typically have an intergranular propagation with smooth fracture facets ranging from a few micrometers to millimeters [88, 89].

Liquation cracks
This type also belongs to hot cracking. In contrast to DDCs, the formation can be attributed to the presence of phases with low melting temperatures within the matrix alloy, such as sulfide films at the grain boundaries. These sulfides can be e.g. either present in the alloy since the alloy manufacturing or be ingressed as impurities during the materials processing. The welding heat melts these low-melting phases in the HAZ, while the rest of the HAZ remains in a solid phase. When the material then subsequently shrinks, the liquid phase leads to a separation of the material, which cannot absorb stresses in the liquid state [89, 91].

Solidification cracks
Solidification cracks occur during the cooling of a material, whereas interactions between liquid and solid phases occur. The propagation of solidification cracks inevitably occurs along the so-called liquid grain boundary films [92, 93]. In welds, crystallization occurs practically, exclusively heterogeneously, and primarily from the FL due to the high-temperature gradients. An essential prerequisite for the occurrence of solidification cracks in the susceptible regions is the presence of strains, mostly caused by thermal effects and perpendicular to the direction of solidification [94, 95]. When these strains finally exceed a critical value, the separation of the liquid grain boundary films takes place, and a solidification crack develops.

Liquid metal embrittlement (LME)
LME is a phenomenon, in which ductile materials deteriorate their mechanical and technological properties when they encounter another metal in the liquid phase. This occurs due to the penetration of the liquid metal at the grain boundaries of the material. This results in a sudden drop in elongation and strength at fracture, often even before the yield strength is reached [96]. Problems with the LME are well known, especially when welding steels coated with Zn [97] but also for Cu coatings on FCC alloys [98, 99]. Here Cu and Zn act as penetrating phases.

2.2.4 Weldability of high and medium entropy alloys of Cantor alloy family

Ten years after the introduction of HEAs, the first study with the term “welding of HEA" was published in 2014 by Cui et al. [100]. Since then, the number of publications has steadily increased but is still very limited if compared to conventional materials. The biggest share of the publications covers MPEAs derived from the CoCrFeMnNi-based “Cantor” family. Meanwhile, there are already some overview/review publications available [101-107]. In the following paragraphs, the current state-of-the-art on the welding of MPEAs is described. The influence of welding processes, including fusion welding and solid-state welding, and the effects of these processes on microstructure, mechanical properties, and welding parameters are discussed. In addition, possible weld imperfections are described.

Fusion welding

Various fusion welding processes have been investigated on HEAs and MEAs of the Cantor family. These include arc welding processes, usually TIG, LB, and EB welding. The processes described also have the advantage that a welding consumable is not necessarily required, as this was not yet commercially available for HEA and MEA.

It has been reported that by adjusting the welding parameters, welding defects such as (hot) cracks or pores can be largely avoided during fusion welding in FCC CoCrFeMnNi-HEA [108-112]. However, it is important to note that these investigations were limited to remelted BM or single-layer butt welds only, neither multi-layer welds nor complex geometries have been investigated so far.

Fusion welding Microstructure
In general, an epitaxial, dendritically grain growth is formed in the WM by directional solidification along the maximum temperature gradient, i.e., in the direction of the liquid-solid interface. The growth direction is also influenced by the preferred crystal growth direction, which is often in the <100> direction for cubic materials [113]. Various studies [110, 112-115] on fusion welding of CoCrFeMnNi-HEA show that a dendritic WM with pure FCC phase is formed. In addition, no study describes the formation of other phases such as a BCC or intermetallic phases during welding for this alloy. Park et al. [110] investigated the influence of the initial grain size of the BM on the WM by LB welding. It is shown that the size of the dendrites and the dendrite arm spacing (DAS) increase with increasing BM grain size. In addition, the interdendritic regions are enriched in Mn and Ni, while the dendritic regions are enriched in Co, Cr, and Fe [113]. This is attributed to the lower melting temperature of Mn and Ni. Buzolin et al. [112] showed similar behavior during EB welding of a CoCrNi-MEA, with Co enriching in the dendritic regions and Cr in the interdendritic regions. Wu et al. [113] presented that in a high energy density process such as EB welding, the amount of Mn in the WM decreases from about 20 % to 15 %. The reason is the evaporation of Mn during welding due to the high vapor pressure. In the same study, this is not observed in the TIG process. Consequently, the welding process or the energy density has an influence on the chemical composition of the WM. Buzolin et al. [112] investigated the formation of the microstructure of CoCrNi-MEA and CoCrFeMnNi-HEA during EB welding. No phase transformation was found in the HAZ of both alloys. The microstructural change is therefore purely due to static recrystallization and/or grain growth, but this can only be seen in an initial cold-rolled condition and not in a tempered. The same is described by Oliveira et al [111]. Furthermore, it is reported that no CGHAZ or FGHAZ form. Lopes et al. [116] describe a cold-rolled $Cr_{29.7}Co_{29.7}Ni_{35.4}Al_4Ti_{1.2}$ alloy

on the one hand a partially melted zone at the transition between the WM and the HAZ. This consists of partially melted and solidified material along the grain boundaries where the melting temperature is reached. On the other hand, a zone of very fine grains is shown in HAZ directly adjacent to the WM, followed by a zone of larger grains. The larger grains are due to recrystallization and grain growth following the weld heat input and conduction into the HAZ. The FGHAZ is assumed in the study [116] to be a so-called fine equiaxed zone (FQZ). This is typical e.g. Ni superalloys [117, 118] or Al alloys [119]. The formation mechanism has not yet been conclusively clarified. There are two hypotheses for the underlying mechanism. The first one was proposed by Shah [120] that the FQZ is in the partially melted zone and is formed by recrystallization. The second theory was proposed by Kostrivas and Lippold [121, 122] and suggests a heterogeneous nucleation in a stagnant liquid layer at the FL.

Mechanical properties of fusion welds

Several factors influence the mechanical properties of a weld. These are, for example, the welding process or the initial condition of the welded materials (see Sections 2.2.1). In the following, the influences of fusion welding on the mechanical properties of a CoCrFeMnNi-HEA are described. It should be noted that all the welds are single-layer butt joints or bed-on-plate welds. The reason is that studies on complex weld geometries or multilayer welds of MPEAs are rare so far. Figure 10 compares available results from selected studies for the mechanical properties of CoCrFeMnNi TIG-welds with different initial treatment conditions (cold rolled-CR, heat-treated-HT) [111, 113, 114]. In principle, there is a large deviation in the mechanical values, whereby the CR material has a significantly higher strength ($R_{p0.2}$ and R_M) and hardness compared to the HT material. However, it has a significantly lower elongation at fracture ε. The welded joints show similar values for $R_{p0.2}$ ~ 230 MPa and R_M ~ 500 MPa. The elongation at fracture, on the other hand, shows a clear increase in elongation at fracture with the HT BM. The reason is the significantly higher strength of the CR BM, which is also tested in the transverse tensile tests. The hardness also behaves differently in the different initial conditions. The hardness of the cold-rolled material increases slightly in the HAZ and decreases significantly in the WM. Recrystallization phenomena are named as the cause of the hardness peak in the HAZ, which causes grain refinement [111]. In the heat-treated condition, the hardness increases constantly from 132 HV to 165 HV from the BM via the HAZ to the WM. The hardness of the two WMs is in a similar range with ~150 HV (CR) and ~165 HV (heat-treated).

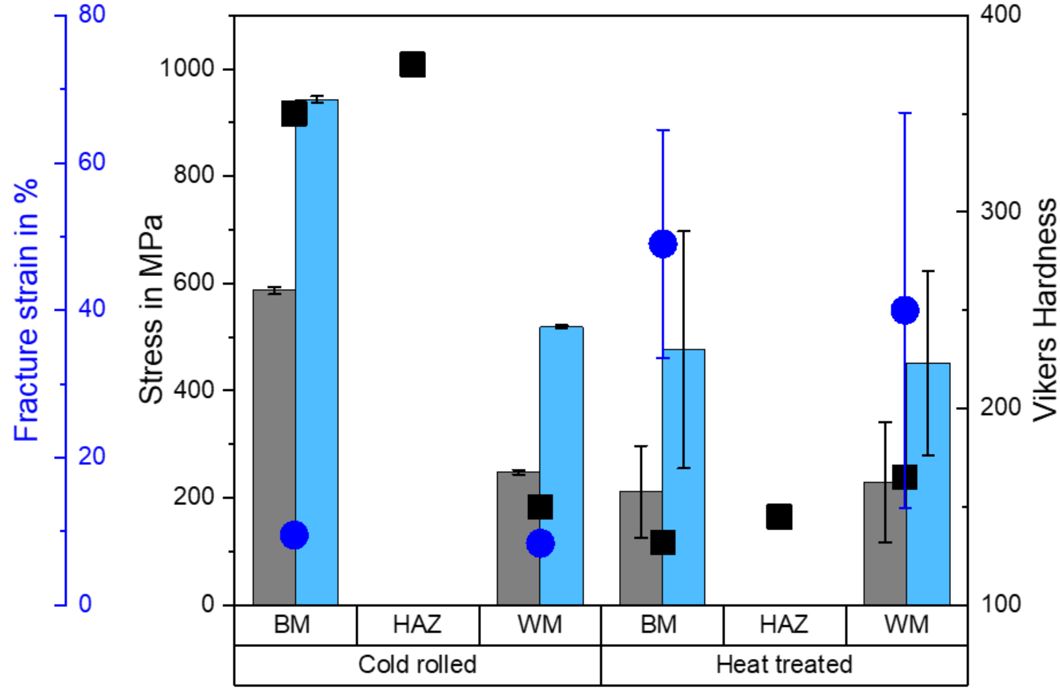

Figure 10: Mechanical properties ($R_{p0.2}$, R_M, Vikers hardness HV, and fracture elongation ε) of TIG-welded CoCrFeMnNi-HEA in relation to the initial condition. Data: CR from [111]; HR from [113, 114]

Park et al. [110] investigated the influence of the initial condition or grain size on the mechanical properties during LB welding of a CoCrFeMnNi-HEA. The results of the tensile tests are shown in Figure 11a. A clear influence due to the initial treatment condition of the HEA can be derived. The as-cast condition with the largest grain size has the lowest strength but the highest elongation at fracture. It is worth mentioning here that the place of failure is located in the BM of the sample. The weld with heat-treated BM has medium strength and elongation at fracture and the weld with cold-rolled BM has the highest strength but very low fracture elongation. It can be assumed that with increasing grain size of the BM, the strength decreases but the ductility increases. The results of Park et al. (shown in Figure 11b) emphasize that the hardness in the WM is always approximately 170 HV0.5, regardless of the initial material condition.

A well-known possibility to improve the mechanical properties of welded joints is a PWHT. Through targeted PWHT, residual welding stresses can be reduced, or desired microstructures can be adjusted. However, there are only a few studies on this for HEA welds. Nam et al. [108] observed a decrease in the mechanical properties of LB welded joints of CR CoCrFeMnNi-HEA sheets. The authors attributed this to the recrystallization of the grains and possibly to the "[…] disappearance of conglomerated dislocations […]" caused by the welding heat input. The PWHT in the temperature range between 800 and 1000 °C had a positive effect on ductility compared to the untreated condition. In PWHT-condition, the HEA-BM and WM exhibited similar strength and ductility properties for. Of course, this is accompanied by a significant decrease in the UTS compared to the cold-rolled BM. Thus, due to the small number of literature studies, no general statement can be made regarding the need for PWHT for welded HEA.

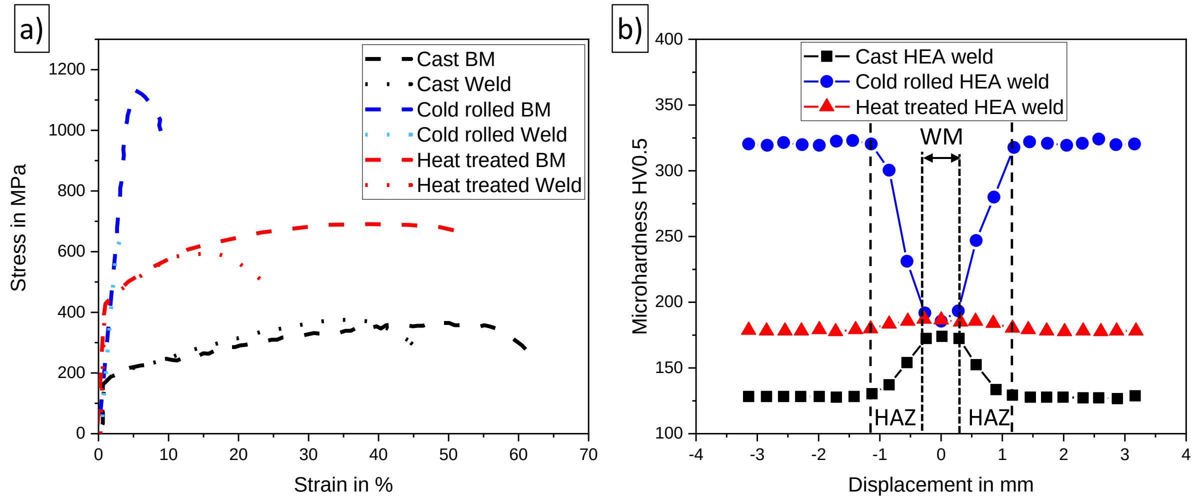

Figure 11: Influence of initial condition of CoCrFeMnNi-HEA during laser welding on mechanical properties: a) engineering stress-strain curves and b) hardness according to [110]

Reported welding defects

The described weld imperfections showed that especially the alloy composition has a great influence. Thus, no weld imperfections for TIG [111, 113, 114], LB [108, 110], or EB welding [112, 113] were described for the CoCrFeMnNi-HEA. A selection of the mentioned studies is presented hereunder.

Nahmany et al. [123] showed for the EB welding of an Al_xCoCrFeNi MPEA (multiphase) with different Al-contents, that at $x = 0.8$ wt.% the occurrence of cracks along the weld center. With $x = 0.6$ wt.% no cracks were described. This is due to the hard and brittle B2 intermetallic phases, the proportion of which increases with increasing Al-content [124]. The authors assume that hot cracks are additionally influenced by the formation of residual stresses during rapid cooling. However, there are no studies on the formation of residual stresses during EB welding of HEA or MPEA so far.

Al_xCoCrCu_yFeNi MPEAs exhibited a significant number of weld defects, including interdendritic hot cracking in the HAZ and WM. These defects include solidification and liquation cracks (see Section 2.2.3), quasi-cleavage fractures, and pores in the WM during TIG, EB, and LB welding [123, 125, 126]. Hot cracking is typically associated with microstructures that consist of at least two phases with different melting temperatures or a certain solidification range, a phenomenon often observed in alloys containing elements such as Al or Ni [95]. Martin et al. [126] showed when the equiatomic AlCoCrCuFeNi MPEA is welded in an as-cast state, Cu-rich phases are present in the interdendritic regions of the weld and at grain boundaries within the HAZ, with the latter remaining in the solid-state. Due to thermal expansion, the welded joint experiences hot cracking in the interdendritic regions where Cu has segregated. Consequently, the limited weldability of Cu-containing MPEA, such as AlCoCr$Cu_{0.5}$FeNi or AlCrCuFeCoNi, can be improved by reducing the Cu-concentration, which tends to promote hot cracking. To provide an explanation for the occurrence of Cu segregation in the interdendritic regions, Martin et al. [126] conducted Scheil solidification simulations. Their results indicated that the as-cast condition of the AlCoCrCuFeNi CCA should feature a dendritic microstructure with a broad melting range between 300 K and 350 K.

Solid-state welding

In addition to the fusion welding processes, there have also been some investigations into the solid-state welding of MPEAs. Different processes such as rotary friction welding [127, 128], diffusion bonding [43, 129], or FSW [70, 71, 130-134] have been investigated. The advantage of these processes is (as described in Section 2.2.2) the process temperature below the melting temperature, whereby the formation of undesired precipitates or brittle intermetallic phases can be avoided, especially due to the complex (and hard to predictable) chemical composition. Most of the publications on the solid-state welding of HEAs and MEAs deal with FSW, which is why it is primarily referred to in the following.

Microstructure of FSW welded HEAs

Basically, all FSW HEA welds show a typical microstructure formation for FSW processes as described in Section 2.2.2. This means a fine-grained WM in the SZ and a TMAZ with a gradient of grain size between the SZ and the BM [70, 71, 131, 134]. Buzolin et al. [71] with the thesis author as co-author describe for FSW-joints of a CoCrNi-MEA and a CoCrFeMnNi-HEA that a HAZ could also be present, but that the temperatures and times achieved here are not sufficient to have a detectable effect on the microstructure. The formation of the TMAZ and SZ are summarized in the study in Table 2. It is also found that the formation is very similar to the austenitic steel AISI 304.

Table 2: Overview of the primary deformation conditions and associated phenomena observed in the various regions of the examined welds, including AISI 304, MEA, and HEA (according to [71])

Region	**TMAZ**	**SZ**
Temperature	• Adequate for dynamic recrystallization • Eventually leading to post-dynamic recrystallization.	Below the melting temperature, but high
Deformation	• Transition from an absence of deformations in the BM to minor deformations occurring towards the WM. • Deformations are significant enough to induce low-angle grain boundary formation, resulting in misorientation spread and, ultimately, dynamic recrystallization.	Severe plastic deformation
Phenomena	• Formation of increased dislocation densities and the spread of misorientation, resulting in work hardening. • Regions exposed to elevated levels of plastic deformation and higher temperatures, dynamic recrystallization and subsequent post-dynamic recrystallization occur.	Elevated temperatures, strain rates, and effective strains experienced in this zone facilitate dynamic recrystallization followed by subsequent post-dynamic recrystallization.

Mechanical properties of FSW welded HEA

To describe the influence of FSW of CoCrFeMnNi-HEAs on mechanical properties, the results from several studies have been summarized in Figure 12. Part a) compares the results of tensile tests on CoCrFeMnNi-HEAs between the BMs and FSW joints from the references [70, 135, 136]. This shows that the welds have strengths in the range of the BM for both $R_{p0.2}$ and R_M. According to Jo et al. [70], this is due to the failure of the weld in the region of the BM, which means that the WM has a higher strength than the BM. This is also supported by the fact that the elongation at fracture ε of the welds is reduced by about half (approx. 0.3) compared to the BM (approx. 0.6). The Vickers hardness for the individual zones of the FSW is compared as a function of the BMs in Figure 12b. Due to the comparison of different studies with each other and thus different experimental conditions, only a qualitative statement can be derived from this. This shows that for cast and cold-rolled BM, the hardness increases from the BM via the TMAZ to the WM. The hardness in the WM is identical for both. On the other hand, the hardness of the heat-treated BM shows the lowest value in the TMAZ, but a significantly higher value in the WM compared to the other conditions.

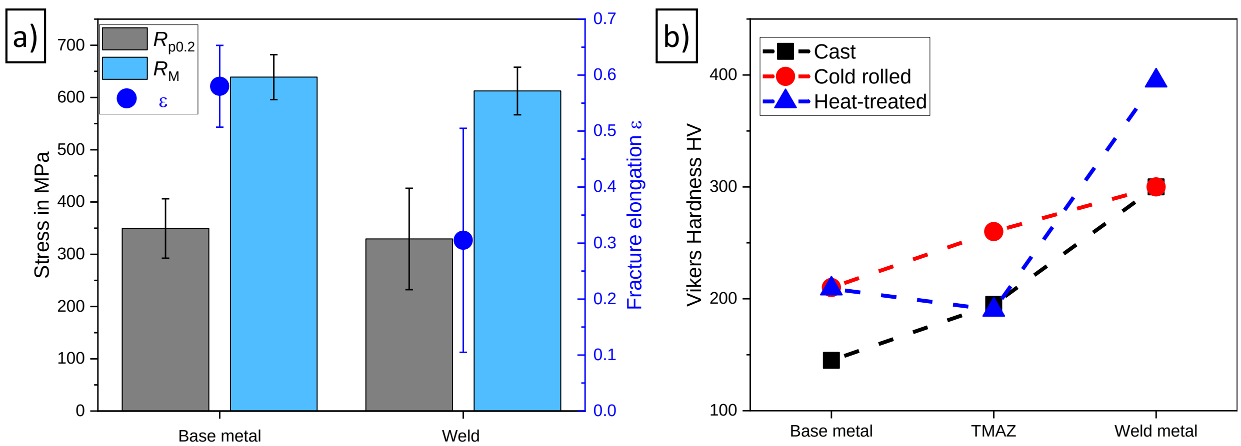

Figure 12: Mechanical Properties of friction stir welded CoCrFeMnNi-HEA from literature: a) tensile test properties of HR-CoCrFeMnNi-HEA as average values from [70, 135, 136] and b) hardness for the BM, TMAZ and WM metal of FSW-joint of CoCrFeMnNi-HEA with cast [131]; CR- [131] and HT-BM [70, 135, 136] base metal

The influence of FSW parameters was investigated by Park et al. [135] for a CoCrFeMnNi-HEA, such as varying rotational tool speeds (400, 600, 800, and 1000 rpm). The results show that the highest strengths ($R_{p0.2}$ and R_M) were achieved at 800 rpm and increased from 400 to 800 rpm. Furthermore, it was described that the sheet thickness in the SZ decreases with increasing speed due to the FSW. Unfortunately, studies on the influence of the welding parameters are very limited. Because no more statements can be made and a great need for research can be derived.

Reported welding defects in FSW welded HEA

In previous studies on FSW on HEAs and MEAs, some weld imperfections have been described. These include the so-called "white bands" [130-132, 134, 135, 137, 138], a strong flash formation [139], tunnel defects [131], or a reduced plate thickness in the WM [71, 135]. The “white band” is an agglomeration of wear particles from the tool, which usually accumulate on the AS in the SZ in metallic materials like the studied MPEAs. Due to the hard surface of the applied tool materials, the transferred wear particles cause increased hardness in the white band defects. According to Park et al. [135] this effect only appears at rotational speeds above 400 rpm for a CoCrFeMnNi-HEA and can therefore be avoided by adjusting the welding parameters. The same should apply to the other described FSW-related imperfections, which are rather process-related and can be avoided by means of a detailed process parameter adjustment [68]. Options for changing the process parameters include the tool geometry or the rotational speed and feed rate.

2.2.5 Dissimilar metal welding of high entropy alloys

The joining of materials by dissimilar metal welds (DMW) offers unique possibilities to meet the specific requirements of modern constructions with different materials. This makes DMW particularly attractive for lightweight construction applications in industries such as aerospace, aviation, and automotive. To produce DMW, different welding processes such as fusion welding [140, 141], and friction welding [142] and their combinations are nowadays used and intensively researched. However, DMW also brings complex challenges. Different material properties can make it difficult or even impossible to form a reliable joint. Especially the differences in the melting temperatures of the welding partners, different heat conductivity and expansions, or the formation of intermetallic phases must be considered [140, 143].

Furthermore, due to the different properties of the welding partners, strong local property gradients can result in the welded joint. This can be (in the word sense) visualized, e.g. by digital image correlation (DIC) during a tensile test [141, 144]. The investigation of GMAW welding CoCrFeMnNi-HEA with an austenitic stainless steel 308L as filler metal clearly shows a strong local elongation in the FLs [144] by means of DIC. This in turn correlates with the formation of large grains in the area and a reduced hardness. It is evident from the only slightly higher elongation at fracture of the CoCrFeMnNi-HEA-BM compared to the joint weld that the WM exhibits increased ductility. DIC shows a local elongation of up to 75 % in the WM, while the BM shows a significantly lower local elongation [144]. In addition to the complex local mechanical properties, Shen et al. [144] also demonstrate the influence of the austenitic filler metal on the microstructure. Thus, in addition to the disordered FCC crystal structure of the HEA, a small proportion (< 3 %) of a disordered BCC structure and the sigma phase (see Section 2.1.3) form in the WM. This shows the complexity of the microstructure that can arise both when using filler metal and when welding extraneous joints.

Olivera et al. in [141, 145] studied laser butt welding for a DMW made of CoCrFeMnNi-HEA and 316 stainless steel. The reference [145] relates to the microstructure formation and mechanical properties of the DMW of a CR-HEA. The WM showed a pure FCC structure, which is described by XRD analysis and a Scheil-calculation. In this context, an increase of the hardness compared to the as-cast BMs was noted, and this can be attributed to solid solution strengthening facilitated by the combination of both the two BMs and the incorporation of carbon from the 316 stainless steel. Additionally, significant columnar grains formed in this area, are expected to have a notable influence on the mechanical properties of the joint. The welded joints demonstrated a UTS of approx. 450 MPa and fracture strain of about 5 %, underscoring the potential suitability of these dissimilar LB welded joints for structural applications.

In the second study by Oliveira et al. [141], a DMW with an annealed CoCrFeMnNi-HEA was used for comparison. Although the Scheil-Guliver solidification model thermodynamically predicted the presence of minor traces of the sigma phase, it was not detected via SEM or high-energy XRD. The disparity between the phases predicted by thermodynamic calculations vs. those experimentally determined can be attributed to the non-equilibrium condition inherent during fusion welding, especially for very fast heating and cooling of LB welding. In this process, the WM experiences significant undercooling, and the slow kinetics associated with the sigma phase formation hinder its development. Although the deformation across the reported joint appears to be relatively uniform, as indicated by the presence of large columnar grains in the fusion zone creates conditions for substantial strain accumulation in this region, ultimately resulting in joint failure. Fracture surfaces of the joint displayed a combination of ductile and brittle failure characteristics. The observed hardness gradient across the welded joint can be attributed to the varying strength of individual compositions, indicating the potential to achieve high-strength materials in the as-cast condition within the CoCrFeMnNi system.

Furthermore, DMW can arise when materials with the same chemical composition, but different material conditions are employed. An examination of DMW composed of rolled and cast CoCrFeMnNi-HEA validates the excellent weldability of HEA [109]. LB welding successfully produced defect-free mixed joints, consistently demonstrating UTS within the range of the cast HEA-BM across a cryogenic temperature range of 77 to 298 K [109].

Samiuddin et al. [146] studied DMWs between CoCrNi-MEA and AISI-304 steel by diffusion welding. The DMW revealed the formation of intermetallic compounds within the diffusion zone. These intermetallic compounds primarily consist of Fe and Cr carbides. Additionally, ultrasonic testing confirmed the formation of a cohesive bond, establishing the foundation for the excellent weldability of this material combination. In conclusion, there are only a few small studies on the DMW of HEAs and no large comprehensive one on weldability as described in Section 2.2. Therefore, there is still a clear need for research.

Previous publications show that DMWs allow the CoCrFeMNi HEA to be fusion welded in various material conditions. In addition, CoCrFeMnNi HEA exhibits good weldability with austenitic steel, as the studies to date describe no weld seam imperfections and acceptable mechanical properties. Nevertheless, it must be noted that due to the small number of published studies, many points are still open with regard to the effect on the application properties. For example, there are no statements on the effect of the corrosion properties, the resulting residual stresses, and some others. In addition, the results to date are limited to DMWs from the CoCrFeMnNi HEA family with austenitic steels. Therefore, the statements can only be transferred to other material combinations to a limited extent.

2.3 Machinability

According to DIN 8580 [147] machining is a process in which the shape is changed by reducing the material bond. A relative movement between the tool and the workpiece, during which energy is transferred, produces the change in shape. According to [148] machinability is the interaction of four mutually influencing factors:

- Cutting force
- Tool life (time or chip volume)
- Surface quality/ integrity
- Chip shape

The physical and technological properties of the material, such as hardness, can have a major impact on machinability. In addition, it is important to consider the functionality of the resulting surfaces when manufacturing a part. This can greatly influence the component life [149], which is further affected by the other factors of machinability. The resulting surface is described by surface integrity, which will be discussed in more detail in Section 2.3.1. The cutting force describes the mechanical load that occurs between the workpiece and the tool during machining. These forces can result in further moments or even temperatures. The tool must be designed depending on the process and the material to be machined. The geometry and the tool material are the major adjusting screws. This means that the tool also influences the material to be machined and the process, as this has a strong influence on the forces and temperatures acting. But the material condition also has an influence on wear. Thus, a tool should always be designed in terms of service life, especially regarding economical component production.Good machinability is characterized by tailored factors, resulting in long tool life, low cutting forces, and good surface integrity. Economic and ecological factors such as energy consumption or the use of cooling lubricants must also always be considered.

In a milling process, the rotating tool has a lateral relative movement to the workpiece (feed), which leads to interrupted cuts. The advantage of milling is the production of complex geometries compared to rotationally symmetrical ones in turning. However, this results in a more discontinuous cutting process due to the higher number of successive cutting operations [148]. Each cut produces a single chip. The material removed per cutting operation depends on several factors, such as tool geometry, tool orientation, and cutting parameters such as depth of cut a_p and feed per cutting edge f_z. All these factors affect the loads between the tool and workpiece, this is described by Kundrak et al. [150, 151] with the theory of the cross-section of an undeformed chip. As mentioned, cutting forces are an important factor in the study of machining processes because they are directly related to the energy consumed, tool wear, and the mechanical load on the resulting surface. Figure 13a shows a schematic of the force compounds generated during cutting on a tool cutting edge in engagement [148, 149]. Here it can also be seen that the resulting force F_{res} can be divided differently. For example, the shear force F_s impacts the chip formation and the normal shear force F_n impacts the surface integrity.

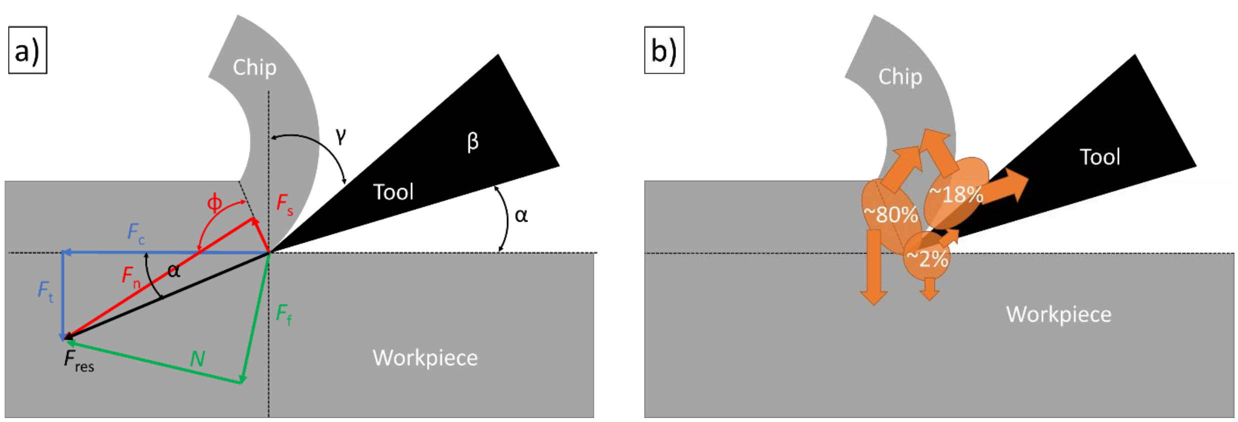

F_s: shear force
F_c: cutting force
F_n: normal shear force
F_t: thrust force
F_f: friction force
N: normal force
F_{res}: resulting force

α: clearance angle
β: friction angle
γ: rake angle
φ: shear angle

Figure 13: Schematic of a) cutting forces (according to [149]) and b) heat generation and transfer (according to [152]) at tool-workpiece-chip contact

The thermal load, resulting from the mechanical load (heat generation due to friction and deformation), is decisive for the machinability. The machinability is significantly influenced by temperature-dependent factors such as tool wear, chip formation, or residual stress formation on the resulting surface. Therefore, heat formation and transfer are schematically shown in Figure 13b. According to [152], ~80% of the heat is generated by material deformation in the shear plane, with the remaining 20% due to friction between tool and chip (~18%) or surface (~2%) [152]. Most of the heat dissipates by the chip (70-90 %) [152]. The actual heat generation and dissipation depend on the respective influencing parameters like the cutting tool geometry (cutting tool angles as shown in Figure 13) or cutting speed v_c. Basically, the low thermal conductivity of the workpiece will lead to reduced heat dissipation and locally higher maximum temperature gradients during the process [153]. Higher temperature and temperature gradients can, for example, lead to phase transformations, and deformation of the resulting surface or introduce residual stresses in the workpiece and tool surface [149].

2.3.1 Surface integrity

The surface integrity is affected by topographic features (surface texture), mechanical and metallurgical properties of the surface, and the edge region [154-156] as shown in Figure 14. Surface integrity is an important concept in manufacturing because it directly affects the service life and component performance by influencing properties such as strength or fatigue and corrosion resistance [156].

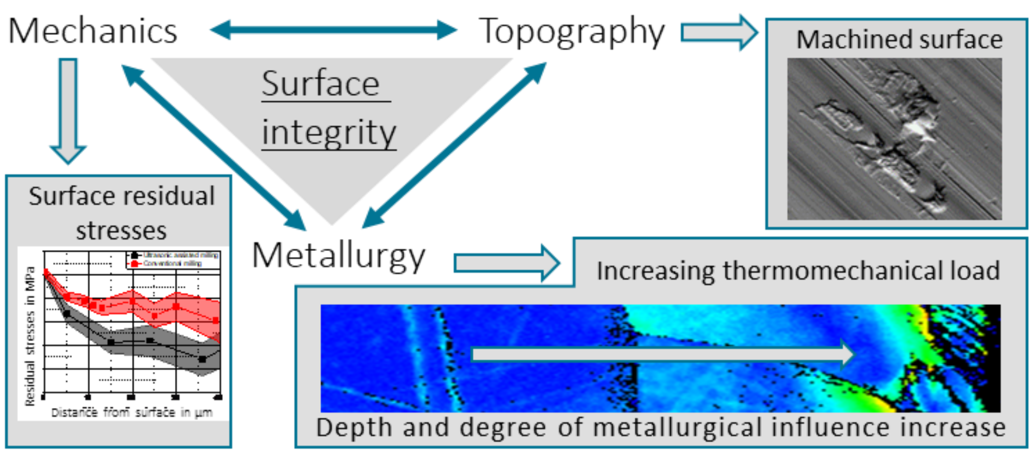

Figure 14: Influential factors on surface integrity (according to [154])

<u>Topography</u>

Surface topography is the most widely used surface integrity characterization method [156]. According to Kalpakjian [149], the topography of a surface is characterized by:

1. <u>Directional surface patterns</u>, which are visible to the naked eye. In finish milling, the cutting tool leaves a pattern on the workpiece.
2. <u>Surface defects</u>. These are, for example, irregularities such as scratches, cracks, or voids.

3. Waviness is a periodic deviation of surface flatness. It is described by the distance between adjacent wavy peaks (width) and the distance between peaks and valleys (height).
4. Roughness refers to periodical or irregular deviations that occur at smaller intervals and scale than waviness. It is expressed by the height and width of deviations from a baseline.

The machining process may cause irregularities in the finished surface. Reasons can be vibrations in the tool and inhomogeneous physical properties of the surface, such as the presence of harder precipitates. According to [157, 158], the most typical surface defects in machining are known as tears, cavities, grooves, and built-up edges (BUE). These are shown in the Figure 15 from the literature [159].

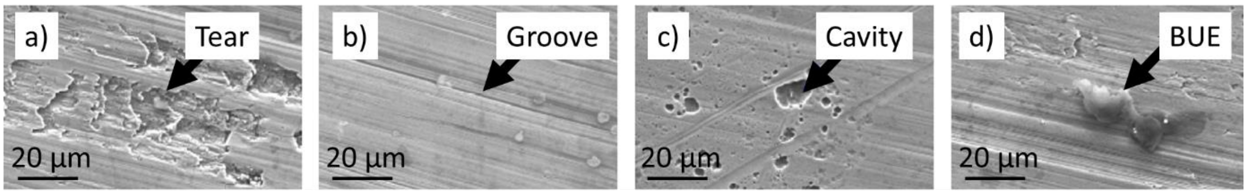

Figure 15: Morphology of surface defects: a) tear; b) groove, c) cavity, and d) built-up edges (BUE) (From [159])

The *tear defect* occurs when a hard particle is struck by the tool tip and the particle tears/cracks under the cutting forces between the tool and the component. This results in an elongated, irregular area where the cracked particles adhere to the surface. This is typically seen at low cutting speeds. High cutting speeds result in higher temperatures and thermal softening of the material. In this situation, the particles lose adhesion in the material and are either forced inward or detached [157, 159].

Cavities can be created when a hard particle, instead of breaking, is detached from the surface. This leaves a cavity with the same surface composition as the surrounding material of the particle. Another possibility is the accumulation of dislocations and microcracks due to friction. This results in rapid fracture of the particle surrounding material, removing a plate-like segment that leaves a cavity [158, 159].

Grooves occur when a hard particle is dragged across the surface by the tool cutting edge, causing long depressions in the direction of tool movement. It may be the result of a hard particle leaving a cavity that has detached from the surface. A built-up edge on the tool can also create grooves on the machined surface [159].

The so-called *built-up edge* (BUE) defect occurs when the material is attached to the cutting edge and adheres to the machined surface. BUE on the cutting tool preferentially forms at high cutting speed [159]. Liu et al. [159] show that for Inconel 718, low cutting speeds result in more numerous and larger tear defects. Higher cutting speeds, on the other hand, cause thermal softening, which leads to fewer tear defects and more cavities, grooves, and BUEs.

Mechanics

The most important mechanical effects on the surface include cracks, plastic deformation, hardness changes, and residual stresses. Cracks in the material can penetrate the subsurface layers and initiate component failure. Therefore, the initiation of cracks should always be avoided. Its occurrence can be prevented by optimal machining conditions, avoiding thermal or mechanical overloads. Plastic deformation occurs in the surface boundary layer while machining and can lead to increased hardness in this area [156]. When no external forces are applied, residual stress is the stress that remains in a body [160]. They result from mechanical load, inhomogeneous heat distribution (temperature gradient), and/or phase transformation associated with volume change. In machining, plastic deformations occur due to the mechanical load applied by the tool to the workpiece. In addition, residual stresses can arise due to local temperature gradients. The generation of tensile or compressive residual stresses is illustrated in Figure 16 using a simplified model. It can be stated that plastic deformation as a result of process forces (interaction between the tool and the workpiece surface) generates compressive residual stresses, while plastic deformation due to thermal stresses leads to tensile residual stresses [161, 162].

Tensile residual stresses reduce the stress reserves of the material before plastic deformation. Therefore, their presence is detrimental as it promotes crack initiation and propagation. Low thermal conductivity of the material leads to higher temperature gradients during milling and thus to detrimental tensile residual stresses. Compressive residual stresses increase the stress reserves of the material. This can be beneficial by reducing crack initiation and propagation. Proper operating parameters during finish milling can improve the fatigue behavior of manufactured components by introducing compressive surface residual stresses [160, 163].

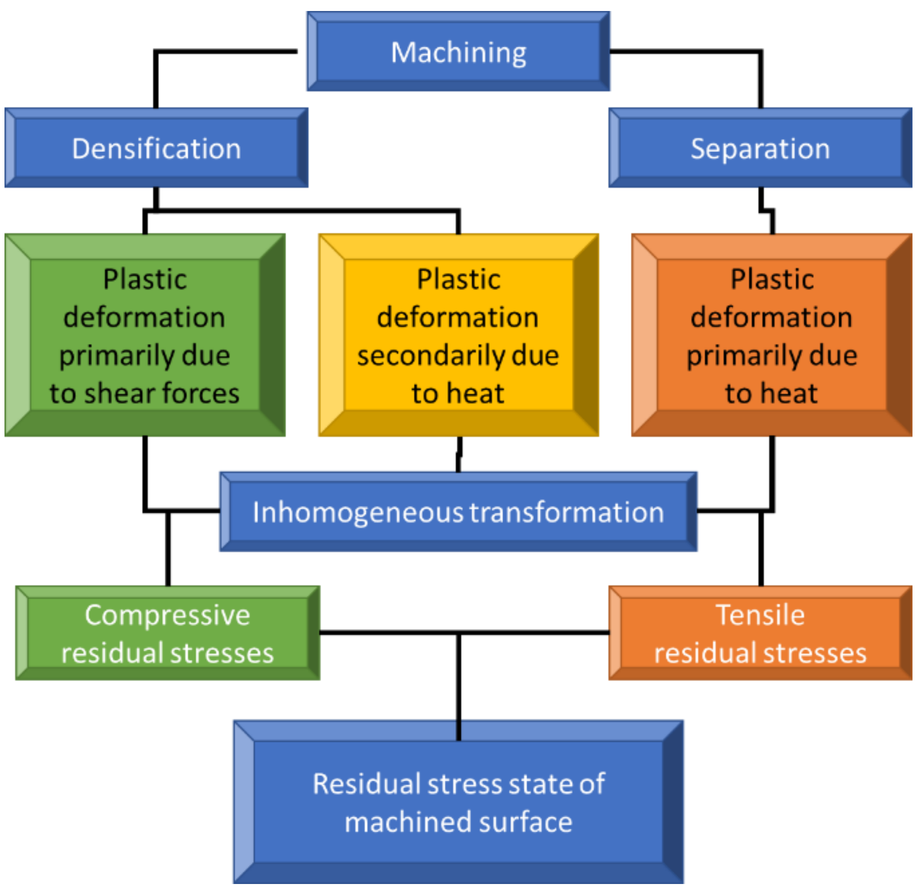

Figure 16: Schematic of the individual processes originating compressive or tensile residual stresses on the machined surface (according to [161])

However, high residual stresses of any kind are generally undesirable. Their relaxation, due to thermal and mechanical loads, can lead to dimensional changes and consequently to failure to maintain dimensional accuracy. Novovic et al. in [164] show the combined influence of external and internal features of the surface on the properties. The authors examined the effect of machining and surface integrity on fatigue performance. They show that residual stresses are a major factor in crack initiation.

Metallurgy

Surface metallurgy is concerned with the material condition on the surface and in the subsurface after machining, and includes metallurgical and chemical effects [156]. Machining causes the surface to behave locally differently from the BM due to the induced thermal and mechanical loading. Figure 17 schematically shows a typical morphology of the subsurface after machining. Studies on steels, Ti, and Ni alloys show a thin layer of highly plastically deformed material. This layer, a few micrometers deep, is also known as the white layer. Plastic deformation can lead to microstructural changes. Possible phenomena include the deformation of the grains, which together with the thermal load causes recrystallization and consequently new grains or phase transformations [154, 165].

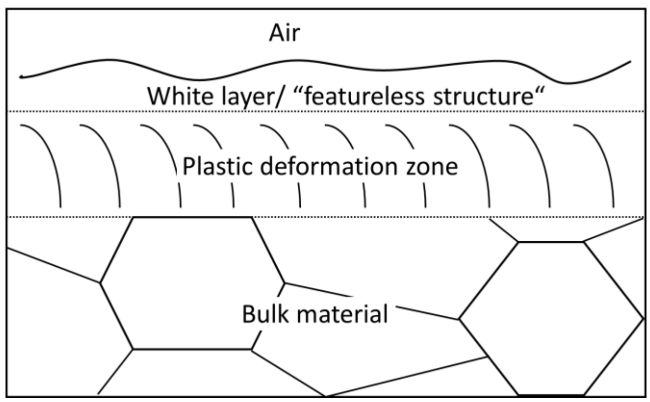

Figure 17: Morphology of machined subsurface (according to [154] and [165])

2.3.2 Ultrasonic-assisted machining

Ultrasonic-assisted machining (USAM) is a hybrid machining technique in which an additional high-frequency vibration with a small amplitude is superimposed on the movement of the workpiece or tool. Examples of USAM include ultrasonic-assisted milling, turning, and grinding. This is intended to improve the machining (reduce cutting forces, heat load at the tool, induce compressive surface residual stress) of materials that are difficult to machine [166, 167]. Periodic reduction of tool-surface contact is the principle of ultrasonic assistance, resulting in reduced contact time. This is shown schematically in Figure 18. Here, the reduced contact time and higher relative speed between the cutting edge and the component surface result in lower friction during the machining [168].

High-frequency vibrations can also soften metallic materials, which is commonly referred to acoustic softening [169, 170]. In dislocation theory, one explanation for acoustic softening is that lattice imperfections such as grain boundaries or dislocations are preferential absorption points for acoustic energy. This in turn reduces the critical shear stress [169, 170]. However, the mechanism is not yet conclusively understood. Experimental acoustic softening has been demonstrated [169] and modeled by Verma et al. in [171, 172]. In addition, a hardening of the resulting surface, referred to acoustic hardening, has been reported. The mechanism for this acoustic strain hardening is assumed to be a mechanically induced increase in dislocation density due to ultrasonic vibration [169, 170]. In addition, depending on the relative angle of the vibration to the surface, an impact effect can be assumed, which can induce compressive residual stresses [154].

The use of ultrasonic vibration has been investigated for several machining processes [173], including turning [163], drilling [174], grinding [175], and milling [154, 166, 176, 177]. USAM uses frequencies above 20 kHz and amplitudes in the micrometer range. In addition, the relative motion between the tool and the workpiece also enhances the process of chip removal and influences the process of surface generation [177]. This shows that ultrasonic machining has many advantages compared to conventional machining.

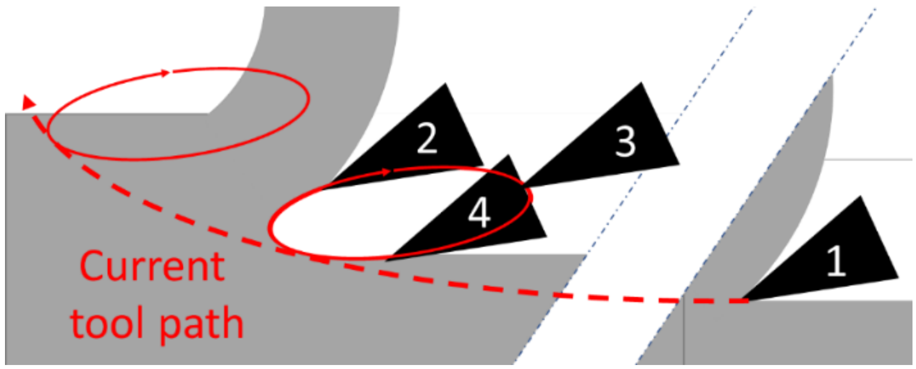

Figure 18: Schematic local of tool, workpiece, and chip relation during ultrasonic-assisted machining (according to [178])

The surface produced by USAM has a characteristic ultrasonic pattern, as shown in Figure 19. The pattern is created by combining axial vibration and tool rotation of the cutting edge relative to the workpiece surface [154]. Chen et al. [178] have demonstrated the functional applicability of the pattern generated by vibration-assisted micro milling in changing the surface texture of Al alloy.

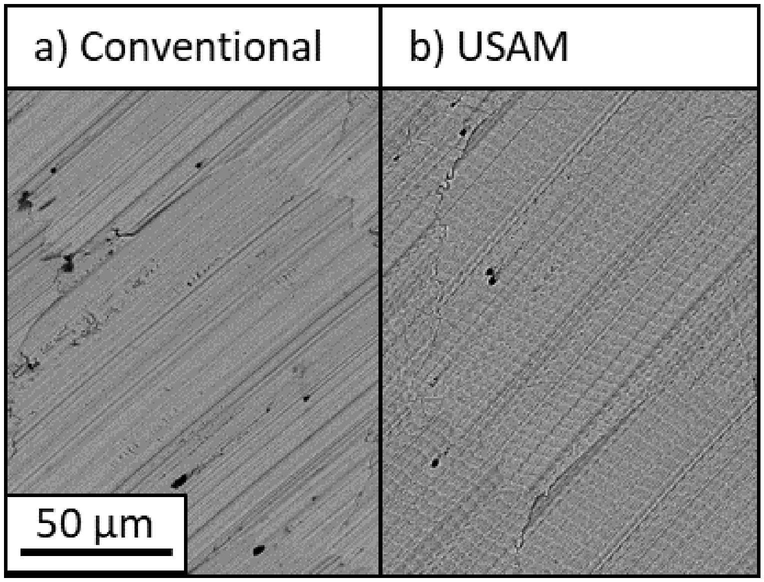

Figure 19: SEM images of a) conventionally and b) ultrasonic-assisted milled (USAM) surfaces of CoCrFeMnNi HEA

Some studies on the influence of USAM on the machinability of hard-to-machine alloys such as Ni-based superalloys [154, 179-181], CoCr alloys [182], or FeAl-materials (iron aluminides) [183] were investigated. Schroepfer et al. [154] studied the effects of USAM on surface integrity in IN725 additive-manufactured structures. It is shown that USAM reduces the cutting forces, especially during dry milling. An improved surface morphology with a reduced density of surface defects is described. Another observation was a reduction of the severe plastic deformation (white layer). USAM leads to a reduction in tensile residual stresses at the surface and induces greater compressive residual stresses in the subsurface. Here, the potential of USAM to inhibit the initiation or formation of cracks or even prevent stress corrosion cracking during subsequent component operation is demonstrated.

Suárez et al. [180] report increased fatigue life for IN718 components after machining by ultrasonic-assisted face milling. Higher roughness values by USAM compared to conventional machining are also reported here, due to the angle of 90° between the surface and the axial tool vibration. Fang et al. [181] show reduced surface defect density and cutting forces when micro milling IN718 using ultrasonic assistance. Here, ultrasonic assistance has a very positive effect on reducing built-up edges.

2.3.3 Machinability of high and medium entropy alloys

HEA and MEA systems have great potential for various applications, as shown in Section 2.1.3. To successfully integrate these materials into actual components, it is imperative to acquire insights into their suitability for machining manufacturing processes. Only a very limited number of studies have been conducted on the machining of HEAs and MEAs. As a result, no extensively structured studies on machinability are available. The existing studies are described below.

Guo et al. [184] conducted a comprehensive investigation into various machining processes applied to CoCrFeMnNi produced via selected LB melting. These processes encompassed milling, grinding, mechanical polishing, wire electro-discharge machining, and electro-polishing. Among these methods, milling had a profound impact on the subsurface, resulting in the highest microhardness (approx. 470 HV) and the highest compressive residual stresses (approx. -650 MPa). However, the influence of the machining parameters is not investigated in this work, so only the individual processes are compared with each other. This does not allow any statement to be made about the

Litwa et al. [185] investigated cutting forces, tool wear, and surface finish on selective laser melted CoCrFeMnNi HEA with lubrication, in comparison to a hot-rolled AISI 304L stainless steel. The study revealed a direct correlation between higher feed rates and depth of cut, leading to increased cutting forces. Interestingly, even at low cutting speeds, higher cutting forces were observed. The conclusions of this study highlighted the superior machinability of the CoCrFeMnNi alloy in comparison to AISI 304L stainless steel. This was attributed to the alloy's ability to accommodate strains, a lower hardening rate, and higher thermal conductivity, all of which contributed to reduced tool wear. It is important to note that the materials are manufactured differently, so comparison is limited due to differences in microstructure.

Kaushik et al. [186] focus on conducting a force and moment analysis of face milling for HEAs, both equiatomic and non-equiatomic ($Co_{0.2}Cr_xFe_{0.2}Mn_yNi_{0.2}$; x= 0.2; 0.25 and 0.3; y= 0.2; 0.15 and 0.1), while varying cutting speed, feed rate, and depth of cut parameters. The study utilizes three different tool diameters to explore the responses. Micro holes and microcracks, primarily attributable to machine vibrations during the machining process are observed. Additionally, the formation of fused particles due to the dry machining condition is shown. Here the machining process led to the generation of microchips, resulting in micro pits on the surface. The recorded milling forces and moments indicate higher feed force values for the $Co_{0.2}Cr_{0.3}Fe_{0.2}Mn_{0.1}Ni_{0.2}$ sample for all tool diameter selections compared to $Co_{0.2}Cr_{0.2}Fe_{0.2}Mn_{0.2}Ni_{0.2}$ and $Co_{0.2}Cr_{0.25}Fe_{0.2}Mn_{0.15}Ni_{0.2}$. Radial forces exhibit a higher magnitude in comparison to feed forces, and there is a clear correlation between forces and chip thickness. An examination of surface microhardness reveals an increase in hardness due to the machining process. Specifically, the $Co_{0.2}Cr_{0.2}Fe_{0.2}Mn_{0.2}Ni_{0.2}$-HEA shows the highest microhardness, of 984 HV after machining.

Delgado et al. [187] studied the effect of conventional and ultrasonic-assisted milling on the CoCrFeNi, $Al_{0.3}$CoCrFeNi and $Al_{0.3}$CoCrFeNi$Mo_{0.2}$ MPEAs. It was shown that the highest cutting speed and the lowest feed rate minimize the cutting forces in the range of the parameters investigated. In addition, the ultrasonic assistance reduces the cutting forces. Hard particles in the CoCrFeNi MEA lead to notches and tear defects, which are detrimental to the surface integrity. The $Al_{0.3}$CoCrFeNi$Mo_{0.2}$ shows material deposits on the machined surface at higher cutting speeds, which is due to the formation of a built-up edge. The highest surface quality is described for the $Al_{0.3}$CoCrfeNi alloy, because of the lowest frequency of surface defects together with the lowest cutting forces.

Constantin et al. [188] studied the dry machining of $Al_{0.6}$CoCrFeNi and compared it with AISI 304, revealing superior machinability in terms of reduced cutting forces and diminished tool wear. Furthermore, their findings led to the conclusion that carbide cutting edges prove effective for machining $Al_{0.6}$CoCrFeNi.

Clauß et al. [189] researched the turning of thermally sprayed MPEA coatings, specifically focusing on the AlCoCrFeNiTi composition. Their investigation employed cubic boron nitride (CBN) tools, characterized by uncertain tool wear. Notably, the study identified that the lowest roughness values were achieved at higher cutting speeds, accompanied by the smallest compressive residual stresses. Liborius et al. [190] investigated face turning of the CoCrFeNi MEA, employing various tool materials. Their findings highlighted that CBN 90 inserts exhibited the most favorable performance, with the lowest cutting forces and minimal tool wear.

The existing research on MPEAs demonstrates that conventional machining techniques can be effectively employed in the processing of these innovative alloys. However, to meet the demands of MPEA components, there is a pressing need for further exploration into milling processes. The overarching objective is to generate functional surfaces characterized by superior surface integrity. This requires extensive studies of the effect of various process parameters on machinability (defined by Section 2.3).

3. Definition of the problem

MPEA is a new alloy concept. These have recently attracted much attention in materials research. HEAs and MEAs have demonstrated substantial potential across diverse applications owing to their distinctive material properties. However, the practical viability of these promising materials necessitates the ability to manufacture components from them. This raises important questions, especially regarding their weldability and machinability. Figure 20, illustrating a chronological sequence of previous milestones in manufacturing technology for HEAs, underscores the rapid progress achieved over the past decade. Nevertheless, the literature review in Section 2 underscores the existing need for further systematic research on the weldability and machinability of HEAs and MEAs before they can be seamlessly integrated into real components.

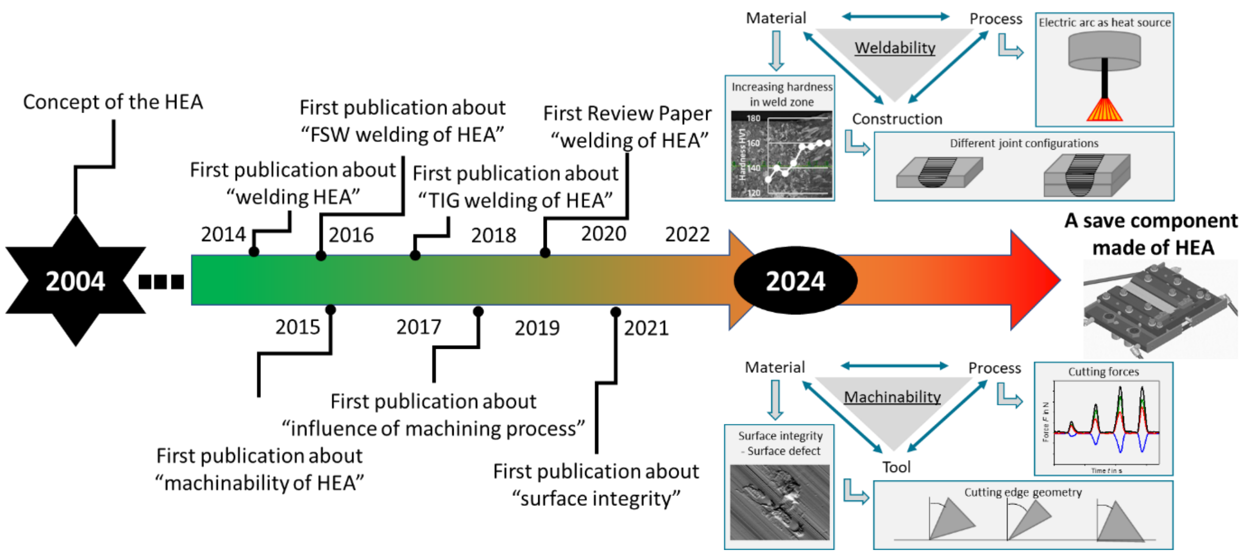

Figure 20: Timeline from the discovery of the HEA concept through the milestones of weldability and machinability of HEAs to the use of HEA in components

1. <u>Scope: Weldability and corresponding welding joint properties</u>

Regarding the weldability of MPEAs, a lot has happened since the first publication in 2014. However, the analysis of the study situation in Section 2.2 also shows that some important factors regarding weldability still need to be clarified and systematically investigated before they can be considered for use in highly loaded components. Beyond the inherent susceptibility of the material to weldability, there arises an inquiry into the consequential application-specific properties. This study explores the interrelation between the structure-property relation, specifically the microstructures that develop, and the ensuing mechanical properties. For this purpose, investigations for a CoCrFeMnNi-HEA and a CoCrNi-MEA are to be carried out within this work for a detailed and systematic description of the weldability with the factors of the weldability triangle (material, process, and design). The influence of the initial condition of both MPEAs is also included, for which a CR and an HT condition will be used. A workflow chart is given in Figure 21.

These materials are to be welded by means of a fusion welding process (TIG) and a solid-state welding process (FSW). Subsequently, the influence of the processing on the material is characterized. For this purpose, the microstructure is analyzed by light optical microscopy (LOM), scanning electron microscopy (SEM) and electron backscattered diffraction (EBSD). The corresponding mechanical properties are determined locally (microhardness and local strain behavior – via DIC) and globally (tensile tests). In addition, the welding-induced residual stresses are analyzed by XRD. Finally, the results of the individual factors are correlated and discussed to predict the weldability and welding joint properties. Furthermore, the effects of weldability on the structural integrity and performance of MPEA components are described. As an important additional investigation, DMWs of the CoCrFeMnNi-HEA (CR and HT) joined to conventional austenitic steel (AISI304/ X5CrNi18-20) using both welding processes were produced, and the properties were characterized.

The aim is to derive practical and scientifically based recommendations for welding MPEAs to each other as well as DMWs with austenitic steels.

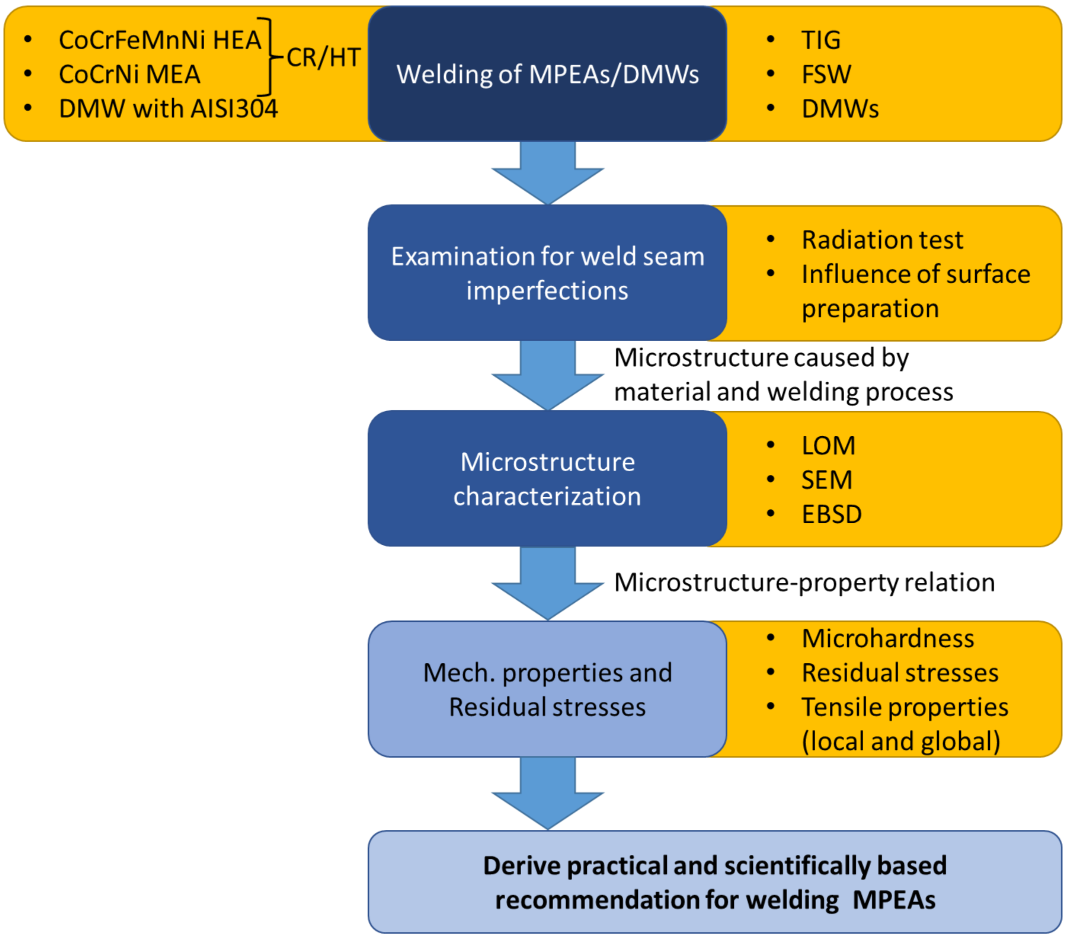

Figure 21: Workflow chart combined with an experimental approach for welding of MPEAs

2. Scope: Machinability of MPEAs and influence on surface integrity

According to weldability, the machinability of MPEAs is important to produce a component. At this point, the timeline in Figure 20 and the literature review in Section 2.3.3 show the development to date of the studies on the machinability of MPEAs. As effects of machining on surface quality and integrity are of crucial importance for HEA components in highly stressed areas for the component service life. As this has not been studied in detail, there is a clear need to investigate the machinability of MPEAs and how this affects the resulting surface/material properties.

In this work, the machinability of CoCrFeMnNi-HEA and CoCrNi-MEA is analyzed for a conventional finish milling and a hybrid USAM process systematically, as shown by the workflow chart in Figure 22. Therefore, the influence of the cutting parameters (feed per cutting edge f_z and cutting speed v_c) is characterized by a design of experiments (DoE). For this purpose, the cutting forces occurring in the process are measured to determine statements about the mechanical load in the process on the surface and tool. In addition, the tool wear is determined. The focus of this work is on the systematic characterization of surface integrity (see Section 2.3.1). This is important for the functional properties and the service life of a component. The first step is the examination of the surface topography for possible surface defects and roughness. Subsequently, the mechanical influence is investigated by determining the machining-induced surface and subsurface residual stresses. The influence on the microstructure in the sub-surface area is determined for selected samples using SEM and EBSD.

The results are used to derive initial recommendations for the machining of CoCrFeMnNi HEA and CoCrNi MEA about the machinability and resulting surface integrity.

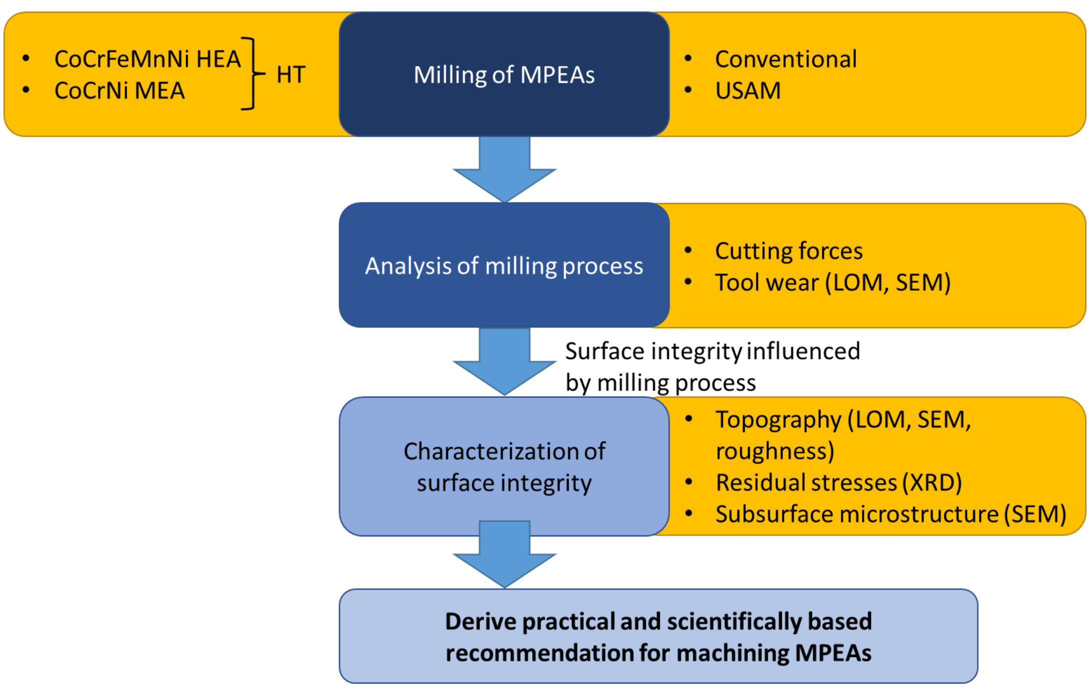

Figure 22: Workflow chart combined with an experimental approach for machining of MPEAs

4. Experimental investigation

4.1 Manufacturing and preparation of the CoCrFeMnNi-HEA and CoCrNi-MEA

In the following chapter, the preparation of the experimental materials is presented. The respective HEA and MEA ingots and CR sheets were synthesized and provided by the research group of Prof. Guillaume Laplanche and Dr. Mike Schneider from the Ruhr-Universität Bochum, Germany.

Base material preparation

Rectangular $Cr_{20}Mn_{20}Fe_{20}Co_{20}Ni_{20}$ and $Cr_{33.3}Co_{33.3}Ni_{33.3}$ (both in at. %) ingots with the dimensions: 145 mm length, 20 mm thickness and 80 mm height, weighing 2.7 kg were prepared. Pure elements (purity > 99.9 wt.%, supplied by Hauner Metallische Werkstoffe GmbH, Germany) were vacuum induction melted in a high purity argon atmosphere (99.998 vol.%) in a Leybold Heraeus IS 1/III furnace with power ranging from 5 to 20 kW, for this purpose. The pure Mn flakes were etched to remove their oxide layer, before melting, using the method described in Ref [191]. To prevent oxidation and evaporation of the elements during casting, the furnace chamber was evacuated to 3 mbar and then filled with Ar (purity: 99.998 vol%) to a pressure of 500 mbar. After casting, the feeder heads of the ingots were removed and the outer cast layer of the rectangular ingots, approximately 2 mm thick, was removed by grinding. Each of the two ingots was then cut into four similar pieces (70 ×35 ×16 mm^3), which were enclosed in individual evacuated quartz tubes (3 × 10-5 mbar), homogenized at 1473 K for 48 h, cooled to RT in air, and removed from the quartz tubes. The resulting chemical compositions are given in Table 3.

Table 3: Estimated and EMPA-measured chemical composition of CoCrFeMnNi-HEA and CoCrNi-MEA

at.-%		Co	Cr	Fe	Mn	Ni
CoCrFeMnNi-HEA	**Estimated**	20	20	20	20	20
	Measured	19.7	20.7	19.7	20.1	19.9
CoCrNi MEA	**Estimated**	33.3	33.3	-	-	33.3
	Measure	33.0	34.3	-	-	32.7

Material preparation for welding experiments

The material preparation for the welding tests is described in the following. One was an electrical discharge machining (EDM) produced surface to introduce targeted contamination, and the other was additionally ground with SiC 600-grit paper. For the investigation of the influence of surface treatment on TIG welding, the rectangular ingots were rotary swaged to a diameter of 16 mm and a length of 100 mm. A final heat treatment for 1 h at 1293 K for CoCrFeMnNi-HEA and 1333 K for CoCrNi-MEA was performed. This results in a single-phase FCC microstructure with a grain size of about 50 µm [192], as shown in Figure 23. Sheets with dimensions 1x14x82 mm^3 (remaining material to the length of 100 mm was used for the milling tests) were produced from the ingots by wire EDM and the geometry is shown in Figure 24. Two different surface preparations were used for the TIG-welding tests.

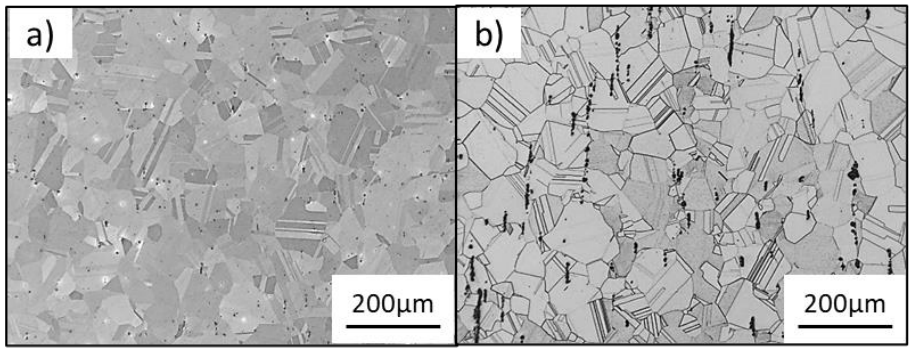

Figure 23: Microstructure SEM-images of the HR ⌀ = 16 mm ingots: (a) CoCrFeMnNi-HEA and (b) CoCrNi-MEA

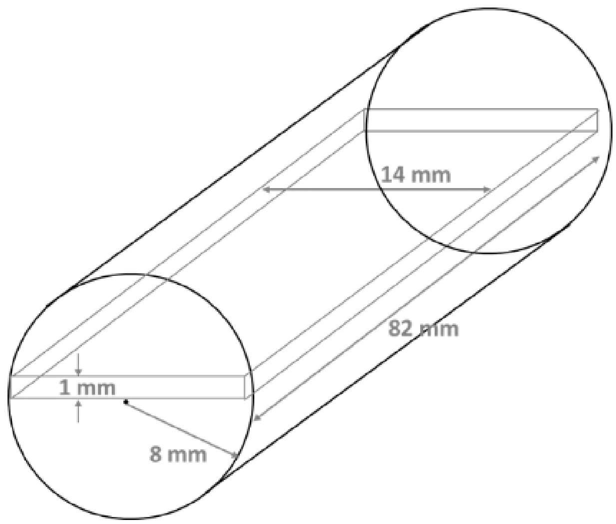

Figure 24: Sample sheet preparation for the influence of surface treatment on the TIG welding, by EDM from the HEA and MEA ingots

For the FSW and TIG-weldability characterization tests, the ingots were CR into sheets with the dimensions 1.2x35x80 mm^3. Half the number of the sheets were additionally HT, the same as the swagged ingots (1 h at 1293 K for CoCrFeMnNi-HEA and 1333 K for CoCrNi-MEA), the other half were used in CR-condition. The resulting single-phase FCC microstructures are shown in Figure 25. The HT sheets in Figure 25a and c show a homogeneous microstructure with equiaxed grains and some twin grain boundaries. In contrast, no individual grains can be seen in the CR micro-structures in Figure 25b and d, only a directional pattern resulting from rolling. In addition, the CR shows a clear number of dark spots, which should be CrMn (HEA) or Cr (MEA) oxides from the material production, but which were not investigated further.

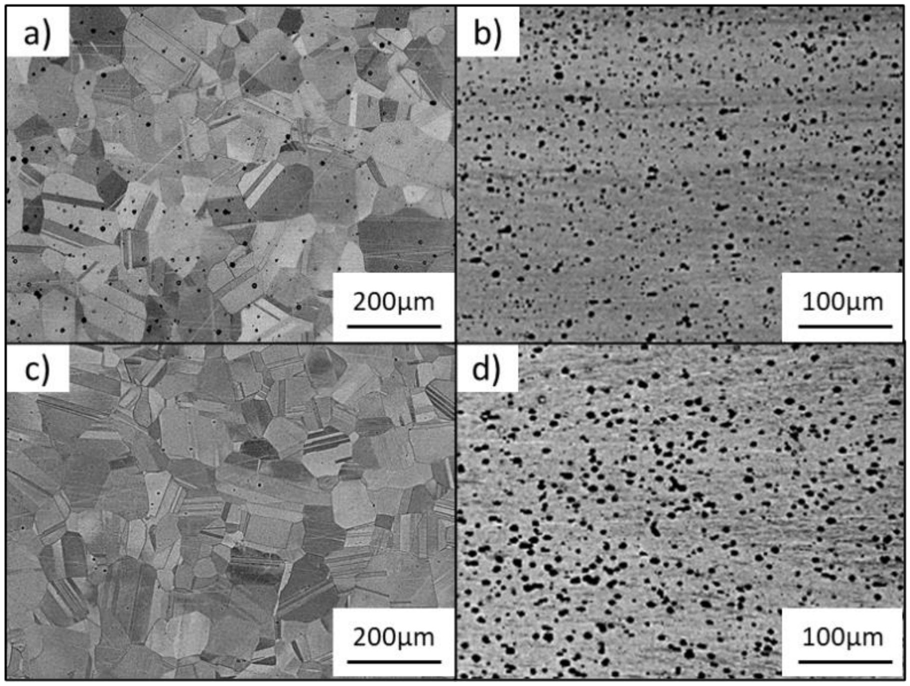

Figure 25: Microstructure SEM-images of the sheets for welding experiments: CoCrFeMnNi-HEA (a) HT, (b) CR and CoCrNi-MEA (c) HT, (d) CR

For the FSW and TIG-DMWs, a conventional austenitic steel AISI 304 (or 1.4301) was used and welded to the CR and HT-condition of the CoCrFeMnNi-HEA. The steel was as-received (specific CR condition with the composition given in Table 4). The geometry of the austenitic stainless-steel sheets was 1.2 x 15 x 80 mm^3. The mechanical properties of both MPEAs and the austenitic stainless steel are given in Table 5.

Table 4: Chemical composition of AISI 304 austenitic steel via the standard DIN EN 10088-3 compared to the optical emission spectroscopy (OES)

Element	DIN EN 10088-3 [193] in at. -%	OES in at. -%
C	≤ 0.32	0.1
Si	≤ 1.93	0.88
Mn	≤ 1.98	1.62
P	≤ 0.08	0.07
Cr	18.27 – 20.36	19.92
Ni	7.86 – 9.71	7.64
Fe	Bal.	69.07

Table 5: Mechanical properties of materials used for welding experiments

Property	HEA-HR	HEA-CR	MEA-HR	MEA-CR	AISI 304
YS $R_{p0.2}$ in MPa	240 ± 13	207 ± 59	254 ± 22	373 ± 134	323 ± 23
UTS R_m in MPa	577 ± 30	1358 ± 70	748 ± 6	1792 ± 4	752 ± 19
Fracture elongation ε in %	46 ± 3	8 ± 2	66 ± 6	8 ± 3	62 ± 2
Vickers hardness in HV0.5	130 ± 3	603 ± 12	187 ± 6	626 ± 9	291 ± 3

Material preparation for milling experiments

For the milling experiments with CoCrFeMnNi-HEA, the rectangular ingots were rotary swaged to a diameter of 16 mm and a length of 100 mm. A final heat-treatment for 1 h at 1293 K for CoCrFeMnNi-HEA was performed. This results in a single-phase FCC microstructure with a grain size of about 50 µm see Figure 23a. Samples with 2 mm thickness were produced via wire EDM and the geometry is shown in Figure 26a. For milling experiments, eight samples were machined, and each plate was used for two milling experiments (each per side). The material for CoCrNi-MEA milling was CR from rectangular ingots. The sheets were additionally HT (1 h 1333 K for CoCrNi-MEA). The resulting single-phase FCC microstructures are shown in Figure 25 c. The sheets were wire EDM in 15 x 15 mm^2 plates, see Figure 26 b. Due to the smaller thickness of 1.2 mm, each plate was used for one milling test.

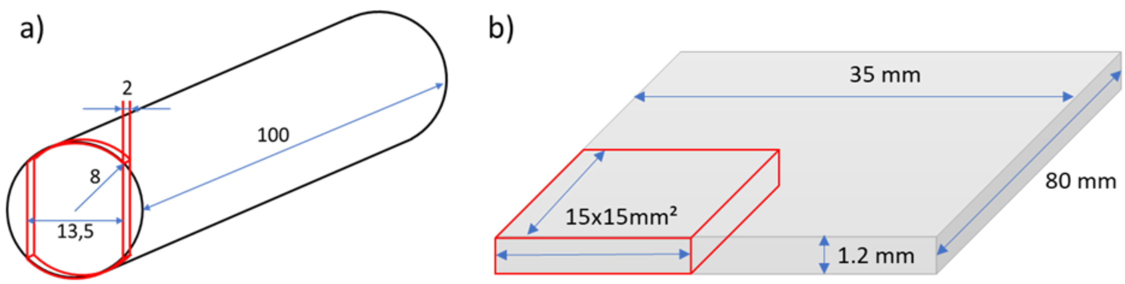

Figure 26: Sample preparation via EDM for the milling experiments; (a) for the CoCrFeMnNi-HEA and (b) for the CoCrNi-MEA

4.2 Welding experiments

In the following sections, the execution, and the methodologies of the analysis of the welding test results are described. It should be noted that due to the low material availability of the HEA and MEA (non-conventional), each test could only be carried out once, i.e., no parameter adjustment could be made. In addition, due to the small sample size for welding tests, a new holder had to be developed for the tests.

Development of sample holder for FSW and TIG-welding experiments

As little material as possible/necessary should be used for each welding test to gain the most knowledge from the limited material available. Therefore, a compact sample size was developed and used for the welding experiment. Consequently, the FSW and TIG process parameters must be adapted. This also includes a suitable specimen holder for small sample sizes. The main requirements for the specimen holder are:

- Usable for FSW and TIG process
- Suitable for bead-on-plate and butt welding
- Applicable for different sheet geometries (1 mm to 2 mm thickness, 30 mm to 120 mm length, 20 mm to 50 mm width)
- Mobility for use in different machines and clamping devices.

A CAD model of the holder design is given in Figure 27. There is a possibility to exchange the base plate. Thus, for the FSW process, an alumina ceramic (low thermal conductivity) can be used, which keeps the heat in the process, is thermally stable, and can withstand the forces. For the TIG process, a Cu base plate with a canal for a backing gas can be used as weld backing, which allows the heat to be dissipated from the sample and provides oxidation protection for the root.

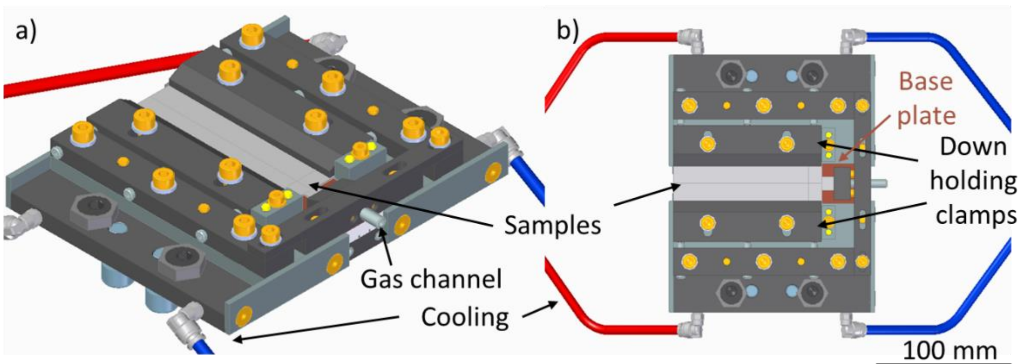

Figure 27: CAD model of specimen holder (a) isometric view and (b) top view

4.2.1 Set-up and applied parameters tungsten inert gas (TIG) welding

Experimental setup for TIG-welding experiments

Before the TIG-welding tests, the surfaces of the weld parts were ground with SiC 600 grit paper (except for EDM surface examinations) and cleaned with ethanol to remove residues of organic compounds such as grease. The welding tests were performed using the specimen clamping system (shown in Section 4.2) specially designed and fabricated for the small specimens. The complete experimental setup is shown in Figure 28. In addition to the TIG torch, a gas trailing gas nozzle can be seen covering the WM even after welding. The same applies to the root, which is protected from oxidation by the backing gas. An I1-Ar (99.996 Vol.-% of Ar, according to DIN EN ISO 14175 [194]) gas quality was applied as shielding gas, and R1-ArH-7.5 (92.5Vol.-% of Ar and 7.5 Vol.-% of H_2, according to DIN EN ISO 14175 [194]) as backing gas. For welding, a Polysoude PC 600 TIG system in pulsed arc mode was used. The applied electrode was a type WR02 (consisting of tungsten and rare earth according to DIN EN ISO 6848 [195]) with a 2.4 mm diameter and an electrode tip workpiece distance of 2.5 mm.

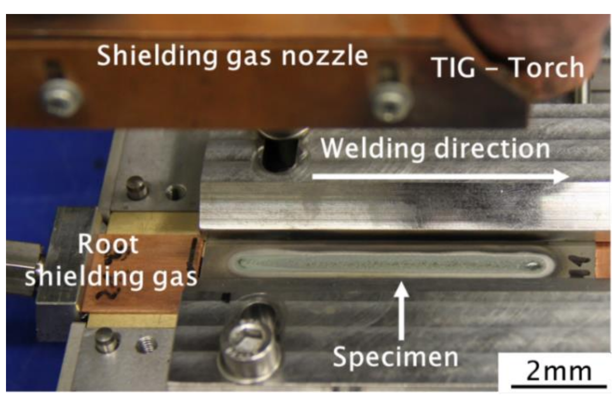

Figure 28: Experimental setup for the TIG-welding experiments

In sum, ten TIG welding experiments were carried out. Due to the mentioned MPEA material quantities, the experiments were set to cover a relatively large material condition framework as shown in Table 6. As a result, the TIG parameters were set constant, and each experiment was welded only one time. In experiments, no. 1 to 4, the influence of surface preparation on weldability was investigated using the cut sheets ingots (⌀ 16 mm, see Section 4.1). For experiments no. 5 to 10, the sheets as described in Section 4.1 were used. Additionally, the MPEA sheets were cut in the longitudinal direction in the center, resulting in the dimensions of 1.2 x 16 x 80 mm^3 (thickness x width x length) for the DMW.

Table 6: Performed TIG-welding experiments with the aim of subsequent investigations

No.	Material	MPEA condition	Seam shape	Aim of investigations
1	CoCrFeMnNi-HEA	HT	Bead on plate	Influence of surface preparation (in as-cut condition by EDM)
2	CoCrFeMnNi-HEA	HT	Bead on plate	Influence of surface preparation (in as-cut condition by EDM)
3	CoCrNi-MEA	HT	Bead on plate	Influence of surface preparation (in as-cut condition by EDM)
4	CoCrNi-MEA	HT	Bead on plate	Influence of surface preparation (ground after EDM)
5	CoCrFeMnNi-HEA	HT	Bead on plate	Metallurgical and mechanical characterization
6	CoCrFeMnNi-HEA	CR	Bead on plate	Metallurgical and mechanical characterization
7	CoCrNi-MEA	HT	Bead on plate	Metallurgical and mechanical characterization
8	CoCrNi-MEA	CR	Bead on plate	Metallurgical and mechanical characterization
9	DMW of CoCrFeMnNi-HEA with AS	HEA-HT	Butt joint	Metallurgical and mechanical characterization
10	DMW of CoCrFeMnNi-HEA with AS	HEA-CR	Butt joint	Metallurgical and mechanical characterization

The underlying TIG-welding parameters were comprehensively determined and optimized by previous experiments in a supervised master's thesis [196] using a single-phase FCC Ni-base alloy (2.4858), since it has comparable thermophysical properties, as shown in Section 2.1.2. The welding parameters for both the bead-on-plate welds and the butt joints are given in Table 7. In that connection, the butt welding was only used for the DMWs (the only difference was increased basic current by 5 A).

Table 7: Welding parameters for the TIG bead-on-plate and DMW butt welds

Bead-on-plate welding			
Basic Current	**Peak Current**	**Arc Voltage**	**Shielding Gas**
30 A (Bead-on-plate) 35 A (DMWs)	90 A	10 V	I1-Ar
Pulse frequency	**Welding speed**	**Heat input**	**Root shielding gas**
4 Hz	300 mm/min	0.13 kJ/mm	R1-ArH-7.5

4.2.2 Set up and applied parameters for friction stir welding (FSW)

The experimental setup and geometry of the FSW tool used are shown in Figure 29 a. A five-axis CNC machining center DMU 65 (by DMG MORI, Germany) was used in position-controlled mode. The FSW tool (cf. Figure 29 b) was made of a sintered W alloy with 1.5 wt.% La_2O_3. The tool shoulder (diameter: 8 mm) was machined in concave condition. The tool pin was 1.1 mm long and tapered (diameter: 2.0-2.4 mm). In addition, three surfaces on the pin were machined to aid in the material transport. During the FSW experiments, the tool was adjusted 2° against the welding direction. During the tests, the temperature was measured directly at the shoulder of the tool (red dot in Figure 29 a) using a ratio pyrometer (measuring range: 350 °C to 1300 °C). In addition, the occurring process force components in the x, y, and z-direction were measured (compare the coordinate system in Figure 29 a) with a dynamometer (Kistler, Germany). Before the welding experiments, the surfaces of all plates were ground with SiC 600 grit paper.

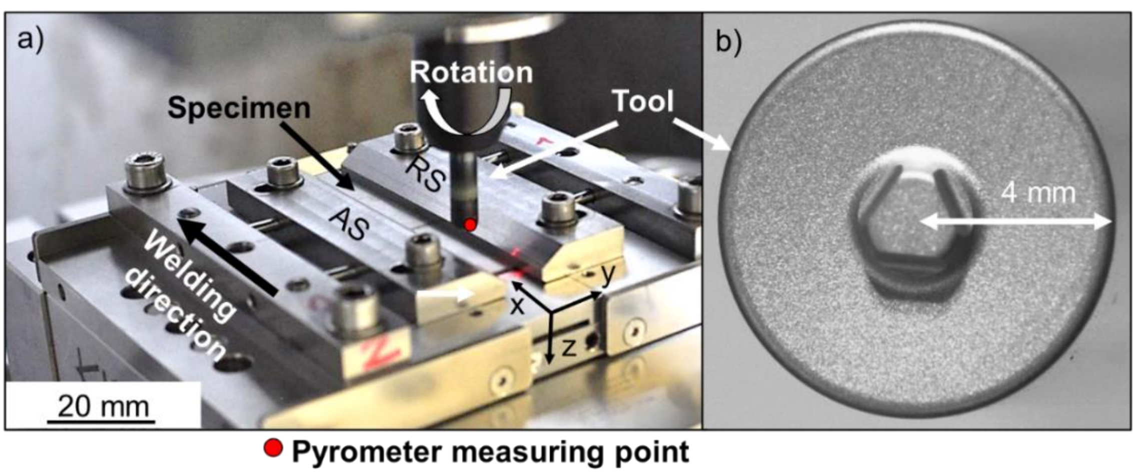

Figure 29: (a) Experimental setup for FSW experiments and (b) geometry of used tool

Six FSW experiments were performed as shown in Table 8. Due to the mentioned material availability, each experiment was performed one time, and only butt joints were welded. In contrast to the TIG-welds, no influence of the surface finish was investigated. All welds were investigated with respect to their metallurgical characteristics and corresponding mechanical properties. In addition, the influence of the AS/RS (advancing and retreating side) was systematically varied for the DMWs with AS on the HEA side and RS on the austenitic stainless steel and vice versa.

Table 8: Performed FSW experiments with the aim of subsequent investigations

No.	Material	MPEA condition	Seam shape	Investigations carried out
1	CoCrFeMnNi-HEA	HT	Butt joint	Metallurgical and mechanical characterizations
2	CoCrFeMnNi-HEA	CR	Butt joint	Metallurgical and mechanical characterizations
3	CoCrNi-MEA	HT	Butt joint	Metallurgical and mechanical characterizations
4	CoCrNi-MEA	CR	Butt joint	Metallurgical and mechanical characterizations
5	DMW of CoCrFeMnNi-HEA (AS) with AISI 304 (RS)	HEA-HT	Butt joint	Metallurgical and mechanical characterizations
6	DMW of CoCrFeMnNi-HEA (RS) with AISI 304 (AS)	HEA-CR	Butt joint	Metallurgical and mechanical characterizations

For all experiments, the sheets described in Section 4.1 were used. The sheets cut into were halve along the center in the longitudinal direction with resulting dimensions of 1.2 x 16 x 80 mm^3. These were then FSW-butt-welded along the longitudinal. The FSW parameters were optimized on austenitic steel AISI 304 sheets (see Chapter 4.1) for a position-controlled process. The parameters are given in the Table 9.

Table 9: Process parameters for FSW tests

Rotation speed	Welding speed	Inclination angle
3000 min^{-1}	100 mm/min	2°
Plunge speed	**Shielding gas**	**Dwell time**
10 mm/min	No shielding gas	0.5 s

4.2.3 Conducted DT and NDT analysis of welded samples

Metallurgical investigation

For each weld specimen, at least two cross-sections were prepared in the welding direction for microstructure analysis. Samples for LOM and SEM were embedded in epoxy resin and subsequently ground to 2000 grit. Afterward, they were polished with a diamond polishing to 1 µm before being etched at RT for 1 min with Adlers etch and for 15 s with Beraha-II. The specimens for EBSD studies were electrically embedded and ground down to 2000 grit. Finally, the specimens were polished with diamond polishing paste to 1 µm and finally, OPS polished. All LOM examinations of the cross-sections were carried out on a POLYVAR MET microscope from Reichert-Jung, with a Gryphax-Altair camera from Jenoptik, Germany. The IMS Client from Imagic Bildverabreitung, Germany, was used as a data acquisition and evaluation program. A Phenom XL from Thermo Fisher Scientific, Germany, was used for the SEM images and the EDX elemental analysis on the cross-sections. EDX scans were performed with an accelerating voltage of 15 kV. In addition, the SEM was also used for fractographic examination of the tensile tests fracture surfaces. The EBSD examinations were carried out in an SEM type Leo 1530VP by Zeiss GmbH, Germany, to characterize the weld microstructure.

Ultrasonic Contact Impedance (UCI) microhardness measurements

The cross-sections of the welds were to be subjected to a hardness measurement for further characterization of the microstructure. For this purpose, a UCI (Ultrasonic Contact Impedance) measurement was carried out on a UT200 from BAQ GmbH, Germany. In this method, a vibrating rod with a diamond attached to its tip in the form of a diagonal pyramid, as in the Vickers test, is placed on a specimen vibrating with a defined force, resulting in a shift in the resonant frequency. The measuring instrument is calibrated before the measurements by means of specimens of known hardness. UCI uses the shift compared to the calibration specimens to assign the corresponding Vickers hardness [197], in this case, HV0.1. Via UCI, the entire corresponding cross-section was mapped. The incremental measuring point distance was 100 µm in the x and y direction to avoid any interdependencies of the local material deformation by the indentation.

Residual stress measurement via XRD

The welding-related residual stresses were analyzed before separating by X-ray diffraction (XRD) by a Stresstech G3 goniometer, Finland, using the $\sin^2\psi$ method to determine the residual stresses (see Table 4). The XRD method was chosen because it determines the near-surface (approx. 5µm for steels [160, 198]) stresses. It has been shown that the maximum tensile residual stresses and the highest residual stress gradients are predominantly present at the surface of TIG-welds and can therefore be detected using XRD [199]. Current comparative investigations in sheet thickness direction, e.g. with neutron diffraction or the contour method on repair welds, confirm this [199]. In addition, possible cracking can be expected at the surface. XRD as NDT-method is more suitable compared to other measurement methods that consider the residual stresses in the volume and require large equipment, such as neutron diffraction.

The following elastic moduli were used to calculate the residual stresses for CoCrFeMnNi (Poisson's ratio ϑ = 0.259; elastic modulus E = 207 GPa, see [200]) and CoCrNi (ϑ = 0.31, E = 235 GPa, see [22]). For the DMWs, ϑ = 0.29, E = 200 GPa (in accordance with [201]) were additionally used for AISI 304 austenitic stainless steel. For the respective intermixed WM of the DMW, the behavior was approximated by the use of the HEA data.

Table 10: Parameters for residual stress analysis

Measuring mode	Radiation	Detector	Diffraction line	2Θ angle
$\sin^2\psi$	Mn-Kα	Linear solid-state	(311)	156°
Collimator	**Tube power**	**ψ–tilting**	**ψ-step**	**Measuring time**
2 mm	30 kV/6.7 mA	0° – 45°	9	2 s

Radiographic testing

X-ray radiographic testing was performed on all welds to check for weld imperfections such as cracks, pores, or tunnel defects. According to DIN EN ISO 17636-1 [202] RTs with a titanium 420 X-ray source were performed. The radiation energy was 100 kV with a fil-focus distance of 1000 mm. The achieved resolution was 50 µm.

Tensile tests instrumented with local strain measurement by digital image correlation (DIC)

Tensile tests were performed to determine the mechanical tensile properties of the welds. The extraction of the tensile specimens with EDM from the welds and their geometry is shown in Figure 30. Dogbone-like flat tensile specimens were used, whereas the geometry is based on DIN EN ISO 6892-1 [203] (scaled sample). The tensile specimens were taken in the as-welded condition for tensile tests, no further surface treatment was carried out.

The specimens were pulled with a high load stretching stage from JPK Instruments after applying a pre-load of 10 N with a constant test velocity (position-controlled) of 10 µm/s. The force and displacement were recorded using the DDS-3 Deformation Devices System from Kammrath Weiss and the associated "Measurement and Control Device Software" (MDS 4.0). The tensile tests and the determination of the mechanical properties were carried out according to DIN EN ISO 6892-1 [203]. However, since the test set-up specially developed within the scope of the present work (see Figure 31) did not allow for strain measurement by means of an extensometer, the strain was approximated by determination from the machine's crosshead displacement. To validate the described procedure of strain measurement, the strain calculated from the machine path was compared with determined strains by means of DIC (which is described later in the text). Due to the agreement of the results of both methods, the procedure is considered valid. The crosshead displacement was converted into a strain ε in % in accordance with Equation 4, using the initial length L_0 in mm of the tensile specimen determined after clamping of the specimen and the measured change in length ΔL in mm:

$$\varepsilon = \frac{\Delta L}{L_0} * 100 \qquad \textit{Equation 4}$$

Subsequently, and in accordance with DIN EN ISO 6892-1 [203], the stress σ in MPa was calculated via Equation 5 from the initial cross-section S_0 in mm² of the specimen and the measured force F in N:

$$\sigma = \frac{F}{S_0} \qquad \textit{Equation 5}$$

Subsequently, an engineering stress-strain diagram was generated for each tensile test. The test set-up as shown in Figure 31, and the underlying procedure for evaluating the local strains using DIC were developed within another supervised thesis (K. Erxleben, see [204]). For the DIC measurements, automated LOM images were taken every 20 s during the tensile test. A VHX Digital Microscope from Keyence was used for this purpose with the lens aligned vertically above the flat tensile specimen. For the 2D image analysis, the weld top surface was monitored. The GOM Correlate software (now ZEISS, Germany) was used for local strain calculation by analysis of the single images, which is based on DIC and point tracking algorithms [205]. For that purpose, both a high-contrast and fine stochastic pattern on the specimen are necessary prerequisites. To achieve this, the samples were previously manually sprayed with black and white paint. To ensure the quality of the pattern, test runs with the GOM Correlate software were conducted for each sample before the tensile test. In the correlate software, a facet size of 25 pixels and a dot spacing of 16 pixels were selected for all tests. The parameters ensured repeatable results. Moreover, the preliminary tests proved that the strain calculated via DIC by the GOM software agrees with the strain calculated via the change in length during the tensile test. Nevertheless, an internal deviation of ± 2 % (absolute error) must be considered for the strains determined by DIC. The deviation was determined based on 25 images of a stationary specimen. The procedure and first results of these investigations are published in [206].

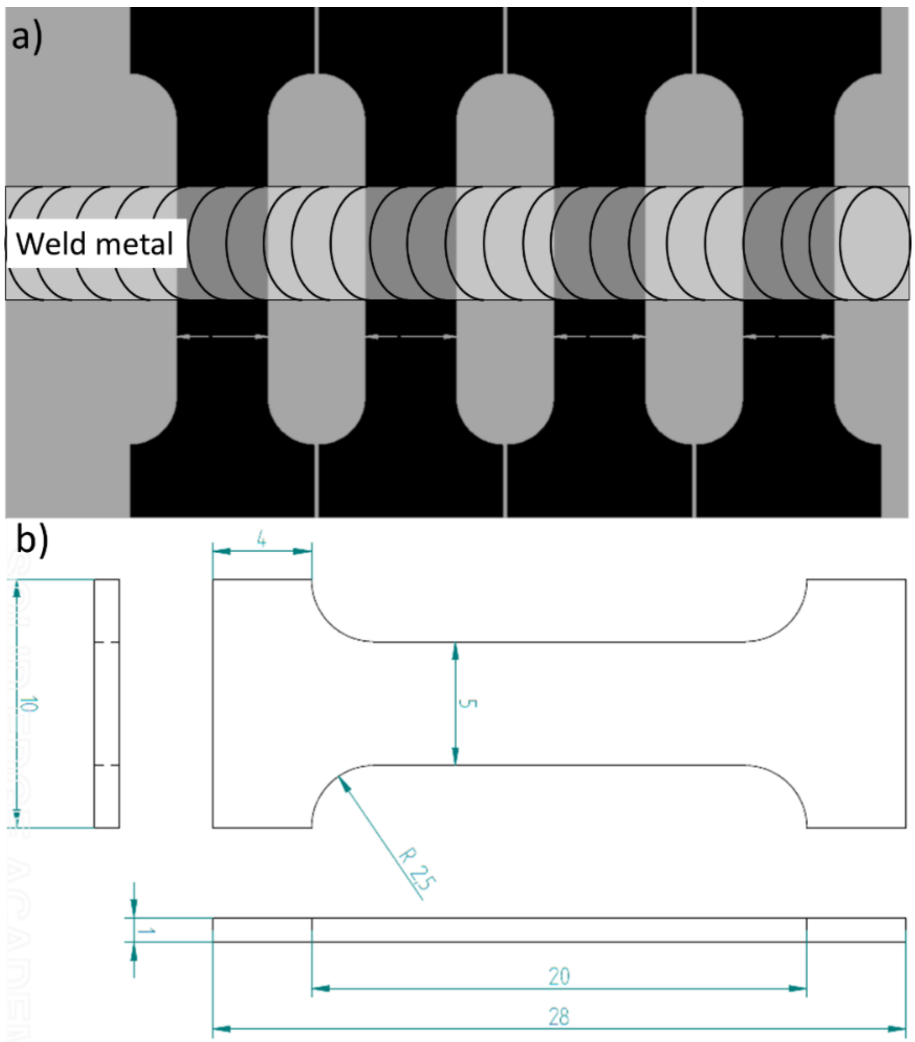

Figure 30: (a) Schematic image of tensile test samples manufacturing from welded joints and (b) geometry of tensile test samples

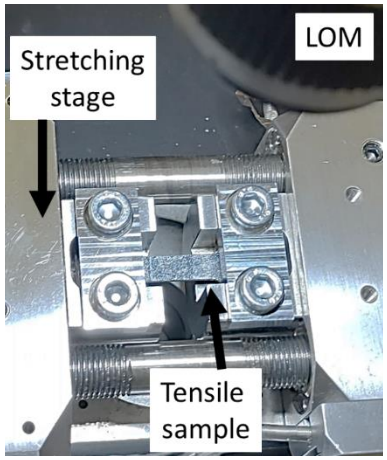

Figure 31: Loading frame setup for DIC-assisted tensile tests

4.3 Finish milling experiments

4.3.1 Experimental setup of finish milling experiments

All milling tests were carried out on a five-axis machine gantry (DMG-MORI DMU 65, Germany) modified for the USAM hybrid process. The experimental setup for down milling is shown in Figure 32 a. During the milling tests, the forces were measured in x-, y-, and z-direction with a dynamometer type 9139AA (Kistler, Germany). Figure 32 b provides a schematic representation of the cutting process with a ball nose end mill. The depth of cut a_p is the tool penetration into the material in the z-axis, defined by the normal direction to the material surface. The cutting tool rotates at a constant rotational speed n and is moving in the feed direction defined by the x-axis. A key parameter is the feed per cutting edge f_z in mm, i.e., the depth of material cut by each cutting edge in the feed direction. The distance between every successive tool pass is the stepover a_e in mm.

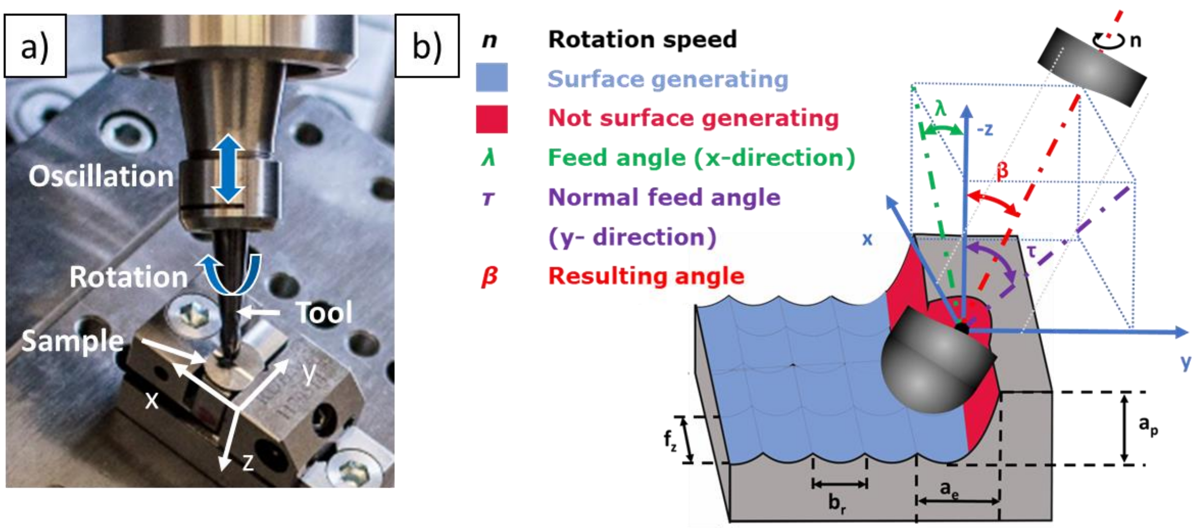

Figure 32: Experimental setup of finish milling experiments; (a) real setup; (b) schematic setup from [207]

The tool inclination angle in feed direction x is the feed angle λ, and τ is for normal feed angle in the y direction. The combination of feed angle and tilt angle provides the resulting angle β of the tool axis above the normal to the specimen surface, as shown in Figure 32 b. The resulting angle β is calculated from λ and τ according to the following Equation 6 [152]:

$$\beta = arcos\,(\frac{\cos\tau * \cos\lambda}{\sqrt{\cos\tau^2 * (\sin\lambda^2 + \cos\lambda^2 + \sin\tau^2)}}) \qquad \textit{Equation 6}$$

Together with a_p, a_e, and f_z, the tool orientation angles λ and τ determine the chip volume removed by each cutting edge as well as the topology of the final surface obtained. The relative speed between the tool cutting edge and the machined surface is a main factor in the process. The cutting speed of ball nose tools varies along the tool cutting edge due to the locally varying tool diameter therefore, an average cutting speed is determined. The tool angle β allows for describing the contact angle κ between the cutting edge and the material, between κ_{min} and κ_{max}, (Figure 33).

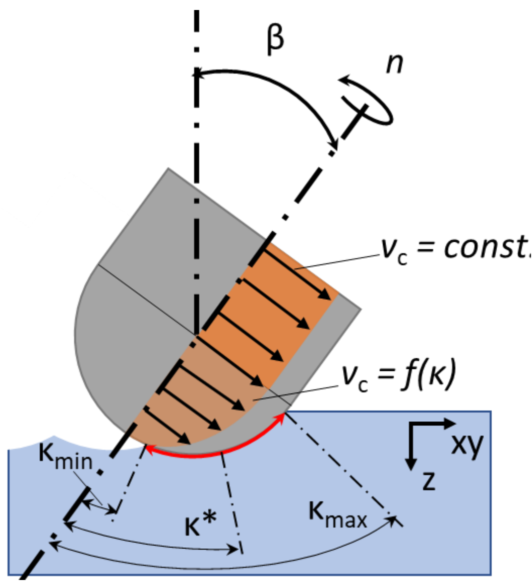

Figure 33: Geometry of tool-workpiece contact according to [152]

The effective tool diameter d_{eff} is defined at the upper contact point κ_{max} and is calculated according to Equation 7 from [208]:

$$d_{eff} = d * \sin(\beta + \arccos(1 - \frac{2a_p}{d})) \qquad \textit{Equation 7}$$

In conclusion, the cutting speed v_c is defined at the effective diameter d_{eff} by *Equation 8*:

$$v_c = 2\pi * \frac{d_{eff}}{2} * n \qquad \textit{Equation 8}$$

The used tool is a right-handed ball nose end milling cutter with four cutting edges according to DIN 6527L [209]. The tools are made by the manufacturer WOLF Werkzeugtechnologie GmbH and have a diameter D_t of 6 mm, a helix angle of 30°; a clearance angle of 15° and a rake angle of 4°. The cemented carbide tools consist of a core with WC particles embedded in a Co-matrix.

The tools are physical vapor deposition (PVD) coated (thickness of 2 to 3 µm) with AlSiTiN for the HEA and with AlTiCrN for the MEA. These coatings are intended for finish milling of hard-to-machine alloys such as the Ni-Cr-alloy IN-718 (EN 2.4668). A new milling tool was used for each series of tests.

Design of experiments (DoE)

The experiments carried out are intended to investigate the influence of the main machining parameters of milling on the resulting surface: the cutting speed (v_c), the feed per cutting edge (f_z), and the use of ultrasonic support (US). These parameters are directly related to the mechanical interaction between the tool and the machined material and using v_c and f_z to define the machining conditions allows the tests to be reproduced with a different tool geometry and still be comparable.

The tool manufacturer has specified the optimum dry-cutting conditions for Ni-base alloys in Table 11. The additionally selected tool orientation prevents cutting with areas with the lowest cutting speeds at the tooltip (compare Figure 33). Yang Pan et al. [210] and Nespor [152] have shown the positive effects of introducing tilt and rotation angles on tool position. With the conditions listed in Table 11, the central points of the experiment (Test No 5 and 6 for conventional milling, 11 and 12 for USAM according to Table 12) were established. The tool orientation, down milling mode, depth of cut a_p, and step over a_e were kept constant. The cutting speed v_c and the feed per cutting edge f_z are varied throughout the DoE (three-level full-factorial with central points), combining low and high v_c (30 – 110 m/min) with low and high f_z (0.04 – 0.07 mm), and all milling conditions are investigated in both conventional milling (CM) and USAM. The central points of the test are performed twice under CM conditions as the first and last points as reference tests in the test series. In this way, the variations caused by tool wear can be assessed. In between, the order of the experiments is randomized. Table 12 shows the tests performed in a full DoE.

Table 11: Optimum milling parameters for dry manufacturing Ni-base alloys with tool given by tool manufacturer

Set milling parameters	
Milling mode	Down milling
Cutting depth a_p	0.3 mm
Step over a_e	0.3 mm
Cutting speed v_c	70 m/min
Feed per cutting edge f_z	0.055 mm
US-amplitude	3 ± 0.5 µm
US-frequency	37.2 ± 0.2 kHz
Tool inclination	**rad/deg**
Feed angle λ	0.785 / 45°
Tilt angle τ	0.785 / 45°
Resulting angle β	0.955 / 54.7°

Measurement and analysis of cutting forces

The cutting forces in the x (F_x feed force), y (F_y infeed or normal feed force), and z (F_z passive force) directions (according to Figure 32) were measured every 1 ms using a Kistler type 9139AA dynamometer to describe the mechanical loads during the milling tests. For further evaluation of the data, they are first smoothed to avoid redundant peaks. For this purpose, a Savatzky-Golay filter in Origin 2019 software with a polynomial order of 10 is used. An example of smoothing is given in Figure 34.

*Table 12: Full design of experiment used for the finish milling experiments of CoCrFeMnNi-HEA and CoCrNi-MEA for 12 samples under different conditions of feed per cutting edge f_z, cutting speed v_c, and ultrasonic assistance. The central point tests are marked with **

Test No.	Order	*Feed per cutting edge* f_z in mm	*Cutting speed* v_c in m/min	Feed rate in mm/min	Ultrasonic assistance in %	Rotation speed in 1/min
6*	1	0.055	70	855	0	3885
9	2	0.07	110	1709	100	6105
4	3	0.04	110	977	0	6105
7	4	0.04	30	266	100	1665
2	5	0.07	30	466	0	1665
11*	6	0.055	70	855	100	3885
12*	7	0.055	70	855	100	3885
1	8	0.04	30	266	0	1665
3	9	0.07	110	1709	0	6105
10	10	0.04	110	977	100	6105
8	11	0.07	30	466	100	1665
5*	12	0.055	70	855	0	3885

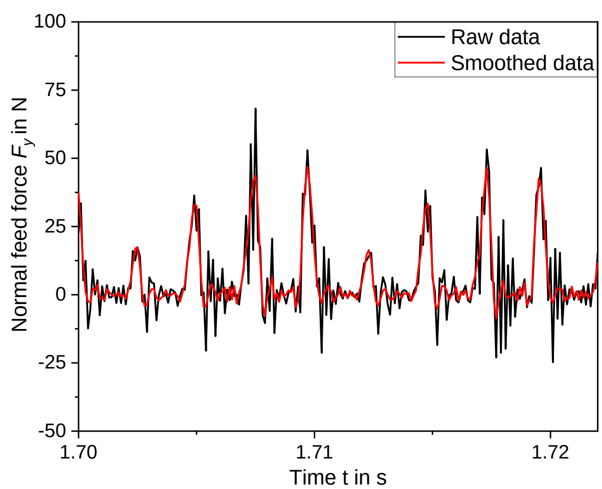

Figure 34: Measured raw data of normal feed force F_y vs. smoothed data with Savatzky-Golay filter

The resulting cutting force F_r is determined from the cutting forces in the x-, y- and z-directions according to the Equation 9:

$$F_r = \sqrt{F_x^2 + F_y^2 + F_z^2} \qquad \textit{Equation 9}$$

For each test, the cutting forces of 10 milling lines were recorded. An exemplary measurement for a milled line and a tool rotation is shown in Figure 35. Here, Figure 35 a and b show the measured forces in x-, y- and z-direction, part c shows F_r, and d shows the forces in all directions together with the resulting one. Each peak refers to a cutting engagement with one cutting edge. The deviation of the peak sizes can be attributed to a deviation in the tool manufacturing process since the tool was not ground in the same tool holder used for the tests. In combination with the rather low engagement parameters (cf. Table 2) for a_e, a_p, and f_z for the finish milling process, this leads to significant deviations in the engagement of the individual cutting edges.

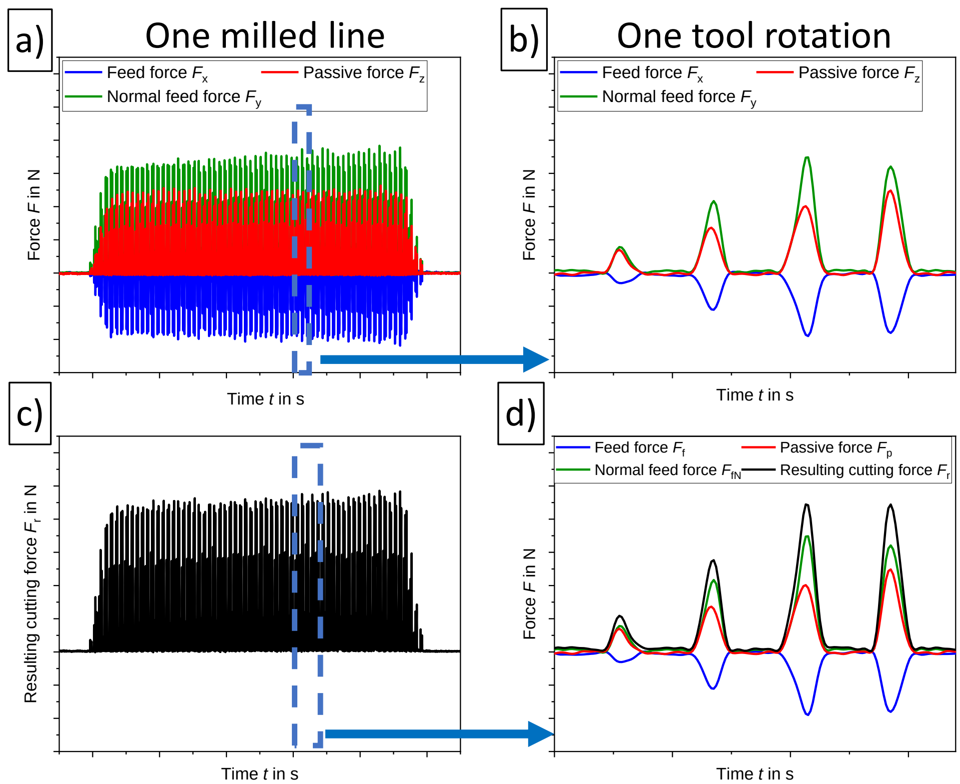

Figure 35: Force measurement and calculation of resulting cutting force; (a) measured forces (F_x, F_y, F_z) for one milled line; (b) measured forces (F_x, F_y, F_z) für one tool rotation; (c) calculated resulting cutting force for one milled line; (d) calculated resulting cutting force F_r and measured forces (F_x, F_y, F_z) for one tool rotation

In order to obtain comparable statistical values based on the force measurements, the average resulting cutting force $\varnothing F_{r,max}$ was determined. For this purpose, a peak detection algorithm of the Origin 2019 software was used to determine the maximum values of each peak ($F_{r,max}$). The average value is calculated afterward, and the result of each measurement corresponds to the average of the maximum forces in five milling lines. For each sample (parameter set), two measurements are taken, from which an average and a standard deviation are calculated. These values were used to plot the results and create linear regression models using RStudio software to determine correlations between milling conditions and forces.

4.3.2 Analysis of surface integrity

Various analytical methods were used to characterize the surface integrity. These methods are based on the individual factors of the surface integrity (cf. Figure 14). LOM and SEM images as well as roughness measurements are used to describe the topography. residual stresses are measured at the surface and in the near-surface region to analyze the mechanical effects. The metallurgical influence is analyzed by means of SEM and EBSD investigations of the edge region. Due to the high experimental effort, this was only carried out for individual samples of the machined HEA.

<u>Analysis of surface topography</u>

For the investigation of the surface condition (topography) and tool wear, the relevant areas were qualitatively examined by LOM (POLYVAR MET microscope from Reichert-Jung, with a Gryphax-Altair camera from Jenoptik, Germany) and SEM (Phenom XL from Thermo Fisher Scientific, Germany). For quantitative topography characterization, the roughness of the machined surfaces was measured in the x- and y-directions using a contact profilometer (HOMMEL-ETAMIC T1000 by JENOPTIC, Germany) according to DIN EN ISO 4287 [211]. The roughness parameters used for the quantitative comparison are R_z and R_a. R_a is the arithmetic mean roughness, calculated as the mean distance between the profile and the centerline, as shown in Equation 10 [211]:

$$R_a = \frac{1}{l}\int_0^l |Z(x)|dx \qquad \textit{Equation 10}$$

The mean roughness depth R_z or average of all maximum peak and valley heights of the profile at each sampling length, calculated according to Equation 11 [211]:

$$R_z = \frac{\sum_{i=1}^{5} R_{zi}}{5};\ R_z = \max Z\ (x) + |minZ(x)|\ for\ x\ \in\ l_i \qquad \textit{Equation 11}$$

where R_{zi} is the single peak-to-valley height or maximum peak-to-valley height of the profile in each of the five scan lengths (li) into which the profile is divided. The results are compared with the theoretical R_z parameter or R_{zth} from [212], which is calculated according to Equation 12:

$$R_{zth} = \frac{D_t}{2} - \sqrt{\frac{D_t^2 - C^2}{4}} \qquad \textit{Equation 12}$$

where D_t is the tool diameter and C is the distance between adjacent cuts, which depends on the measuring direction. The distance C is the feed per cutting edge f_z in the feed direction and the step over a_e in the normal feed direction.

<u>Analysis of mechanical influence of milling</u>

The residual stresses were determined by XRD measurements (analogous to the residual stress analysis of the welds in Section 4.2.3) with a G3 Stresstech goniometer to analyze the mechanical influence of machining on the surface and the subsurface (see Table 13 for parameters). For the investigation of the subsurface (residual stress profile in depth-/ x-direction), the surface was removed by electrochemical polishing (see Table 13) to avoid further mechanical influence on the material. Electrochemical polishing was performed for selected specimens (Test No. 5 and 11) for the CoCrFeMnNi-HEA, to investigate the effect of USAM on the residual stress depth profile.

Table 13: XRD-residual stress analysis and electrochemical polishing parameters

XRD-Measurements			
Measuring mode	$\sin^2\psi$	Collimator	3 mm
Radiation	Mn-Kα	Tube power	30 kV/6.7 mA
Detector	Linear solid-state	Ψ – tilting	0° to ±45°
Diffraction line	(311)	Ψ – step	9
2ϴ angle	156°	Measuring time	2 s
Electrochemical polishing			
Solution	A2 – electrolyte	Polishing time	5 s
Voltage	25 V	Polishing depth	~5 µm

The calculation of residual stresses is based on material data from the literature for the alloys CoCrFeMnNi (Poisson's ratio ϑ = 0.259; Young's modulus *E* = 207 GPa) [200] and CoCrNi (ϑ = 0.31, *E* = 235 GPa) [22]. The residual stresses are measured in the x-(σ_x), xy-(σ_{xy}), and y- (σ_y) directions (see Figure 32) to calculate the maximum principal residual stresses σ_{max} using the XTronic software via Equation 13 according to [154]:

$$\sigma_{max} = \frac{(\sigma_x + \sigma_y)}{2} + \sqrt{(\sigma_{xy} - \frac{\sigma_x + \sigma_y}{2})^2 + (\frac{\sigma_x + \sigma_y}{2} - \sigma_y)^2} \qquad \textit{Equation 13}$$

Analysis of subsurface metallurgy

The subsurface influence was examined by SEM and EBSD in an SEM type Leo 1530VP (Zeiss) to characterize the microstructural degradation and a possible phase change in the boundary zone. To investigate the effect of USAM on the microstructural depth profile, selected specimens of the (test No. 2, 4, 8, and 10) CoCrFeMnNi-HEA were investigated. For this purpose, the specimens were separated perpendicular to the milled surface and embedded in an electrically conductive manner. Subsequently, the specimens were ground to 2000 grit and polished with 1 µm diamond paste. Finally, the surfaces were oxide polishing suspension (OPS) polished for the EBSD investigation carried out in a Leo 1530VP SEM by Zeiss, Germany.

5. Results and discussion of TIG-welded CoCrFeMnNi-HEA and CoCrNi-MEA

This section delineates the outcomes of TIG bead-on-plate welds conducted on both investigated MPEAs as explained in Section 3 and shown in Figure 21. The impact of specific surface preparation (EDM, grinding), particularly concerning residual contaminants, on weldability is expounded upon. The metallurgical aspects of weldability are explored with a focus on microstructure and encountered weld imperfections through the utilization of LOM, SEM, and EBSD. The analysis of constructional weldability is characterized by scrutinizing the residual stresses occurring in the bead-on-plate welds through XRD. The mechanical properties are elucidated through microhardness measurements and tensile tests. Local strain during the tensile tests is quantified using DIC.

5.1 Influence of surface preparation on cracking during TIG-welding of CoCrFeMnNi-HEA and CoCrNi-MEA bead-on-plate samples

5.1.1 Characterization of EDM and ground surface

In order to describe the influence of surface preparation on weldability, the surfaces are to be characterized. Figure 36 shows SEM images of the surfaces of both investigated MPEAs in the "as-cut" condition by wire EDM and further grinding of the machined surfaces. In the case of the as-cut condition, both alloys show clear bright deposits on the surface after EDM (Figure 36a, c). These were removed by further grinding, which is indicated by the grinding grooves without a predominant orientation (Figure 36b, d). The chemical composition of the mentioned deposits in the as-cut condition was investigated by EDX and revealed significant amounts of Cu and Zn (see the corresponding values next to the figure parts). This is due to the electrical and chemical dissolution of the brass wire used (Cu63Zn37) since EDM requires a rinsing electrolyte (for electrical connection between wire and workpiece as well as the removal of dissolved particles from workpiece surface [213]). This was confirmed as the further ground surfaces did not contain any Cu or Zn deposits.

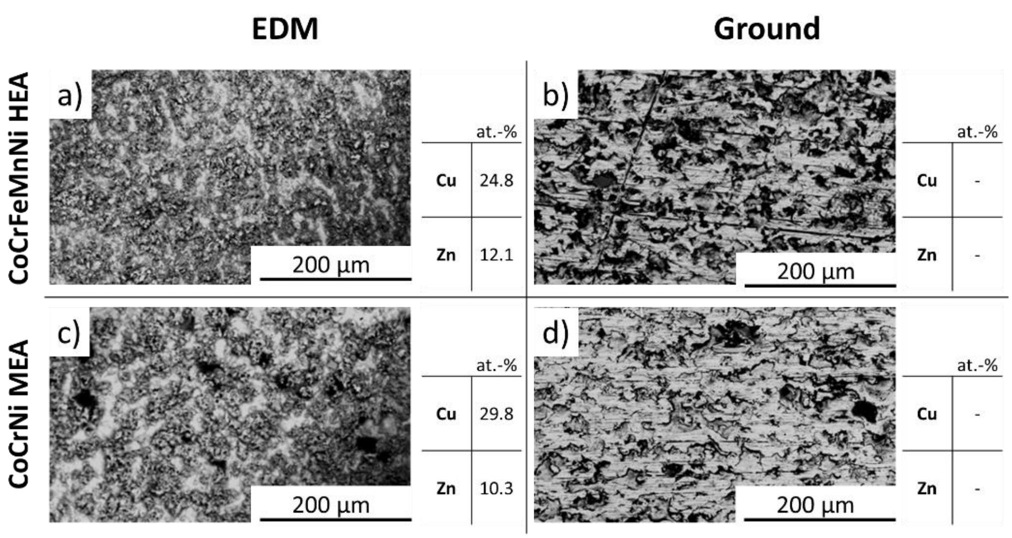

Figure 36: SEM images of surface topography and identified amount of Cu and Zn in at. % measured by EDX before welding: CoCrFeMnNi-HEA (a) as-cut by EDM, (b) after grinding; CoCrNi-MEA (c) as-cut by EDM and (d) after grinding, published in [214]

5.1.2 Identification of welding-induced imperfections related to the surface preparation

The radiographic inspection of the TIG bead-on-plate welds in as-cut condition without grinding of the Cu/Sn deposits revealed certain weld defects/imperfections in terms of multiple cracks in the welt seam. The radiographic test images of the TIG-welds confirmed the formation of cracks as shown in Figure 37. The welds in as-cut condition show cracks in the HAZ along the entire weld seam for both the CoCrFeMnNi-HEA (Figure 37a) and the CoCrNi-MEA (Figure 37c). These run at an angle of about 45° from the FL, opposite to the welding direction. In contrast, the images of the welds with ground surfaces after radiographic inspection did not show any weld defects (Figure 37b, c). Hence, any insufficient surface preparation of the weld plates in terms of residual deposits can lead to cracking and must be anticipated for processing of the MPEAs and influences the suitability for certain welding processes like TIG.

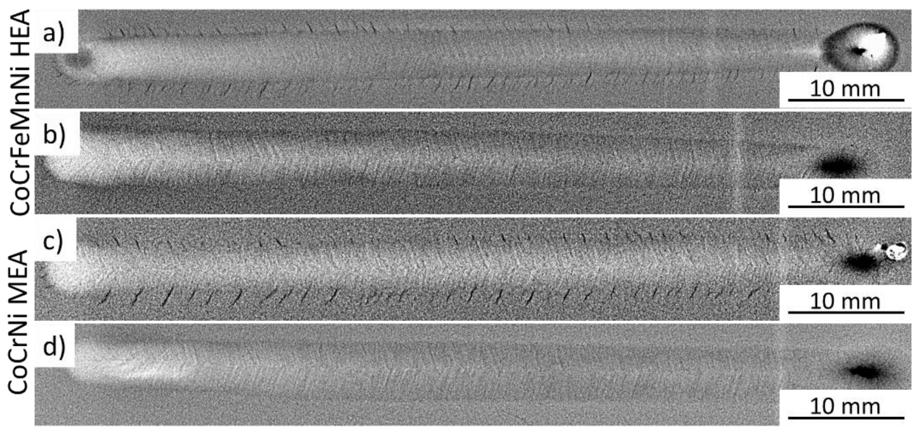

Figure 37: Radiation test images of CoCrFeMnNi-HEA in: a) as-cut, b) ground condition and CoCrNi-MEA in c) as-cut, d) ground condition, published in [214]

As shown in the cross-sections in Figure 38a to d, no other weld defects were identified except the mentioned cracks. A more detailed view of the crack surfaces can be found in Figure 38e (CoCrFeMnNi-HEA) and in part f (CoCrNi-MEA) respectively. Here, an intergranular characteristic of the cracks in the CoCrNi-MEA and the CoCrFeMnNi-HEA can be clearly seen. On the crack flanks of the HEA, brightness differences to the directly adjacent grain occur in some cases (counter-drawn in the white box in Figure 38e, f). For MEA, changes also occur on the crack flanks relatively to the surrounding material (marked in the white box). Such differences at the crack flanks may indicate the presence of a different phase. On the other hand, these effects may also be due to inconsistent etching or edge effects.

The identified intergranular cracks in the HAZ can initiate and propagate due to a variety of crack mechanisms. On the one hand, the well-known hot cracking in terms of liquation or ductility dip cracking (DDC) [95]. On the other hand, the cracks may also be initiated by a liquid metal embrittlement (LME) mechanism, which can occur, for example, in the welding of Zn-coated steels [97, 215]. Further welding-related mechanisms like cold cracking should be ruled out since both MPEAs exhibit an increased fracture strain at temperatures below 400 °C [25], which contradicts a brittle failure (here intergranular). In addition, hydrogen-assisted cracking is of less importance as e.g. the CoCrFeMnNi and CoCrNi alloys show superior hydrogen embrittlement resistance [36, 216].

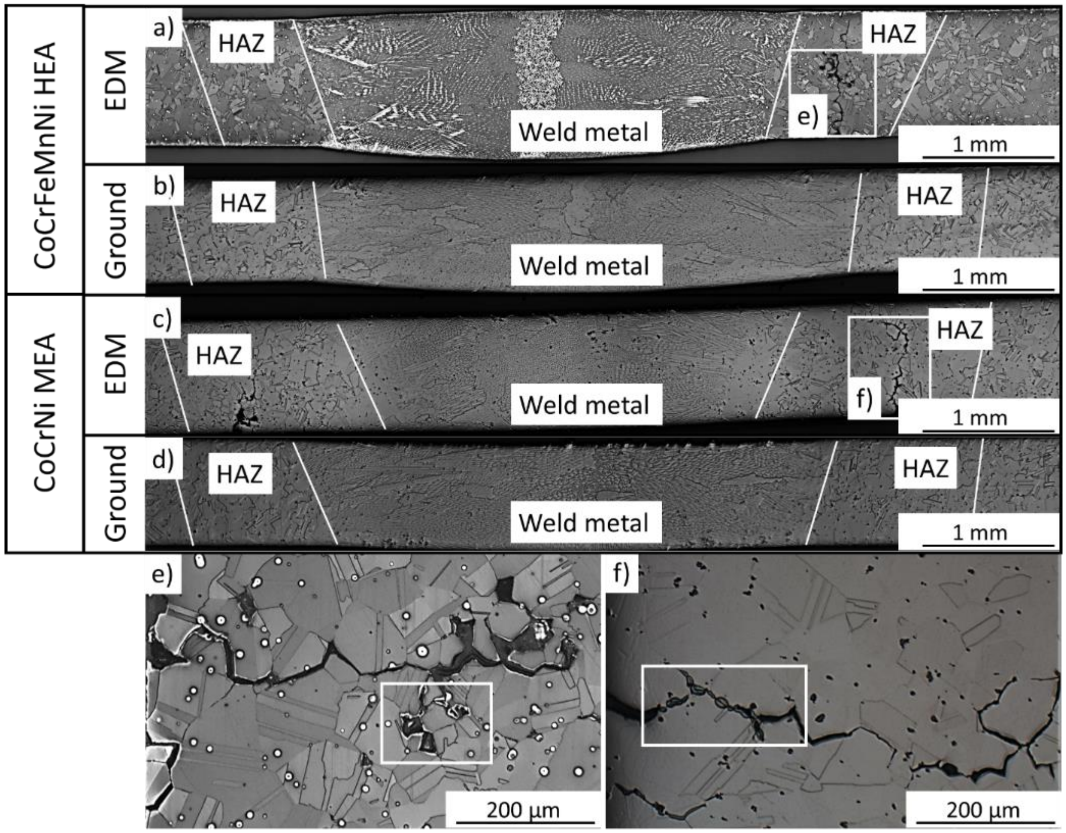

Figure 38: LOM-images (grayscale image for better contrast display) of the weld cross-sections of CoCrFeMnNi-HEA a) EDM, b) EDM + ground, e) detail of crack and CoCrNi-MEA c) EDM, d) EDM + ground f) detail of crack. Published in reference [214]

Figure 39 presents the results of SEM and EDX examinations of the cracks and possible deposits on the crack flanks. Figure 39a and b support the described effects derived from Figure 38, as bright layers (in the white boxes) are clearly visible on the cracks of both alloys (image taken with the BSD of the SEM). Since in SEM studies the intensity of backscattered electrons increases with atom weight, i.e., irradiated elements [217], these brighter areas in the images indicate a changed chemical composition at the crack flanks and grain boundaries, containing on average higher order elements. Further conducted EDX investigations (of the area marked in Figure 39b) are shown in Figure 39c. Clearly, this region is enriched in Cu compared to the surrounding material. As there was no Cu present in the BM, it must necessarily be molten Cu from the electrical discharge machining that liquefied at the high welding temperatures. As a result of capillary forces, the Cu is assumed to have diffused or flowed into the crack as a liquid phase, since the cracks extend from the FL to the specimen surfaces.

It has been demonstrated that the CuZn deposits resulting from EDM induce the formation of cracks within the HAZ. Furthermore, it has been established that welding without cracks is achievable when working with a ground surface. The crack mechanism is described in detail in the Ref. [214]. As the discussion of the crack mechanism does not substantively contribute to the clarification of the working hypothesis, it is not expounded upon further.

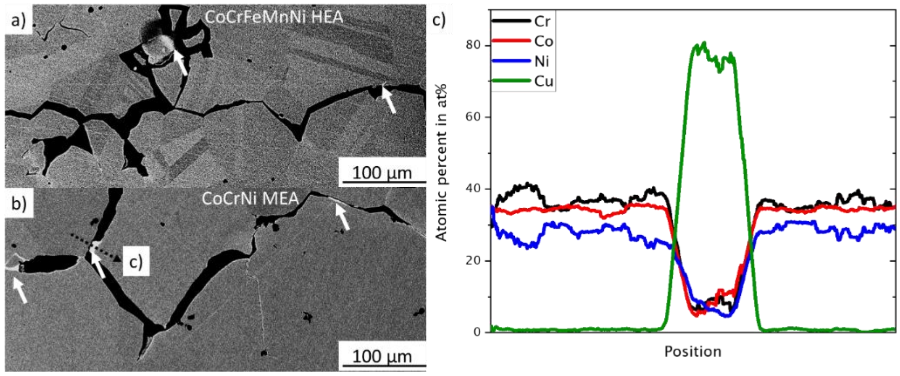

Figure 39: SEM-images of the crack areas of (a) CoCrFeMnNi-HEA, (b) CoCrNi-MEA, (c) EDX line scan marked in (b), published in [214]

5.1.3 Proof of defect-free welds for microstructure analysis and determination of mechanical properties

Figure 40 shows the radiation test images and the corresponding weld joint surfaces by bead-on-plate welding to investigate the TIG-weldability of both MPEAs (in HT- and CR-condition). None of the radiographic images showed weld imperfections such as cracks or pores in the WM or HAZ. Therefore, in addition to the characterization of the resulting microstructure, these welds were used as reference conditions to investigate the mechanical properties as well as the welding-induced residual stresses.

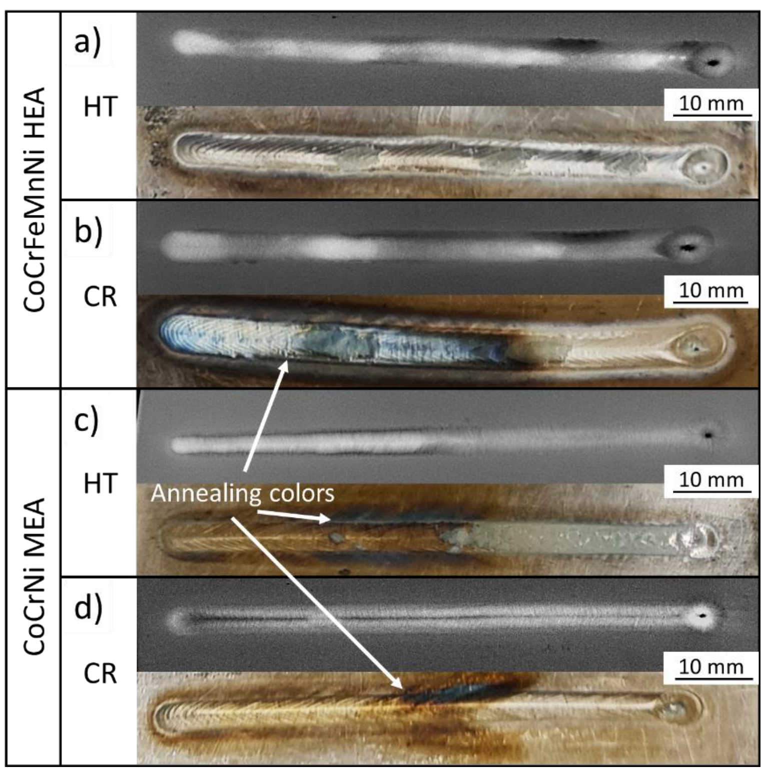

Figure 40: RT-images and corresponding weld joint surface for the TIG bead on plate welded CoCrFeMnNi-HEA in (a) HT- and (b) CR-condition and CoCrNi-MEA HEA in (c) HT- and (d) CR-condition

Except for the HT-HEA in Figure 40a, the surface images show annealing colors due to the oxidation caused by insufficient shielding gas coverage in the front part of the weld [81, 218]. In the back part of the weld, the samples have a bright metallic surface, since the shielding gas coverage was sufficient to prevent oxidation and thus annealing colors due to the used shielding gas nozzle. In addition, a flake-like morphology can be seen on all surfaces of the WM, which is caused by the pulsed arc and the different arc forces during the process [219] and is therefore process-related.

5.2 Microstructure analysis of TIG-welded CoCrFeMnNi-HEA and CoCrNi-MEA

5.2.1 Microstructure examination with LOM

Figure 41 shows the LOM examination of the TIG bead on plate welds in terms of cross-sections for the HEA (parts a and b) and the MEA (parts c and d), each in the corresponding material HT- or CR-condition. In all four WM microstructures, typical fusion welding-like features were observed. These are: an epitaxial solidification of the WM from the partially melted HAZ grains in the direction of the weld center along the temperature gradients in solidification as known for austenitic stainless steels [220] and HEAs [106, 113, 114] can be seen. The solidification is mostly dendritic due to the relatively fast cooling of the melted material. As a result, dendrites and interdendritic spacing form with micro-segregations indicating solubility differences of the elements in the liquid and solid phases [113, 220, 221]. No precise statement can be made about the formation of a HAZ based on the LOM examinations since these cannot be clearly resolved and will be characterized in Section 5.2.2 using SEM.

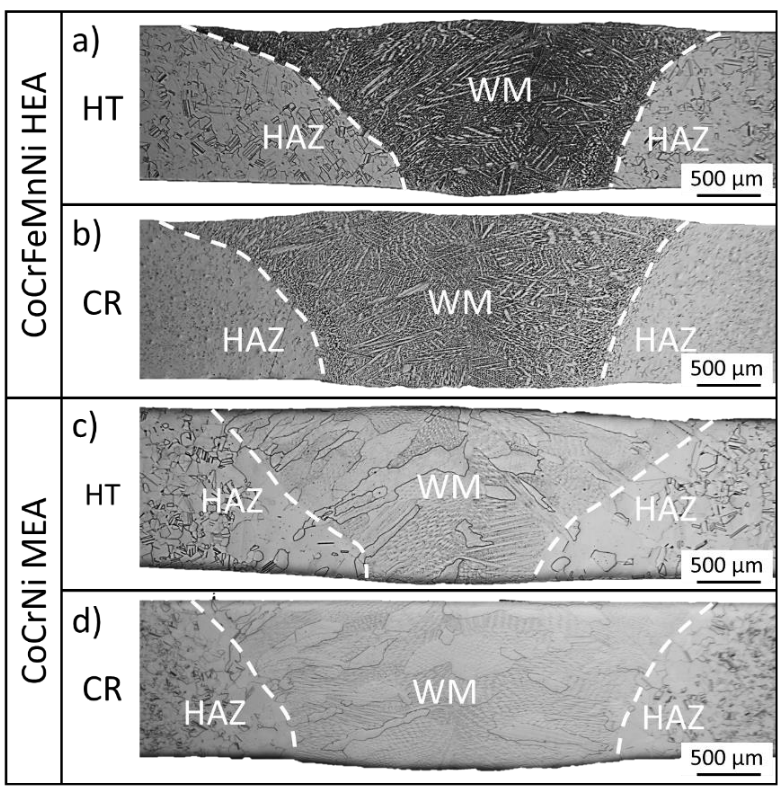

Figure 41: LOM (grayscale image for better contrast display) of cross-sections for the TIG bead on plate welded CoCrFeMnNi-HEA in (a) HT- and (b) CR-condition and CoCrNi-MEA in (c) HT- and (d) CR-condition

5.2.2 Detailed microstructure examination via SEM and EDX

For the TIG-welded HT-HEA, the transition from the WM to the HAZ using SEM BSD is shown in Figure 42a. Here it can be seen that the WM is solidified epitaxial from the FL. Moreover, in the HAZ, there was no obvious influence of the TIG welding in terms of grain size on the recrystallized microstructure. The reason is the very short time of the locally elevated temperature during welding and cooling. For the investigated HEA, the temperature must be > 700 °C for distinct grain growth [222]. The already recrystallized grains in HAZ would need higher temperatures for a longer time for further diffusion-driven grain growth, especially since sluggish diffusion (see Section 2.1.1) is one of the four main postulations of these alloys [5, 11, 223]. Figure 42b shows the dendritic microstructure of the WM, further investigated using EDX mappings as shown in Figure 42c. It can be clearly seen that the dendritic regions are enriched in Cr, Co, and Fe (dendrites are darker) whereas the interdendritic regions show enrichment in Ni and Mn (interdendritics are darker). This was also confirmed by Wu et al. [113] for the CoCrFeMnNi-HEA. This is due to the individual T_s of the respective element. A low T_s results in the enrichment of these elements in the interdendritic regions (in this case Ni and Mn) regions, as shown for the CoCrFeMnNi-HEA [113]. According to Laurent-Brocq et al. [224], this distribution is evident in the dendrites at sufficiently slow cooling. Black dots can be seen in Figure 42b; according to Figure 42c, these are Cr, and Mn oxides which partly originate from the fabrication process, but are more abundant in the WM, as can be seen in Figure 42a. According to Stephan-Scherb et al. [33], these are $(Cr, Mn)_3O_4$.

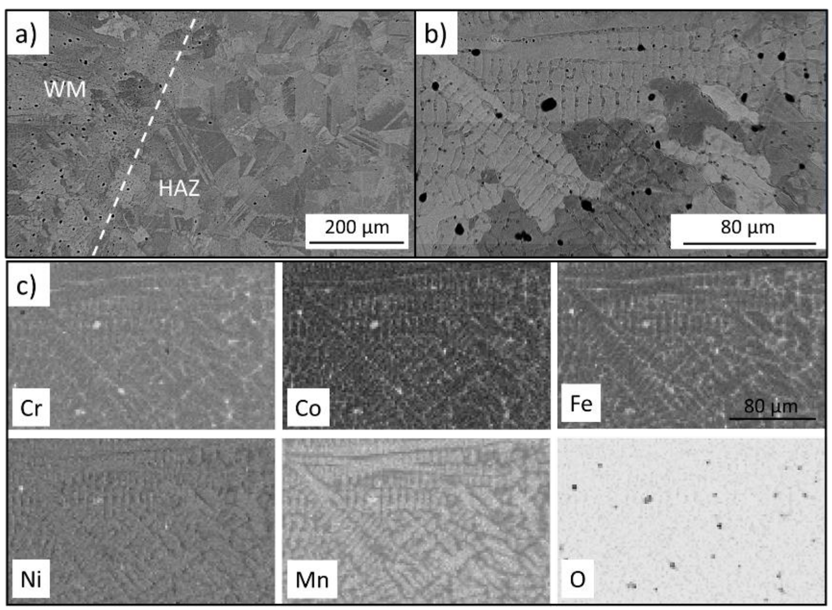

Figure 42: SEM-images of TIG-welded CoCrFeMnNi-HEA in HR-condition: (a) WM and HAZ; (b) dendritic WM; (c) EDX-mappings (grayscale image for better contrast display, darker means a higher concentration) of area b

Figure 43a shows the gradient from WM to HAZ to BM for TIG welding with the CR-HEA. Grain growth in the HAZ is clearly visible here. This is due to recrystallization processes as well as grain growth of the heavily cold-formed HEA-CR-BM [111, 222], from the welding heat input (see Figure 7 in Section 2.2.1). In addition, tempering twins can be seen, which originate from stacking faults during grain growth, the reason being the drive to reduce the surface energy of the grain boundaries [225, 226], as shown for an FCC CrCoNiAlTi MPEA in GTAW [116]. The dendritic WM of the CR-HEA in Figure 43b in combination with the EDX mappings in Figure 43c results in literally identical pictures, if compared to the HT-HEA in Figure 43 b and c. In other words, the dendrites are enriched in Cr, Co, and Fe and the interdendritic regions are enriched in Ni and Mn. Of course, one could also discuss it vice versa: the dendrites show a depletion of Ni and Mn. The reasons are the same as for the HT-HEA. The aforementioned Cr and Mn oxides were also found in the WM of CR-HEA.

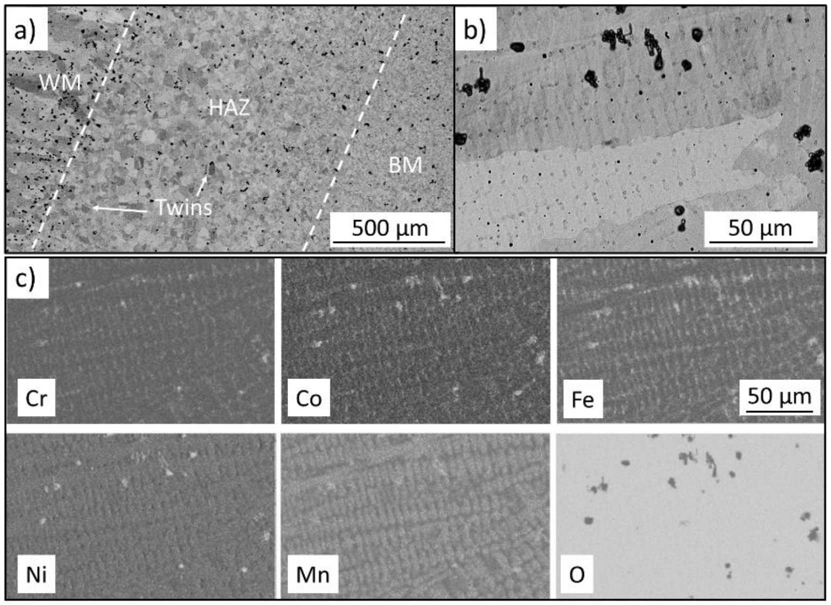

Figure 43: SEM images of TIG-weld CoCrFeMnNi-HEA in CR-condition (a) WM, HAZ, and BM; (b) dendritic WM; (c) EDX-mappings (grayscale image for better contrast display, darker means a higher concentration) of area b

The chemical composition of the different TIG WM is compared with the BMs as shown in Table 14. The values correspond to five EDX measurements of different 0.9 x 0.6 mm^2 areas. It is obvious that no significant difference in the WM or BM composition was obtained. This indicates the elements in the investigated HEAs show a comparable behavior as known for EB welding of CoCrFeMnNi-HEA [113] in terms of the loss of Mn in the WM due to its high vapor pressure [109, 113, 227]. Nonetheless, for generalized statements, these results must be confirmed by further investigations of arc welding processes on CoCrFeMnNi-HEA using filler metals. In terms of TIG or GMAW, fillers are not yet available but first applications as a powder for additive manufacturing by selective laser melting.

Table 14: Average chemical composition of CoCrFeMnNi-HEA-BM (BM) and well (WM) for TIG-welds, measured via EDX for five different areas of 0.9 x 0.6 mm²

at.-%	Co	Cr	Fe	Mn	Ni
BM –HR	20.6 ± 0.2	20.0 ± 0.2	19.5 ± 0.5	19.9 ± 0.3	20.0 ± 0.8
WM –HR	20.4 ± 0.1	20.3 ± 0.1	20.2 ± 0.2	20.1 ± 0.3	19.1 ± 0.4
BM –CR	20.6 ± 0.2	19.9 ± 0.2	20.0 ± 0.0	20.0 ± 0.2	19.5 ± 0.2
WM –CR	20.7 ± 0.1	20.1 ± 0.2	20.1 ± 0.1	19.8 ± 0.1	19.3 ± 0.1

The SEM and EDX examinations of the TIG WM and HAZ for the CoCrNi-MEA in the HT condition are shown in Figure 44. A dendritic directionally oriented solidified microstructure can be seen (Figure 44b). The solidification direction is vice versa to the heat gradient and thus from the FL to the weld center [59]. In addition, starting from the unmolten grains, the directionally solidified grains continue to grow and thus have the same orientation [113]. The EDX mapping of the dendritic WM is shown in Figure 44c. The interdendritic regions show an enrichment of Cr and a depletion of Co. The reason is that an element with a high melting temperature (like Cr) is enriched in the interdendritic regions due to delayed solidification. No significant conclusions can be given if Ni either enriches or depletes. Similar to the HT and TIG-welded HEA, no influence of welding on the microstructure in the HAZ can be deduced from the SEM investigations. The same effect was reported by Buzolin et al. [112] for the EB welding of the identical material and chemical composition CoCrNi-MEA. This indicates that the energy density (which is much higher for EB welding compared to TIG welding [61]) had no significant influence on the segregation during dendritic solidification. In addition, Cr oxides were identified in the WM, which should originate from the material synthesis. However, compared to the Cr-Mn oxides in the HEA-WM, the number of Cr oxides in the MEA is significantly lower. This shows that the HEA is significantly more susceptible to the formation of oxides in the WM than the MEA for the same welding process.

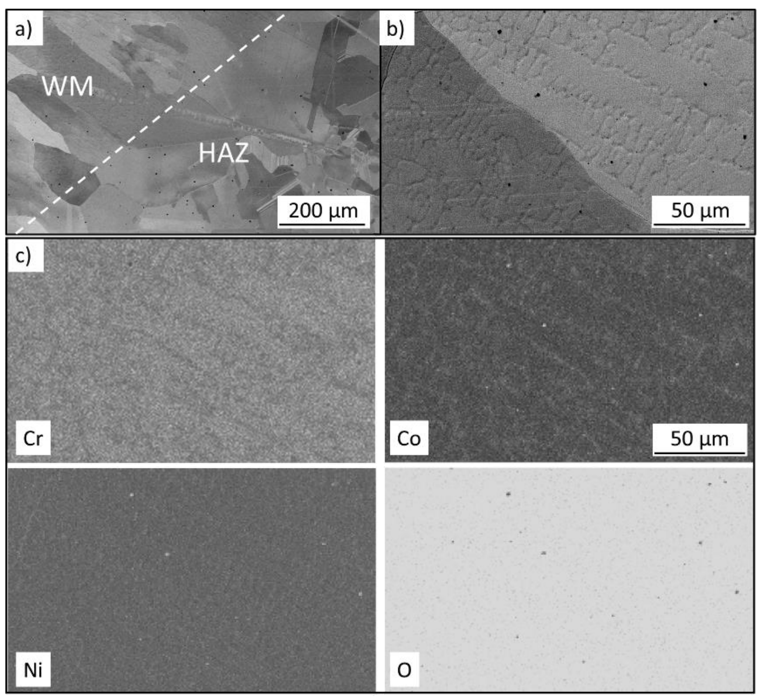

Figure 44: SEM-images of TIG-welded CoCrNi-MEA in HR-condition (a) WM and HAZ; (b) dendritic WM; (c) EDX-mapping (grayscale image for better contrast display, darker means a higher concentration) of section b

SEM and EDX examinations of the microstructure gradient from the WM to the BM of the TIG-welded MEA in the CR condition are shown in Figure 45. Figure 45a clearly shows a grain growth in the HAZ similar to the CR-HEA (compare with Figure 43). The reason for the larger grain size is the recrystallization with subsequent grain growth of the CR, i.e. heavily deformed, material [222]. In the WM in Figure 45b, a cellular structure can be seen, which indicates high cooling rates. Cellular microstructures indicate rather isotropic properties. There are segregations between the cells which, like the interdendritic region in the WM of the HT-MEA, show an increased Cr and decreased Co-content (EDX mapping in Figure 45c). The EDX mapping also shows a low proportion of Cr oxides in the WM, which originate from the material synthesis.

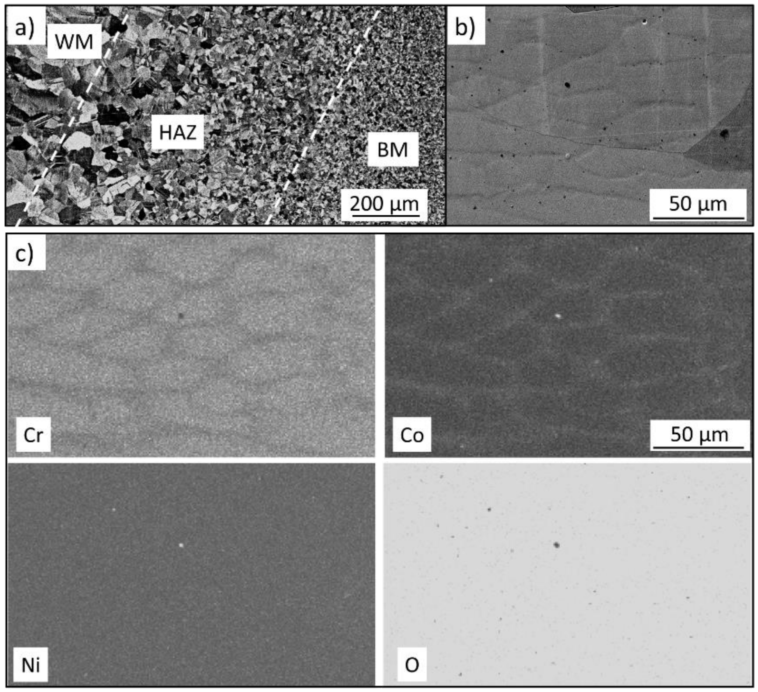

Figure 45: SEM-images of TIG-welded CoCrNi-MEA in CR-condition (a) WM and HAZ; (b) dendritic WM; (c) EDX-mapping (grayscale image for better contrast display, darker means a higher concentration) of section b

Investigating the influence of TIG welding on the chemical composition, XRD measurements were made in five different areas (5 x 0.54 mm^2) for every state. The results for the WM are compared with those for the BM in Table 15. No significant change in chemical composition because of TIG-welding can be deduced from the results so that no burn-off of an element can be described in this arc process. For the CoCrNi-MEA welded with other fusion welding processes with higher energy densities, such as LB or EB welding [61], the burn-off has to be investigated further, as it is not described in the literature. However, it must be considered that due to the small plate thickness, a low heat input was investigated. Hence, a general interdependency between welding heat input and change of any chemical composition cannot be established. This would have to be investigated for an arc process with higher heat inputs.

Table 15: Chemical composition of CoCrNi-MEA-BM and WM for TIG-welds, measured via EDX for five areas, each 0.9 x 0.6 mm²

at.-%	Co	Cr	Ni
HT-BM	34.5 ± 0.1	32.3 ± 0.2	33.2 ± 0.3
HT-WM	34.6 ± 0.1	32.4 ± 0.1	33.0 ± 0.1
CR-BM	34.5 ± 0.1	32.5 ± 0.1	33.0 ± 0.1
CR-WM	34.7 ± 0.1	32.5 ± 0.1	32.8 ± 0.1

The EBSD results for the welded HT-HEA are presented in Figure 46. The investigated area is shown by SEM image in Figure 46a. Due to the high experimental effort and limited accessibility of the EBSD equipment, they were performed only for the TIG-welded HEA in HT condition. The inverse pole map (Figure 46b) shows grains directed epitaxially from the FL towards the center of the weld. It is noticeable that the grains in the WM which are closer to the FL tend to be smaller and more oriented in the (101) and (111) directions (green and blue). Whereas the grains further towards the center of the weld are oriented more in the (001) direction (red/yellow/purple). Since the biggest investigated area is covered by the WM, the inverse pole frequency (Figure 46c) also clearly shows that the skin orientation in the WM is the (001), so the assumption of a preferred direction of solidification is reasonable. This has also been shown so far for an LB welded CoCrFeMnNi-HEA [228] and a GTAW of CrCoNiAlTi MPEA [116], respectively. The reason for the different orientation could be the local cooling/solidification rate, which is greater if closer to the FL than in the center of the weld [59].

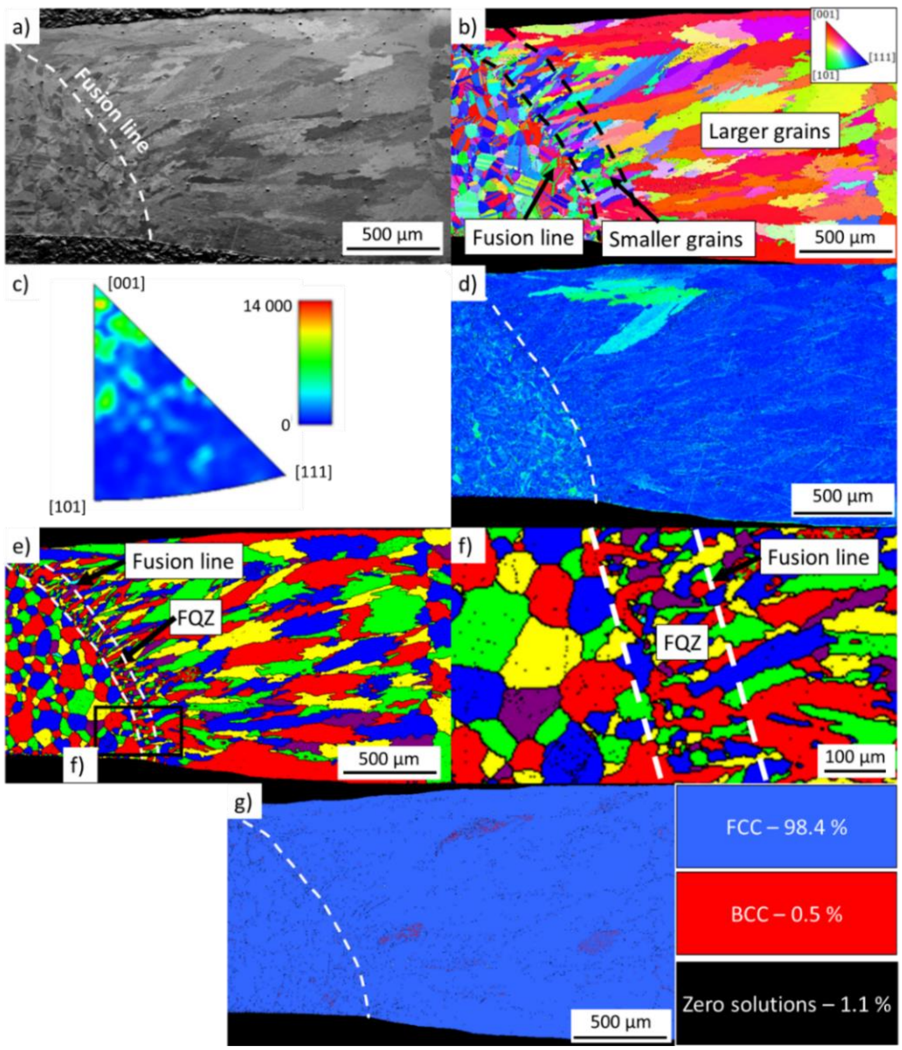

Figure 46: SEM and EBSD Analysis of TIG bed-on-plate welded CoCrFeMnNi in heat-treated condition: (a) SEM-image; (b) inverse pole map; (c) inverse pole frequency; (d) average misorientation map; (e,f) grain distribution map; (g) phase map

Figure 46b shows a significant number of twins in the HAZ, which originate from stacking faults during grain growth, the reason being the drive to reduce the surface energy of the grain boundaries[226]. But these twins could be mechanical driven as well. The reason is the high stacking fault energy [229], which leads to twinning as a deformation mechanism next to dislocation gliding in the CoCrFeMnNi-HEA [230]. The increased local deformation in the HAZ can be confirmed by the misorientation average map in Figure 46d.

The grain distribution maps in Figure 46e and f confirm the described small grains near the FL and larger ones near the center. In addition, a FGHAZ of approx. 100 µm width is clearly visible. This is a "fine equiaxed zone" (FQZ). The formation mechanisms are described in the literature, e.g. for Ni superalloys [117, 118] or Al alloys [119]. However, this has also been characterized for a CrCoNiAlTi MPEA [116]. The alloy composition, the heterogeneous nucleation, and the welding parameters have an influence on the FQZ formation, which is described in detail in [231]. There are two hypotheses for the formation mechanism, one according to Shah [120], where the FQZ is located in the partially melted zone and is formed by recrystallization. The second is based on Kostrivas and Lippold [121, 122] and describes a heterogeneous nucleation in a stagnant liquid layer of the FL.

The phase map of the TIG-weld is shown in Figure 46g. Mainly FCC areas, with 98.4 %, can be seen. This is to be expected since the CoCrFeMnNi-HEA is a very stable FCC phase [224]. However, Figure 46g also shows 0.5 % BCC regions in the WM and HAZ. These are assumed to be unavoidable measurement errors, as they only affect individual measurement points and not the contiguous areas. Furthermore, no BCC phase is described in the literature for the present alloy. Each transformation of the FCC into hexagonal and further to an amorphous phase was solely presented within the plastic zone of a crack tip, i.e. at very high degrees of deformation [28].

5.3 TIG-welding induced surface residual stresses for CoCrFeMnNi-HEA and CoCrNi-MEA

In this Section, the TIG welding induced residual stresses are discussed. Figure 47 shows the residual stress profiles of the welds at the top of the HEA (Figure 47a and b) and the MEA (Figure 47c and d) with HT (Figure 47a and c) and CR (Figure 47b and d) initial condition. In that case, the longitudinal direction corresponds to both the welding and rolling direction, and the transverse direction is normal too. However, XRD analysis in WM was not always feasible or resulted in very high deviations due to the columnar and large grains (see Section 5.2), as a result of the welding process [232]. Since the surfaces were ground before welding, all conditions exhibit compressive residual stresses in the BM. These are directionally independent at -400 to -500 MPa for the HT-HEA (Figure 47a) and at -300 to -500 MPa for the HT-MEA (Figure 47c). For the CR-BMs, the compressive residual stresses in the longitudinal direction, i.e. rolling direction, are higher than in the transverse direction in each case. The compressive residual stresses in the longitudinal direction for the CR-HEA up to -1000 MPa and for the CR-MEA up to -800 MPa.

In the case of the HT-MPEAs, the transverse residual stresses, see Figure 47a and c, in the HAZ and the WM increase up to 100 MPa (tensile residual stresses) in the case of the HEA and 200 MPa in the case of the MEA, which is still below the measured $R_{p0.2}$ strength of the materials (+240 MPa - HEA and +254 MPa - MEA) (compare Section 4.1). This means that despite the welding process, there are strength reserves transverse to the welding seam, even without stress relieving heat-treatment, which should have a positive, i.e. reducing, effect on the tensile residual stresses [233]. In the longitudinal direction, the HT-MPEAs also show an increase in residual stresses in the HAZ and WM. While the residual stresses in the HEA increase up to +200 MPa (tensile), the compressive residual stresses in the MEA are resolved and are at approx. 0 MPa.

The residual stresses in the HAZ and the WM also increase in the CR materials. In that case, the tensile residual stresses reach higher values compared with the HT materials. For the CR-HEA in Figure 47b, the tensile residual stresses are up to +200 MPa longitudinally and just under +300 MPa transversely and thus in the range of $R_{p0.2}$. With tensile residual stresses of +350 MPa longitudinally and up to +200 MPa transversely (see Figure 47d), the MEA shows higher values than the HT-MEA, especially in the longitudinal direction. This is probably due to the higher strength of the CR-BM. Since both CR-MPEAs reach particular tensile residual stresses in the range of $R_{p0.2}$, stress-relief heat-treatment should be performed to obtain further strength reserves of welded components [233]. The behavior described with respect to the residual stress state was to be expected for transformation-free austenitic materials [233, 234]. The highest tensile residual stresses were measured in the WM and decreased with increasing distance from the weld center, changing to compressive residual stresses.

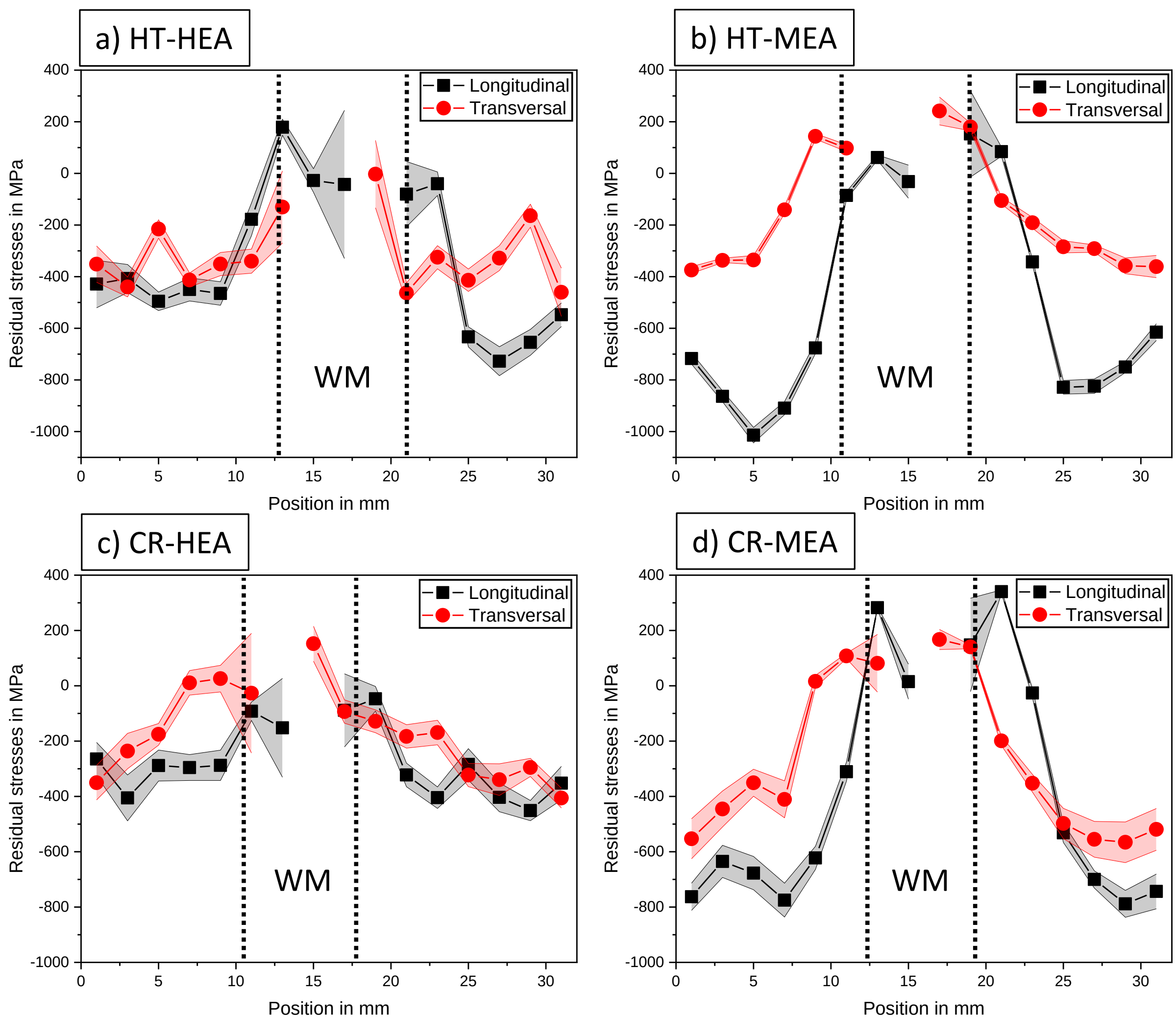

Figure 47: Residual stresses for the TIG-welded CoCrFeMnNi-HEA in (a) HT-, (b) CR-condition and CoCrNi-MEA in (c) HT- (d) CR-condition

5.4 TIG-welding induces hardness distribution for CoCrFeMnNi-HEA and CoCrNi-MEA

In Figure 48, the microhardness mappings with HV0.1 are given for the TIG-welded HEA (a and b) and MEA (c and d) in HT (a and c) and CR (b and d) initial condition. A clear influence of the initial material condition on the local hardness is shown here. For this reason, the initial condition of the materials is primarily used in the following discussion.

The welds of the HT materials do not show any significant influence of the TIG welding on the local hardness, as there are constant values in the blue to green range (150-250 HV0.1). This means that the local hardness does not influence the HAZ. This confirms the SEM and EBSD investigations from Section 5.2, in which hardly any effect on the microstructure was detectable. Only an increased number of twins in the HAZ of the HT-HEA was shown in Figure 46, but this seems to have no influence on the microhardness. The WM of the HT-MPEAs also shows similar microhardness values as the BM. Although both welds show, increased hardness, light green areas (approx. 250 HV0.1) on the weld and root side surfaces. These slight hardenings could be related to the higher shrinkage restraint at the surface and thus higher local cold deformation since the highest tensile residual stresses were also measured in these areas at the surface (see Section 5.3). However, the hard embedding material used could also have a supporting function, especially at the edge areas, and thus increase the locally measured hardness.

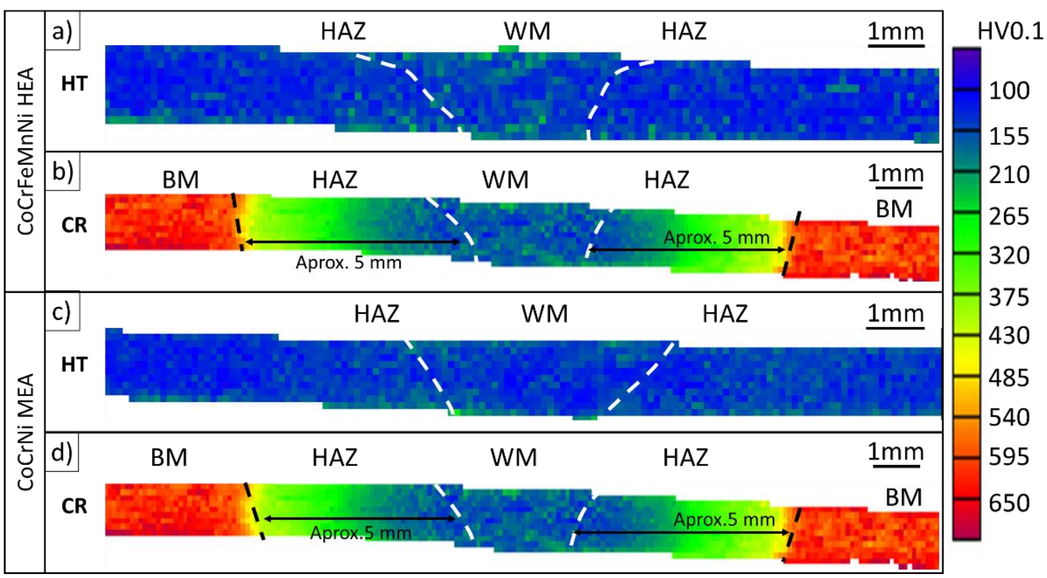

Figure 48: UCI microhardness (HV 0.1) mapping of cross-sections for the TIG bead-on-plate welded CoCrFeMnNi-HEA in (a) HT-, (b) CR-condition and CoCrNi-MEA in (c) HT-, (d) CR-condition

The CR-MPEA joints in Figure 48b and d show a clear influence on the local microhardness. A significant hardness gradient can be seen from the WM across the HAZ to the BM. The CGHAZ directly at the respective FLs, shown in Figure 43 and Figure 45, have a significantly lower hardness within the range of 150 HV0.1 to 250 HV0.1 (indicated by the colors blue/green) compared with the FGHAZ with a greater distance to the FL with 250 HV0.1to 450 HV0.1 (green to yellow). This can be explained by the grain refinement (Hall-Petch relationship). The BMs in CR-condition show the highest hardness with values up to 650 HV0.1 due to the plastic deformation during rolling and the resulting increased dislocation density. The WM specimens indicate the same hardness compared to the HT-BM specimens due to the presence of green and blue pixels (approx. 150 – 250 HV0.1). The reason is a comparable dendritic microstructure for TIG WM of both MPEAs in the initial conditions (see Section 5.2). To homogenize the hardness over the complete weld seam a PWHT could be useful. The influence of PWHT on the hardness of LB welding was investigated by Nam et al. [108]. It was found that with increasing PWHT temperature (800 °C to 1000 °C for 1 h) the hardness of both the BM and the WM can be slightly reduced (approx. 180 HV0.5 to 145 HV0.5 in WM).

Summarized, the hardness maps reflect the literature on fusion welded CoCrFeMnNi-HEAs [108, 109, 111], as only the initial condition in terms of work hardening has an influence on the hardness in the BM and HAZ. The recrystallization and grain growth in the HAZ results in decreased hardness compared to the CR-BM. The initial conditions have a minor influence on the WM-hardness as stated in the Literature in Figure 11b (Section 2.2.4) for the CoCrFeMnNi HEA.

5.5 Tensile properties of TIG-welded CoCrFeMnNi-HEA in HT- and CR-condition

5.5.1 Overall tensile properties of TIG-welds

The results of the tensile tests of both TIG-welded HEAs in HT- and CR-conditions are presented below. For this purpose, the engineering stress-strain curves of the welds drawn in the as-welded condition are compared with those of the BMs in Figure 49a. For comparison, the mechanical properties, obtained from the engineering stress-strain curves, are shown in Figure 49b. The strength values ($R_{p0.2}$ and R_M) of the TIG-welds (HT and CR) are clearly within the range of the HT-BM. Since all TIG-welds failed in the WM, this shows that the WM has the strength of the HT-BM without further PWHT. It also indicates the same strength of the dendritic microstructure in the WM as the recrystallized BM, described in Section 5.2. However, this is a new finding for the CoCrFeMnNi alloy, and all results of tensile tests described in the literature showed a reduced strength in the WM compared to the BM for the CoCrFeMnNi-HEA [108, 113, 235]. This shows that a better adapted welding process was used compared to the literature.

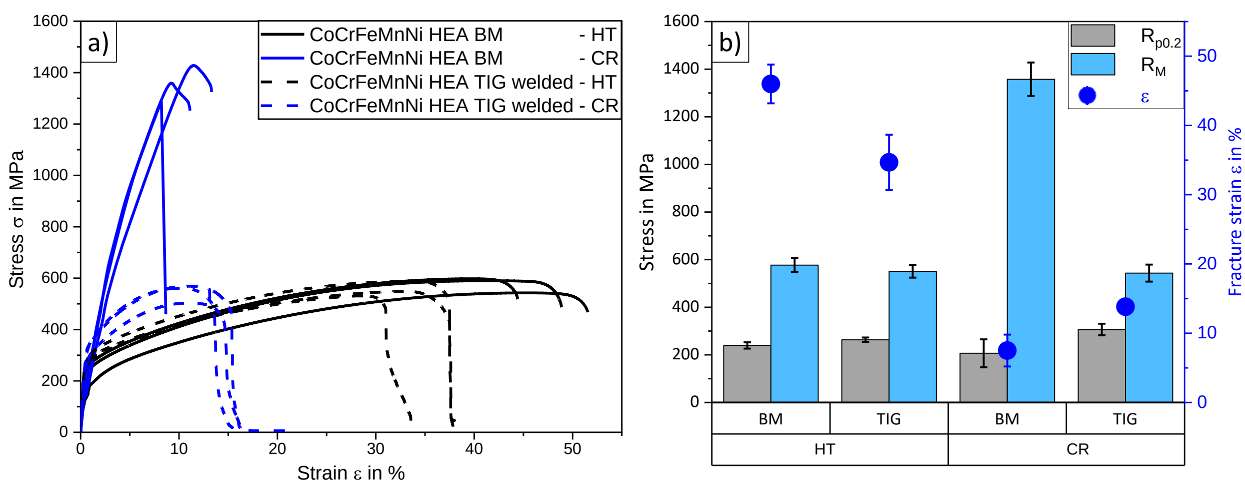

Figure 49: (a) Engineering stress-strain curves of CoCrFeMnNi-HEA base material (HT and CR) and the TIG-welded CoCrFeMnNi-HEA (HT and CR) and (b) YS $R_{p0.2}$, UTS R_M and, fracture strain ε for the CoCrFeMnNi-HEA base metals (BM) and TIG-welds in HT- and CR-condition

Compared with the CR-BM, an increase in $R_{p0.2}$ can be seen for the TIG-weld, which is consistent with the results of Wu et al. [113]. This could be due to the transition from the elastic to the plastic range for the CR-BM is not as precise as for the other three conditions investigated (see Figure 49a). This has an influence on the values, as can be seen from the larger scatter of the $R_{p0.2}$ values in Figure 49b. The UTS R_M, on the other hand, is significantly reduced for the CR condition due to welding, from approx. 1400 MPa to 600 MPa. The reason for this is the significantly lower plastic strength of the dendritically solidified microstructure in the WM compared with the CR and thus highly work-hardened starting material. Regarding the fracture strain, there is an influence on the initial state of the material before TIG welding. Welding of the HT material shows a significantly higher ductility with approx. 35 % fracture strain than that with CR-BM (approx. 14 %). Nevertheless, the HT-condition material shows a reduction in fracture strain due to TIG-welding from approx. 45 % to 35 %. The reason may be the lower ductility of the dendritic WM. Also, the influence of the tensile test specimen preparation in the as-welded condition could be a reason for failure in WM. Since there is no homogeneous surface and thus the smallest surface unevenness could act as a notch and support cracking [236]. TIG-welding with CR-BM, on the other hand, shows an increase in fracture strain from approx. 7 % to 14 %.

5.5.2 Local tensile strain properties of TIG-welds

In Figure 50, the engineering stress-strain curve (a) and the local strain maps ε_{loc} for three global stress-strain conditions I to III (b) are given for an example tensile specimen of TIG-welded HT-HEA. In all DIC tests, the three conditions shown, are at about approx. 50 % of the fracture strain, at approx. 90 % of the fracture strain and immediately before failure. Here, for global strain condition I of approx. 17 %, a homogeneous local strain distribution is shown, similar to what would be expected from a tensile specimen in pure BM, before necking [237]. Consequently, the average local strain for condition I is 17 %, as indicated by the colors in the primarily turquoise (transition from blue to green). Condition II is in the R_M range at approx. 34 % global strain and approx. 520 MPa stress. In addition to the onset of necking, a significantly increased local strain of up to 60 % can also be seen in the WM. The local strain in the BM here is in the green to yellow range at 30 % to 40 %. For the HT-BM, this local strain also remains unchanged until shortly before fracture in condition III. The WM, on the other hand, shows local strains up to 100 %, values that are clearly above the fracture strain. Values above 80 % have also been achieved for FCC materials after necking [144, 238]. This shows that the strength of the WM is lower compared to the BM and the weld seam. Hence, it is reasonable to assume that it would be likely the “weak point” of those TIG-welded components. The reason for the locally significantly increased local strain could be the dendritic microstructure in the WM (see Section 5.2 and Figure 42).

The influence of the microstructure should be reducible by PWHT [239] and this should have a positive effect on the increased weld-induced residual stresses (see Figure 47) as well [240]. The microstructure in particular raises the question about the effectiveness of further PWHT for a real component. A homogenization at 1200°C for 48 h [42, 224], was required for the elimination of the dendritic microstructure with both local micro segregations and chemical gradients. However, in terms of welding processing, high welding energy input causes a significant increase in the manufacturing costs of a potential component.

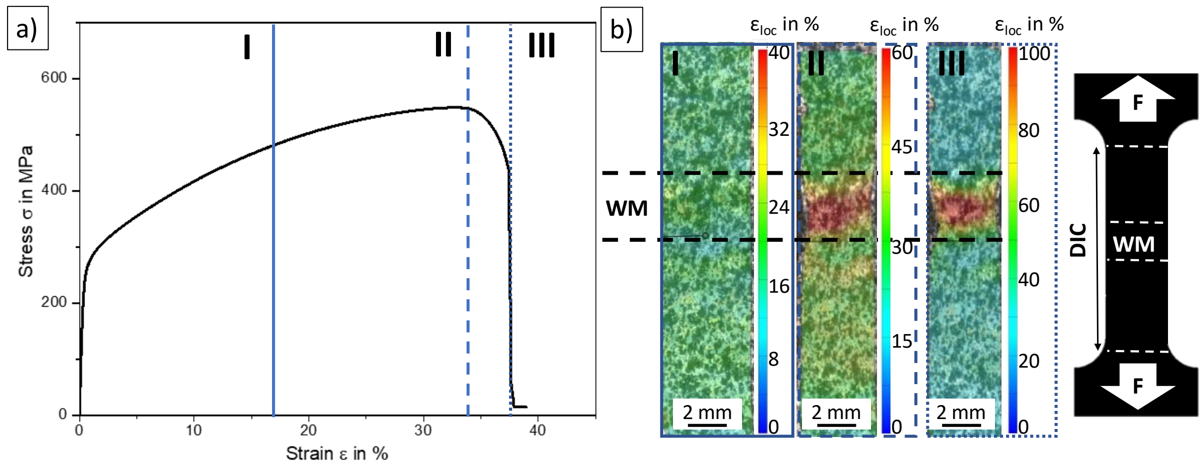

Figure 50: TIG-welded CoCrFeMnNi-HEA in HT-condition: (a) engineering stress-strain curve and (b) local strain in tearing direction ε_{loc} for conditions I to III

Figure 51 shows, the global engineering stress-strain curve (part a) as well as the local strain patterns for the stress-strain conditions I to III for the TIG-welded CR-HEA. Thereby, a local strain of approximately 0 % in the CR-BM is consistently shown for conditions I to III. For that reason, the specific strains accumulate in the WM and HAZ and increase the global strains in these regions of the welded joint. In the HAZ local strains ranging from approx. 8 % in condition I to approx. 40 % in condition III. The reason is the HAZ softening compared to the CR-BM, which can be also seen in terms of the reduced microhardness in the HAZ, shown in Figure 51. The softening results from the grain growth due to tempering of the CGHAZ [111]. In addition, in the FGHAZ, tempering leads to recrystallization and reduction of cold-working state (reduced dislocation and twin density) [108, 241]. The largest local strains can be seen in the WM, independently of condition I to III. The reasons for the reduced strength in the WM have already been described for the WM of HT-HEA and are based on the dendritic solidification (see Figure 43) and the high local tensile residual stresses (see Figure 47). In addition, compared with the CR-BM, there is a significantly lower degree of strain hardening, which primarily determines the high strength of the BM.

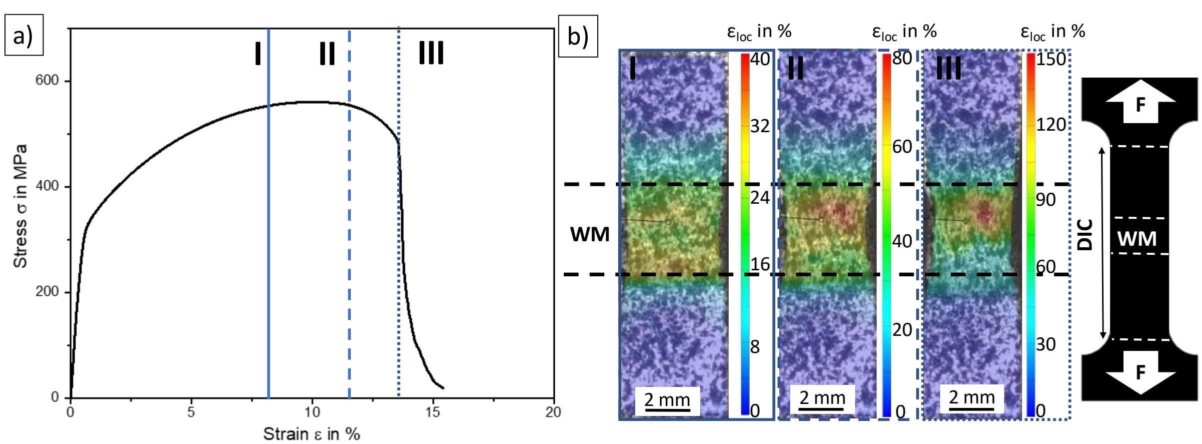

Figure 51: TIG-welded CoCrFeMnNi-HEA in CR-condition: (a) Engineering stress-strain curve and (b) local strain in tearing direction ε_{loc} for conditions I to III

Comparing both initial conditions (Figure 25a: HEA-HT and Figure 25b: HEA-CR), the CR-HEA shows a local strain of up to approx. 150 % in the WM, which is still 50 % higher than the HT-HEA. This could be due to the stabilizing effects of the very strong BM. In the literature [242], the conceptualization was proposed that a weld joint may be conceptualized as a "composite material" exhibiting deformation under isotropic stress conditions in tensile tests. This arises from the intricate interactions among different local welding microstructures (gradients in microstructures as described in Section 5.2), leading to the establishment of interdependencies. Notably, the hardening state of a material can exert a pronounced influence on the behavior when compared with a material of greater hardness. Reynolds et al. [242] postulate that the deformation of a material is constrained by the encompassing material.

5.5.3 Fracture morphology of tensile tests

Figure 52 shows the SEM results of the fracture surfaces after the tensile tests of the TIG-welded HEA in HT- (a, b) and CR-condition (c, d). Thereby, both weld microstructures show similar fracture morphology and are discussed together. Both fracture surface morphologies show distinct dimpled structures and are similar in their respective size. This indicates a ductile fracture. This confirms the ductility in the WM with high local strains in the failure range of 100 % and 150 %, respectively (compare Figure 50 and Figure 51). Furthermore, round particles can be seen in some dimples, these cannot be determined unambiguously due to their position. However, it is assumed that these are the Cr and Mn-containing oxides shown in Section 5.2. The shown dimpled morphology is typical for ductile materials at a uniaxial load with a low strain rate [243]. A similar ductile behavior of the CoCrFeMnNi-HEA was reported for different fusion welding processes [109, 111, 113]. The general explanation is that dimples result from dislocation slip processes and from slip obstructions that occur as a result of increasing dislocation buildup at obstacles, this process is called micro void coalescence. Obstacles to the hindered dislocation movement in engineering materials can be grain: boundaries, hard phases such as carbides, inclusions, and/or precipitates [80, 244].

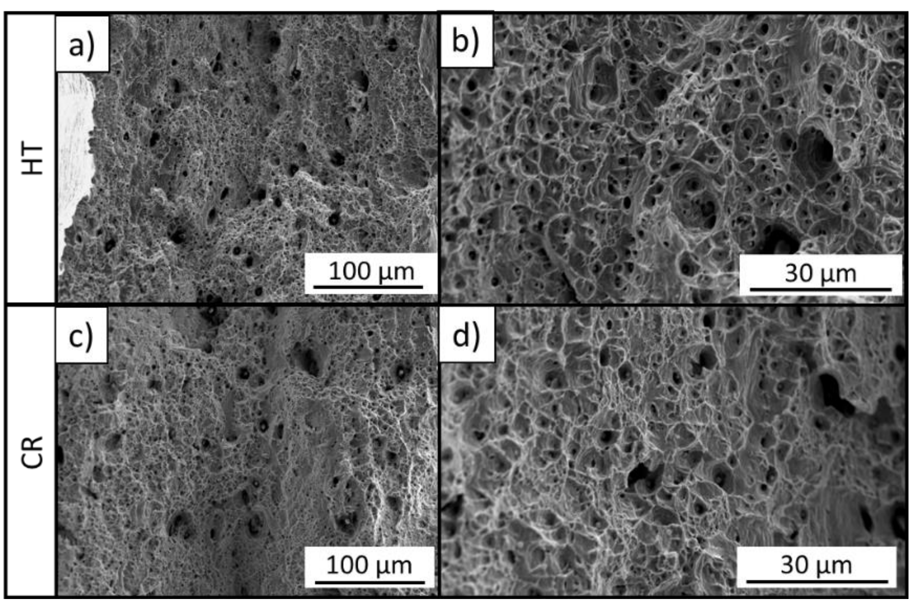

Figure 52: SEM examination of fracture surface morphologies of TIG-welded CoCrFeMnNi-HEA in (a, b) HT- and (c, d) CR-condition after tensile tests

5.6 Tensile properties of TIG-welded CoCrNi-MEA in HT- and CR-condition

5.6.1 Overall tensile properties of TIG-welds

In Figure 53 the engineering stress-strain curves (part a) and mechanical properties (part b) of the MEA-welds in the as-welded condition are compared with those of the BMs. In that case, comparable results are shown as for the HEA TIG-welds as described earlier. The strength values ($R_{p0.2}$ and R_M) of the MEA TIG-welds (HT and CR) are in the range of the HT BM, TIG-welding results just in a small decrease of UTS R_M. This shows that the dendritic microstructure of the WM has comparable strength to the recrystallized BM. Since all the TIG-welds failed in the WM, has been seen as the “weak point” of the joint. Compared to the CR-BM, the UTS R_M is significantly reduced due to welding processing from approx. 1800 MPa to 700 MPa. The reason is the significantly lower plastic strength of the dendritic WM microstructure compared to the CR and thus highly work-hardened BM.

As far as fracture strain is concerned, the same behavior described above for the HEA (see Section 5.5.1) is also shown for the MEA. Welding of the HT material shows significantly higher ductility with approx. 38 % fracture strain than welding with CR-BM (approx. 16 %). Nevertheless, the HT-material shows a reduction of the fracture strain due to TIG-welding from approx. 67 % to 38 %, a significant reduction of approx. 43 %. Similar to HEA, the reasons should be the lower ductility of the dendritic WM, as well as the influence of the tensile test in as-welded condition [236]. TIG welding with CR-BM, on the other hand, shows an increase in fracture strain from approximately 7 % to 16 %. The exact causes are described below based on local elongation.

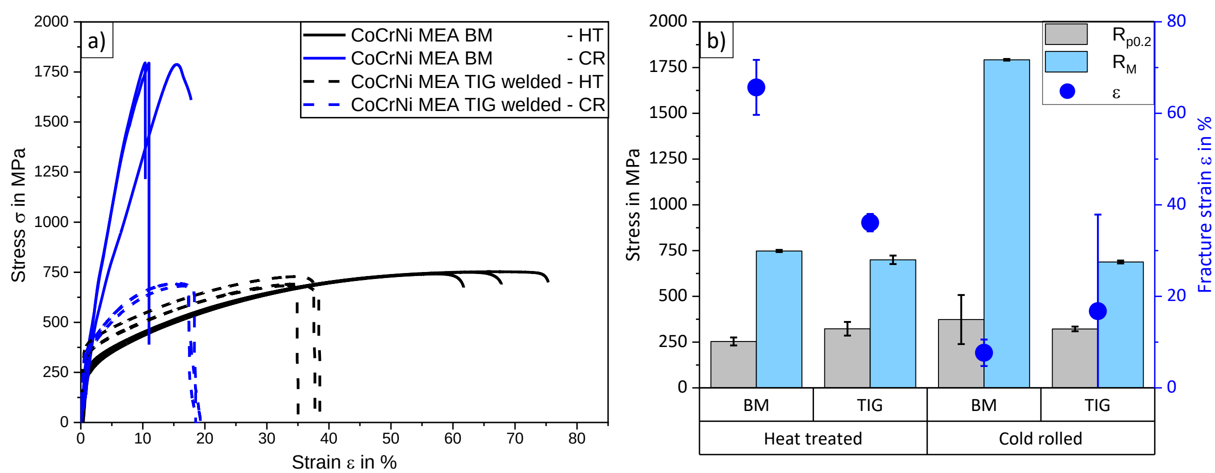

Figure 53: (a) Engineering stress-strain curves of CoCrNi-MEA-BM (HT and CR) and TIG-welded CoCrNi-MEA (HT and CR); (b) YS $R_{p0.2}$, UTS R_M and fracture strain ε for the CoCrNi-MEA-BM and TIG-welds in HT- and CR-condition

5.6.2 Local tensile strain properties of TIG-welds

Figure 54 shows the engineering stress-strain curve (a) and the local strain maps ε_{loc} for three global stress-strain conditions I to III (b) for an example tensile specimen made of TIG-welded HT-MEA. The highest local strain is shown for all three conditions in the WM, approximately 20 % global strain at approximately 600 MPa stress with local strains in the WM showing up to 40 % (red) and 8-16 % (blue to turquoise) in the BM for condition I. This increases to 110 % local strain in WM and approx. 30 % in the BM for condition III. Values above 80 % local strain were also obtained for other WMs of FCC materials [144, 238] as well as the HT-HEA (see Figure 50b). Following the WM reveals a lower strength than the BM. The reasons should be the same as shown for the HEA in Section 5.5.2, which is the dendritic microstructure [245], as in the MEA described previously (see Section 5.2 and Figure 44).

The global engineering stress-strain curve and the local strains for stages I to III of the TIG-welded CR-MEA are shown in Figure 55. Just as for the CR-HEA in Section 5.5.2, a local strain of approx. 0 % is shown in the CR-BM from stage I to III. Therefore, the strain accumulates in the WM and in the HAZ. In the HAZ, the local strains range from up to 16 % in stage I to approximately 40 % in stage III. This is due to the softening of the HAZ which has already been described for the CR-HEA in Section 5.5.2. The reasons for the softening are the recrystallized microstructure with additional grain growth in the CGHAZ [108] (see Figure 45). Like the CR-HEA, the largest local strains, consistently from stage I to III, are seen in the WM. The reason for the reduced WM tensile properties is the same as for the welded HEA: the dendritic WM microstructure (see Figure 45) and the high local tensile RS (see Figure 47d). In addition, compared to the CR-BM, there is a significantly lower degree of strain hardening, which mainly determines the high strength of the BM. Comparing the two initial stages in Figure 55b (MEA-HT) and Figure 54b (MEA-CR), the CR-MEA shows a local strain of up to approximately 90 % in the WM, which is albeit only slightly lower than the HT-MEA (approximately 110 %). The reason is assumed to be an effect e.g., of the surface condition (geometric imperfections in terms of notches in the as-welded condition), or an accumulation of local defects (higher dislocation density, particle or inclusion clustering such as Cr-oxides).

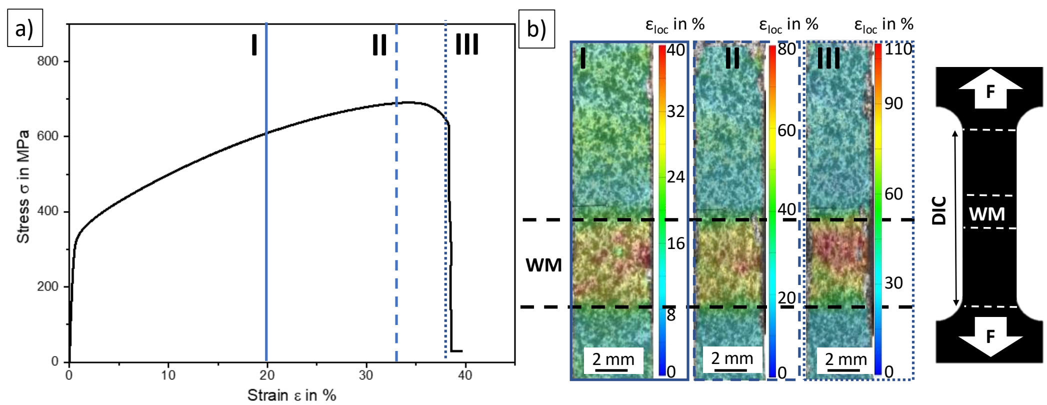

Figure 54: TIG-welded CoCrNi-MEA in HT-condition: (a) Engineering stress-strain curve and (b) local strain ε_{loc} for conditions I to III.

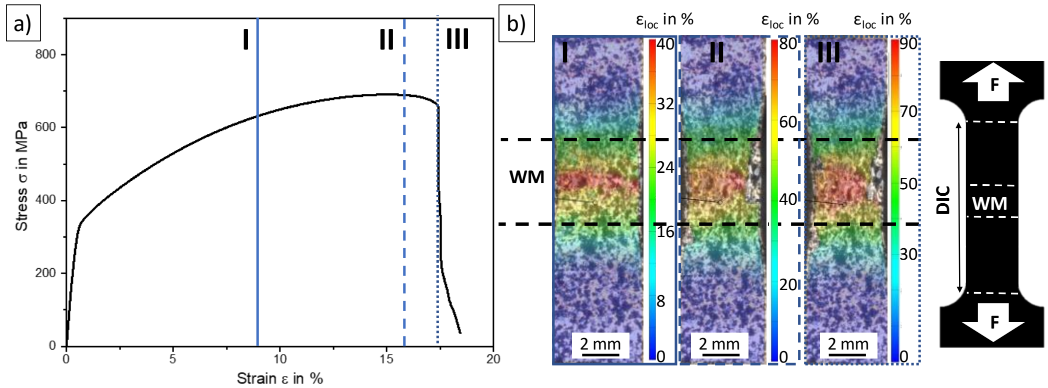

Figure 55: TIG-welded CoCrNi-MEA in CR-condition: (a) Engineering stress-strain curve and (b) local strain ε_{loc} for conditions I to III

5.6.3 Fracture morphology of tensile tests

Figure 56 shows the fracture surfaces of the TIG-welded CoCrNi-MEA, examined by SEM. Both the TIG-welds in HT- (a, b) and in (c, d) initial CR-condition show significant dimple formation across the entire fracture surface. The significant formation of dimples indicates a ductile failure [243, 244]. The dimples are about the same size in both conditions since the local elongation ε_{loc} shortly before fracture is also in a similar range at 90 % (CR-condition in Figure 55b) and 110 % (HT-condition in Figure 54b). Thus, the fracture surface shows similar morphology to the HEA (Figure 52), except that no particles such as the Cr and Mn oxides (with suitable dimensions) are visible in the dimples.

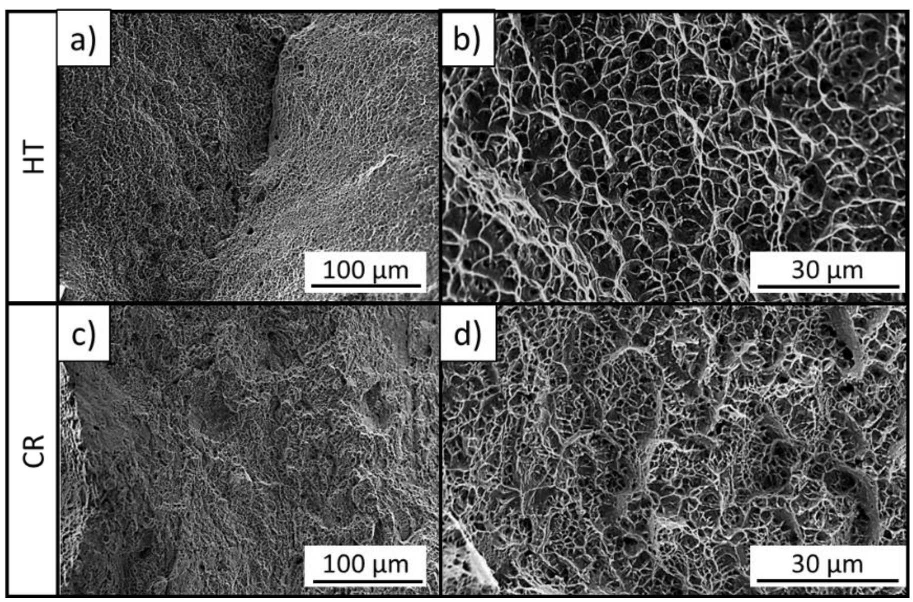

Figure 56: SEM of fracture surface morphologies of TIG-welded CoCrNi-MEA in (a, b) HT- and (c, d) CR-condition.

Both MPEAs showed for their respective CR- or HT-condition comparable properties to each other. For example, the dendritic WM microstructure and the significant HAZ grain growth in CR-condition were regarded for both MPEAs. In addition, qualitatively similar residual stresses and microhardness distributions across the welded joint were obtained independently of the investigated chemical composition. Furthermore, the tensile properties and fracture surfaces are very similar. Therefore, both MPEA materials are assumed to show good TIG-weldability. The main reason is that no welding imperfections occurred, which must be lined out as the first important finding of this work, because it is fundamentally for a component integrity. Furthermore, sufficient mechanical strength of the weld joint (comparable to the respective MPEA in HT-BM) was achieved. Consequently, the welding parameters (see Section 4.2.1) selected and transferred from the Ni-based alloy can also be considered suitable.

6. Results and discussion of dissimilar metal TIG-welding of CoCrFeMnNi-HEA and AISI 304 austenitic steel

This section elucidates the results of TIG-DMW experiments conducted on the CoCrFeMnNi HEA and the austenitic stainless steel AISI 304, as detailed in Section 3 and illustrated in Figure 21. The metallurgical aspects of weldability are investigated, focusing on microstructure and identified weld imperfections, utilizing LOM, SEM, and EBSD techniques. The examination of constructional weldability involves a thorough analysis of residual stresses using XRD. Mechanical properties are clarified through microhardness measurements and tensile tests. The local strain during the tensile tests is quantified employing DIC.

6.1 Proof of defect-free welds

In order to detect weld defects such as cracks or pores, radiation tests, and LOM-investigations were carried out. The images of the weld surface and radiation tests are shown in Figure 57 for the TIG-DMWs with HT (a) and CR (b) HEA. Here it can be seen that there are no unacceptable defects such as cracks. Therefore, the welding parameters used (see Section 4.2.1) are well-suited for these material combinations. Both welds show a dark area at the FL on the HEA side. In this case, a higher radiation dose can penetrate the specimen and expose the film [246]. The reason could be a smaller sample thickness or a difference in local density (a lower density allows more radiation to pass through) [246]. This will be discussed in Section 6.2. The surfaces did not show other defects. Only the weld with the HT-HEA shows annealing colors in the weld center. This may be due to insufficient shielding gas coverage, which causes oxygen to oxidize the surface [81, 218].

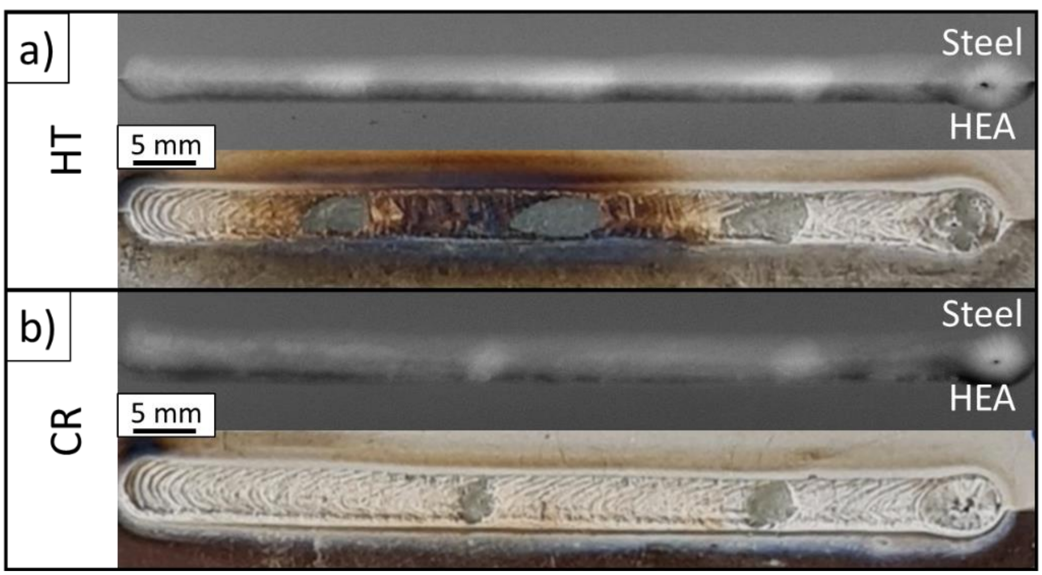

Figure 57: Radiation tests- and LOM-images of TIG-DMWs of CoCrFeMnNi-HEA in (a) HT- and (b) CR-condition welded to AISI 304 (radiation test image of a is published in [247])

6.2 Microstructure analysis of DMW-TIG-welded CoCrFeMnNi-HEA with AISI 304

Figure 58 shows the cross-sections of the TIG-DMWs with HT (a) and CR (b) HEA. A complete weld penetration was achieved and no weld imperfections, such as pores, cracks, or lack of fusion, appeared in both welds. The WM shows the typical dendritic structure, although no epitaxial grain growth can be seen as shown for the TIG-WM in Section 5.2. On the HEA side, a dark seam is visible at the FL in both welds. It is conceivable that partial melting results in pronounced micro segregation [245], which should result in Mn-rich areas as shown for the HEA TIG-welds in Figure 42 and Figure 43. This can lead to a susceptibility to selective corrosion during etching in the Mn enriched region [248] and should be examined in more detail by corrosion studies, which are out of this work scope. Also, near the FL on the HEA side, the WM shows reduced thickness, which explains the darker areas in the radiographic test results from Section 6.1.

On the steel side, a shoulder can be seen in the lower region of both welds, where the WM does not extend through the entire plate thickness. This was shown before in the literature [249] for TIG-DMW of $Al_{0.1}CoCrFeNi$ HEA with AISI 304. The reason for this should be the relatively large difference in the melting temperature ($T_{s,\ steel}$= 1450 °C [46]) and $T_{s,\ HEA}$= 1289 °C [44]) of both materials. This suggests that a higher amount of HEA material is melted than the steel. On the AISI 304 side, an HAZ can only be assumed, based on the LOM investigations. For that reason, they are presented in more detail via SEM investigations in this section.

The main difference between the two welds is the offset of the welded plates from each other in the HT-HEA (Figure 58a). This is due to distortion of the HEA caused by thermomechanical interactions [234, 240] when the degree of clamping is too low. This should be considered in the evaluation for possible applications and welding safety. The second difference is the pronounced HAZ in the CR-HEA, see Figure 58b. The HAZ shows grain coarsening with decreasing distance from the FL, comparable to the TIG bead on plate welds (see Section 5.2).

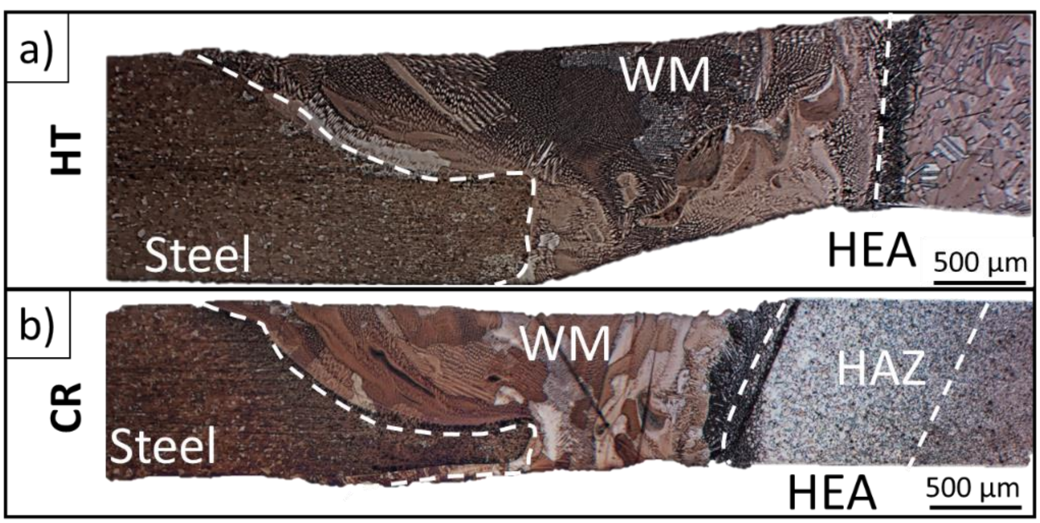

Figure 58: LOM figures of TIG-DMWs of CoCrFeMnNi-HEA in: (a) HT- and (b) CR-condition with AISI 304 (part a is published in [247] and part b is published in [206])

Due to the extensively researched HAZ formation of fusion welded AISI 304 [82, 250] and an identical HAZ formation in both TIG-DMWs (on the steel side) investigated. The formation of HAZ on the steel side is described below for only one example (AISI 304 with HT-HEA). For this purpose, SEM (a) and EBSD investigations (b) are shown in Figure 59. Observation by SEM revealed dendritic structures at the grain boundaries in the HAZ. These dendritic structures are described in the literature [82, 250] as dendritic ferrite between the austenite matrix, which is confirmed by the BCC content in the EBSD analysis. The proportion and size of dendrites decrease with increasing distance from the FL. The reason is the decreasing heat input. Furthermore, the precipitates show the rolled structure, which is resolved into an isotropic structure only immediately at the FL.

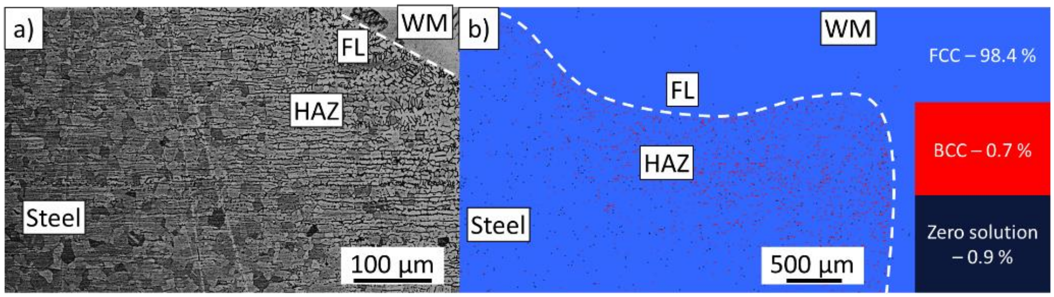

Figure 59: HAZ on steel side on DMW AISI304 with HT-HEA: (a) SEM and (b) EBSD analysis (part a published in [206])

The microstructure formation in the TIG-DMW with HT-HEA is shown in Figure 60 by SEM and EDX. Figure 60a shows the transition from steel BM to WM. A dendritic microstructure with epitaxial grain growth from the FL is shown. Using EDX, the change in chemical composition from the steel to the WM was investigated by means of line scanning (see Figure 60d). This shows a heterogeneous chemical composition in the WM, with Cr content remaining constant. The Fe-content decreases in the WM and varies between 30 at.-% and 50 at.-%. The reason is perhaps the dendritic structure as well as incomplete intermixing during the relatively short time in the liquid phase. In contrast, the Co-, Mn-, and Ni-content increases, due to the higher proportions in the HEA compared to the steel.

A dendritic microstructure with epitaxial growth from the FL can be seen on the HEA side as well (Figure 60b). The EDX examination results of the dendritic WM are shown in Figure 62c. Unfortunately, no conclusions about the local Co, Cr, and Ni distributions can be drawn from the results. Only an enrichment of Fe in the dendrites and of Mn in the interdendritic regions can be seen. Due to the change in the chemical composition, only the increased proportion of Fe can lead to the avoidance of Cr and Co accumulation in the dendrites and Ni in the interdendritic areas, e.g. shown in Section 5.2 and in [2, 113]. Oliveira et al. [141] showed similar behavior for an LB DMW of CoCrFeMnNi-HEA with an austenitic stainless steel AISI 316. In addition, depending on the WM intermixing, a ferritic fraction is described in an equilibrium state for < 20 % of the HEA as dissolved BM in the intermixed WM. However, for an average mixed chemical composition, pure FCC solidification is described [145]. Furthermore, a partially melted zone can be seen in the region close to the FL which causes preferred pitting corrosion at this surface during sample etching. This demonstrates again (see cracking due to Cu-containing contaminations in Section 5.1) the necessity for the consideration of material processing conditions for further property characterization. Figure 60e shows the results of the EDX line scan of the WM in the HEA-BM direction. In addition to the heterogeneous WM composition, two further areas of interest were identified. On the one hand, there is an area with a microstructure that strongly resembles the HAZ on the steel. In that case, the line scan also shows a clear increase in Fe, whereby this can be determined as a steel particle. This is not melted due to the higher melting temperature of the steel compared to the HEA [249]. Furthermore, a strong local increase in O-content can be seen. These are Cr, Mn oxides in the HEA from the material production [33] (compare Section 5.2).

Due to the strong differences in the local chemical composition and microstructure, local dependencies of the corrosive and mechanical properties around the FLs and the WM can be assumed. PWHT could be used to achieve homogeneous microstructure and suitable properties in a targeted manner. Currently, no studies on PWHT-effect of DMW on HEAs have been published so far.

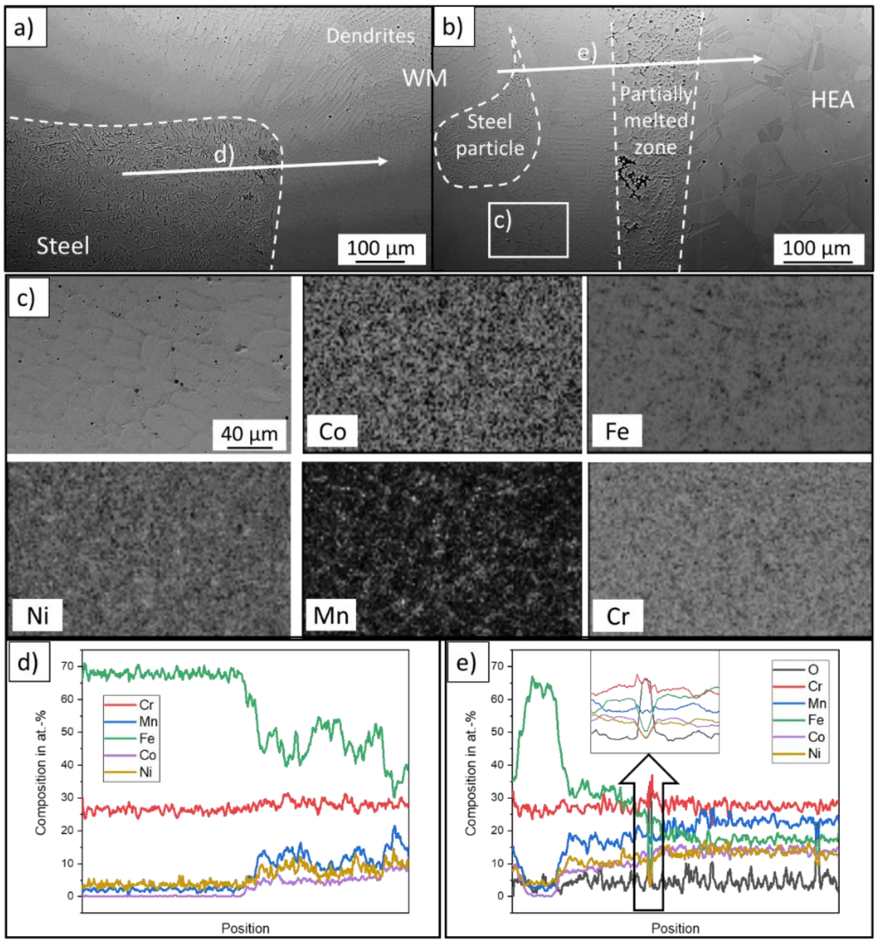

Figure 60: SEM-images of TIG-DMW of AISI 304 with CoCrFeMnNi-HEA in HT-condition: (a) area around FL at steel site; (b) area around FL at HEA site; (c) EDX-mapping of marked by white frame in figure part b; (d) EDX line scan as shown in a(arrow); (e) EDX line scan as shown in b (arrow) (published in [247])

The microstructure characterization results of TIG-DMW with CR-HEA are shown in Figure 61. In that connection, Figure 61a shows the transition area from steel-BM to WM. Segregation is only slightly visible on the SEM images. The EDX line scan (Figure 61d) from the steel to the WM also shows a change in the chemical composition from the steel to the WM with decreasing Fe- and increasing Co-, Mn-, and Ni-content. The Cr-content remains nearly constant as it is present in both materials at approximately 20 at. -%. The mixed WM has an inhomogeneous chemical composition. A sharp increase in Fe content can be seen in the WM. This increase in Fe-content is due to the unmolten steel particle, which is present here as already described for the other DMW-WM.

Figure 61b shows the transition from the WM to the CR-HEA-BM. The partially melted zone can be clearly seen, which shows clear pitting due to the specimen preparation. Segregation is also only slightly visible in the WM. The EDX line scan from the WM to the HEA-BM in Figure 61e shows increased Fe (approximately 30-40 at. -%) in the WM and reduced Co-, Cr- and Mn-contents. Again, a strongly heterogeneous chemical composition is evident in the WM. However, the partially melted zone also shows a strong inhomogeneity compared to the BM. This inhomogeneity in the partially melted zone can also explain the pitting or the local corrosive solutions during etching as previously described.

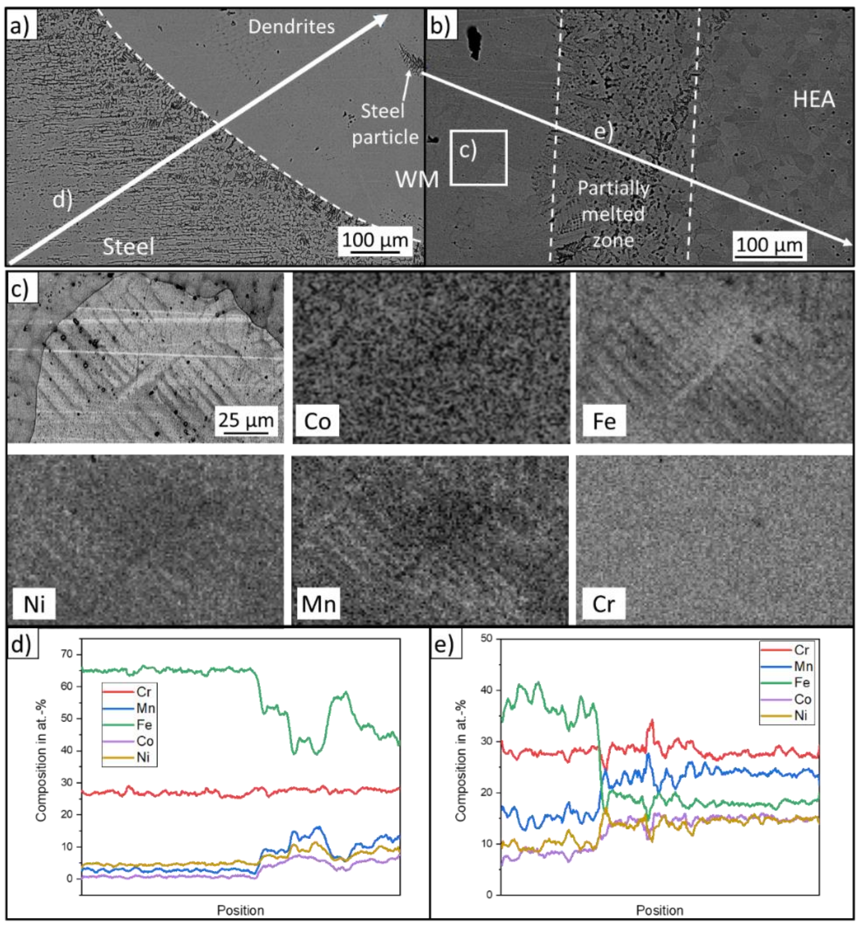

Figure 61: SEM-images of a TIG-DMW of AISI 304 with CoCrFeMnNi-HEA in CR-condition: (a) area around the FL at the steel site; (b) area around FL at HEA site; (c) EDX-mapping of the section marked min b; (d) EDX line scan as shown in a; (e) EDX line scan as shown in b

Figure 61c shows the WM with a distinct dendritic solidification structure. The EDX elemental maps show that Fe is enriched in the dendrites. Ni and Mn are enriched in the interdendritic areas. Co and Cr show a homogeneous distribution. This local segregation was also observed by Wu et al. [113] and by the results from Section 5.2 (TIG-welding of pure CoCrFeMnNi-HEA). In this case and in addition to Fe, an increased Cr and Co-content in the dendrites was demonstrated. Since welding of the HEA material with steel explains the predominant occurrence of Fe in the WM, its chemical composition is likely to be dependent on that. The steel AISI 304 with its additional alloying elements (e.g. C, Si; could not be locally resolved by EDX) showed a ferritic (BCC) primary solidification followed by a phase change to FCC [251]. In contrast, the HEA shows FCC solidification and no phase changes [145]. It currently remains open, which intensity the local chemical compositions have on the solidification behavior. This needs further investigation and simulation but was not considered in the current work. One of the very isolated references [145] on DMW of MPEAs encompass LB welding of CoCrFeMnNi-HEA in CR-condition with an AISI 316 (slightly increased Cr- and Ni-contents compared to the AISI 304). In that case, thermodynamic Scheil solidification simulation (in Thermocalc) suggested 100 % FCC solidification in the mixed WM. In the present study, the DMWs showed a pure FCC phase in the intermixed WM (see Figure 62b: EBSD investigation). However, at least local ferritic solidification and subsequent phase transformation cannot be ruled out.

Figure 62 shows the EBSD examinations of the TIG HEA (HR) steel DMW. The images clearly show that the WM contains very large grains compared to the BMs. These are larger and do not indicate directionality but are columnar in shape, unlike the TIG blind welds of pure HEA in Figure 46.

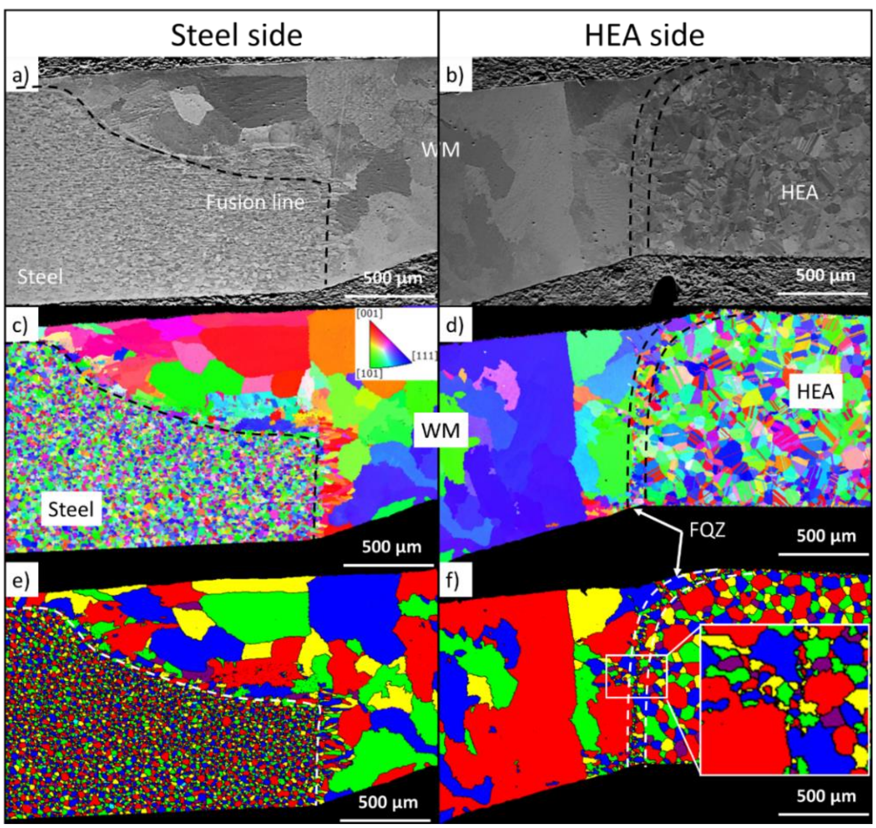

Figure 62: SEM and EBSD Analysis of TIG-DMW of AISI 304 with CoCrFeMnNi in HR-condition, shown for the areas around the steel (a, c, e, g) and HEA (b, d, f, h) FL: (a, b) SEM-image; (c, d) inverse pole map; (e, f) grain distribution map

No preferred orientation can be deduced from the inverse pole maps (Figure 62c and d) either. Indentation in Figure 62d shows a very large grain running across the entire plate thickness in a (111) orientation with apparently very strong grain growth. These large grains without preferential orientation in the WM are also shown by Sokkalingam et al. [249] for a TIG-DMW of $Al_{0.1}$CoCrFeNi HEA with the AISI 304. In the FL region, a distinct FGHAZ is present especially at the grain distribution map on the HEA side (Figure 62f). The cause is assumed to be the fine equiaxed zone mechanism, as described for the HEA bead-on-plate TIG-weld in Section 5.2. The main feature is the presence of annealing twins, as typical for the HEA [252] or FCC materials in general [226].

6.3 TIG-welding induced residual stresses in DMWs

In the next section, the surface-near residual stresses of the TIG-DMWs made of CoCrFeMnNi-HEA and the AISI 304 are described. For this purpose, the resulting residual stresses were measured by XRD. Both welds in Figure 63, i.e. those with the HEA in HT- (a) and CR-condition (b) show basically similar characteristics in the welding direction, i.e. in the longitudinal direction. Here, due to the ground surface prior to welding, compressive residual stresses are present in the BM of the HEAs and in the steel. In the CR-HEA in Figure 63b, these are slightly more pronounced, up to -900 MPa, because the longitudinal direction also corresponds to the rolling direction. However, even in the HT-HEA a maximum compressive residual stress, approx. 5 mm apart from the weld seam were seen (at around -750 MPa). This is higher as expected after grinding (approx. -400 MPa, compare Figure 47). On the steel side, the compressive residual stresses of about -200 MPa due to grinding are not as pronounced as on the HEA. For the CR-HEA, the maximum residual tensile stress of about 3 mm from the weld is approx. +300 MPa and thus higher as YS ($R_{p0.2}$ = approx. 240 MPa). This means the local stress reserves are discharged before further plastic deformation [233]. Subsequently, this changes to the weld in the compressive range at approx. +100 MPa. This is also evident, although less pronounced, on the steel side. In the case of the HT-HEA, the residual stresses in the longitudinal direction increase to approx. 0 MPa on the HEA side and to approx. +150 MPa (tensile) on the steel side. In each case at the edge of the weld near the FL are the highest residual stresses present. In the WM the residual stresses cannot be significantly determined due to the very large grains [232] as described in Section 5.3.

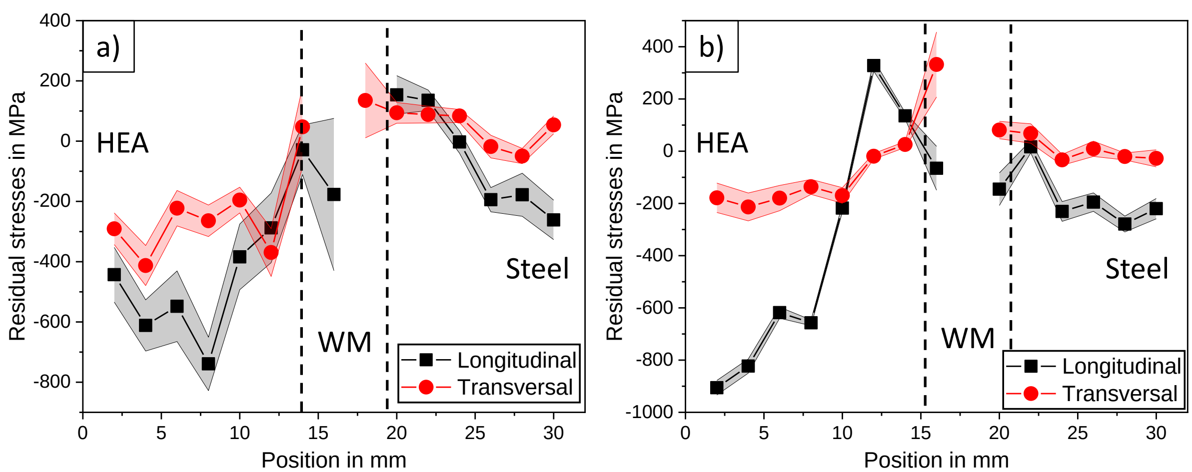

Figure 63: Residual stresses in a longitudinal and transversal direction in TIG-DMW of AISI 304 with CoCrFeMnNi-HEA in: (a) HT- and (b) CR-condition

In the transverse direction, compressive residual stresses are present in both HEAs up to -400 MPa for the HT and -200 MPa for the CR condition. In the case of the steel, there are hardly any residual stresses, as these were determined in the range around 0 MPa. In both welds and on both sides, the residual stresses increase with a smaller distance from the weld and pass into the tensile range. In the case of steel, these values reach approx. 100 MPa and thus not even a third of the YS $R_{p0.2}$ = 323 MPa). This shows that on the steel side, there are still some stress reserves in the transverse direction before plastic deformation. On the HEA side, the values increase for both, up to approx. +50 MPa for HT and up to approx. +300 MPa for the CR. The reason for the significantly higher residual stresses in the CR-HEA should be the higher strength and thus higher resistance to thermomechanical lateral contraction [233]. In addition, the higher tensile residual stresses in the HAZ, i.e. the area with coarser grain and reduced work hardening (compare Section 6.2), which is why it is softer and more likely to absorb the strain (plastic deformation) as the stronger CR-BM. Additionally, the local stress reserves are exhausted and therefore this part of the welded joint represents a possible failure weak point. In order to reduce the partially excessive tensile residual stresses, a stress-relieving treatment could be used [233]. However, no results are yet available for PWHT of HEA and the general thermal effect on residual stresses.

6.4 Hardness distribution in TIG-DMWs

The UCI microhardness maps for TIG HEA steel DMW are given in Figure 64. For both compounds, the hardness distribution is the same on the steel side. A clear HAZ cannot be detected, and the average hardness is approx. 250 HV0.1. Only in the area of the steel shoulder (see Section 6.2) on the root side a slight increase of the hardness to 300 HV0.1 can be detected. The reason may be an increased dislocation density due to strain hardening, which is thermomechanical introduced by shrinkage restraint during cooling [253]. Whether the shoulder geometry plays a role cannot be evaluated.The WM of both DMWs shows clear differences. The WM with the HT-HEA shows significantly higher values up to approx. 300 HV0.1. In comparison, the WM with the CR-HEA has only approx. 150 HV0.1. The reason may be an increased cold working due to a different shrinkage restraint with the plate offset. So rather a multi-axial load leads to higher work hardening and thus higher hardness. This would be a phenomenon that could be avoided by a suitable design of the welded component. Another possibility to explain the increased hardness would be a higher proportion of melted steel particles (higher hardness in the BM). However, this could not be confirmed by the SEM investigations. The HEA materials also show significant differences. The CR-HEA Figure 64b shows a pronounced HAZ. In contrast, no HAZ based on hardness can be identified for the HT-HEA in Figure 64a. However, the hardness formations are identical in each case for the investigated HEA bead-on-plate welds (detailed results in Section 5.4).

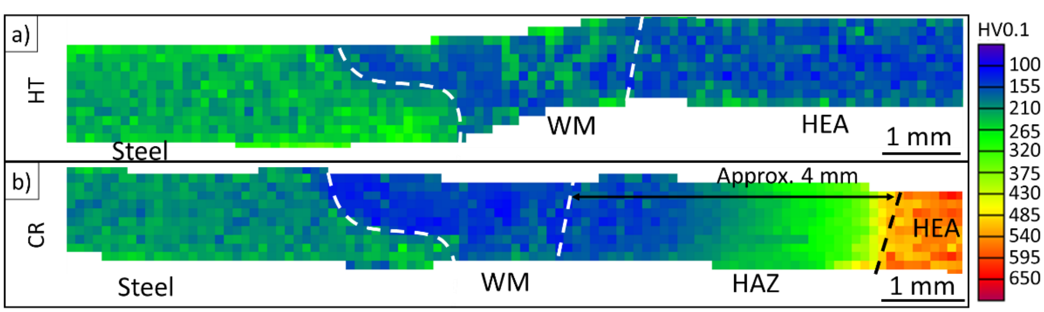

Figure 64: UCI microhardness HV0.1 mapping in TIG-DMWs of AISI 304 and CoCrFeMnNi-HEA in: (a) HT- and (b) CR-condition (published in [206])

6.5 Tensile Properties of TIG-welded DMWs

6.5.1 Overall tensile properties of TIG-welds

The engineering stress-strain diagram of TIG-DMWS and the BMs are shown in Figure 65a and b. The mechanical properties are given in Figure 65c, to compare the properties of the TIG-DMWs to the three BMs (HEA in CR and HT-condition and AISI 304). It is noted that all welded joints failed in the WM. The engineering stress-strain diagram and the mechanical properties obtained from it show increased R_M and elongation at fracture for the DMW with the HT-HEA compared to the CR-HEA, while $R_{p0.2}$ (286 MPa) is the same for both joints. The UTS of the DMW with the HT-HEA reaches its theoretical maximum, which is limited by the R_M of the weaker BM (HEA in this case). Nevertheless, the DMW with HT-HEA shows a significantly reduced fracture strain at 41.3 % of the HEA and 30.6 % of the steel. This shows theoretical potential for improvement of the mechanical properties in the TIG-DMW process between the HT-HEA and the AISI 304 steel. Possibilities for optimization would be a reduced offset, as this creates a multi-axial stress state in the tensile test, which results in a higher equivalent stress (comparable to a lap joint) for the material/WM [254]. Another possibility would be a PWHT to reduce or resolve the microstructural inhomogeneities [239] shown in Section 6.2, residual stresses [233] (Figure 63), or local hardening [44] (Figure 64).

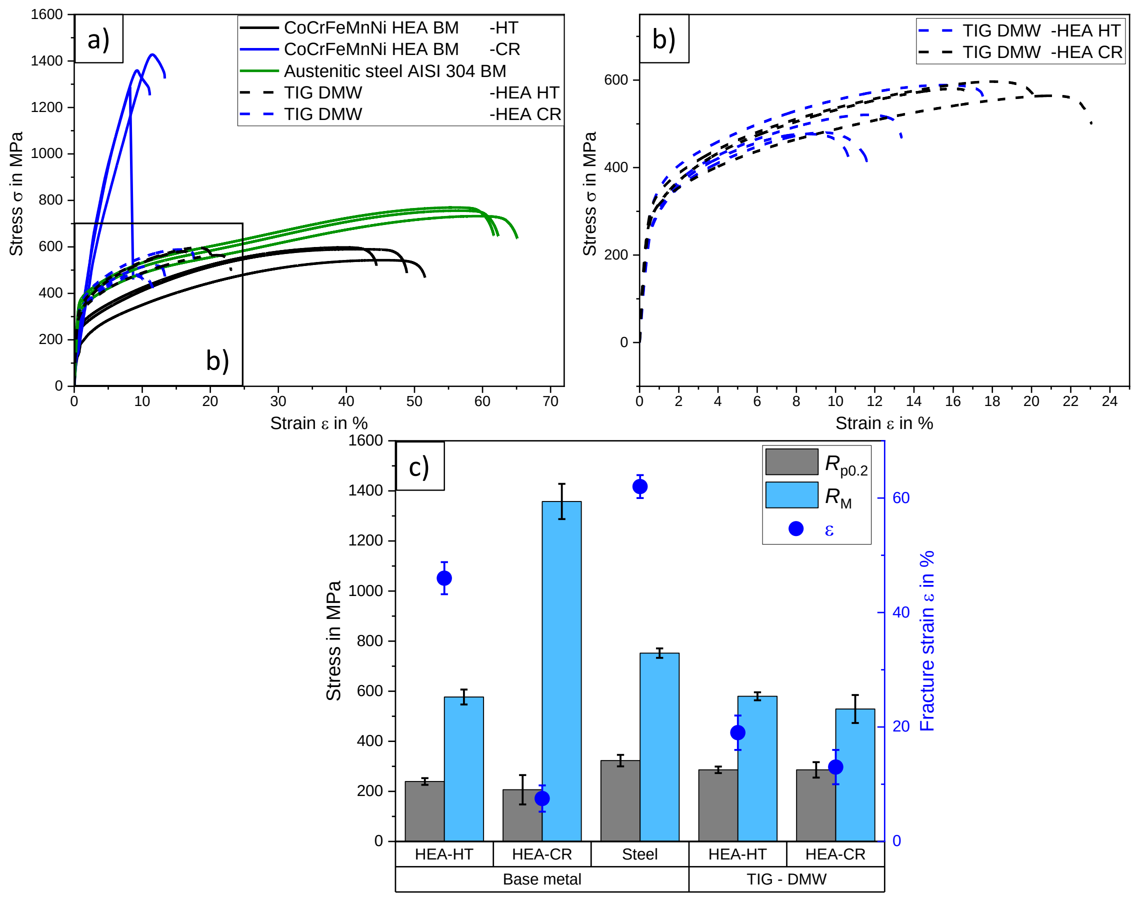

Figure 65: Engineering stress-strain curves of: (a) CoCrFeMnNi-HEA base material (HT and CR), austenitic steel BM, and the dissimilar metal TIG-welds (TIG-DMW); (b) dissimilar metal TIG-welds and (c) YS: $R_{p0.2}$, UTS: R_M and fracture strain ε (part a is published in [206])

The CR-HEA-DMW, with R_m = 529 MPa, does not reach R_M of the corresponding BMs of steel (752 MPa) and the CR-HEA (1359 MPa). The fracture strain (13 %) of DMW reaches 162.5 % of the CR-HEA but only 21.0 % of the steel, which is intermediate between the two BMs. In Ref. [145], a CR-CoCrFeMnNi-HEA and AISI 316 austenitic stainless steel are dissimilar LB-welded, the DMW has lower UTS (R_M = 449 MPa)) and significantly reduced fracture strain (5 %), compared to this work's TIG-DMW. What points out a clear improvement of this works TIG-DMW.

With respect to tensile properties, good weldability can be attributed to both TIG-DMWs. This is due to the $R_{p0.2}$ and R_M in the area of the HT-HEA. The YS and UTS) of the HT-HEA should be considered as a theoretical maximum for YS and UTS due to the weld microstructure and a strong tempering in the HAZ. Regarding the fracture strain, there is further potential for optimization, as already mentioned. It should also be noted that the welds were tested in the welded condition and therefore notch effects or similar damaging effects cannot be ruled out, as described for the bead-on-plate welds in Section 5.5.

6.5.2 Local tensile strain properties of TIG-DMWs

In Figure 66a global engineering stress-strain curve (a) and the local strain maps (b) for the global strain conditions I to III for the TIG-DMW with the HT-HEA are given. Condition I at approx. 7.5 % global strain shows the highest local strains in the WM with up to 20 %. Comparing the BMs, the HEA has a significantly higher average strain of approximately 14 % than the steel with approx. 5 %. The reason is the increased strength ($R_{p0.2}$ and R_M) and, thus, the resistance to deformation of the steel compared to the HEA (see Table 5). Only the area of the HEA-HAZ shows a reduced elongation of 5 %.

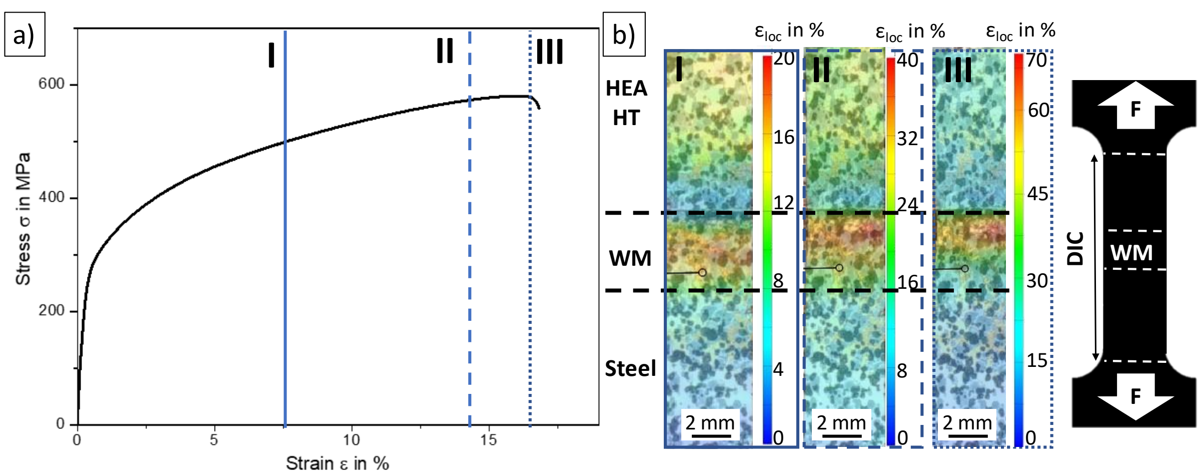

Figure 66: TIG-DMW of AISI 304with CoCrFeMnNi-HEA in HT-condition: (a) engineering stress-strain curve and (b) local strain ε_{loc} for stage I to III (published in [206])

As there is no change in the microstructure (Section 6.2) or local hardness (Figure 64a) compared to the rest of the BM, it is assumed that the offset is the reason for this phenomenon. In stage III (ε = 16.5 %), this area is not distinguishable from the BM based on the local strains. In that case, the HEA-BM with approx. 23 % average local strain has still absorbed more strain compared to the steel with 9 %. The WM absorbs significantly more strain than the BMs with an average of 41 % and local strains of up to 70 %. This shows that it has the lowest strength. The reason for this is perhaps the geometrical misalignment, which creates a multi-axial stress state and a higher equivalent stress (comparable to a lap joint) [254] in the WM, resulting in increased mechanical load. In addition, the TIG-DMWs always failed in the WM close to the HEA-FL. The steel shoulder described in Section 6.2 (see Figure 58) will further stabilize the WM close to the steel FL. The steel, with a higher strength compared to the WM, is part of the cross-section, which results in increased local strength. This results in a weak point for mechanical failure in the WM close to the HEA-FL.

Figure 67 shows (a representative global engineering stress-strain curve and (b) the strain maps for the local strain stages I to III for the TIG-DMW of the CR-HEA with the AISI 304. Stage I at approx. 4 % global strain shows the highest local strains in the WM with up to 25 %. Comparing the BMs, the CR-HEA with 0 % has on average a significantly lower elongation than the steel with approx. 4 %. The reason for this is the higher strength ($R_{p0.2}$ and R_M) and thus resistance to deformation of the highly work-hardened HEA compared to the steel (see Table 5). However, the CR-HEA shows a clearly pronounced HAZ in terms of the identified microstructure (Section 6.2) and hardness change (Figure 64b) compared to the BM. This is not reflected in the local strains, as no local strains are represented in the HEA-BM close to the FL. This is consistent with stage III. In these cases, a virtually local strain of "zero" in the CR-HEA-BM appeared. The reason for this could be that the strength in the HAZ is still significantly higher than that of the WM or steel. In contrast, the AISI 304 shows an average of 13 % strain. The largest strains are in the WM with up to 90 % (local) and an average of 59 %. The highest amount of local strain and the failure area is in the WM close to the HEA-FL. As these welds do not show any geometrical offset (i.e.: uniaxial stress state), the steel shoulder (Section 6.2) is identified as the cause, which stabilizes the WM close to the steel FL, as described for the DMW with HT-HEA. The higher maximal local strains in the WM compared to the DMW with HT-HEA (approx. 70 %) can be attributed to the lack of offset but also to stabilizing effects of the very strong CR-HEA-BM, as noticed for the CR-HEA bead-on-plate welds in Section 5.5.2.

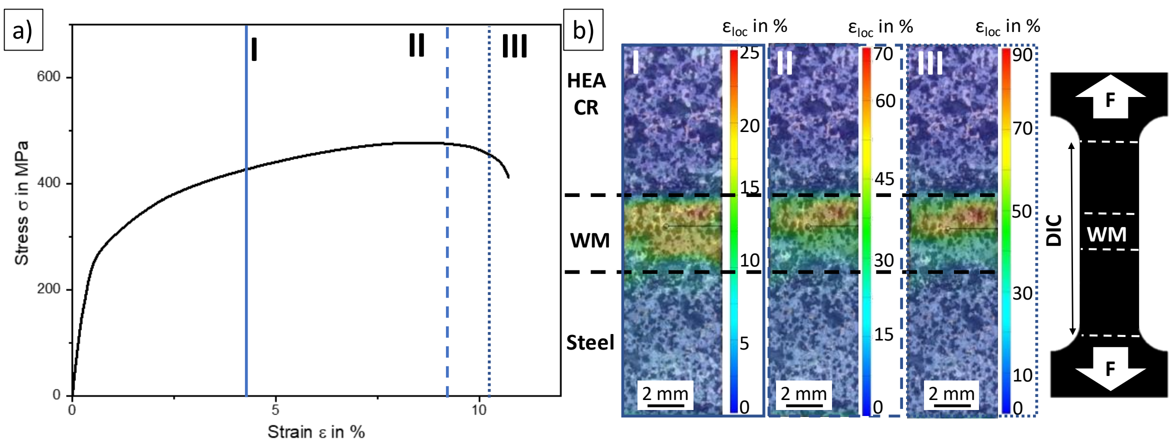

Figure 67: TIG-DMW of AISI 304 with CoCrFeMnNi-HEA in CR-condition: (a) engineering stress-strain curve and (b) local strain ε_{loc} for stage I to III (published in [206])

6.5.3 Fracture morphology of TIG-DMW tensile tests

The fracture morphologies for the tensile tests of the TIG-DMWs are presented in Figure 68. There are no clear differences between the fracture surfaces of the two HEA-DMWs. Both mixed joints show the dimpled structures characteristic of a ductile fracture. Qualitatively, there is no difference in the average dimple size. Nevertheless, both DMWs show locally strong deviations of the dimple diameters. Possibly this reflects the anisotropic dendritic microstructure (see Section 6.2) occurring in the same order of magnitude. Büttner [245] describes that local microsegregation in the dendritic microstructure of DMW has an influence on both the mechanical properties and the fracture morphology. Both fracture surfaces also have round particles in the dimples, which are Cr, Mn oxides from the HEA production [33], as already described in Section 5.2.

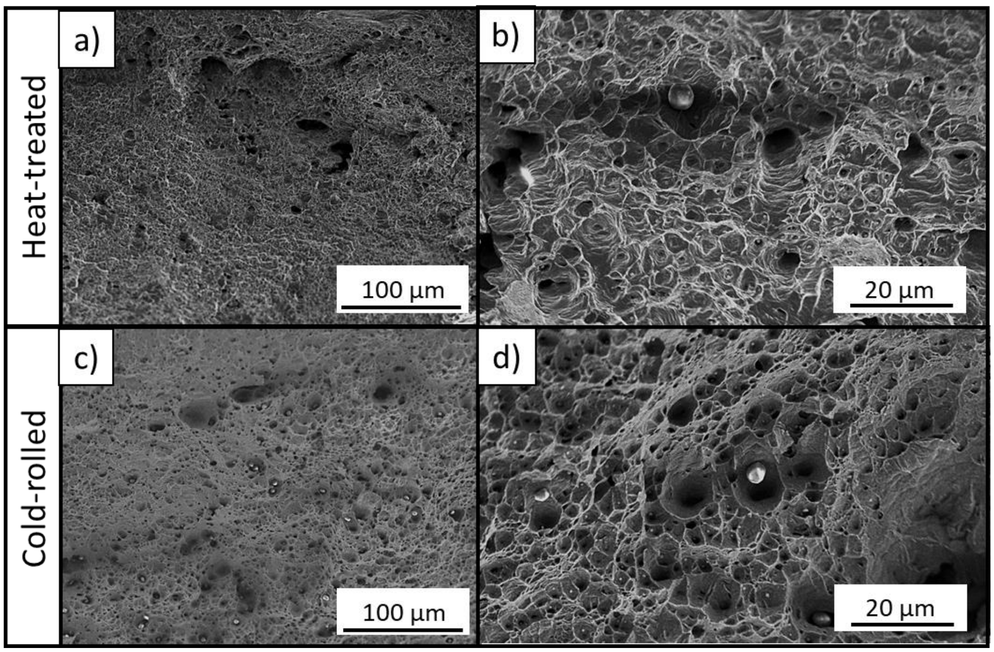

Figure 68: SEM-images of the fractured cross-weld samples of TIG-DMW of AISI 304 with CoCrFeMnNi-HEA in (a, b) HT- and (c, d) CR-condition with AISI 304: (a,c) overview; (b, d) dimples in higher magnification (published in [206])

Finally, conditional weldability can be concluded based on the investigation of the mechanical properties. The reason is that a sound and defect-free weld could be produced. The tensile tests showed that the WM is the weak point of the DMW joints and thus limits the mechanical load-bearing capacity (and hence its later application possibilities). But as mentioned, further TIG process optimization could improve the mechanical properties. The aim of process optimization should be to avoid offset and achieve a more homogeneous microstructure. However, it is precisely the prevention of the offset that should be the focus of further welding to avoid multi-axial stress conditions [254].

7. Results and discussion of FSW welding of CoCrFeMnNi-HEA and CoCrNi-MEA

In the following sections, the weldability of both MPEAs by FSW is presented. Butt joints of both MPEAs were examined in HT- and initial CR-condition in terms of defect-free welds by visual inspection, and radiographic testing. In addition, the weldability in terms of the resulting microstructure was characterized by LOM, SEM, and EBSD. The hardness is examined via UCI as well as the resulting residual stresses due to the FSW-processing by XRD-measurement. In addition, the global and local mechanical tensile properties were determined by means of DIC-instrumented tensile tests. Based on these results, statements on the FSW-weldability of both MPEAs are concluded.

7.1 HEA and MEA FSW-joints and possible welding-induced defects

For the description of possible weld imperfections, visual images of the weld surface (lower part) and the corresponding radiographic test images (upper part) of the FSW-joints of the HEA (a, b) and MEA (c, d) in HT- (a, c) and CR-condition (b, d) are shown in Figure 69. Both the HT-HEA (Figure 69a) and HT-MEA (Figure 69c) show a homogeneous weld after a short run-in area, which is about 10 mm for the HEA and 5 mm for the MEA. In the area of the weld seam, a typical FSW surface pattern (also known as shoulder friction marks) [68] with a semicircular structure with an opening in the welding direction, i.e. in the direction of the end crater, can be seen here for both welds. A flash formation can be seen on the surface at the sides of the weld, but this is not excessive and is therefore to be regarded as grossly damaging. In the weld seam, a stripe can be seen next to the center of the SZ for the HEA and in the middle of the weld seam for the MEA. Since this area is rather brighter than the surrounding area, it indicates a lower radiation penetration on the detector, which excludes a tunnel defect and rather indicates a weld nugget or a white band effect, since areas of high deformation and any deposits of tool wear particles (W with 1.5 % LaO) reduce the radiation penetration [68]. As shown, no welding imperfections were detected for the HT-MPEA weld joints (except for the unavoidable FSW run-in area).

In contrast, the welds of the CR materials do not show a similar result. The CR-HEA in Figure 69b shows excessive flash formation on the sides of the weld, which leads to a lack of material in the area of the weld and thus to a very dark, i.e., diluted, area in the radiographic image of the weld seam. This shows a reduced plate thickness in the weld seam. Reasons for excessive flash formation can be too high process temperature or too deep plunging of the tool [68]. This imperfection can therefore be avoided by adapting the process parameters. The surface also does not show such homogeneous surface stripes as the HT-joint, but in some cases only smearing from the AS towards the center of the weld, which is not constant. In addition, the CR-HEA has a bright stripe along the welding direction in the center of the weld joint. This could also indicate the weld nugget, or a white band, as previously described for the HT-MPEAs. Thus, the first weld imperfections (flash formation, surface smearing) appear during the welding of the CR-HEA, which could theoretically be prevented by adjusting the welding parameters, as they are process-related [68].

The CR-MEA in Figure 69d shows a homogeneous surface after a run-in area of approx. 10 mm. The run-in area here shows clear brown and blue tarnish colors, as no oxidation prevention was used. Compared with the CR-HEA in Figure 69b, the MEA shows only a very slight flash formation, which is not assumed to be a weld imperfection. The radiographic test of the welded joint shows a somewhat prolonged run-in area of approx.15 mm since a material separation in the welding direction can be seen beforehand. From the radiation test, it is not possible to determine whether it is a crack or a lack of weld penetration. Similar results can be seen in the area around the end crater. These material separations are perhaps cracks, but due to their location directly in the center of the weld and their straight shape in the direction of the weld, it is more likely to be an insufficient weld penetration. Between these material separations, no further weld imperfections were identified. However, a light-colored area along the weld direction in the center of the weld seam is again evident. In conclusion, a white band or a weld nugget is also assumed here, albeit less clearly pronounced.

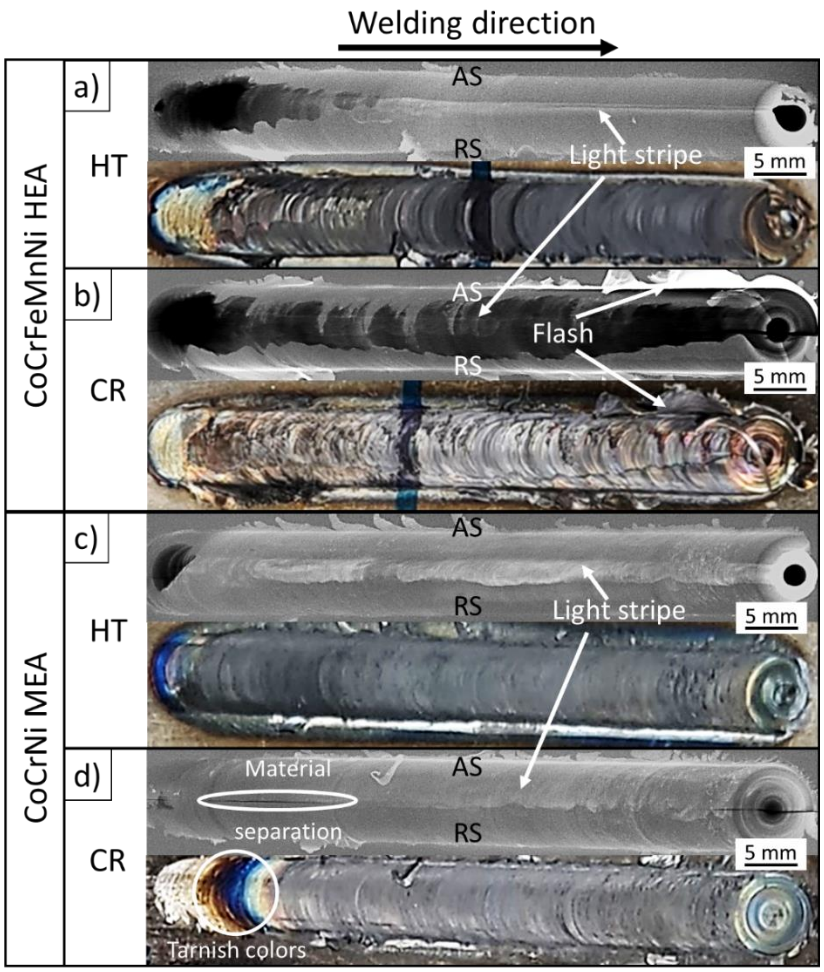

Figure 69: RT-images and corresponding weld joint surface of FSW butt joints: CoCrFeMnNi-HEA in (a) HT-, (b) CR-condition and CoCrNi-MEA in (c) HT-, (d) CR-condition

The force and temperature measurements of the individual FSW joints are shown in Figure 70. The temperature was measured at the tool shoulder and the force in the x, y, and z directions, as described in Section 4.2.2. The temperature measurements show a typical curve for FSW [255] for all four welds. The temperature increases at the start of the process. Subsequently, a constant temperature is established during the welding until it sharply decreases at the end of the weld. The constant temperature during FSW represents a quality parameter in terms of a constant and homogeneous FSW process [256]. This behavior appears in the HT-HEA (Figure 70a) and the two MEA welds (Figure 70c and d). The CR-HEA shows a large temperature variation at about mid-process. This cannot be directly attributed to weld imperfections regarding the radiation image in Figure 70b. Since there is a brief heating and subsequent cooling, part of the flash may have entered the measuring zone. However, the cause of the temperature variation cannot be clarified clearly. The CR-HEA, with 1027.7 ± 15.2 °C (79.7 % of T_S), shows almost the same temperature compared to the HT-HEA at 1049.6 ± 14.5 °C (81.4 % of T_S). This shows that the process temperature with a difference of approx. 2 % T_S, should not be the reason for the weld imperfections in the CR-HEA-joint. Hence, the previously described weld imperfections in the CR-HEA could not be avoided or reduced by increasing the FSW process temperature. Other parameters to avoid excessive flash formation are a reduced depth penetration, an adapted tilt angle, or an improved tool geometry (e.g. round shoulders, tool pin with zero offset) [68, 257].

The two MEA FSW joints in Figure 70c and d show a nearly identical FSW process temperature of about 1123.6 ±7.6°C (HT) and 1121.3 ± 7.7 °C (CR, which is about 79.2 % of T_S.) Only the temperature increase at the welding start is sharper for the HT-MEA than for the CR-condition. This should also be due to the highly cold-working state of the CR-MEA, which should need more energy for deformation than the HT-HEA. This is the reason why the CR-MEA has a longer run-in area (compare Figure 69c and d).

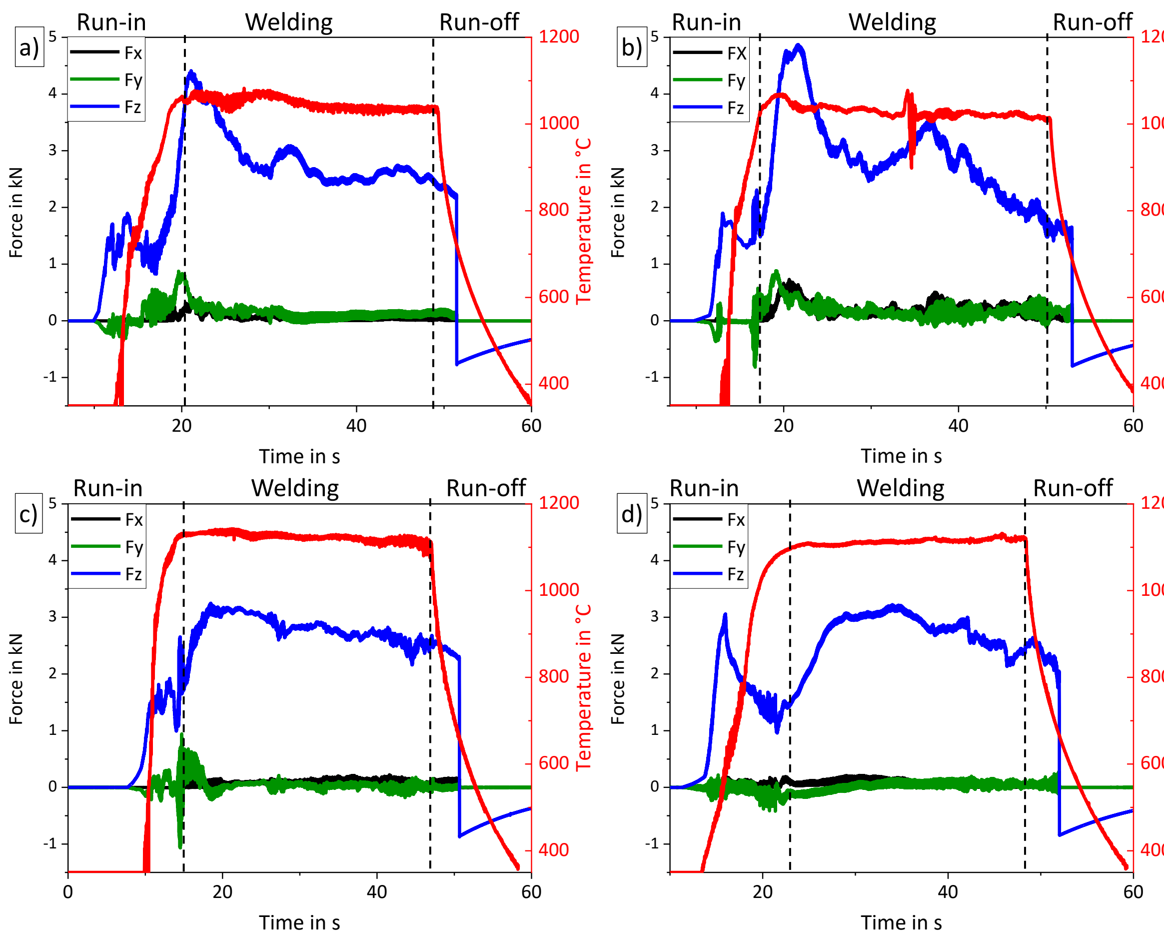

Figure 70: Measured forces and temperature at tool shoulder during FSW of CoCrFeMnNi-HEA in: (a) HR-, (b) CR-condition and CoCrNi in (c) HR- and (d) CR-condition

The measured force in z-direction F_z is the most important, as it is the highest force. The forces in the x- and y-direction can be neglected, as shown in Figure 70. In both HT and CR-HEA welds (Figure 70a and b) and the HT-MEA weld (Figure 70c), during FSW, the run-in is the same with respect to F_z. The force in the z direction (F_z) increases and remains a few seconds to approx. 1.5 kN until it increases. This stage characterizes the penetration (or “dive-in”) of the FSW tool pin into the material. The second increase of the force indicates the full contact of the tool shoulder with the surface [258, 259]. In both HEA welds, the force then decreases again, indicating the end of the penetration phase. For the HT-HEA, the subsequent welding phase shows a relatively constant F_z between 2.5 kN and 3 kN (Figure 70a). In contrast, the force in the CR-HEA in Figure 70b shows an increase and a subsequent decrease, i.e. a relatively discontinuous course. The maximum (axial) force F_z is somewhat higher for the CR-HEA at 4.9 kN compared to the HT-HEA at 4.5 kN. The reason is the higher hardness of the CR-HEA. In addition, the rather unsteady force during FSW of the CR-HEA also indicates an inconstant process, which increases the probability of the occurrence of weld imperfections. In the case of the CR-MEA (shown in Figure 70d), F_z decreases after the first sharp increase and increases afterward again. This represents the run-in area with the described material separation (compare Figure 69d) and indicates a weld imperfection. In both MEA welds, F_z is relatively constant between 2.5 kN and 3.0 kN after the run-in area, until the weld finish. Within this range, a homogeneous weld surface was observed without the occurrence of weld defects (see Figure 69c and d). The results of both the measured force and temperature suggest the suitability to predict a certain weld seam quality just based on the welding parameters.

7.2 Microstructure analysis of CoCrFeMnNi-HEA and CoCrNi-MEA FSW-joints

7.2.1 Microstructure characterization with LOM

Figure 71 shows the LOM investigations on cross-sections of the FSW butt welded HEA (a, b) and MEA (c, d) in HR- (a, c) and initial CR-condition (b, d). Both HT-MPEAs (HT-HEA: Figure 71a, HT-MEA: Figure 71c) achieved full weld penetration and did not show weld imperfections in the investigated cross-section. From that point of view (and incorporating the results described in Section 7.1,) the used FSW parameters based on the AISI 304 could be successfully transferred to the FSW of both MPEAs, indicating similar weldability like austenitic stainless steels. In addition, a typical FSW microstructure formation can be seen in the HT-HEA, similar to Qin et al. [134] showed for FSW joints of CoCrFeMnNi-HEA. A SZ with very fine grain and a weld nugget is present. The fine grain is formed by a very strong mechanical deformation during the FSW process and a subsequent recrystallization due to the elevated process temperature of >0.8*T_s [64, 260]. The weld nugget in the HEA weld is located on the AS of the SZ in the upper half of the weld and is the area of greatest deformation and mechanical stress [64]. This confirms the results from the radiographic testing from Section 7.1 and shows that these areas can be detected by radiographic tests. In HT-MEA, the weld nugget appears across the entire width of the SZ in the upper half of the plate thickness and is thus larger than in HEA. Due to the more difficult preparation of the cross-sections with respect to the etching of the new materials, it can only be recognized to some extent that there is a TMAZ next to the SZ. Here, a gradient in the grain size (increased grain sizes in the direction of BM) can be seen due to the decreasing thermomechanical load and dynamic recrystallization with increasing distance from the SZ. This is also a typical microstructure formation of an FSW joint [64]. This TMAZ is more pronounced on the MEA.

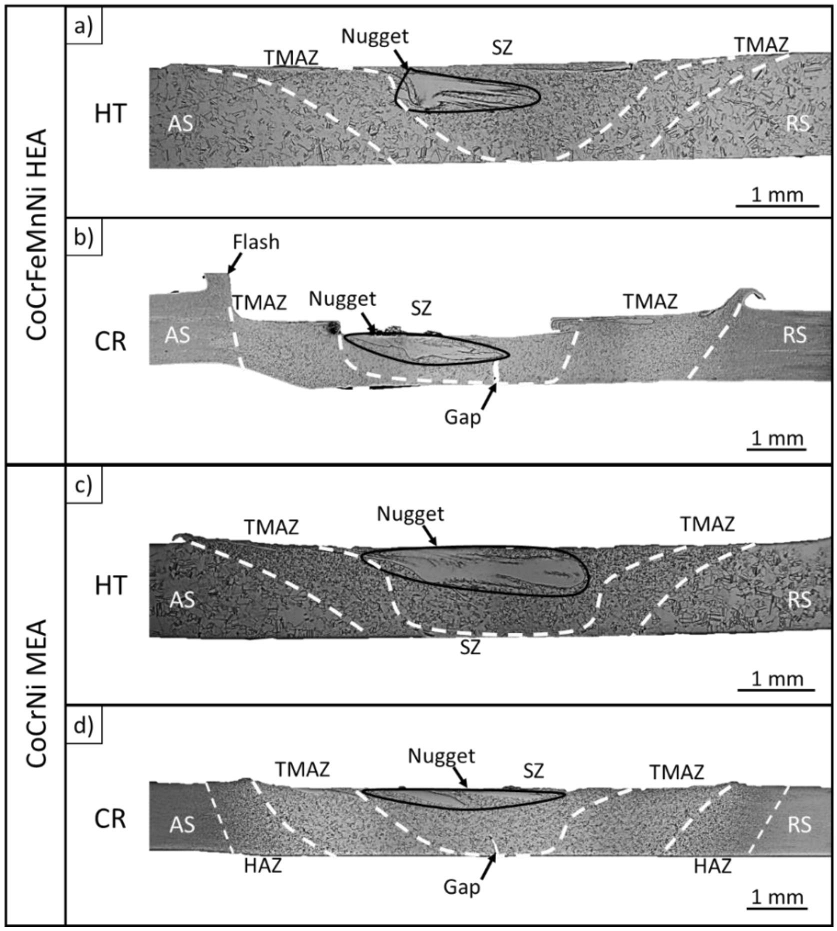

Figure 71: LOM-images (grayscale image for better contrast display) of cross-sections for the FSW butt joints: CoCrFeMnNi-HEA in: (a) HT-, (b) CR-condition and CoCrNi-MEA in (c) HT -, (d) CR-condition

The cross-section of the FSW butt weld of the CR-HEA is given in Figure 71b and of the CR-MEA is given in Figure 71d. Here, for both welds, a gap can be seen at the bottom of the weld. Whether this is a crack, or a lack of penetration cannot be deduced from the picture. However, it can be deduced that this is an impermissible weld seam imperfection [68], and therefore the transferred welding parameters must be further adjusted. Possibilities of adaptation in case of insufficient weld penetration would be the adaptation of the tool geometry, especially regarding pin length and shape since these have a great influence on the material flow during welding [68]. But also, the parameters described in Section 7.1 (tool geometry, plunge depth, etc.) can have a positive influence on weld penetration depth [68]. In addition to the gap, the SZ shows a fine-grained microstructure, although coarser compared to the CR-BM. The reason for the fine grain is, as previously described the dynamic recrystallization (see Section 2.2.2). The CR-HEA (Figure 71b) also shows a reduced plate thickness in the SZ together with a distinct flash formation. The reason for this may be excessive frictional heat between the material and the shoulder. The material is thermally softened and is pushed out of the process zone under high contact pressure from the tool shoulder, creating the flash [68]. The flash material is removed from the SZ and explains the reduced sheet thickness. This effect is not seen in the CR-MEA. The fact that this only occurred with the CR-HEA among all four welds with identical welding parameters could be due to an uneven plate thickness of the rolled and not completely straight plates. As a result, they could not be clamped exactly in the fixture.

Both MPEAs in CR-condition show a weld nugget in the SZ. For the HEA (Figure 71b), it is located on the AS in the upper half of the plate thickness. In contrast, in the MEA (Figure 71d), the weld nugget is present across almost the entire width of the SZ. In both CR-MPEA welds, a TMAZ adjoins the SZ. In both cases, a coarser grain structure than in SZ or BM can be seen. The reason is diffusion-induced recrystallization and grain growth of the plastically deformed material (by CR and FSW) at the respective (but relatively high) FSW temperature [64]. The MEA (Figure 71d) also shows a HAZ formation outside the effective area of the tool shoulder width, indicated by a significant grain size gradient from the TMAZ in the direction of the BM. In the CR-HEA (Figure 71b), a HAZ could not be identified.

7.2.2 Microstructure characterization with SEM

Figure 72 shows the SEM images for two significant areas of the FSW joints in terms of (1) the weld nugget (Figure 72b) and (2) the transition area of the SZ to the BM (Figure 72c). In Figure 72a, the areas are marked in the cross-section of the LOM image. The area of the weld nugget (Figure 72b) shows a brighter phase, in the BSD-image. This contrast could be due to the material itself, indicating an area or phase with increased density [261]. While in the left part of Figure 72b, this phase is arranged along a line and a bulk, in the right part of Figure 72b it is formed from a center almost lamellar outward. Additional EDX mappings (shown in Figure 72d) of the marked areas were obtained to verify the local chemical composition. As a result, a formation of W-clusters can be seen in the specific white band. The reason is the well-known abrasive wear of the W-tool, which agglomerates in this area. This effect was reported several times for FSW of CoCrFeNi-based HEAs [130-132, 137, 138] and other materials like Al-alloys [262]. Consequently, the elements Co, Cr, Fe, Mn, and Ni showed a local more or less significant depletion in the white band. No enrichments of the HEA elements can be detected.

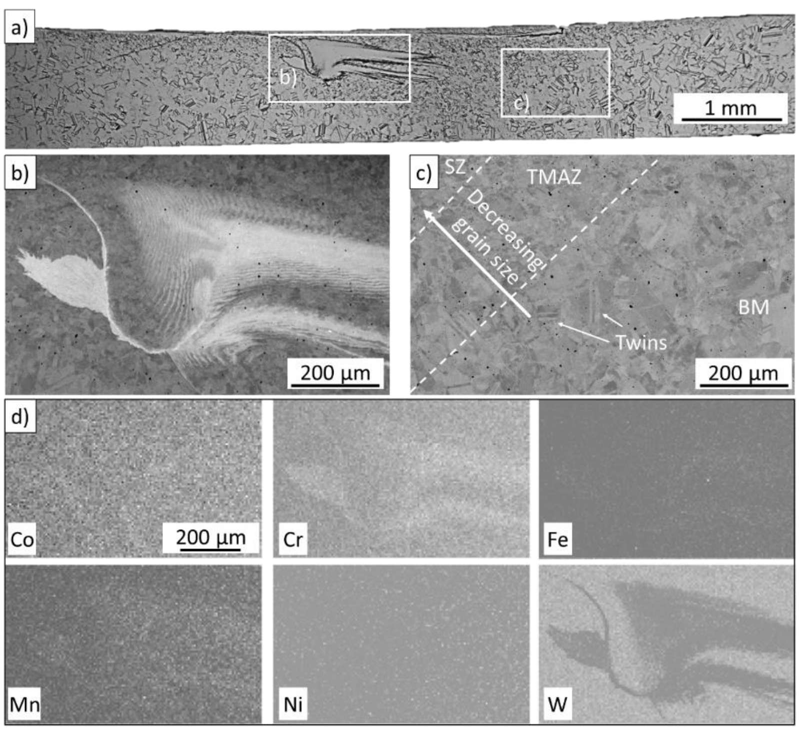

Figure 72: FSW butt weld joint of CoCrFeMnNi-HEA in HT-condition: a) LOM overview figure, detailed SEM-figures of (b) white band, (c) transition from SZ via TMAZ to BM, (d) EDX mapping of white band region.

Figure 72c shows the area from the SZ to the BM. Here, above all, a grain size gradient from SZ to the BM with small grains was identified as described in Section 7.2.1. In that case, the reason is the already described dynamic recrystallization (see Section 2.2.2) due to the FSW heat generation [64, 71]. Furthermore, twins can be seen in the BM. These are not present in the fine grains as they are induced by the grain coarsening due to the heat treatment. Thus, these are annealing-induced twins [263], which are dissolved by the recrystallization in both the SZ and TMAZ [64, 71]. Both SEM images in Figure 72b and c show black dots. These indicate Cr, Mn oxides from the underlying material synthesis [33] (although this was not investigated in detail it is reasonable to assume).

Figure 73 shows the SEM and EDX results of the FSW butt weld of the CR-HEA. Again, two locations were singled out and presented in detail: (1) the white band (see Figure 73b) and the area from TMAZ to BM (Figure 73c). The white band exhibited a lamellar structure as previously described for the HT-HEA (see Figure 72).

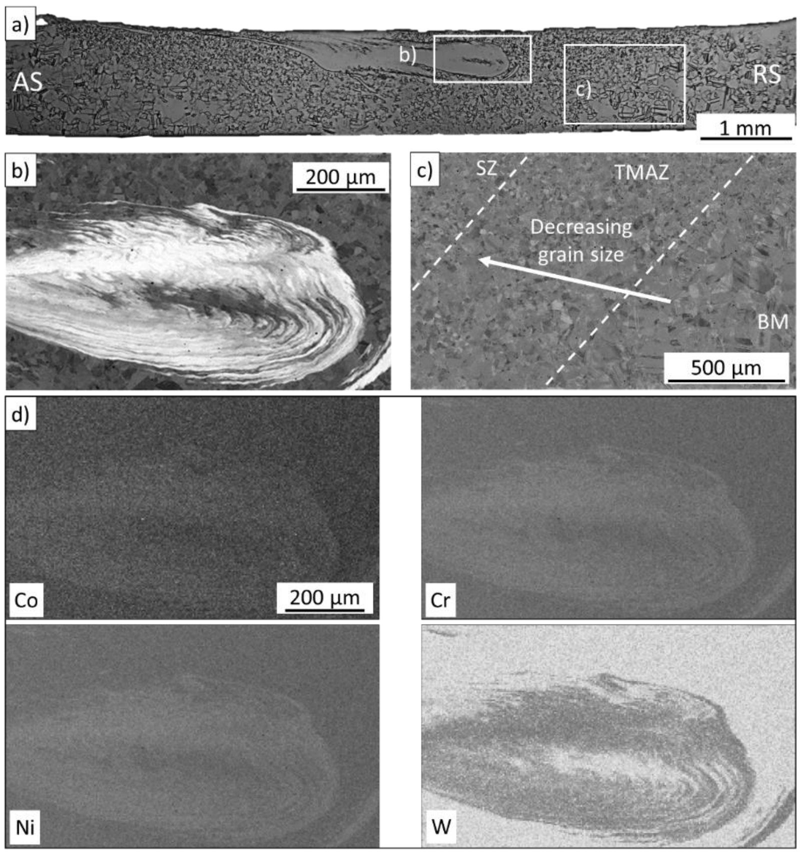

Figure 73: FSW butt weld joint of CoCrFeMnNi-HEA in CR-condition: a) LOM overview figure, detailed SEM-figures of (b) white band, (c) transition from SZ via TMAZ to BM, (d) EDX mapping of white band region

The EDX images in Figure 73d show again the agglomeration of W-clusters (by abrasive tool wear). In addition, this region shows a slightly reduced Fe and Cr content. Nonetheless, the EDX mappings do not allow generalized conclusions in terms of the enrichment or depletion of Co, Mn, or Ni. In the transition area from the CR-BM to the TMAZ (see Figure 73c), an increase in the grain size can be seen in the TMAZ. The reason is the pronounced recrystallization of the severely plastically deformed BM (by CR and FSW stirring) due to the generated welding process heat [44, 45]. From that point of view, it is not reasonable to give precise statements based on the presented results whether the specific microstructure is a pure TMAZ or HAZ. In other words, it is not trivial to distinguish in FSW joints if the combined thermomechanical load or a single temperature increase is the predominant influence on the microstructure.

The SEM and EDX results of the FSW-joint of the MEA in CR-condition are presented in Figure 74. Again, the white band shows a lamellar structure with an enrichment of W due to the abrasive tool wear and the depletion of the MEA elements Co, Cr, and Ni (see Figure 74d). The transition of the SZ to the BM in Figure 74c shows a clear grain refinement from the BM towards the SZ. The reason for the reduced grain size in the SZ and the TMAZ is a plastic deformation in the FSW process as well as the dynamic recrystallization caused by the FSW process [64, 71]. Twin grain boundaries appear in the BM, which are not visible in the SZ and the TMAZ. The identified annealing twins are rather typical for materials with low stacking fault energy [191, 226]. However, they are dissolved during recrystallization, which is why they are not present in both the SZ and TMAZ.

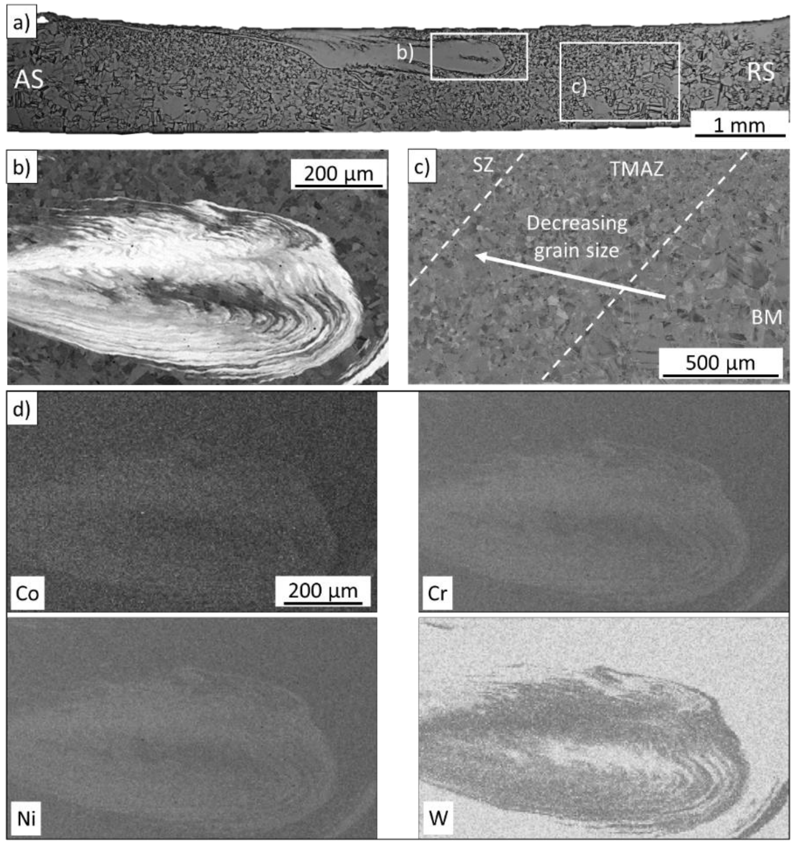

Figure 74: FSW butt weld joint of CoCrNi-MEA in HT-condition: (a) LOM overview figure, detailed SEM figures of (b) white band (c) transition from SZ via TMAZ to BM, (d) EDX mapping of region b.

The SEM and EDX results of the FSW joint with CR-MEA are presented in Figure 75. The white band is shown in Figure 75b and is located directly below the surface. The EDX results in Figure 75d emphasize again the W enrichment in the white band due to the abrasive tool wear accompanied by the depletion of the MEA-elements Co, Cr, and Ni. The transition area of the TMAZ to the BM is shown in Figure 75c. Three areas can be seen here:

(1) the CR-BM with a very small grain size. It should be noted here that the rolling direction runs into the depth of the picture and a certain linearity can be seen by means of LOM in Figure 75a (compare Figure 25, BM).

(2) the TMAZ is in the top area with a medium grain size, where a deformation and dynamic recrystallization, as described before, took place. This results in larger grains as in the BM [64, 71].

(3) The largest grains can be seen in the area below the TMAZ. It is not clear whether this is also a TMAZ or only a HAZ, since the mechanical influence in this area was not investigated further. However, there must be a lower share of mechanical and higher effectiveness of thermal stresses, which cause the grain growth (as an accompanying effect to the dynamic recrystallization).

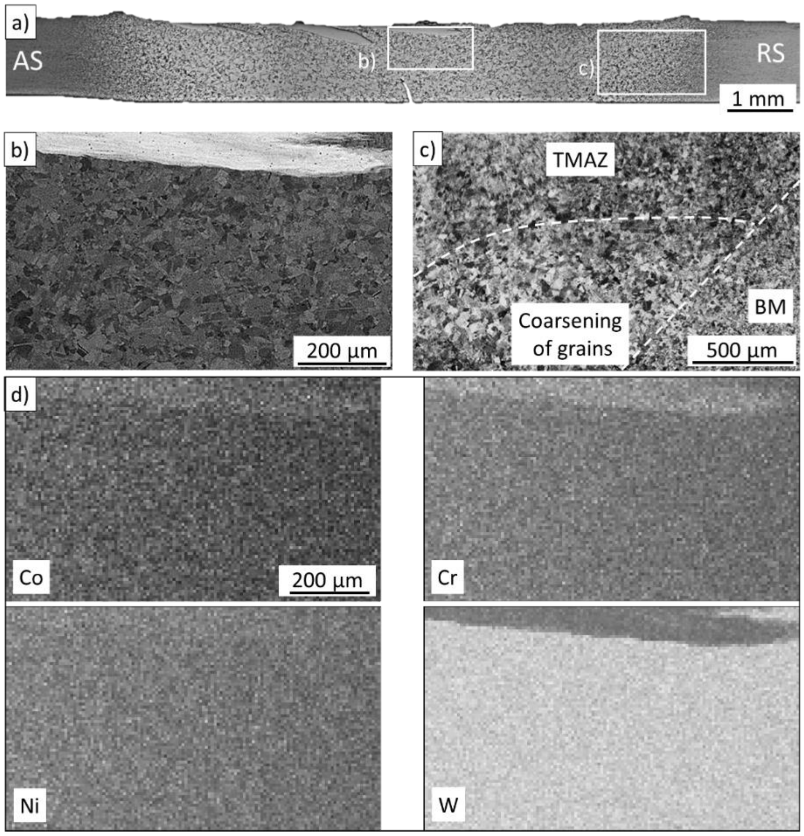

Figure 75: FSW butt weld joint of CoCrNi-MEA in CR-condition: (a) LOM overview figure, detailed SEM figures of (b) white band; (c) transition from SZ via TMAZ to BM, (d) EDX mapping of white band

Overall, SEM examinations show a white band and fine grain from dynamic recrystallization in the SZ for all FSW butt welds. In the case of the HEA, the white band is somewhat offset in the direction of the AS, while in the case of the MEA, it extends over the entire SZ. The formation of the TMAZ is also similar for all joints and shows a gradient of grain size between the SZ and the BM, which is also dependent on the initial material state.

7.2.3 Microstructure characterization of CoCrFeMnNi-HEA FSW butt joints in HT-condition by EBSD

Figure 76 shows the results of the EBSD analysis of the FSW butt weld joint of the HT-HEA. Due to the high experimental effort and limited accessibility of the EBSD equipment, they were performed only for the FSW joint from HEA in HT-condition. Only the part of the SZ on the AS is shown since the white band is located here as described in Section 7.2.2. In particular, the SEM-image (a), the inverse pole map (b), and the grain distribution map (e) show the difference in grain size in the SZ and the TMAZ compared to the BM. This is also shown by the grain size distribution in Figure 76d, where a large portion of the grains lie in the range below 20 µm, which can rather be assigned to the SZ and the TMAZ. The remaining part of the larger grains at an average of approx. 100 µm can be assigned to the BM. The inverse pole frequency in Figure 76c does not show a clear preferred direction, although some directions are more likely, such as the [001] or the [111] direction. A closer look at the inverse pole map in Figure 76b shows that blue to green areas are more prevalent in the white band. This indicates a preferred orientation in the [111] direction. The phase map shows that the entire weld and the BM contain an FCC phase. The 0.2 % BCC phase can be neglected as a measurement inaccuracy or are effects at grain boundaries. Therefore, a phase transformation of the very stable FCC material can be excluded.

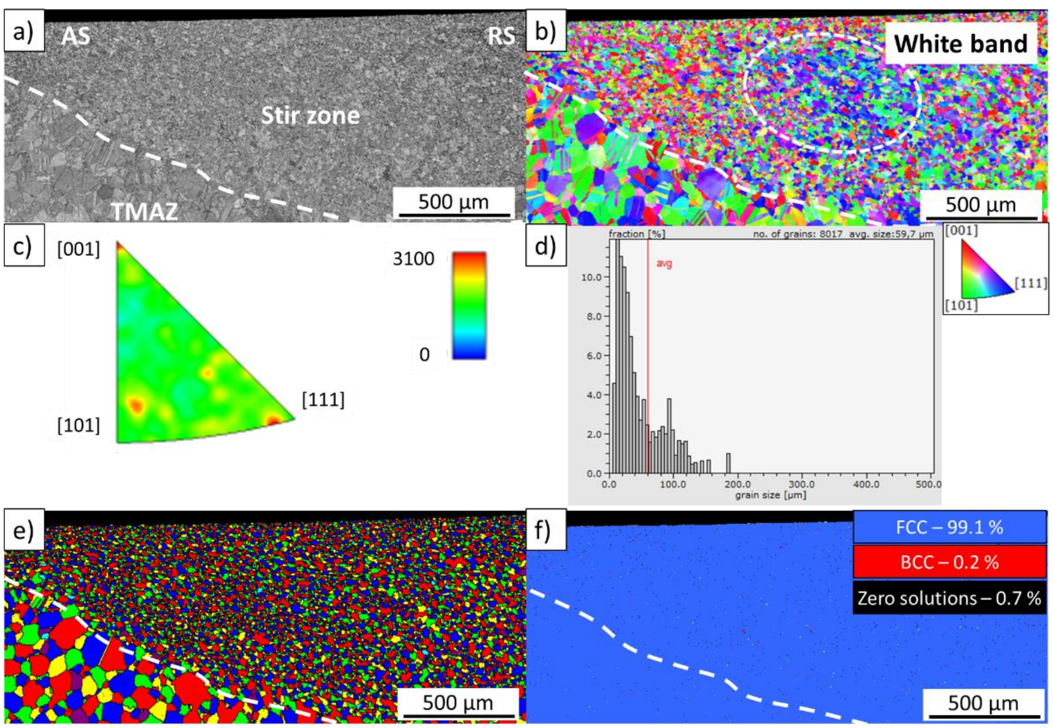

Figure 76: SEM and EBSD Analysis of FSW butt joint with CoCrFeMnNi in HR-condition: (a) SEM-image; (b) inverse pole map; (c) inverse pole frequency; (d) grain size distribution histogram for a; (e) grain distribution map; (f) phase map

7.3 FSW-induced surface residual stresses for CoCrFeMnNi-HEA and CoCrNi-MEA

Figure 77 shows the residual stresses at the FSW butt weld surface analogously to the TIG welds. Due to the surface-near measurement of residual stresses by XRD, it is important for the interpretation of the results that the surfaces were ground with 600 grit paper before FSW. As a result, compressive residual stresses are present in the BM [264]. The residual stresses are shown in the longitudinal/welding direction (black curve in the diagram) and transverse direction (red curve in the diagram). The results show a strong influence of the initial condition, since the residual stress curves of the HT-HEA (a) and MEA (c) are similar, as are those of the CR-HEA (b) and MEA (d).

At first, the FSW butt welds of both MPEAs in HT-condition are discussed (HEA in Figure 77a and MEA in Figure 77c). In both BMs, compressive residual stresses in the range of -200 to -250 MPa were identified in the transverse welding direction. These stresses result from the grinding of the surfaces before welding [264]. In the area of the weld seam (shoulder) on the RS, residual stresses of around 0 MPa are shown for the HEA, whereas they increase to approx. +100 MPa tensile residual stresses for the MEA. In the direction of the AS, the residual stresses decrease in the compression range to approximately -400 MPa for both materials. Compressive residual stresses are due to mechanical loading or phase changes [160]. Since phase changes are not known for either HEA or MEA or have been demonstrated for HEA using EBSD (Figure 76), the compressive residual stresses in the WM can be inferred to have a mechanical origin. This is the high plastic deformation of the FSW process [64]. Regarding the transverse welding direction of the HT FSW joints, no high tensile residual stresses are present at the surface. Together with the compressive residual stresses, the welds exhibit sufficient load capacity under transverse mechanical loading.

In the longitudinal/welding direction, both HT materials exhibited compressive residual stresses of approx. -200 MPa on the AS. On the RS, however, the HEA consistently shows compressive residual stresses up to -400 MPa while the MEA shows residual stresses around 0 MPa. The obtained differences in the residual stress distribution in both MPEAs have also been described for identical materials with a different processing route (forging instead of rolling), in accordance with [232]. However, both alloys show strong compressive residual stresses on the RS at the transition area between BM and WM (shoulder edge). For the HEA, these range up to -800 MPa, and for the MEA up to -300 MPa. This shows a clear mechanical stress in this area. A similar situation, only in the tensile range, can be seen at the shoulder edge of the AS. Here, high tensile residual stresses are present for the MEA (approx. +200 MPa) and the HEA (approx. +600 MPa). In the case of the MEA, this as well as the high tensile residual stresses in the adjacent BM region can be justified by the highest relative speed (between tool and workpiece) in this region and thus the highest thermal and mechanical loading. In the HEA, the residual stresses of approx. +600 MPa are clearly above the YS ($R_{p0.2}$ = 240 MPa). The cause of these significantly excessive stresses may be that there is no flat surface directly at the junction and thus measurement errors may have occurred. Alternatively, an extremely deformed part of a remaining flash that was not completely removed may also have been measured. The residual stress results in the longitudinal direction of the HT FSW joints show that significant tensile residual stresses are present in the outer shoulder area on the AS. Therefore, a large part of the local load capacity is exhausted in this area. This leads to faster plastic deformation and a higher local susceptibility to failure [160] under longitudinal mechanical loading.

In the case of the CR-condition of both MPEAs (HEA in Figure 77b and MEA in Figure 77d), compressive residual stresses in the BM and tensile residual stresses in the WM are evident in both directions. The compressive residual stresses reach increased values of approx. -800 MPa in the longitudinal direction, based on cold rolling since the rolling direction corresponds to the longitudinal direction. In the transverse direction, the compressive residual stresses are in the range shown for the HT materials at approx. -300 MPa and can be attributed to the grinding of the surface before welding as well as to the cold rolling. In the shoulder area, the welds show tensile residual stresses in both directions. These are up to approx. +200 MPa. The reason for this may be the hindered shrinkage during cooling, which acts more strongly on the initial CR condition than on the HT due to the higher strength [233]. However, the strong mechanical load of the FSW process may also be at least a considerable reason for the measured tensile residual stresses. The increased tensile residual stresses are also evident in the area next to the shoulder on the AS. In general, as with the HT condition of the MPEAs, the highest tensile residual stresses are found at the tool shoulder edge of the AS, i.e., the area with the highest relative speed (tool vs. workpiece) and with the highest thermal and mechanical stress [64].

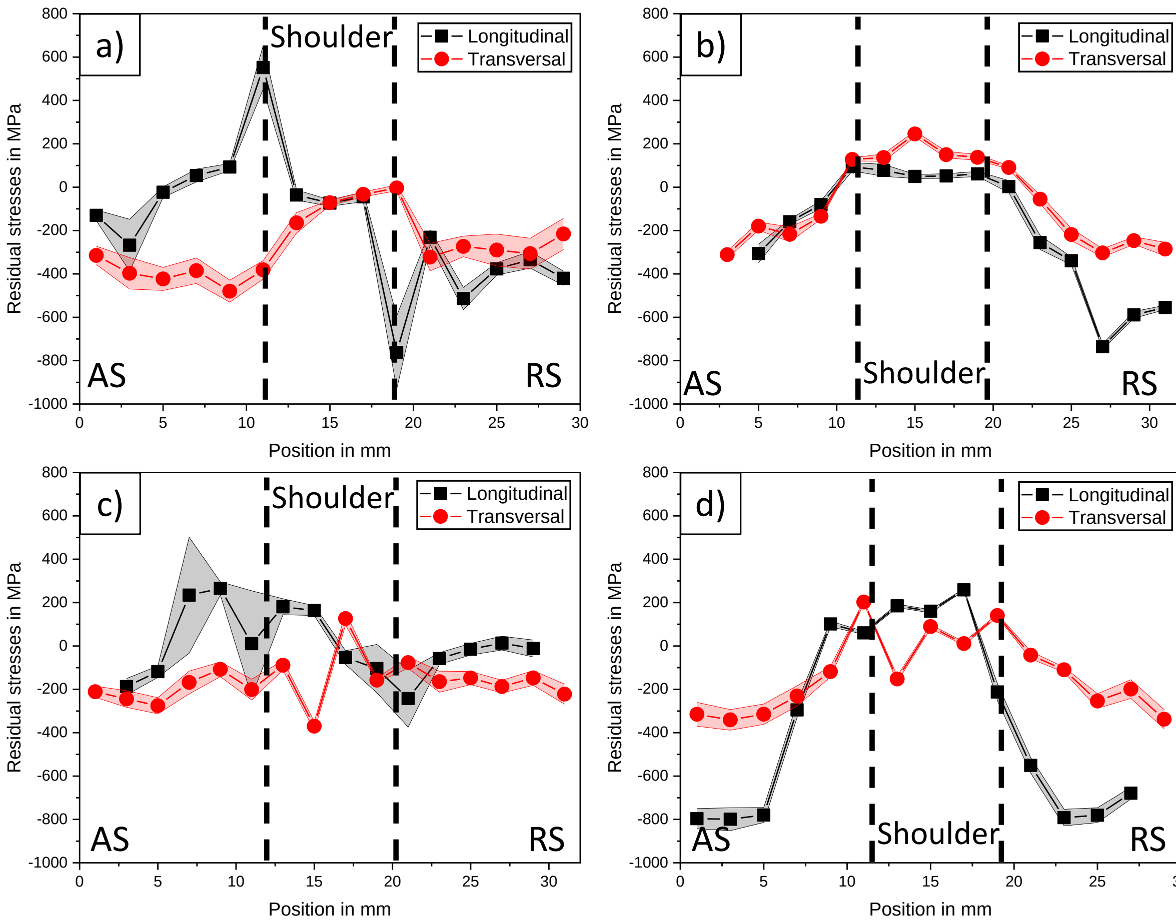

Figure 77: Residual stresses for CoCrFeMnNi-HEA FSW butt joints: (a) HR-, (b) CR-condition and CoCrNi-MEA in (c) HR-, (d) CR-condition

Finally, it can be stated that the highest tensile residual stresses are present in the WM on the AS. These are tensile residual stresses of approx. +200 MPa. These are in the range of the YS of the materials (HEA-$R_{p0.2}$ = 207 MPa and MEA-$R_{p0.2}$ = 373 MPa). This is also true for both directions.

Therefore, this area has hardly any further load capacity before plastic deformation and can be considered a weak point under mechanical load. Moreover, it shows a qualitatively same residual stress state as FSW of AISI 304 [69]. A possible improvement of the residual stress state, i.e. a reduction of the tensile residual stress, could be achieved by stress relief heat treatment [233]. However, no studies have yet been carried out on this topic for FSW joints of the respective MPEAs. This would have to be investigated further.

7.4 UCI microhardness distribution in FSW joints

The microhardness HV0.1 (identified by UCI hardness testing) maps are shown in Figure 78. The HT-HEA (Figure 78a) and MEA (Figure 78c) FSW joints show a comparable microhardness distribution. The entire FSW hardly affects the local microhardness, as it is similar to the BMs in the range around 200 HV0.1. Even though there is a slight hardening in the SZ and the TMAZ due to a slightly higher percentage of green spots. The reason why, despite the strong plastic deformation in the SZ and the TMAZ, no fundamental hardening takes place is the dynamic recrystallization [64]. This causes a decrease in strain hardening, thus reducing the dislocation density [265].

Nevertheless, both MPEAs show a clear hardening in the white band area (HV0.1 increases to 350 HV0.1). The reason is the strong initial cold deformation as well as the particle and/or solid solution strengthening due to the W-particles in this area (see Section 7.2). Which of the two strain hardening mechanisms is present due to the W input, or whether it even affects both, could not be conclusively clarified. Based on the SEM and EBSD (for the HT-HEA) from Section 7.2 no individual W particles (in the case of particle hardening) or a phase enriched with W (solid solution hardening) could be detected.

The HV0.1 mappings of the FSW butt welds with CR-BM are given in Figure 78b (HEA) and d (MEA). The hardness in the SZ is comparable to those of the welds with HT BM at about 200 HV0.1. Again, both alloys show hardening in the white band region also at about 350 HV0.1. The effects discussed for the HT welds also apply here and are therefore not repeated. However, for the FSW joints with CR BM, there is a clear hardness gradient from the SZ (approx. 200 HV0.1) to the BM (HEA at approx. 500 HV0.1 and MEA at approx. 650 HV0.1). The high hardness of the CR-BM is due to the strong work hardening (high dislocation density) of the cold rolling process. The mentioned hardness gradient crosses both the TMAZ and HAZ. Both zones exhibited reduced hardness compared to the respective HEA- or MEA-BM, which is due to the combined recrystallization and tempering effect. In that case, the increased temperature of the welding process leads to recrystallization of the severely cold-worked material.

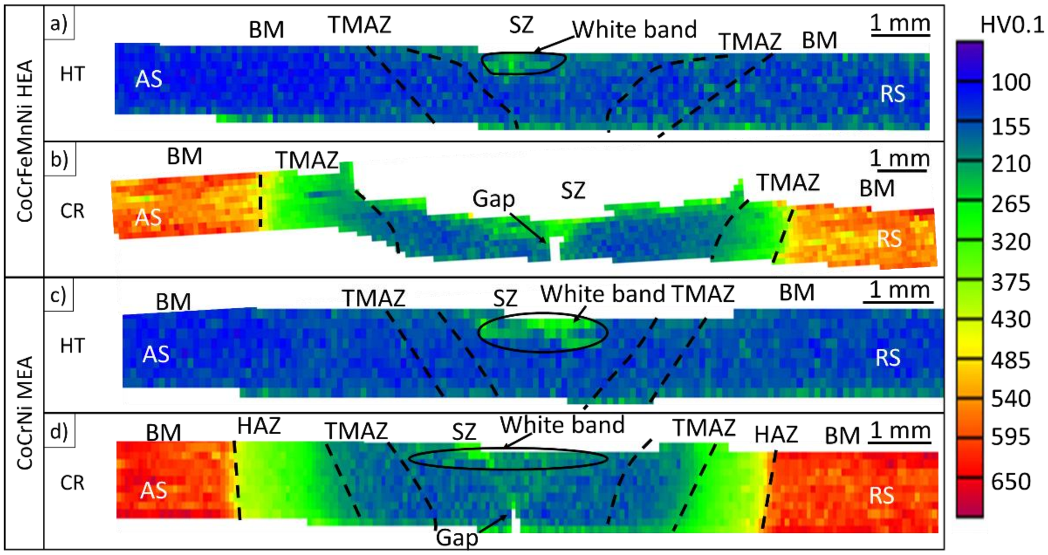

Figure 78: Microhardness (HV 0.1) mapping of FSW butt joints cross-sections of CoCrFeMnNi-HEA: (a) HT-, (b) CR-condition and CoCrNi-MEA in (c) HT-, (d) CR-condition

7.5 Tensile properties of FSW-joints of CoCrFeMnNi-HEA in HT- and CR-condition

In the next section, the cross-weld tensile tests of the HEA FSW butt joints are discussed. It is noteworthy that the tensile tests were carried out in the as-welded condition and the mechanical stress values refer to the initial cross-section of the BMs (1.2*5 mm^2). Therefore, the measurement range in FSW specimens contained at least three different characteristic microstructures (see Section 7.2): the BM, the TMAZ, and the SZ. Each of these zones has a different deformation resistance (tensile strengths) due to its different microstructure and does not exist constantly in the cross-section.

To determine the tensile properties of each respective weld microstructure/zone, tensile specimens with a more or less homogenous specific weld similar microstructure would have to be tested. In this study, this was not feasible due to the small sample size and material availability of the HEA. Nonetheless, partial data on weld-like microstructures can be found in [63]. The stacking fault energy of CrMnFeCoNi is comparable to that of austenitic stainless steels and allows a good comparison with the data of the present thesis. Analogous to the TIG-welds, the global engineering stress-strain curves are discussed at first, followed by the results of the local strains during the tensile tests using DIC for stages I to III. The final aim was to characterize the local strains of the individual weld zones due to the limited usefulness of cross-weld samples e.g. for prediction of failure position just due to stress-strain-curve.

7.5.1 Overall tensile properties of HEA FSW-joints

Figure 79a compares the global engineering stress-strain curves of the FSW-welded HEA in CR- and HT-condition. The calculated mechanical properties are summarized in Figure 79b. The significant influence on the initial CR- or HT-processing condition of the HEA is evident. Due to the insufficient weld penetration in the CR-HEA, the fracture strain is significantly reduced (combined effect of decreased cross-section area and certain notch effect due to the specific joint geometry).

The tensile specimens consequently (and as expected) failed in the area of insufficient weld penetration. Therefore, these values were not used for further calculations. As a result of follow-up, the welding parameters have to be further adjusted to obtain a sound and defect-free weld. For further details see Section 7.2.

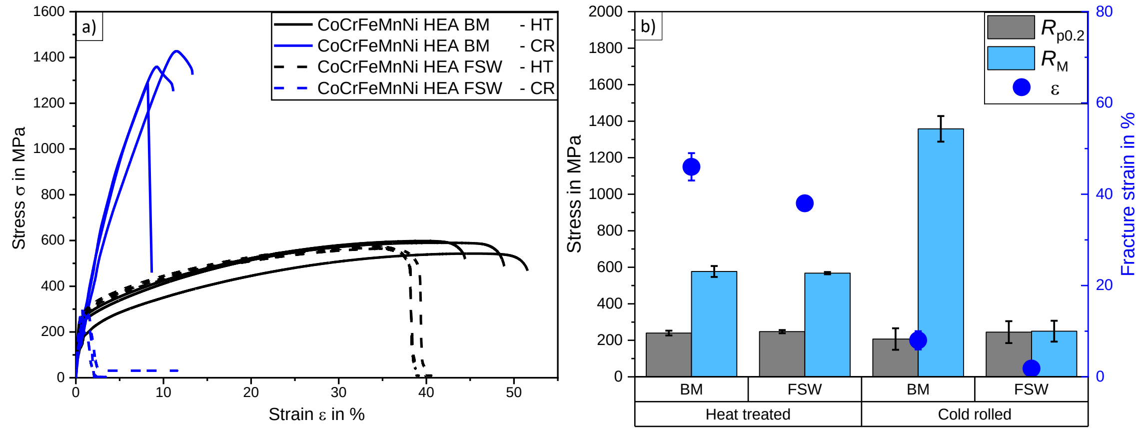

Figure 79: (a) Engineering stress-strain curves and (b) YS: $R_{p0.2}$, UTS: R_M and fracture strain ε of CoCrFeMnNi-HEA base material (HT and CR) and the FSW butt joints CoCrFeMnNi-HEA (HT and CR)

The FSW butt joint cross-weld tensile samples with HT-BM shows a completely different behavior compared to the CR-BM. Both calculated values of R_M and $R_{p0.2}$ (see Figure 79b) are literally identical to the HT-BM. The reason is the fact, that all joint tensile specimens failed in the BM. The obtained cross-weld tensile failure location in the BM is comparable to FSW joints of CoCrFeMnNi-HEA reported in [70]. A reduction of the fracture strain of the BM to approx. 83 % of the BM is in agreement with recently published data (84 %) in [70]. The root causes for the degradation of the ductility are described in the DIC investigations and analysis of the local strains in Section 7.5.2. Hence, these results suggest and support good weldability of the HT-HEA by FSW. In addition, the strength characteristics are in the range of the BM and the reduced fracture strain also shows high ductility at 38 %.

7.5.2 Local strain properties of HEA-FSW-joints

Figure 80b shows the local strains in the tensile test on an FSW butt joint of the HT-HEA for strain conditions I to III (Figure 80a). It can be clearly seen that for all strain conditions, the lowest local strains (up to approx. 40 % for condition III) are present in the SZ of the FSW joint. The reason is the grain refinement due to the FSW processing (cf. Figure 72), i.e. with respect to the Hall-Petch relationship, which results in a certain hardening [63, 70]. In addition, due to the incomplete dynamic recrystallization during the FSW processing, a residual work hardening (increased dislocation density) is perhaps and additionally present. Tungsten particle hardening in the white band region, due to the abrasive wear could also contribute to the locally decreased deformability of the weld [64]. The increased resistance to deformation also causes the previously described reduction of the global fracture strain of the FSW joints compared to the BM. The BM indicates the highest local strains up to 100 % (at condition III). This is the area where the fracture occurs. It is noteworthy that all specimens failed in the BM on the AS. This could be due to the higher tensile residual stresses in this region shown in Figure 77 (in accordance with [160]).

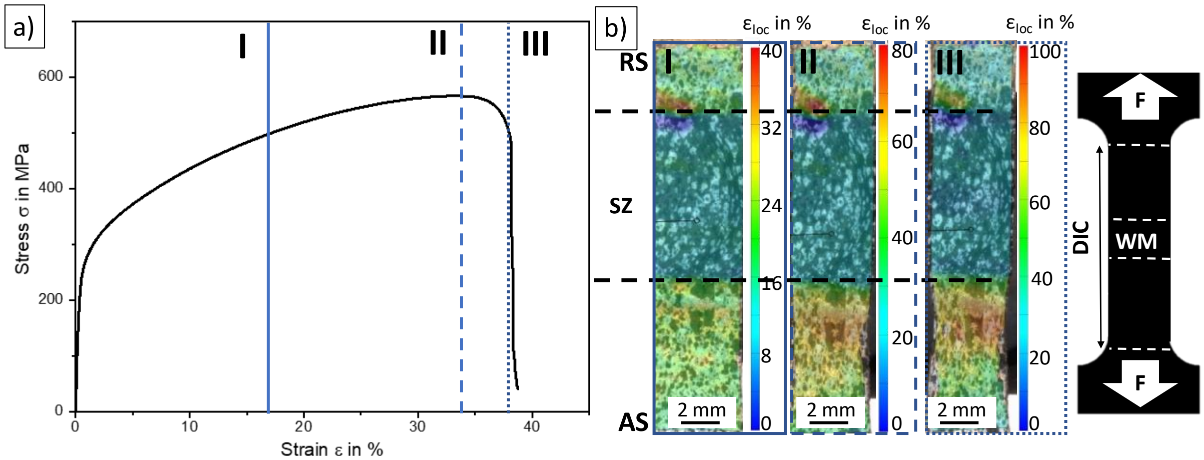

Figure 80: FSW butt joint of CoCrFeMnNi-HEA in HT-condition: (a) engineering stress-strain curve and (b) local strain ε_{loc} for stages I to III

7.5.3 Fracture morphology of HEA-FSW-joints

Figure 81 shows the results of SEM examinations of the corresponding fracture surfaces of the cross-weld tensile samples of the FSW butt-welded HEA in HT-condition. The overview image in Figure 85a shows a homogeneous surface morphology with larger dimples over the entire plate thickness. The large dimples (Figure 85b) indicate high ductility [243]. Due to the local strain of approx. 100 % in the failure region shortly before failure (see Section 7.5.2 and Figure 80), this can also be confirmed by the DIC evaluations. Some bright particles are present in the dimples which indicates microvoid coalescence. Due to the rough surface, these particles could not be successfully analyzed by EDX. However, they should be Cr and/or Mn-containing oxides, which originate from the material synthesis as described in Section 4.1.

Due to the very low fracture strain and the clear cause of failure of the FSW butt joint (lack of weld penetration see Section 7.2) with the initial CR condition, the results of the DIC investigations and the characterization of the fracture surface morphology are not shown and discussed in detail. This allows the following conclusions to be drawn with regard to weldability: (1) CoCrFeMnNi HEA in the CR condition exhibits poorer weldability than HEA in the HT condition, meaning that heat treatment is recommended prior to FSW. (2) Further process optimization must be carried out for FSW in the CR condition, as weldability cannot be ruled out based on a single test.

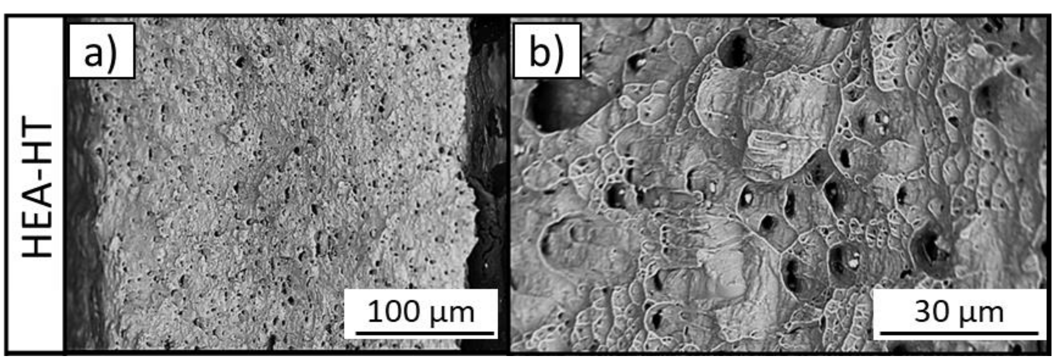

Figure 81: SEM figures of fracture surface morphologies of CoCrFeMnNi-HEA FSW butt joints in HT-condition (fracture in BM) after tensile tests

7.6 Tensile properties of FSW-joints of CoCrNi-MEA in HR- and CR-condition

7.6.1 Overall tensile properties of MEA-FSW-joints

The cross-weld tensile samples of the MEA-FSW butt welds are discussed below. The engineering stress-strain curves of the FSW-welded MEA are compared to those of the MEA-BMs in Figure 82a. The resulting characteristic values are shown in Figure 82b. An increase in YS/$R_{p0.2}$ and a reduction of UTS/R_M compared to the HT-BM is shown for the FSW of the HT-MEA. The reason for the increased $R_{p0.2}$ is assumed to be similar to the previously described hardening of the metallurgically similar CoCrFeMnNi-HEA, which can be caused by grain refinement, precipitation, and/or work hardening in both the SZ and TMAZ [64]. The reasons for the reduced R_M, just like those for the fracture strain reduced to one-third (33.2 % compared to the BM), will be described based on the DIC investigations in Section 0. In general, conditional weldability was achieved, e.g., indicated by the mechanical properties of the HT-MEA. The reason is the failure in the weld seam in all tensile tests, which indicates the WM as a weak point. Furthermore, the reduced R_M and fracture strain compared to the HT-BM points out a conditional weldability. Based on the presented results, it cannot be concluded whether an FSW parameter optimization would be beneficial for the weld joint performance at all. For that reason, further welding experiments would be useful.

The FSW-joint of the CR-MEA shows an YS/ $R_{p0.2}$ in the range of the CR-BM. Nonetheless, R_M (30.1 % of the BM) and the fracture strain (67.5 % of the BM) are significantly reduced. The main reason is the insufficient weld penetration (see Section 7.2) and a certain geometric notch effect. It is reasonable to assume that the mechanical performance could be significantly improved by optimized FSW processing. Consequently, only a conditional weldability based on the mechanical properties can be concluded for CR-MEA.

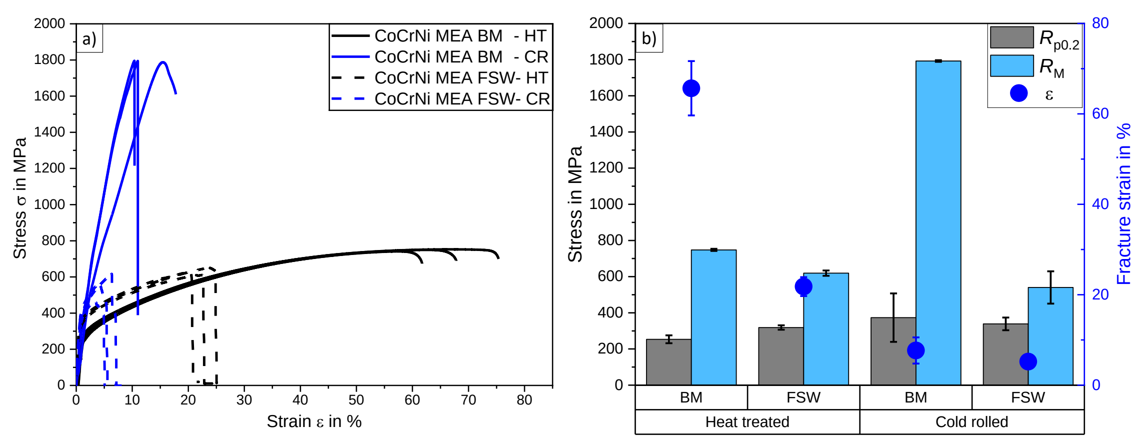

Figure 82: CoCrNi-HEA-BM in HT and CR-condition and corresponding FSW butt joints; (a) engineering stress-strain curves and (b) tensile properties YS: $R_{p0.2}$, UTS: R_M and fracture strain ε

7.6.2 Local strain properties of MEA-FSW-joints

In Figure 83, an example of a global engineering stress-strain curve (a) and the local strains (b) for conditions I to III is presented. Condition I shows a significantly higher local strain in the BMs (yellow to orange, i.e. 14 % to 18 %) compared to the SZ (blue to green with 4 % to 10 %). The reason is the higher strength in the SZ due to the previously described fine grain, particle, and work hardening in the FSW-WM.

Two green stripes are clearly visible in the WM. The reason is suspected to be non-uniform elongation across the plate thickness during straining. Since the white band is located in the upper area of the FSW-joint (compare Figure 74) (high strain hardening) and only a grain refinement in the lower area (lower strain hardening). It is assumed that there is an inhomogeneous strain distribution in the weld. This results in a deflection towards the bottom of the weld seam of the specimen. The DIC investigations only evaluate the strain on the upper side of the weld seam, here the deflection causes the two parallel green stripes. The consequence of this deflection is also a multiaxial stress condition. Moreover, the highest transverse stresses are at the outer curvature during bending. Therefore, after condition II (in the area R_M), which is qualitatively identical to condition I, a break from the bottom in the middle of the two previous green strips succeeds. This spreads and subsequently leads to a failure in the weld. Shortly before failure in condition III, compared to condition II, it can be seen that the entire further strain occurs around the failure area and there is no further elongation in the BM.

An improvement of the behavior in the tensile test could be a more homogeneous weld formation, for example, a weld nugget/white band that extends through the entire plate thickness. This is probably a process optimization to achieve, as has already been shown for other metals like Al-alloys or steels [63, 64].

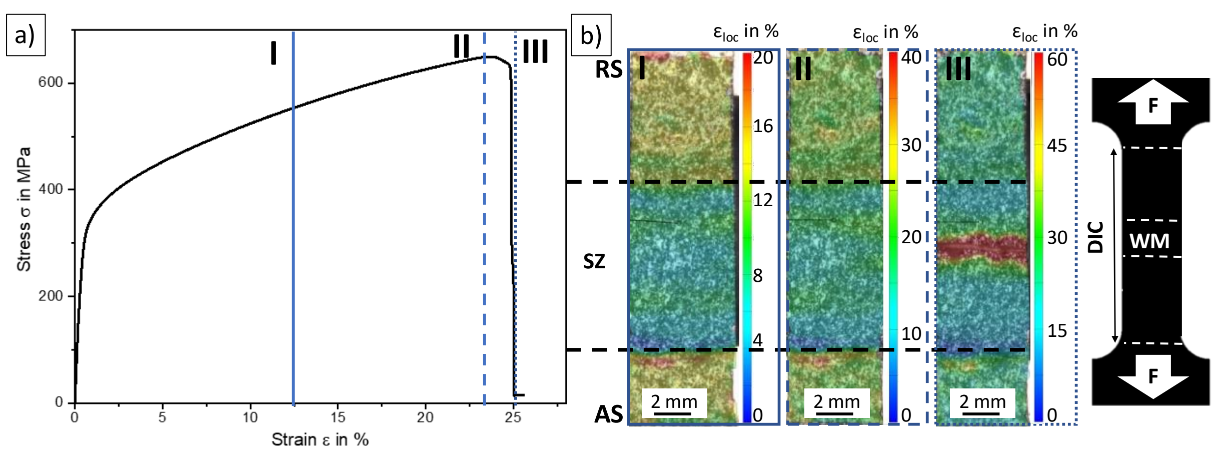

Figure 83: FSW butt joint of CoCrNi-MEA in HT-condition: (a) Engineering stress-strain curve and (b) local strain ε_{loc} for stages I to III

Figure 84a shows a global engineering stress-strain curve of an FSW butt weld with an initial CR condition. The local strain maps for conditions I to III are shown in Figure 84b. At stage I, approx. 50 % of the fracture strain (approx. 2.6 %), literally a strain of zero was observed in the CR-BM (indicated by the dark blue area). This means the complete strain is absorbed by the less “strong” WM and locally reaches up to 9 %. This can be interpreted in terms of a “restraint” effect of a surrounding stiff vs. soft construction. At about 4 % global strain there is a dip in the engineering stress-strain curve. In that case, the specimen continues to tear due to the notch effect of insufficient weld penetration (see Figure 71) in the weld center. The white band (i.e. the area with the highest hardness in the SZ as shown in Figure 78), is in the upper region of the weld joint. Due to the reduced cross-section, a significantly elevated stress level should appear. Figure 84a shows that the specimen can still absorb further straining up the failure, close to stage III, in the fracture area.

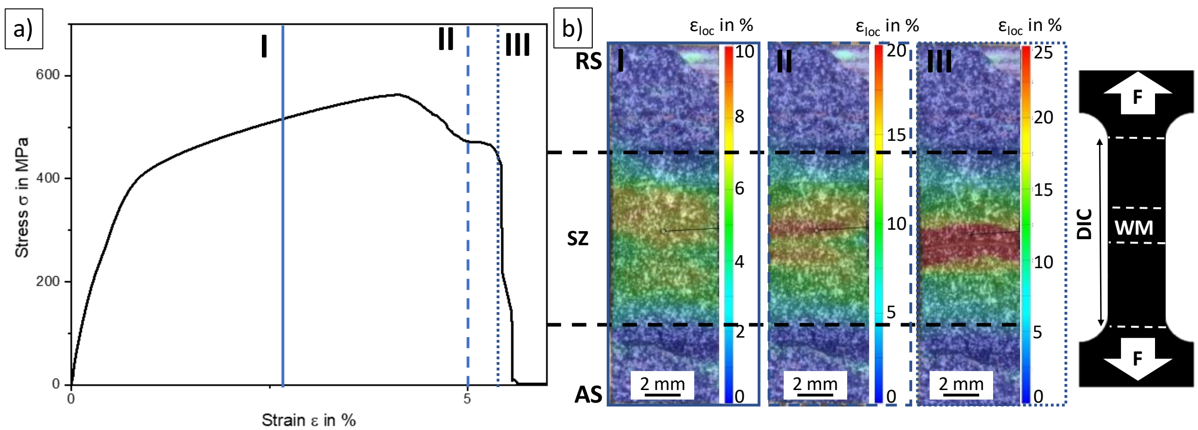

Figure 84: FSW butt joint of CoCrNi-MEA in CR-condition: (a) engineering stress-strain curve and (b) local strain ε_{loc} for stages I to III

Following, significantly better results can be expected with an optimized process, which leads to a complete weld penetration, a weld nugget through the entire plate thickness. Whether a process optimization with the aforementioned result is possible for a CR-MEA cannot be determined on the basis of the one welding performed. However, it can be stated that heat treatment before welding improves weldability. In addition, the FSW results are similar to those of the HEA, and an influence of the chemical composition on weldability can be ruled out.

7.6.3 Fracture morphology of MEA-FSW joints

The fracture morphology of HT-MEA FSW-joint is shown in Figure 85a and b and for CR-MEA in Figure 85c and d. The fracture surfaces can be generally divided into three areas for both initial HT- and CR-conditions: (1) the near-surface strongly plastically deformed top region, (2) the FSW-joint center region with the white bath/weld nugget, and (3) the bottom region with clearly visible grains. The fracture topography indicates ductile failure in the (3) bottom region (Figure 85a) by clearly identifiable dimples. In the (2) middle, smaller dimples are visible, which also indicates a ductile failure. In contrast, a mixed fracture can be seen in the FSW-joint (1) top area. Here brittle areas are shown in addition to ductile areas. Ductile areas are based on a few dimples. These brittle, i.e. low-deformation capability-indicating topographies show plain areas and secondary cracks [243]. The failure morphology reflects the heterogeneous failure as described in Section 0, which is based on the microstructure gradient (see Figure 74 in Section 7.2) in the failure area. This means the welded material was gradually deformed from the bottom (less) to the top area (severely deformed).

As presented in Figure 85c and d, the FSW joint of the CR-MEA showed a ductile failure in the top and center region, which is characterized by the dimpled fracture morphology (in accordance with [243]). In that connection, the dimples are smaller in the FSW-joint top area (white band/weld nugget location, see Figure 75 in Section 7.2). In the FSW-joint center (SZ) area, the dimples are larger with clearly visible grains. The FSW-joint root area was not examined in detail since the lack of weld penetration was present.

This investigates the weldability of CoCrNi MEA by FSW, focusing on the impact of initial conditions. The results are similar to those of the HEA FSW joints (in Section 7.5), which indicates a rather low influence of the chemical composition on weldability. The fracture strain of FSW butt joints in the CR condition was found to be significantly low, primarily attributed to inadequate weld penetration (see Section 7.2). The DIC results and fracture surface morphology discussions lead to the following conclusions regarding the weldability of the MEA: (1) MEA in the CR condition exhibits inferior weldability compared to its counterpart in the HT condition. Therefore, a pre-weld heat treatment is recommended to enhance the weldability of the alloy. (2) It is emphasized that further process optimization is imperative for FSW in the CR condition. A single test cannot unequivocally determine weldability, necessitating ongoing efforts to refine the FSW process parameters. This study underscores the critical importance of initial conditions, specifically the influence of heat treatment, in achieving desirable weldability for MEA through FSW.

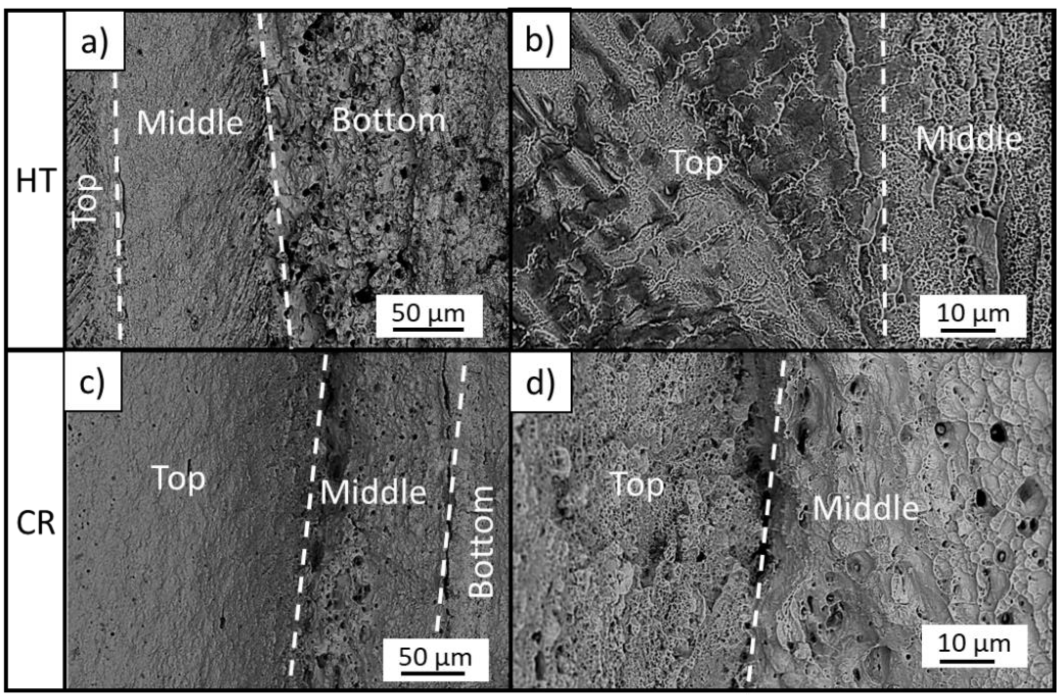

Figure 85: SEM figures of fracture surface morphologies of CoCrNi-MEA FSW butt joints in: (a, b) HT and (c, d) CR-condition

8. Results and discussion of FSW dissimilar metal welding of CoCrFeMnNi-HEA with AISI 304 austenitic steel

In the following section, the dissimilar metal weldability by FSW is discussed as illustrated in Section 3 by Figure 21. For this purpose, FSW butt joints of the CoCrFeMnNi-HEA in HT- and initial CR-condition with the austenitic stainless steel AISI 304 were examined. Due to the limited HEA material quantity, both the position of the HEA material and its initial condition were systematically varied to investigate the combined influence on the FSW-joint performance. For the first case, the HT-HEA was placed on the AS and the AISI 304 was on the RS. In the second case, the CR-HEA was placed on the RS, and the AISI 304 steel on the AS. In accordance with the previous sections, the weld microstructure is discussed as well as occurred weld defects. From the current state-of-the-art, the mechanical properties of FSW-joints dissimilar metal weld joints of CoCrFeMnNi-HEA have a pioneering character due to the very limited data in scientific literature. In addition, the mechanical effects of FSW on resulting residual stresses (determined by XRD) are very useful and are presented for the first time.

8.1 FSW-DMW-joining process and identification of weld imperfections

The FSW-DMW butt welds are examined with respect to weld imperfections based on the resultant surfaces and radiographic inspection. In addition, the forces and temperatures measured during welding are correlated with the identified weld defects. In that connection, Figure 86 shows radiographic test images (upper part of the corresponding sub-figure) and the respective top-view of the DMW-joint (lower part) of the AISI 304 steel with the CoCrFeMnNi-HEA in (Figure 86a) HT- and (Figure 86b) initial CR-condition. As shown in Figure 86a, the FSW-DMW with the HT-HEA showed an insufficient weld with a lack of fill of the surface [68]. This was characterized by the dark band in the HEA-close WM on the AS. Since this behavior was consistently found along the entire weld length, it is reasonable that the FSW process parameters must be further optimized. Unfortunately, due to the limited material quantities, this processing issue could not be further investigated. In contrast, the FSW-DMW with CR-HEA on the RS, in Figure 86b, did not show any obvious weld imperfections in the radiographic test images (upper part of sub-figure b), except a bright band in the center of the WM, which corresponds to the already described typical FSW defect of white band formation, see Section 7). In addition, the FSW-joint surface appeared to be way more homogeneous (lower part of sub-figure b).

The root cause for this divergent behavior is directly linked to the advancing side (AS). This can be seen by the process temperature measured at the tool shoulder, shown in Figure 87. In the DMW with the HT-HEA on the AS, a temperature of 850 °C is reached whereas in the second case of the CR-HEA on the RS significantly increased temperatures from 1050 °C to 1100 °C were measured. The different temperatures are due to the specific T_s of the respective material on the AS since the highest relative speed between the tool and the material occurs at the AS, i.e. the largest frictional heat is generated here (in accordance with [63]). As mentioned in the state-of-the-art, FSW reaches 80 % to 90 % of T_s [63]. Considering the specific T_s of the AISI 304 with 1,450 °C [46] compared to the CoCrFeMnNi-HEA with 1,289 °C [44], it is obvious that in the case of the AISI 304 on the AS significantly more friction-based heat is generated, which facilitates the plasticization of the two materials. If the HEA is placed on the advancing side (AS), only insufficient heat is generated and the plasticization, i.e. the “stirring” is hindered and welding defects are likely to occur. This is already known for other material pairings in the FSW-DMW, so the Al alloy (lower

Ts) should always be used on the RS for steel to Al alloys [142, 266] or Ti to Al alloys [142, 267]. For alloy combinations with only a slight difference in the Ts, the distribution is not clear, e.g. for Al to Cu [142, 268, 269] or Al to Mg [142, 270, 271] combinations, where the Al alloy is used on the RS or As. Above all, the results show that the arrangement of the two different materials or welding direction is decisive for a successful welding process and that the initial state (HT or CR) of the HEA has less influence in this case, since even the CR-HEA (see section), which is actually not so well suited for welding, shows a better result (more constant process and weld seam without imperfections) than the HT-HEA.

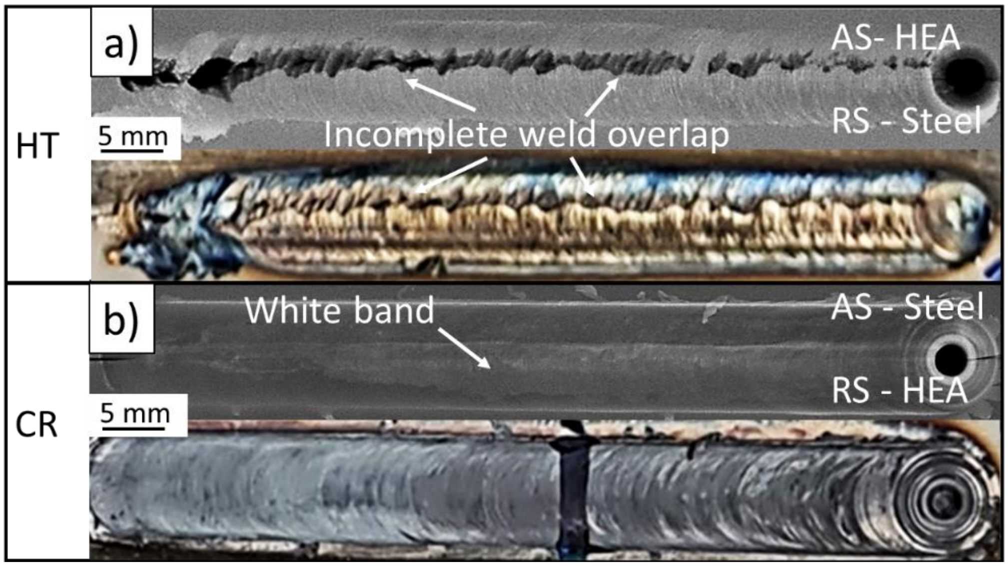

Figure 86: Radiographic test images and corresponding weld joint surface of FSW-DMW of AISI 304 with CoCrFeMnNi-HEA in: (a) HT- and (b) CR-condition

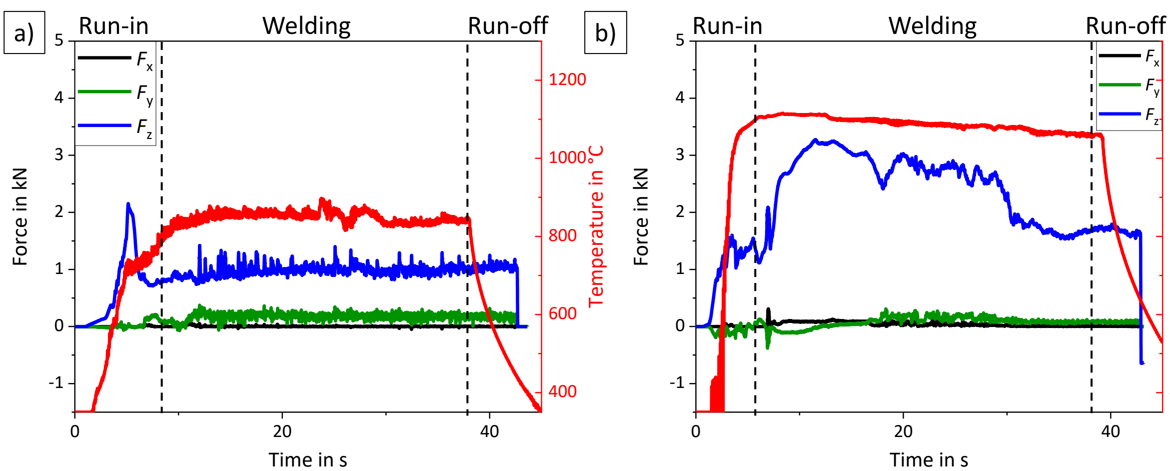

Figure 87: Force and temperature at tool shoulder of FSW-DMW of AISI 304 with CoCrFeMnNi-HEA in: (a) HT- and (b) CR- condition

8.2 Microstructure analysis of FSW-DMWs

In the following section, the resulting microstructure of the FSW-DMWs of the HEA with the AISI 304 is analyzed. For that purpose, the results from the LOM, SEM, and EBSD investigations are presented.

8.2.1 Microstructure characterization with LOM

At first, the LOM investigations of the cross-sections (Figure 88) of the FSW-DMWs are presented for the AISI 304 with the HEA either on the AS- or on the RS-side. In the case of the HT-HEA on the AS and AISI 304 steel on the RS in Figure 88a, on both sides of the DMW, hardly any TMAZ was identified. The SZ shows a rather lamellar structure consisting of a lighter and a darker phase. This indicates that the steel and the HEA are present in a “sandwich-like” pattern and hardly any stirring or intermixing of the materials occurred (detailed SEM and EDX results can be found in Section 8.2.2). As a result, several weld-defects appeared:

(1) One defect was the material separation starting from the weld root side, which occurs due to lack of penetration [68] (already discussed for the HEA-to-HEA and MEA-to-MEA FSW butt welds in Section 7.2).

(2) Another defect at the lower interface between SZ and BM/TMAZ was identified as a tunnel defect and can be attributed to insufficient plasticization of the materials during FSW [68, 272]. Material flow is impeded, and tunnel defects can occur, some of which extend along the entire weld length. Again, it can be attributed to the relative movement of the pin and AS- vs. RS-side and thus as insufficient heat generation in case of a “wrong” material pairing.

(3) Furthermore, a geometrical factor like the insufficient weld overlap was identified (see Section 8.1). The cause is the same as for the tunnel defect, i.e. insufficient material flow due to hindered/minor-pronounced plasticization of the steel.

The weld defects accumulate in a significant reduction of the cross-section of the weld joint and could lead to a limitation of its corresponding tensile properties. This means that the FSW process parameters should be further optimized for defect-free weld penetration. For example, a tool optimization in terms of a longer pin could be effective in avoiding tunnel defects [68, 257] as well as a higher rotational speed or swapping the welding partners with respect to AS or RS of the FSW-DMW [142] for sufficient plasticization of the materials as described in Section 8.1.

In contrast, the FSW-DMW joint of the CR-HEA with AISI 304 steel did not show defects like pores or cracks within the weld seam (see Figure 88b). Nevertheless, it is questionable whether complete weld penetration was achieved. It is assumed that a complete metallurgical bond was not created at the root side because specimen thickness and pin length are identical to those of the other FSW-DMWs, where a significant lack of penetration was observed [68]. Accordingly, it is assumed that a lack of fusion is present on the root side. Hence, the weld partners are merely joined by a geometrical form closure instead of a metallurgical bond between the materials [273].

Figure 88b shows a bright area within the SZ on the AS and corresponds to the white band as in the case for the HEA-to-HEA and MEA-to-MEA welds (see Section 7.2 and in accordance with [64, 131]). Like in the aforementioned FSW joints, it is located in the SZ on the AS. In other words: the area with the highest thermomechanical stresses. Next to the white band the SZ and the TMAZ show fine globular grains, due to dynamic recrystallization (further details on the mechanism and its effect can be found in Sections 2.2.2 and 7.2). The formation of a HAZ was regarded in the HEA at the RS in terms of a heat-affected area like in the case of the TIG-welded of CR-HEA (see Section 5.2). The reason for the HAZ-formation is the combined effect of the prior cold-working of the HEA-BM, further tempered by the process heat, and the resulting recrystallization and grain growth [64].

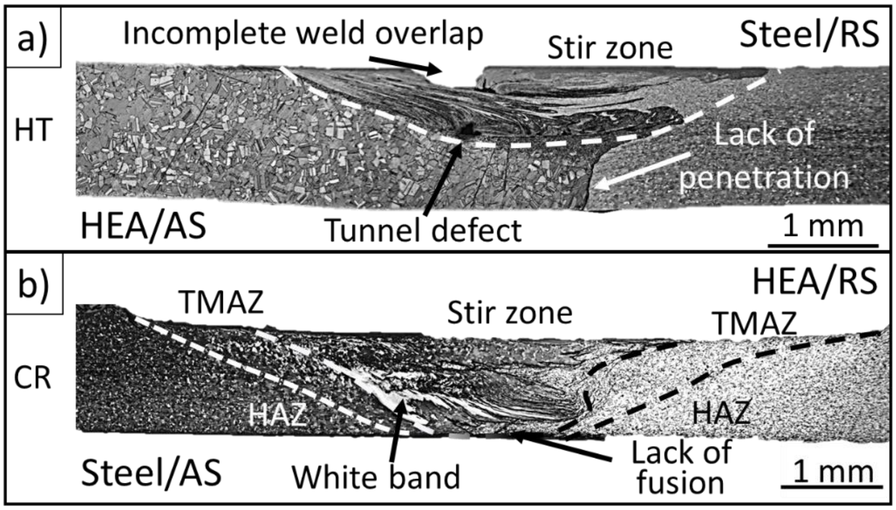

Figure 88: LOM of cross-sections for FSW-DMW of AISI 304 with CoCrFeMnNi-HEA in: (a) HT-, (b) CR-condition

8.2.2 Microstructure analysis with SEM

Figure 89 shows SEM images and EDX element mappings of FSW-DMW with HT-HEA. The SEM image at the transition of the SZ to the HEA in Figure 89a clearly shows the tunnel defects already described in Section 8.2.1. The EDX elemental distribution maps in Figure 89c of this area show a clear transition between the BM and the lamellar SZ. The lamellae formation is typical for FSW-DMWs [142] and can be easily identified by the Co, Mn, or Fe mappings since these elements show the largest differences in alloy content between the HEA and the steel. This also shows that there is no mixing of the BMs, and the two BMs are lamellar side by side. Thereby, the Fe rich (bright in Fe map) are assigned to the steel. The Co- and Mn-rich areas are HEA material.

Figure 89b shows an SEM image at the transition region between the SZ and the BM AISI 304. Here, the SEM image shows a lighter phase. From the element distribution in Figure 89d, it is clear that W-rich regions with chemical mixing of both BMs are present. This is particularly clear from the Fe-distribution in Figure 89d, as three different Fe-concentrations can be seen. The W-rich regions with chemical mixing of the BMs are locally confined to the outer edge of the weld nugget and exclusively to the RS of the AISI 304 steel. This suggests that a white band is involved [131], which is present here on the RS unlike in the previous FWS joints (see Section 7.2).

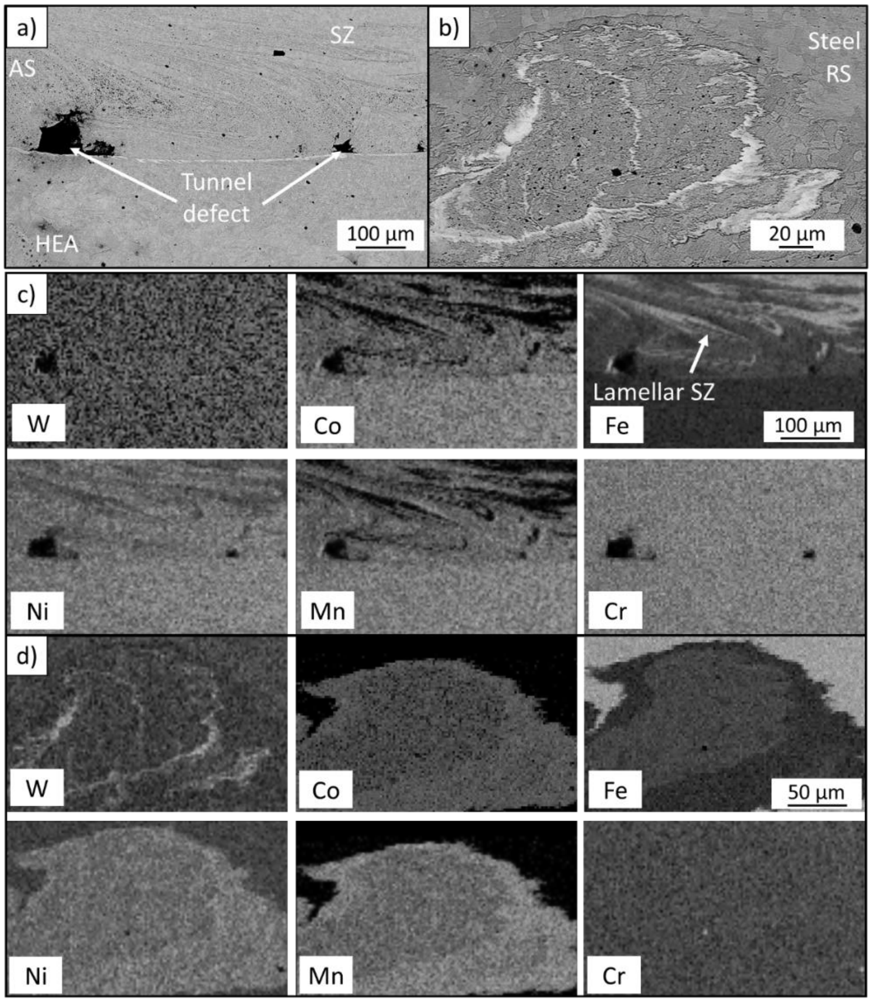

Figure 89: SEM images of FSW-DMW of CoCrFeMnNi-HEA in HT-condition with AISI 304: (a) transition from TMAZ to SZ (HEA-material) on AS, (b) white band/ weld nugget, (c) EDX mapping of marked region a) and (d) EDX mapping of marked region in b)

Figure 90 shows the SEM and EDX results of the FSW-DMW joint with CR-HEA. Figure 90a shows the SEM image of the SZ, characterized by a lamellar structure in the “root” region of the joint. The EDX results in Figure 90c suggest the lamellar arrangement of the two BMs. This is evident due to the absence of Co and Mn in the Fe-rich lamellae. Whereas a chemical mixing (see Figure 90c for the Fe-part) of the materials, as well as an increase in W-rich regions can be seen, which indicates the white band. In an area, marked in Figure 90c the Co-part, the chemical composition indicates HEA material. This material consists of relatively large globular grains, suggesting dynamic recrystallization with strong grain growth [64].

An increased W-content can also be observed in the bright lamellae (see Figure 90b), which is why the elemental composition was additionally measured in the bright region of the white band. It can be seen that, apart from a W-content of 3.7 at.-%, the bright area as part of the intermixed WM consequently exhibits a chemical composition that is influenced by both BMs (see Figure 90d). Thus, the Fe-, Ni-, and Co-content in the white region is in between the respective element concentrations of both BMs. The increased W-content in the bright region is due to the tungsten tool (see Section 7.2), after which abrasive wear particles remain in the white band.

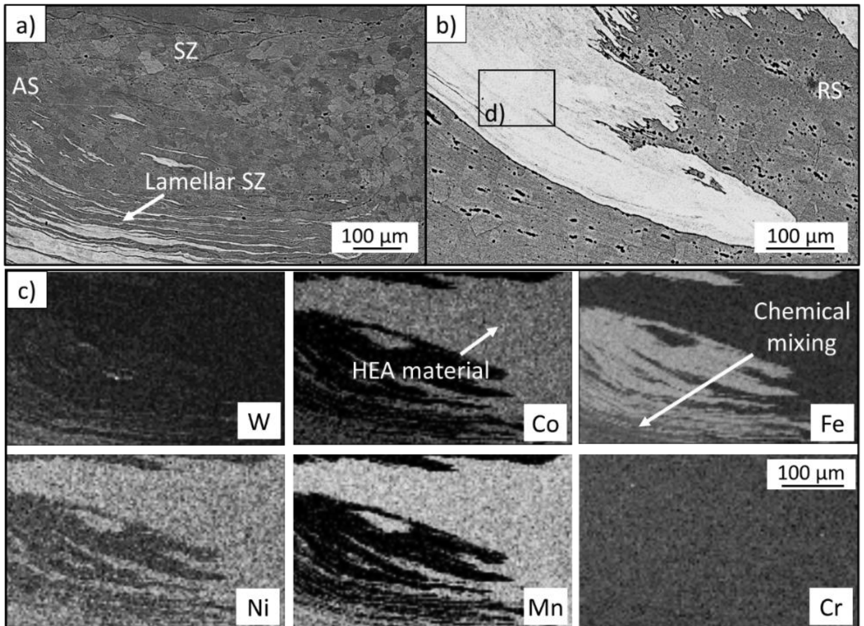

d)

Composition in at.-%	Co	Cr	Fe	Mn	Ni	W
In b) marked region	12.2	18.4	33.2	15.9	16.0	3.7
BM CR-HEA	20.6	20.1	20.0	19.9	19.5	-
BM steel AISI 304	-	20.7	69.1	1.8	6.7	0.1

Figure 90: SEM-investigation of FSW-DMW of AISI 304 with CoCrFeMnNi-HEA in CR-condition: (a) SZ on AS (HEA side); (b) white band/ weld nugget; (c) EDX mapping of the region (a) and (d) chemical composition via EDX of the region marked in b) compared to respective BMs

8.2.3 Microstructure characterization of FSW-DMW with HT-HEA by EBSD

Figure 91 shows the EBSD results of the FSW-DMW of the AISI 304 with the HT-HEA. The SEM image in Figure 91a shows (already described) weld imperfections in terms of a tunnel defect and lack of penetration. The inverse pole map (Figure 91b) and frequency (Figure 91c) show no preferred orientations of the grains, which is characteristic of the dynamic recrystallization effect in FSW joints [64]. The grain distribution (Figure 91d) clearly shows the typical grain-refining in the SZ. In addition, no significant influence on the TMAZ or HAZ grain size was identified. The Kernel average misorientation (KAM) map (Figure 91e) shows very low values (dark blue) in the SZ, which also indicates dynamic recrystallization [64] as a predominant mechanism.

A TMAZ is evident. High KAM values were present in the area next to the SZ (see Figure 91e) on the HEA and steel sides, which indicated local plastic straining. In other words: it must have been preceded by an intensive mechanical loading. In addition, high KAM values in the TMAZ were also confirmed in a recent and (personally) co-authored study for an FSW joint of a CoCrFeMnNi-HEA [71]. Nevertheless, these results show that a TMAZ is present on both sides. The phase map in Figure 91f clearly shows that only the FCC was present after welding. Hence, even the intensive and very high thermomechanical loads of the material by FSW did not change the initial phase, as the HEA reveals a very stable FCC phase [26, 252] which needs a very high mechanical load for phase transformation [28]. The steel forms neither the δ ferrite, described for the TIG in the HAZ (Section 6.2), nor a possible strain-induced ε or α' martensite due to strong local deformation [274].

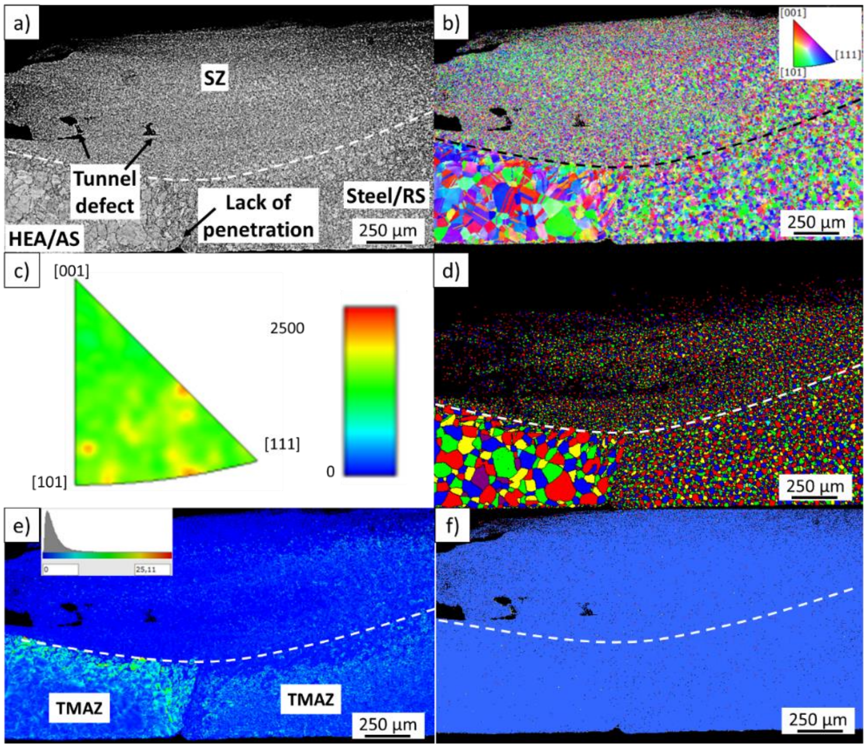

Figure 91: SEM- and EBSD- results of FSW-DMW butt joint with CoCrFeMnNi in HT-condition at AS and austenitic steel AISI 304 at RS: (a) SEM-image, (b) inverse pole map, (c) inverse pole frequency, (d) grain distribution map, (e) KAM-map, (f) phase distribution map

8.3 FSW-induced residual stresses for DMWs

Figure 92 shows the residual stress in the FSW-DMWs (determined by XRD) in both longitudinal / welding and transverse direction. Both welds show similar residual stress distributions. The highest tensile residual stresses in the longitudinal direction occurred in the WM, i.e. within the area affected by the tool shoulder. In the DMW with HT-HEA (Figure 92a), the stresses reach approx. +300 MPa, which is above its YS ($R_{p0.2}$ = 240 MPa, see Table 5) and in the range of the AISI 304 ($R_{p0.2}$ = 323 MPa, see Table 5). Thus, the load-bearing capacity is significantly reduced [160]. In the DMW with CR-HEA, the tensile residual stresses reach approx. +100 MPa. On the one hand, higher load capacities are available. On the other hand, the tensile residual stresses in the WM can be reduced by an optimized FSW process/parameters. In the BM, both DMWs show an influence, on the residual stresses, of the arrangement. The residual stresses are identical in both longitudinal and transverse directions. On the RS, compressive residual stresses of -300 to -400 MPa are present, which are highly attributed to the initial material synthesis (e.g., by cold-rolling). On the AS, hardly any compressive residual stresses (approx. 0 MPa) are present in the transverse direction, as well as compressive residual stresses up to approx. -200 MPa in the welding direction.

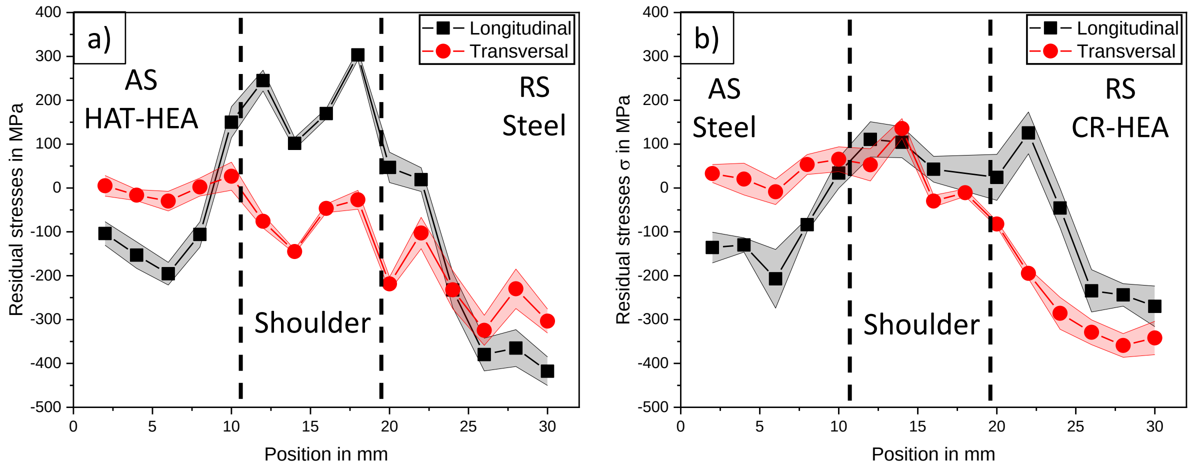

Figure 92: Residual stresses in longitudinal and transversal direction in FSW-DMW of AISI 304 and CoCrFeMnNi-HEA in: (a) HT- and (b) CR-condition

The aforementioned results indicate that the highest (tensile) residual stresses occur in the WM, which can negatively influence the service lifetime of the component if subjected to additional mechanical loading [160]. In that connection, the limitation of FSW-processing initiated (tensile) residual stresses or a further stress relief heat treatment would be beneficial. However, there are hardly any studies in the literature regarding the effect of heat treatments on the residual stress condition of HEAs. From that point of view, it currently remains somewhat speculative if it is either beneficial for the service lifetime or if it is necessary.

8.4 UCI microhardness distribution in FSW-DMWs

The local hardness mappings of the corresponding FSW-DMWs are shown in Figure 93. The FSW-DMW of the AISI 304 with the HT-HEA showed a significant increase of the hardness from 350 HV0.1 to 450 HV0.1 in the SZ, which is significantly higher compared to the HT-HEA-BM with approx. 150 HV0.1. The reasons are: (1) the fine grain hardening in accordance with the well-known Hall-Petch-relationship. In the case of the HEA, twinning, which favors the dynamic Hall-Petch effect, also has a decisive influence on hardening [131, 275]. Further reasons are (2) a high degree of cold or work hardening and (3) particle hardening due to the intake of W-particles into the SZ by the abrasive tool (in the white band as described in Section 8.2). Also in the TMAZ, a certain hardening is evident as described by the KAM-value map (see Figure 91e: EBSD investigations in Section 8.2.3). Therefore, the TMAZ hardness up to approx. 350 HV0.1 is higher compared to the HEA- (approx. 150 HV0.1) or steel-BM (approx. 250 HV0.1).

The microhardness map in Figure 93b shows a significantly increased hardness of CR-HEA BM with approx. 600 HV0.1. This is also due to the initial work hardening and corresponding grain refinement prior to the FSW processing. The FSW results in the formation of a TMAZ and a HAZ in the CR-HEA with significantly reduced hardness. This softening is due to the introduced FSW temperature, which leads to (dynamic) recrystallization [64] and stress relief due to annihilation effects [108]. The TMAZ on the HEA side had the lowest hardness (150 HV0.1) within the entire FSW joint. In addition, the white band has a slightly increased hardness compared to the TMAZ (due to the aforementioned causes like the abrasively introduced W-particles).

As a general statement, it is obvious that independently of the initial HT- or CR-condition of the HEA, the highest microhardness within the FSW joints occurred in areas of severe plastic deformation, i.e. in the SZ and in the sub-surface area close to the tool shoulder. As further proof for this assumption, it is noteworthy that the area with the lowest hardness was located within the TMAZ at the HEA side, which experienced a certain additional “tempering” from the FSW process heat. This means the initial HEA-BM has a minor influence on the hardness state of the TMAZ hardness.

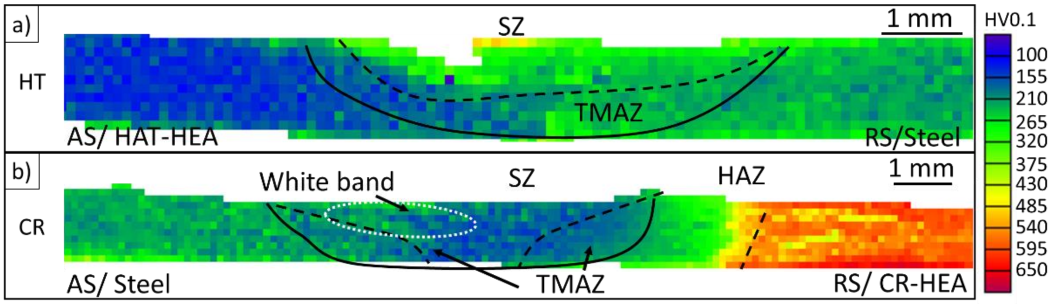

Figure 93: Measured microhardness HV0.1(by UCI) of FSW-DMW of AISI 304 with CoCrFeMnNi-HEA in: (a) HT- and (b) CR-condition

8.5 Tensile properties of FSW-DMWs

In the following section, the cross-weld tensile samples of the FSW-DMW of the AISI 304 with the HEA are discussed. As mentioned for the HEA-to-HEA FSW joints, the tensile tests were carried out in the as-welded condition and the calculated stress values refer to the initial cross-section of the BMs (1.2*5 mm^2).

8.5.1 Overall tensile properties of FSW-DMWs

Figure 94 shows the engineering stress-strain diagrams (sub-figure a FSW-joints compared to the BMs and sub-figure b closer look at the FSW-DMWs) and the resulting mechanical properties (sub-figure c). As a result, the YS / $R_{p0.2}$ hand UTS / R_M of both FSW-DMWs are comparable, but the DMW with CR-HEA experienced a higher strain at fracture. Compared to the individual BMs, the DMW with HT-HEA had an UTS of R_M = 528 MPa, which is just below the UTS of the HT-HEA (R_M = 577 MPa). This means the achieved UTS of the respective DMW was limited by the UTS of the “weaker” BM (in this case the HT-HEA). Noteworthy, this UTS was reached despite the insufficient weld penetration, tunnel defect, and further surface-near weld imperfections (see Section 8.2). According to Taheri et al. [273], FSW-joint welds typically achieve 80 % of the UTS of the respective welded BM. However, the fracture strain was reduced to 17 % compared to the HEA and to 13 % compared to the steel BM. The reason (and the “kink” in the stress-strain curve shown in Figure 94b) are described in detail in Section 8.5.2 with the DIC measurements/local strain evaluation. As already shown for the HEA-to-HEA FSW joint in Section 7, it should be possible to use an optimized FSW process to produce weld-defect-free joints with improved mechanical properties.

The FSW-DMW with CR-HEA shows a reduction in UTS R_M= 534 MPa compared to the two BMs (steel and CR-HEA), but also an increased fracture strain to 133 % compared to the CR-HEA (Figure 94c). Nevertheless, the UTS is similar to that of the HT-HEA. However, for both DMW with CR-HEA, the final failure occurred in the WM, i.e. which represented the “weakest” point of the joint. This was further indicated by the lowest hardness which usually corresponds to the lowest strength of a material [276]. Possibilities to obtain an improved mechanical performance MPEA FSW-joints are, e.g. precipitation hardening by the intentional "alloying" of particles like in the case of WC (nanosized tungsten carbides) into a $Fe_{50}(CoCrMnNi)_{50}$ MEA [277].

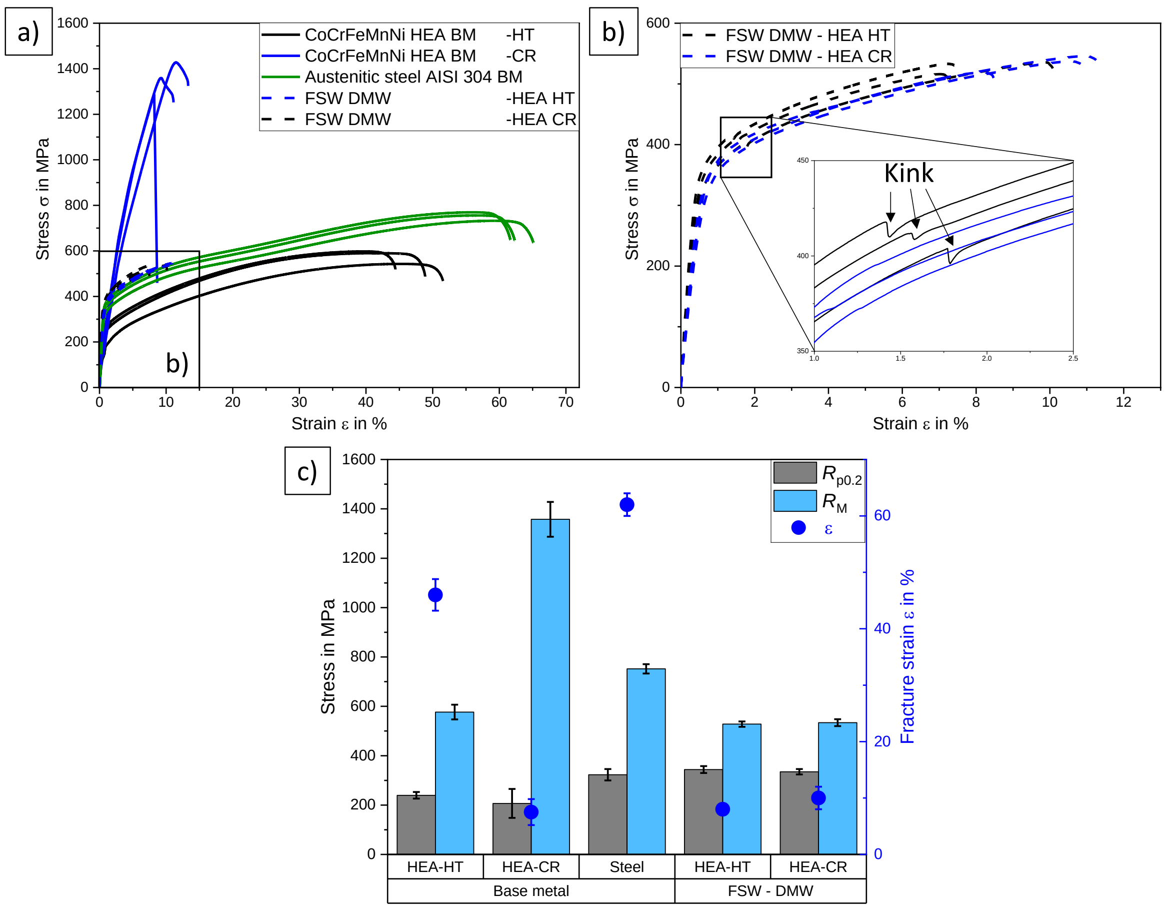

Figure 94: Engineering stress-strain curves of: (a) CoCrFeMnNi-HEA-BM (in HT- and CR-condition), AISI 304 and DMWs (b) just FSW-DMWs, (c) overview of YS: $R_{p0.2}$, UTS: R_M and fracture strain: ε

8.5.2 Local strain properties of FSW-DMWs

In the following section, the local strains of the cross-weld samples of the FSW-DMW with HT-HEA are discussed. For this purpose, (a) the global stress-strain curve and (b) the local strain maps for stages I to III are given in Figure 95.

From Figure 95b, is obvious that the strain in the FSW joint, except for the strong local strain in the region of the fracture, is lower than in the BMs. This is particularly evident in stage II. While the area of the TMAZ at the transition to the BM of the HT-HEA is locally strained by approx. 2 %, the HEA-BM showed approx. 5 %. This confirmed the already mentioned deformation resistance of the weld (due to work hardening and grain refinement, compare Section 8.2). The area of failure, in the weld center, is also the area of insufficient weld penetration, a tunnel and surface defect, i.e. a reduced cross-section as shown in Section 8.2.

The kink in the engineering stress-strain curve between stages I and II is caused by tearing at the root side of the weld. The notch continues to tear due to incomplete weld penetration but does not fail at this point. As a result, the SZ (see Figure 89) withstands high local mechanical loading despite the notch effect (resulting from insufficient weld penetration as shown in Section 8.2.1 in Figure 88). This and the fact that the material can still sustain high local strains of up to 40 % (stage III), shows the potential of an FSW-DMW made of HT-HEA and AISI 304 steel with an optimized welding process.

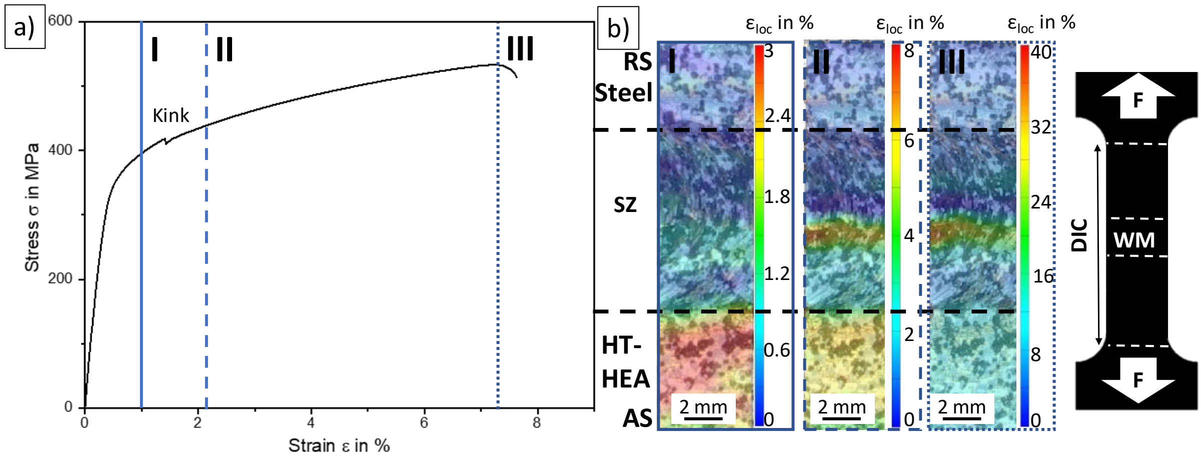

Figure 95: FSW-DMW of AISI 304 with CoCrFeMnNi-HEA in HT-condition: (a) engineering stress-strain curve and (b) local strain ε_{loc} for stage I to III

In the following section, the local strains of the cross-weld samples of the FSW-DMW with HT-HEA are discussed. For this purpose, (a) the global stress-strain curve and (b) the local strain maps for stages I to III are given in Figure 96. The FSW-DMW with CR-HEA, as already observed for the corresponding TIG-DMWs, shows no identifiable deformation by DIC measurements (ε_{loc} < 2 %, see Section 6.5.2 and Figure 67) during the tensile test. The reason is the high work hardening (cf. Figure 96b from stage I to III). The largest local straining is exhibited in the SZ for all stages. In addition, the previously observed heterogeneous local strain distribution within the SZ forms shortly after the linear-elastic region. The areas next to the weld center show an increased local strain. This effect was attributed to a curvature of the specimen (compare Section 0) caused by a partial fracture starting from a notch at the root side. However, in the DMW with CR-HEA, there was no notch present at the root side (Figure 90). It supports the assumption that a bonding defect is present at the root side, which does not exhibit a material-to-material bond of the BMs and thus could show the same effect as a notch.

Figure 93b shows the local hardness, which was the lowest within the TMAZ on the HEA side. However, the heterogeneous strain in the SZ may also originate from the highly heterogeneous microstructure and the embedded weld defects (white band, lamellar texture, different behavior of pure HEA and AISI 304 steel, e.g., see Figure 90) and not be due to bending. For that reason, this behavior cannot be currently clarified. Nevertheless, it can be stated that a maximum local fracture strain of approx. 40 % was achieved, accompanied by a certain reduced strength compared to the BMs. However (and as already explained), there is a potential to improve both the strength and ductility via FSW-process optimization or by precipitation hardening.

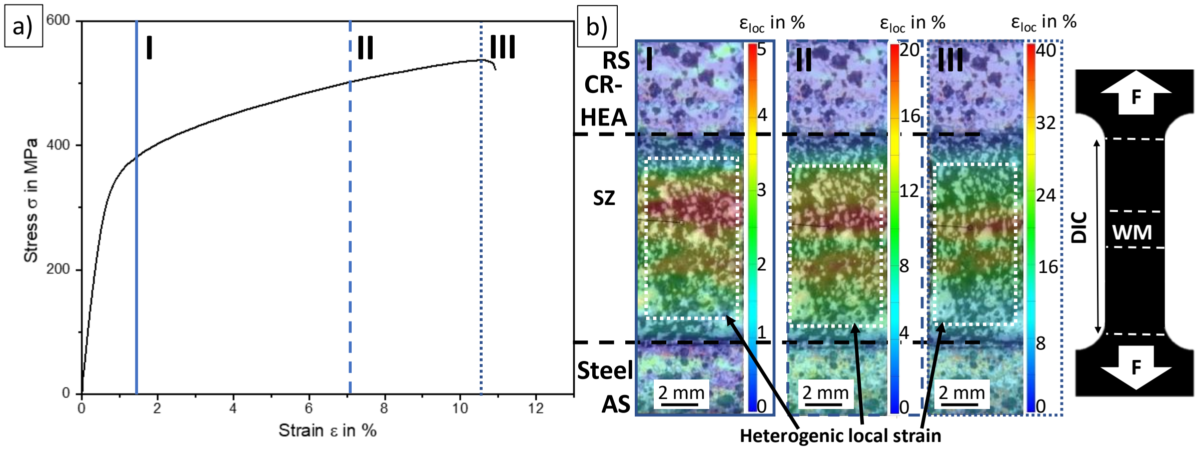

Figure 96: FSW-DMW of AISI 304 with of CoCrFeMnNi-HEA in CR-condition: (a) engineering stress-strain curve and (b) local strain ε_{loc} for stage I to III

8.5.3 Fracture morphology of FSW-DMWs

The fracture morphologies of the DMWs after the tensile tests are described in the following. SEM figures of the fractured cross-weld samples of the FSW-DMW with HT-HEA are shown in Figure 97. They can be divided into two areas, the top and the root side. There is fracture morphology indicating low deformation, starting from the notch on the root side, and a fracture morphology indicating higher deformation, in the top side area of the SZ (see Figure 88). This results in a material separation (Figure 97c) between the low-deformation region and the high-deformation dimple fracture [278]. Sharp-edged structures can be seen in the material separation, with partly plain surfaces (see Figure 97c). This indicates a brittle fracture with intragranular fracture components [278] and therefore confirms the assumption of a brittle partial fracture at the kink in the engineering stress-strain diagram between stages I and II in Figure 95. The local strain is anticipated to be further diminished, primarily attributable to the HT-HEA-BM effectively absorbing a significant proportion of the strain, as previously conditioned. The augmented strength and ductility observed in the SZ are conjectured to have absorbed the energy associated with the initial rupture or notch effect, thereby impeding crack propagation. Subsequent failure is ascribed to a shift in crack propagation direction, facilitated by the defect-rich interface existing between the SZ and the TMAZ on the HEA side. Nevertheless, the dimpled morphology of the top side (Figure 97b) confirms a ductile failure, which was indicated by local strains of approx. 40 %.

The fracture surface of the FSW-DMW with CR-HEA (in Figure 98a) can be divided into three areas. The area at the root side of Figure 98d indicates low deformation, while the weld center (Figure 98c) and top side (Figure 98b) show a high deformation dimpled fracture [278]. In addition, (d) shows the lateral view of the fracture surface. The clear curvature of the specimen in the area of the fracture surface towards the root side illustrates the occurrence of the bending during the tensile test, which was already suspected by the local strain distribution. Therefore, it is assumed that a partial fracture occurred at the root side. This is attributed to the suspected bond failure at the root side, which is why the metallurgical bond was apparently too low to absorb force. As a result, this has separated directly from the first application of force, which means that no kink is shown in the engineering stress-strain diagram for this case.

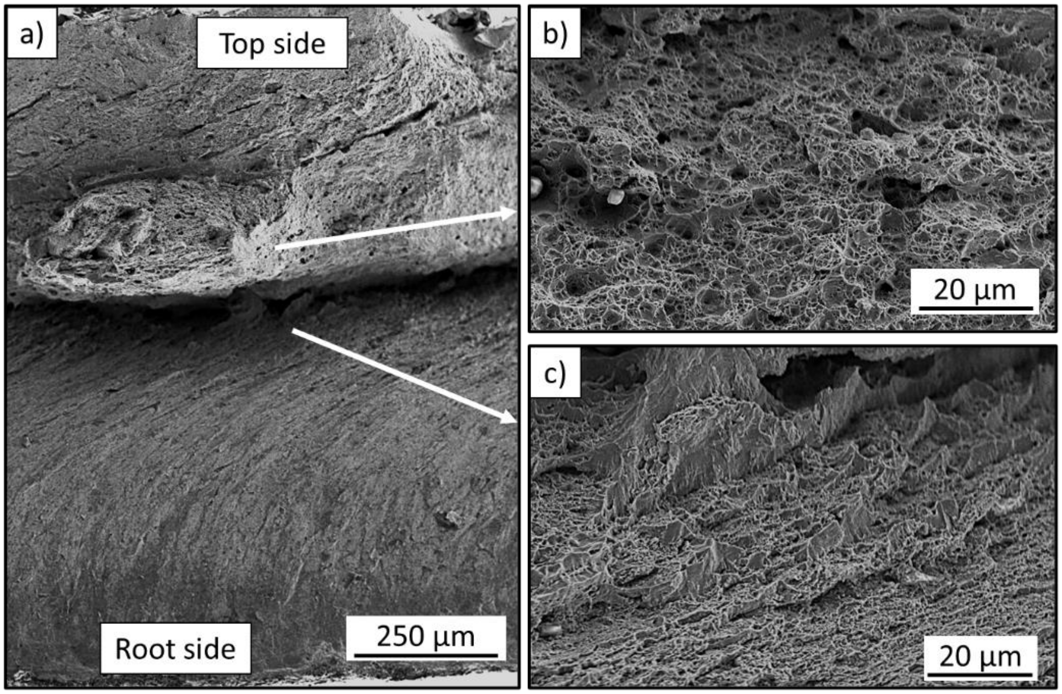

Figure 97: SEM-images of the fracture surface after tensile test für the FSW dissimilar metal butt joint of CoCrFeMnNi-HEA in HT-condition with AISI 304: (a) overview; (b) detailed top side region; (c) detailed root side region

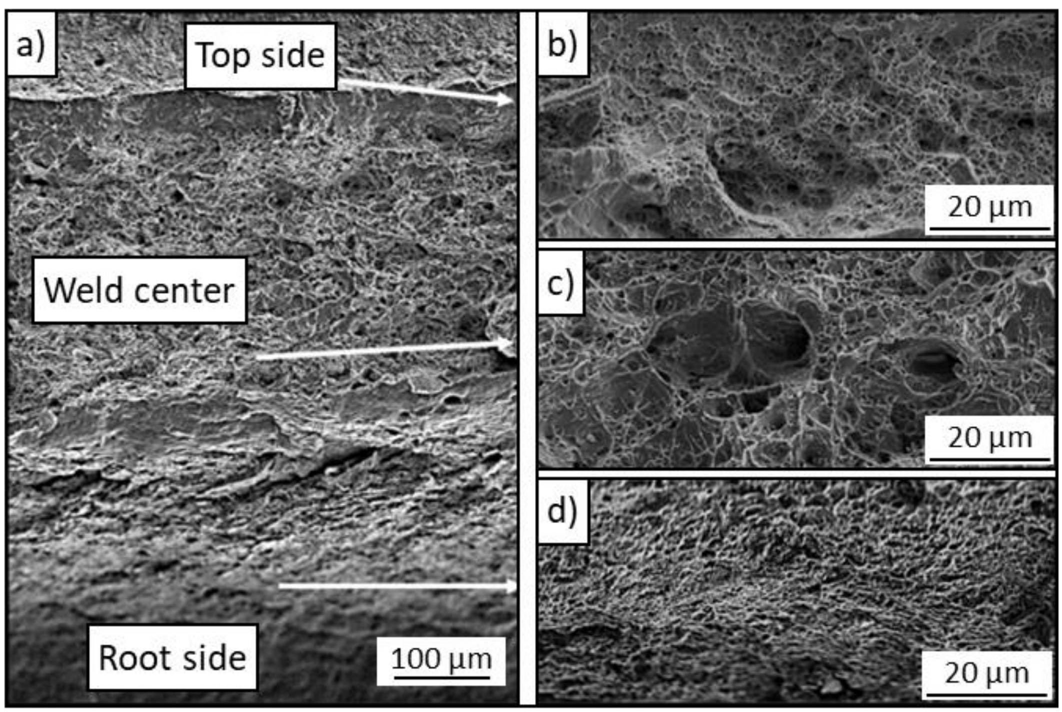

Figure 98: SEM-images of the fracture surface after tensile test für the FSW-DMW of CoCrFeMnNi-HEA in CR-condition with AISI 304: (a) overview; (b) detailed top side region; (c) detailed center region; (d) detailed root side region

9. Comparison of process-specific weldability

In this section, an investigation is conducted to compare the weldability as defined in Section 2.2 of MPEAs achieved through FSW and TIG welding for the first time in general. This means that the interaction of the material-related weldability (properties of the MPEA) and the process-related weldability (TIG and FSW process) have an influence on the constructive-related weldability (mechanical properties for the design of components). As the microstructure formation markedly varies between the two procedures, as shown in Section 2.2, the discussion here primarily avoids microstructural considerations. Instead, importance is placed on contrasting weld imperfections and the consequent mechanical-technological properties from tensile tests.

9.1 MPEA-to-MPEA welding of CoCrFeMnNi-HEA and CoCrNi-MEA

The subsequent analysis undertakes a comparative examination of the weldability between FSW and TIG processes applied to MPEAs. In this regard, Table 16 initially contrasts the weld imperfections observed in each weld. Notably, it is observed that only the FSW welds of the CR MPEAs exhibit weld imperfections surpassing acceptable thresholds (as shown in Section 7). Consequently, FSW is considered insufficiently suitable for welding the CR-MPEAs. It is relevant to reiterate that these evaluations are based on one single test, thus implying the potential for enhanced outcomes through refined procedural adjustments or optimized process parameters, as expounded in Section 7.

Table 16: Weld imperfections of TIG and FSW MPAE to MPEA welds

	HEA		**MEA**	
	HT	**CR**	**HT**	**CR**
TIG	- none	- none	- none	- none
FSW	- none	- insufficient weld penetration (gap) - reduced plate thickness in weld seam - flash formation	- none	- insufficient weld penetration (gap)

To assume good weldability, the welds must meet certain requirements in terms of mechanical properties. As there are no predefined benchmark values for welds of the new MPEAs, the mechanical properties of the BMs are used. For comparison of the mechanical properties, the stress-strain curves (a and c) and the resulting mechanical properties (b and d) of the welds are given for the BMs of the HEA (a and b) and the MEA (c and d) in Figure 99. This shows that all welds that have no weld imperfections (FSW of the CR-MPEAs, see Table 16) have strength values (UTS and YS) in the range of the respective HT-BMs. Following, there is good constructive-related weldability with regard to the strength values. The UTS of the CR-BM cannot be achieved due to the high degree of work hardening of the BM. The fracture strain for all welds without weld imperfections is >15 % and therefore higher than for the CR-BMs. Therefore, sufficient ductility for good weldability can be assumed, even if the fracture strain of the HT-BMs is not achieved. The results also show how the initial condition of the MPEAs has a major influence on weldability. The welded MPEAs with HT-BM consistently show better combinations of mechanical properties compared to the welds with CR-BM. Regarding the CR-BM, there is also significantly better constructive-related weldability using TIG compared to FSW based on the significantly higher UTS and fracture strain for both MPEAs.

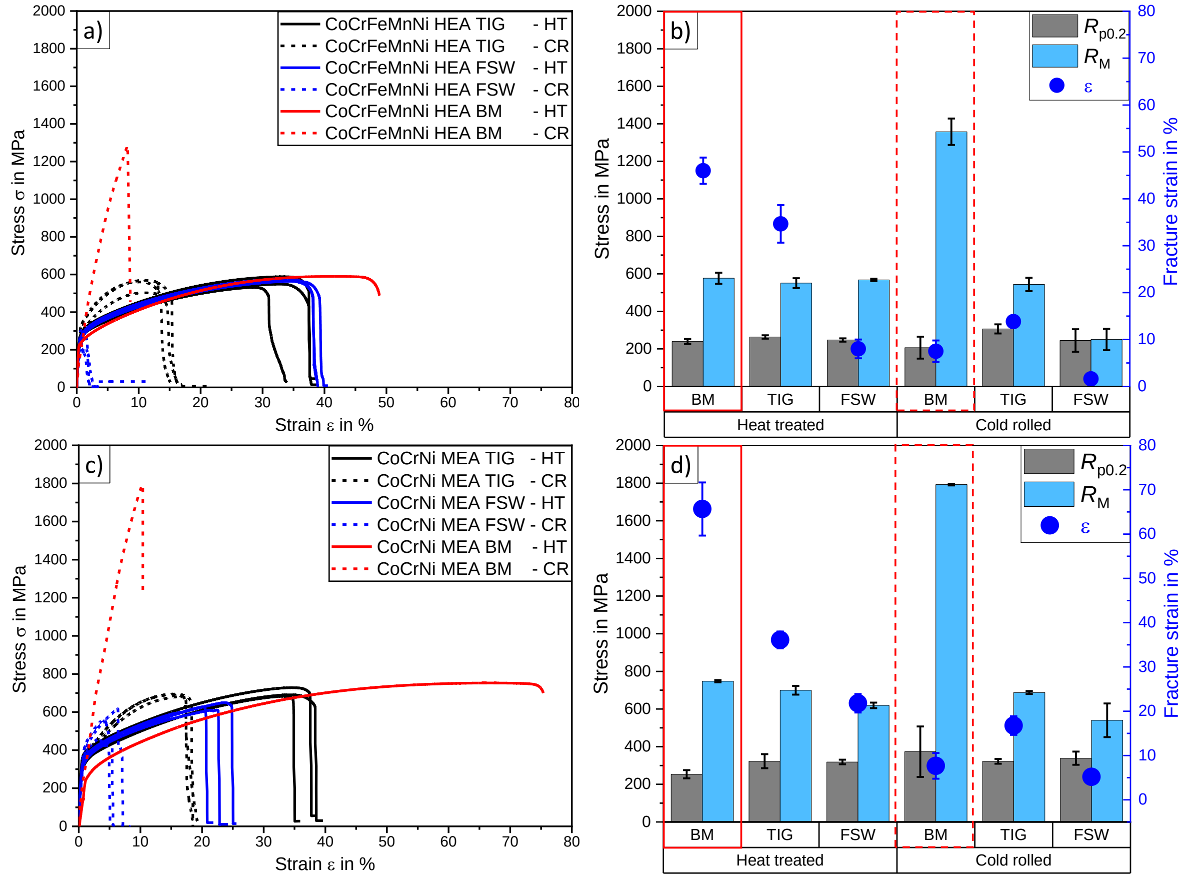

Figure 99: TIG and FSW specific weld joint mechanical properties of (a and b) CoCrFeMnNi-HEA and (c and d) CoCrNi-MEA: (a and c) engineering stress-strain curves and (b and d) calculated mechanical properties

Finally, for the first time recommendations and process instructions for welding of MPEAs (CoCrFeMnNi HEA and CoCrNi MEA) are derived from the results:

- The MPEAs should be welded in the HT condition, as better mechanical-technological properties (YS, UTS, fracture strain) are obtained compared to the CR condition regardless of the welding process (TIG or FSW).
- MPEAs in CR condition should be TIG welded to avoid weld seam imperfections.

9.2 Dissimilar metal welding of CoCrFeMnNi-HEA with AISI 304

This section compares the weldability of the FSW and TIG processes for DMWs of CoCrFeMnNi HEA with austenitic steel. For this purpose, the weld imperfections of the DMWs are compared in Table 17. The TIG DMW of the HT-HEA shows an offset as described in Section 6.2. The reason for the offset is distortion, which is typical for austenitic steels in fusion welding and can be reduced or even avoided by known handling instructions from the literature [279]. The TIG DMW of the CR-HEA shows no weld imperfections, which is the basis for good weldability.

The two FSW DMWs both show unacceptable weld imperfections. Both show insufficient weld penetration, the DMW with the HT-HEA also exhibits incomplete weld overlay and a tunnel defect. As a result, similar to the FSW joints in Section 9.1, good weldability cannot be described here. However, it should also be mentioned here that these are single welding tests and the weld imperfections shown can possibly be avoided by optimizing the process parameters as discussed in Section 8.

Table 17: Weld imperfections of TIG and FSW DMWS (HEA to austenitic steel AISI 304)

	HT-HEA	**CR-HEA**
TIG	- offset	- none
FSW	- incomplete weld overlap - tunnel defect - insufficient weld penetration	- insufficient weld penetration

To be considered as having good weldability, DMWs must also fulfill certain requirements in terms of mechanical properties. The mechanical properties of HT-HEA are used as a benchmark in the absence of standards for HEA DMWs. The stress-strain curves (a) and derived mechanical properties (b) of the TIG and FSW DMWs are shown in Figure 100 to compare the tensile test results with the BMs. This shows that both TIG welds achieve UTS/R_M in the range of HT-HEA, although there is a reduction in fracture strain in both cases. The good strength values and fracture strain > 10 % show that good mechanical properties can be achieved with the TIG DMW of HEA with austenitic steel and thus good constructive-related weldability can be described.

The FSW DMWs achieved UTS/R_M values only slightly lower than those of the HT-HEA BM. This was despite the welding imperfections shown previously. Fracture strain of approx. 10 % were observed. Therefore, it can be concluded that the FSW DMWs of HEA have at least a limited constructive-related weldability. However, as already mentioned, this indicates a great potential for improvement through process optimization.

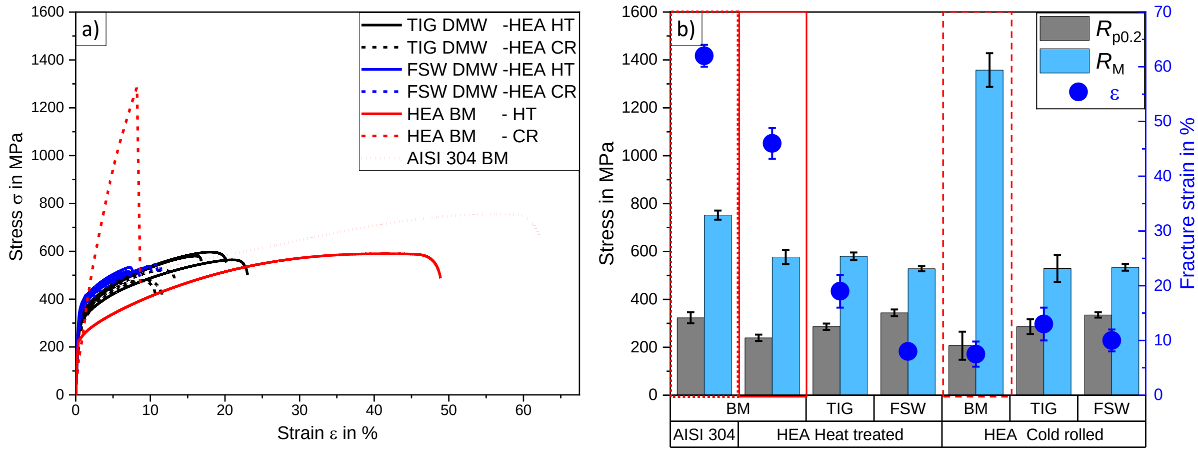

Figure 100: TIG and FSW specific DMW joint mechanical properties of CoCrFeMnNi-HEA: (a) engineering stress-strain curves and (b) calculated mechanical properties.

The results will be used for the first time to derive recommendations and process instructions for the DMW of CoCrFeMnNi HEA with austenitic steel AISI 304:

- DMWs of HEA with austenitic steels should be TIG welded as there are considerably fewer weld imperfections and the mechanical properties are improved compared to FSW.
- Distortion-reducing procedures should be used for TIG DMW of HEA with austenitic steels.

10. Process analysis of machinability

This chapter delineates the machining procedures for HEA and MEA alloys, detailing the machining process and parameters' impact on cutting forces. It also examines resultant surface integrity concerning topography, mechanical effects, and resulting microstructure. Insights garnered informed process recommendations for machining CoCrFeMnNi-HEA and CoCrNi-MEA using geometrically determined cutting edges.

10.1 Forces during conventional and ultrasonic-assisted finish milling

The machining process is outlined with emphasis on cutting forces, tool wear, and the effect of the process parameters f_z, v_c, and ultrasonic assistance on CoCrFeMnNi-HEA and CoCrNi-MEA alloys. The discussion concludes with an examination of tool life and wear.

10.1.1 Influence of process parameters f_z and v_c on cutting forces.

The effects of f_z and v_c on the cutting forces F_r is shown in Figure 101 for the HEA. A contour plot of $\varnothing F_{r,max}$ versus the process parameters derived from the linear regression model (accuracy of the regression model: R^2 = 91 %) is shown in Figure 101a. $\varnothing F_{r,max}$ is the average of the maximum values for all peaks of a given parameter set. Within the investigated parameter range, $\varnothing F_{r,max}$ = 41 N was determined for test No. 2 (see Figure 101a). The cutting force can be reduced by approx. 38 % when f_z is reduced from 0.07 mm to 0.04 mm (Test No. 1 of Figure 101a). This result of reduced cutting force with decreased f_z is consistent with current literature for MPEAs [187] and the theory on the cross-section of an undeformed chip [150, 151]. Increasing v_c from 30 m/min to 110 m/min results in a further 28 % reduction in $\varnothing F_{r,max}$, a similar effect was shown for $Al_{0.3}$CoCrFeNi MPEA [187]. Milling at higher speeds leads to higher temperatures (deformation-related), resulting in thermal softening. This can increase ductility, allowing greater shear deformation with less cutting force [280]. Overall, the cutting force can be reduced by approx. 47 % at a cutting speed of 110 m/min and a feed per cutting edge of 0.04 mm (Test No. 4, upper left corner of Figure 101a).

The resulting cutting forces F_r of the tests are compared in Figure 101b, plotting F_r against milling time. Despite similar maximum cutting forces in tests no. 1 and 3, a 13.5 mm line was milled in 3 s for no. 1, and 0.5 s for no. 3. In essence, no. 3 parameters enable a sixfold reduction in machining time compared to no. 1, enhancing productivity. Test no. 4 obtains a balance, with the lowest F_r and the second shortest machining time, illustrating that minimal F_r and efficient machining can coexist, bolstering productivity. However, considerations of tool wear, tool life, and surface properties are imperative in this context.

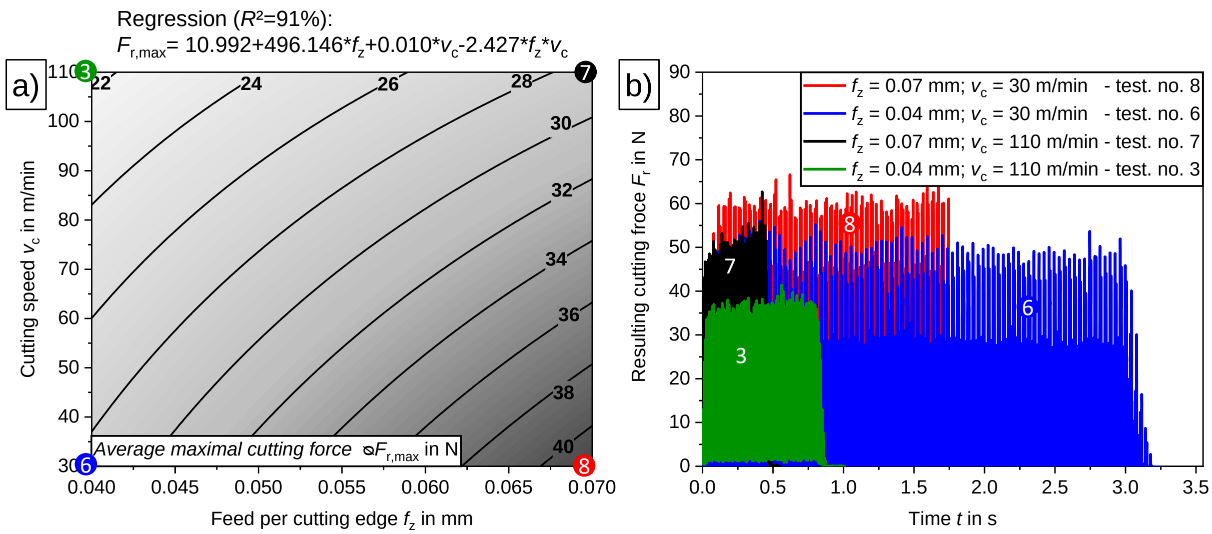

Figure 101: Influence of cutting parameters f_z and v_c on CoCrFeMnNi-HEA conventional milling: (a) average maximum cutting force ⌀$F_{r,max}$; (b) on resulting cutting force F_r of one milling line of 13.5 mm (published in [207])

Figure 102 illustrates the impact of process parameters f_z and v_c on cutting forces for CoCrNi-MEA. In Figure 102a, a linear regression model for ⌀$F_{r,max}$ is depicted. As cutting speed v_c increases, ⌀$F_{r,max}$ also rises, albeit marginally, with an approx. 5% increase. This contrasts with HEA behavior, possibly due to MEA's higher susceptibility to work hardening [23]. The influence of f_z remains consistent for both MEA and HEA. Consequently, for MEA, ⌀$F_{r,max}$ can be decreased by approx. 17% by reducing f_z from 0.07 to 0.04 mm. This aligns with the current theory on the cross-section of undeformed chip [150, 151], the literature on milling MPEAs [187], and the results for the HEA. Notably, test no. 1, featuring a 0.04 mm feed per cutting edge and a low cutting speed of 30 m/min, yields the lowest ⌀Fr,max. Within this parameter range, cutting force ⌀$F_{r,max}$ for MEA can be reduced by about 21%, approx. 11 N.

MEA typically exhibits higher force values (⌀$F_{r,max}$: 43 – 55 N) compared to HEA (⌀$F_{r,max}$: 22 – 41 N), likely due to its higher hardness (187 HV0.5 for MEA, 130 HV0.5 for HEA). This implies increased mechanical stress on the tool during MEA machining.

Figure 102b compares the resulting cutting force F_r during MEA milling, plotted against milling time. tests no. 2 and 3 exhibit similar maximum cutting forces. Nevertheless, a 15 mm line was milled within 2 s in test no. 2 and within 0.5 s in test no. 3. Put simply, test no. 3 parameters enable a fourfold reduction in machining time compared to test no. 2, enhancing productivity. As with HEA, test no. 4 strikes a balance between small cutting forces and milling speed, featuring the lowest cutting forces and the second shortest machining time. This underscores that minimal cutting forces, indicating low tool load, are compatible with efficient machining and high productivity. Nonetheless, considerations of tool wear, lifespan, and surface properties remain crucial for an economically efficient milling process (tool life vs. cutting time).

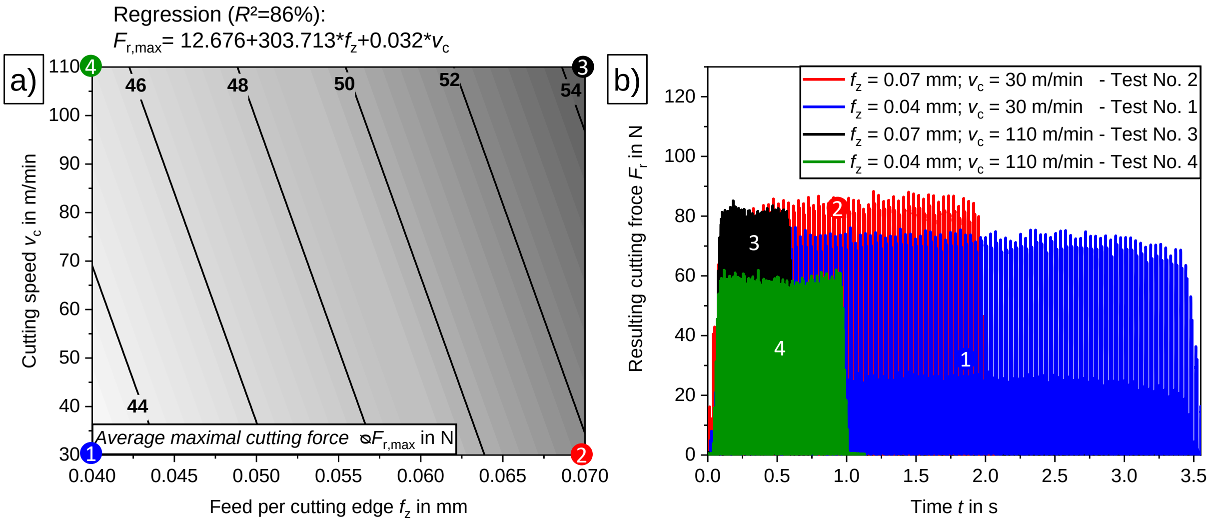

Figure 102: Influence of cutting parameters f_z and v_c on CoCrNi-MEA conventional milling: (a) average maximal cutting force ⌀$F_{r,max}$; (b) on resulting cutting force F_r of one milling line of 15 mm

10.1.2 Influence of ultrasonic support on cutting forces

In the following, the influence of USAM and the interactions with the milling parameters f_z and v_c on the cutting forces is discussed.

Figure 103 shows cutting forces for USAM vs. the conventional process in x (a), y (b), and z (c) directions for the HEA. The component of the resultant force in the normal feed direction (F_y) shows the largest maxima approx. 40 N (b), while the peak loads in the opposite feed and passive directions (F_x; F_z) show amounts between 20 and 25 N (a and c). A comparison of the components of the resulting forces from conventional and US tests shows a reduction in the force maxima for all three components. The result is a net decrease of F_r for all investigated machining parameters with US. The effect of ultrasonic support compared to conventional milling on the ⌀$F_{r,max}$ is shown in d. The US provides the opportunity to increase productivity by optimizing the machining parameters (f_z, v_c) in terms of reduced cutting forces, machining times (see b), and tool wear. It is assumed that lower cutting forces which are shown for the US in all three directions are beneficial in terms of tool load for the machining process and the resulting surface. For given machining parameters, ultrasonic assistance can reduce cutting forces by approx. 5 % on average compared to conventional milling. The forces reduced by USAM are consistent with the literature for NiCr alloys. As shown in Section 2.3.2 this is mainly due to reduced contact time, reduced friction, and the effect of acoustic softening.

Figure 103 illustrates cutting forces for USAM versus the conventional process in the x (a), y (b), and z (c) directions for HEA. The largest maxima are observed in the component of the resultant force in the normal feed direction (F_y), approximately 40 N (Figure 103b), while peak loads in the opposite feed and passive directions (F_x; F_z) range between 20 and 25 N (Figure 103a and c). A comparison of resultant force components from conventional and US tests reveals a reduction in force maxima across all three components, resulting in a net decrease of F_r for all investigated machining parameters with the US. The effect of US on ⌀$F_{r,max}$ compared to conventional milling is depicted in Figure 103d. The US allows increased productivity by optimizing machining parameters (f_z, v_c) for reduced cutting forces (mechanical tool load) and machining times (see Figure 101b). Lower cutting forces, evident in all three directions with the US, are presumed to be beneficial for tool load and resulting surface quality.

For given machining parameters, the US can reduce cutting forces by approx. 5% on average compared to conventional milling, consistent with literature findings for NiCr alloys [154, 181, 281]. This reduction in forces with USAM is attributed mainly to reduced contact time [168], friction, and the acoustic softening effect [171, 172].

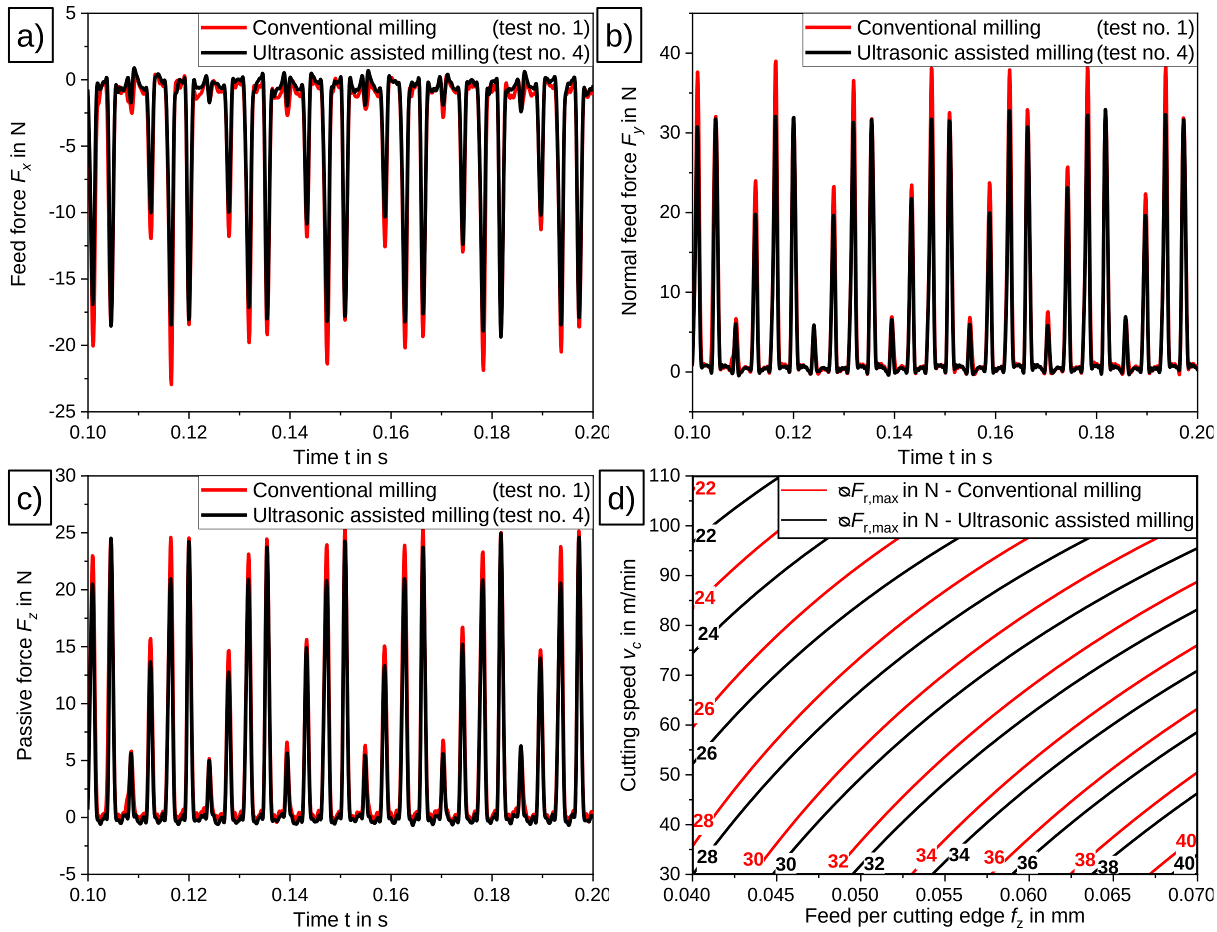

Figure 103: Comparison of cutting forces for USAM (test no. 4; f_z = 0.055 mm and v_c = 70 m/min) versus conventional milling (test no. 1; f_z = 0.055 mm and v_c = 70 m/min) for CoCrFeMnNi-HEA: (a) feed force F_x; (b) normal feed force F_y; (c) passive force F_z and (d) average resulting cutting force $F_{r,max}$ vs. cutting parameters f_z and v_c (published in [207])

Figure 104a to c shows the cutting forces of US and conventional milling in x, y, and z directions for MEA. The component of the resultant force in the normal feed direction (F_y) exhibits the largest maxima, around 50 N (Figure 104b), while peak loads in the feed and passive directions (F_x; F_z) range between 25 and 30 N (Figure 104a and c). However, a comparison of resultant force components from conventional and USAM tests reveals an increase in force maxima for all three components with USAM. The linear regression model for US versus conventional milling is depicted in Figure 104d, indicating an increased cutting force $\varnothing F_{r,max}$ by approx. 4% with USAM. CoCr alloys [182] also exhibited similar behavior during USAM. This could be attributed to the increased initial hardness or work-hardening capacity of MEA compared to HEA [23]. The hammer effect of ultrasonic support might intensify material work hardening in the vicinity of the cut, requiring higher cutting forces for USAM than for conventional machining. For this effect to prevail, it would need to outweigh the force-reducing effects described previously for HEA, such as reduced contact time and acoustic softening.

The increased cutting force could potentially have a negative impact on tool wear and tool life, thereby impacting process economics. However, given the low 4% increase in force, the positive effects of ultrasonic assistance, such as increased cutting stability and improved chip shape or surface integrity, may outweigh these concerns.

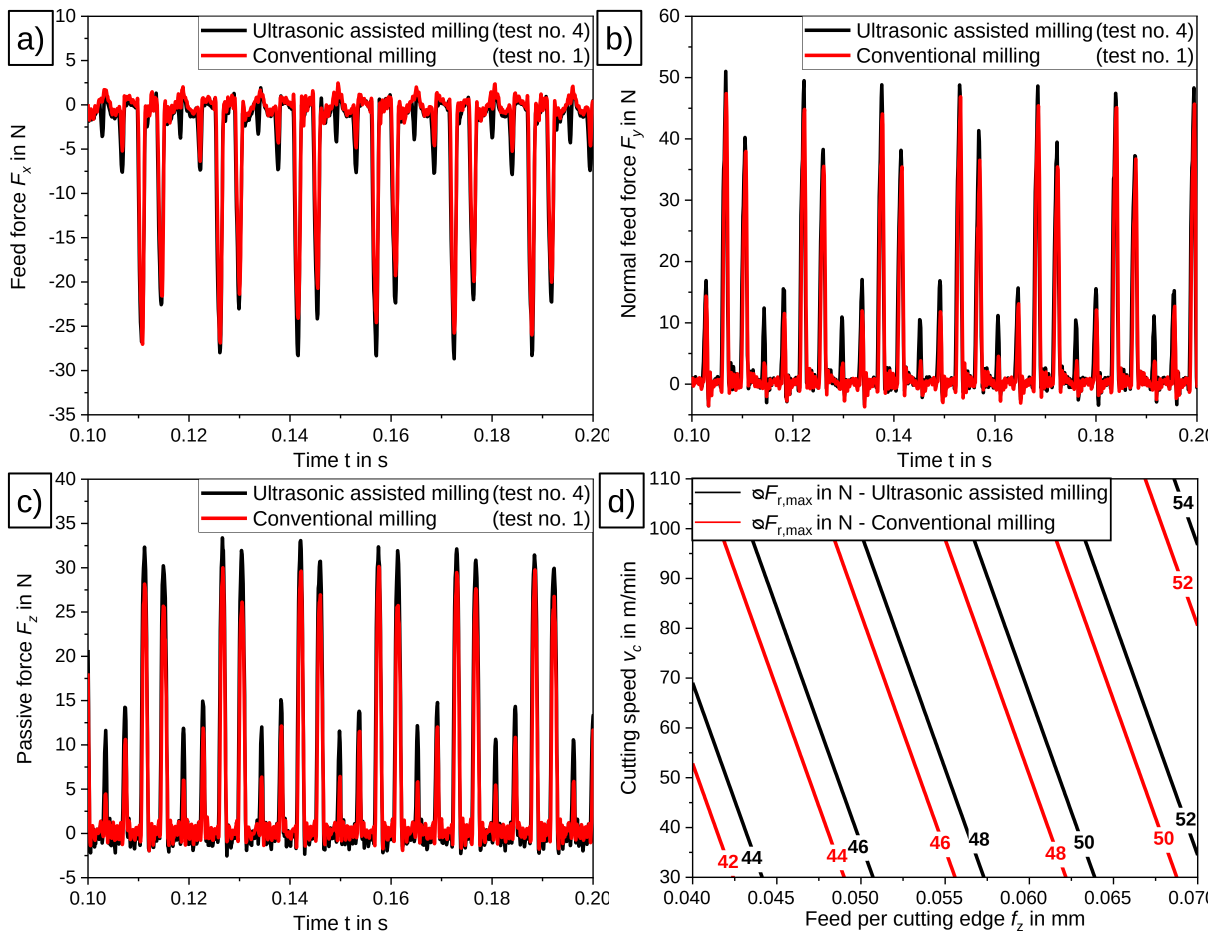

Figure 104: Comparison of cutting forces for USAM (test no. 4; f_z = 0.055 mm and v_c = 70 m/min) versus conventional milling (test no. 1; f_z = 0.055 mm and v_c = 70 m/min) for CoCrNi-MEA: (a) feed force F_x; (b) normal feed force F_y; (c) passive force F_z and (d) average resulting cutting force $F_{r,max}$ vs. cutting parameters f_z and v_c

10.1.3 Tool wear

Figure 105 shows the tool cutting edges before and after the complete DoE for the HEA (material removal V_c=720 mm³) and MEA (V_c=810 mm³). The manufacturing deviation of the individual cutting edges already shows differences in the individual force peaks and the resulting difference of the engagement parameters, the load, and thus the wear of the individual cutting edges. Therefore, the two worn cutting edges with the highest and lowest wear marks are always shown here. The cutting edges with low wear, show initial abrasive wear marks after machining of both the

HEA and the MEA. Whereas the cutting edges with higher wear show clear abrasive wear marks. However, the wear should not have a major influence on the surfaces and the surface integrity, since in Table 18 the average resulting maximum cutting forces $\varnothing F_{r,max}$ of the first and last tests (both conventional process with central point parameters, test no. 5 and 6 in Table 12) of the DoEs are compared. Here $\varnothing F_{r,max}$ is only slightly different in the first and last tests for both the HEA and the MEA.

However, to make accurate statements about tool wear, tool life tests should be carried out, for which an insufficient amount of material was available in this work. The aim of these tests should be to achieve at least an average chip volume of approx. 3200 mm^3 until wear leads to tool rejection, as is the case for a Ni-base superalloy Inconel 718 [282].

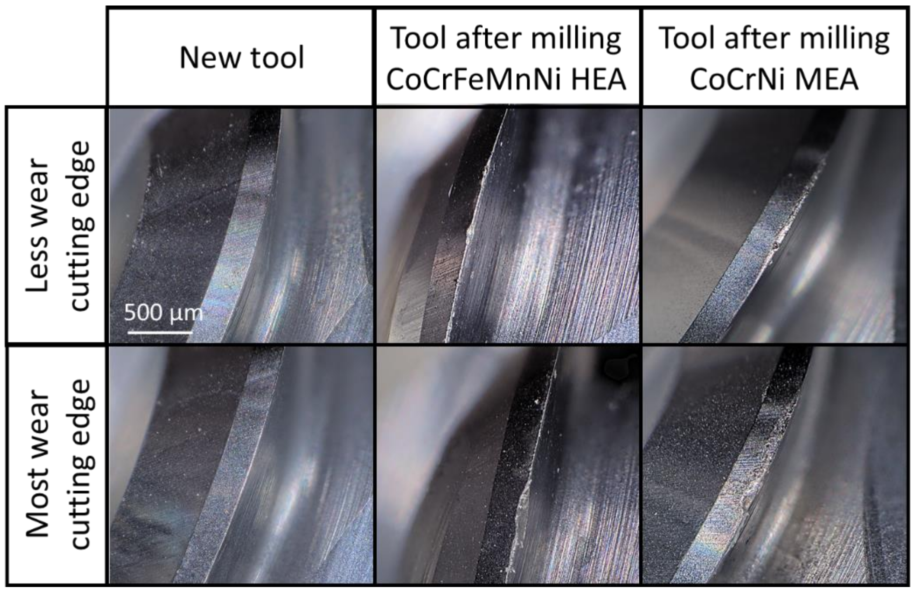

Figure 105: LOM of new cutting edges, cutting edges after milling a complete DoE of CoCrFeMnNi-HEA, and cutting edges after milling a complete DoE of CoCrNi-MEA. For the cutting edges after milling the ones with the most and less wear are shown

Table 18: Resulting cutting force for the first and last milling tests of the DoE with the central point parameters (f_z = 0.055 mm; v_c = 70 m/min; conventional)

Resulting cutting forces $\varnothing F_{r,max}$	**Test No. 6 (first test)**	**Test No. 5 (last test)**
HEA tests	33.3 ± 22.0 N	29.2 ± 19.2 N
MEA tests	54.0 ± 23.6 N	53.6 ± 25.0 N

10.2 Surface integrity

In the following chapter, the resulting surface integrity of machined surfaces is characterized for both MPEAs, focusing on topography, mechanical effects, and subsurface microstructure. The influence of DoE parameters such as f_z, v_c, and USAM is discussed, followed by formulating machining guidelines based on these findings.

10.2.1 Topography

Figure 106 compares LOM images of conventionally milled HEA surfaces with USAM images for the parameter variations of cutting speed and tooth feed. Typical surfaces are shown after machining with a ball end mill [212]. Where the surface resembles a regular square-like pattern, and each square corresponds to a cutting engagement (force peaks from Section 10.1) of one of the four cutting edges. The width in the x-direction increases with a larger feed per cutting edge f_z. In the y direction, the individual sections are of equal size in the test series since the step over a_e was kept constant. The resulting surface topography depends on the primary geometry of the cutting edges in connection with the engagement-determining parameters (f_z, a_e, and a_p) [152]. In addition, the tool inclination affects the shape of the individual cuts if varied. Both the surfaces milled conventionally and with USAM show milling marks in the direction of the cut, which are oriented 135° clockwise to the x-direction. These are caused by material removal, adhesion, and cutting-edge microgeometry [283]. The surface machined by USAM also exhibits a series of wavy and parallel lines perpendicular to the milling marks. These features are due to the oscillation of the tool with an amplitude of about 3 µm and a frequency of 39.7 kHz, which is significantly higher than the cutting frequency (0.11-0.41 kHz). Due to the different cutting speeds (rotational speeds) and thus oscillations per cut, the USAM surfaces show different patterns. The number of USAM patterns per cutting engagement increases with reduced cutting speed.The surfaces machined at a lower cutting speed of v_c = 40 m/min show several surface defects (blue rounds in Figure 106), independent of the milling process. The surface defects are caused by the Cr and Mn oxides from the material production process (see Figure 25), which are scratched over the surface by the cutting edge and form grooves. These are characterized in more detail below using SEM examinations.

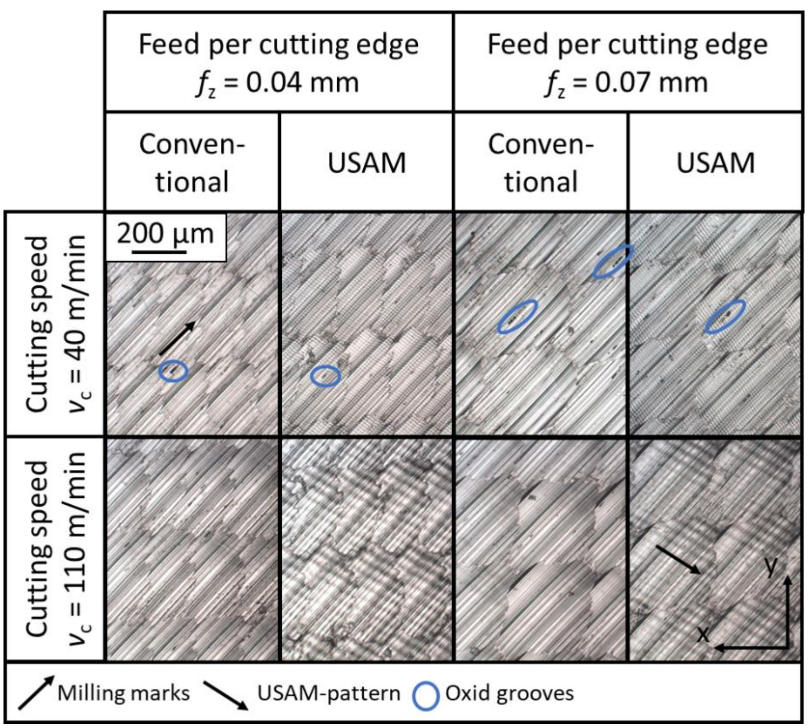

Figure 106: LOM of milled surfaces with different milling parameters of CoCrFeMnNi-HEA; cutting speed v_c = 40–110 m/min; feed per cutting edge f_z = 0.04–0.07 mm; conventional and ultrasonic assisted milling (USAM)

SEM examinations of the machined HEA surfaces are shown in Figure 107. As with the LOM examinations, the difference between conventional and USAM-produced surfaces is shown by the USAM marks. The SEM examinations are intended to characterize the defects in more detail. Two different defect morphologies are detectable. The first is a dark spot with a groove following in the direction of the cut, which are oxide grooves (blue rounding in Figure 107) [157, 159]. The second defect morphology shows several small grooves along the cutting direction without a clearly pronounced starting point (orange rounding in Figure 107), which is a tear defect [157, 159]. The formation mechanism is schematically shown in Figure 107b. The difference between the two defect mechanisms is that in oxide grooving, an oxide is pulled out of the surface by the cutting edge and forced across the surface, forming a groove. In a tear defect, the impulse of the cutting edge crushes the oxide and pulls the individual smaller pieces of oxide across the surfaces.

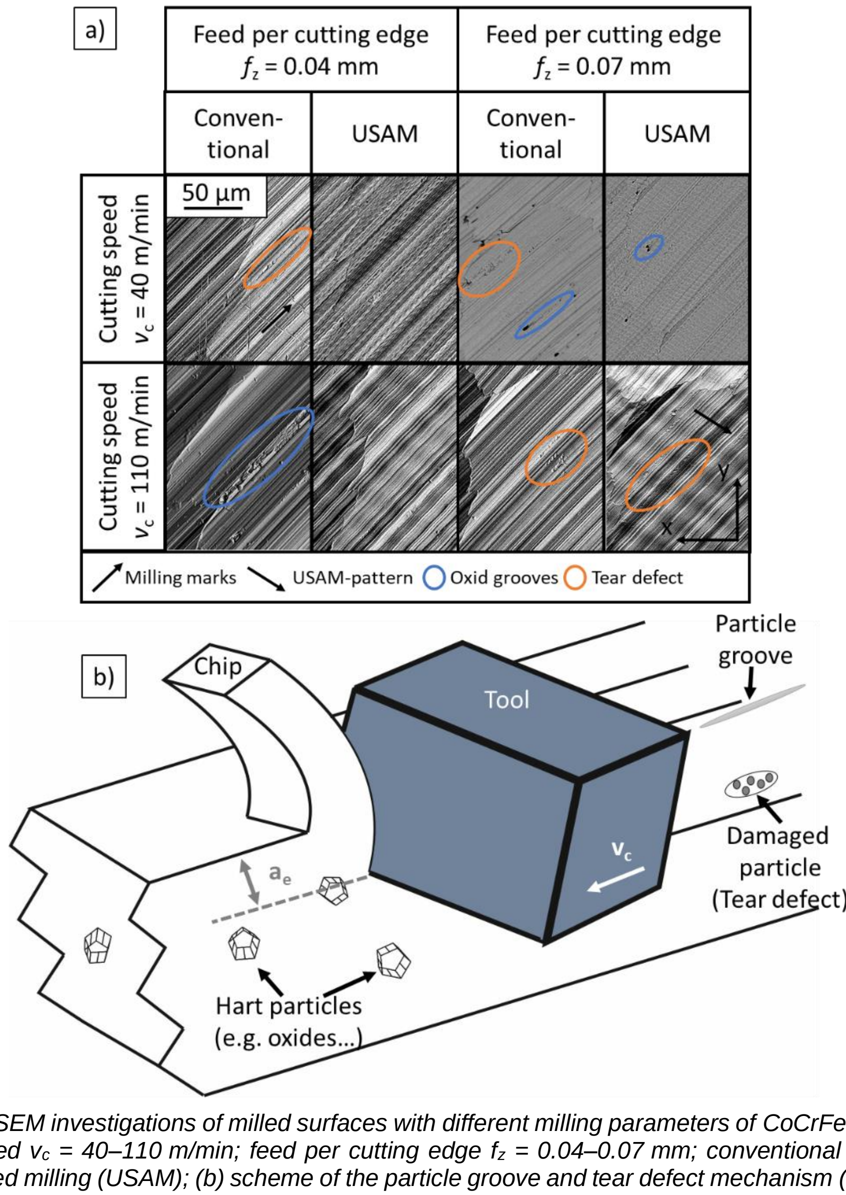

Figure 107: (a) SEM investigations of milled surfaces with different milling parameters of CoCrFeMnNi-HEA; cutting speed v_c = 40–110 m/min; feed per cutting edge f_z = 0.04–0.07 mm; conventional and ultrasonic-assisted milling (USAM); (b) scheme of the particle groove and tear defect mechanism (adapted according to [159])

In finish machining surface defects are to be avoided to ensure high surface integrity. Defects may serve as a starting point for crack initiation or local corrosion phenomena such as pitting [284, 285] and consequently may cause premature failure of a component. Figure 107a also shows that the formation and number of grooves and tear defects cannot be avoided with the USAM, but their number and size are considerably reduced.

A quantitative statement about the influence of the parameters feed per cutting edge f_z and cutting speed v_c on the defect formation cannot be derived from the investigations. The influence of the parameters f_z and v_c is evaluated qualitatively. Surfaces with low f_z and USAM show the lowest defect frequency, while low f_z without USAM tend to show severe defect propagation. Higher v_c leads to larger defect sizes compared to surfaces with lower v_c.

The EDX map of a defect region in Figure 108, shows an increased proportion of Cr and O as well as no reduction of Mn in the defect area. This measurement result confirms the Cr-Mn oxides originating from the production are the cause of these defects.

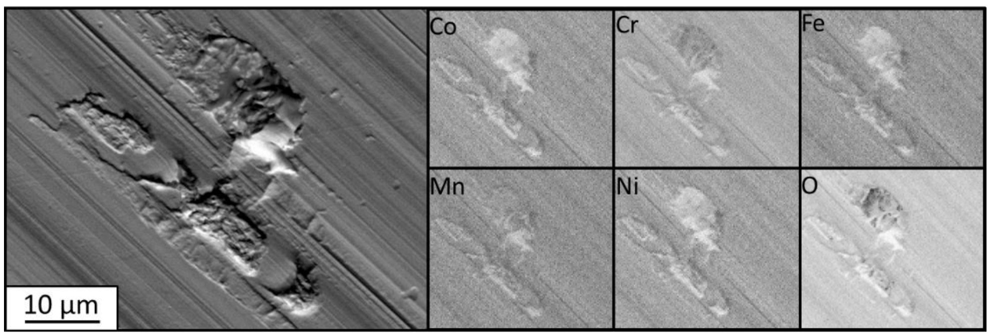

Figure 108: EDX measurement of a tear defect on milled CoCrFeMnNi-HEA surface (published in [207])

LOM images of conventionally milled CoCrNi-MEA surfaces are compared with USAM images for the parameter variations of cutting speed and tooth feed rate in Figure 109. As described for the HEA, typical patterns of machining with a ball nose end milling tool are obvious. The influence of the cutting parameters and the USAM on the resulting surface morphology is according to the HEA. No surface defects can be identified by means of LOM.

SEM images of the finished surfaces of the MEA are shown in Figure 110. There are similarities to those of the HEA surfaces regarding the formation of the milling marks and the USAM pattern. Several surfaces indicate so-called built-up edges (BUE), which are caused by material accumulating in front of the cutting edge during cutting and subsequently deposited on the surface. These BUE are exhibited occasionally on conventionally machined surfaces. No BUE was found for USAM surfaces. This has also been described by Engelking et al. for the Ni-base alloy [166]. The reasons for avoiding BUE with USAM are the interrupted cut and the higher relative movements of the cutting edge and the material, as well as the material's adhesion to the tooltip, decreases due to the US, thereby effectively preventing the formation of a BUE [166].

Very few tear defects were observed at high magnification. An EDX map in Figure 111 reveals that Cr oxides that stem from the production (see Figure 25) are the predominant cause of these defects in the MEA. The tear defects occur sporadically and only during conventional machining. This indicates a lower tendency of the Cr oxides in the MEA to cause tear defects compared to the HEA with Cr-Mn oxides.

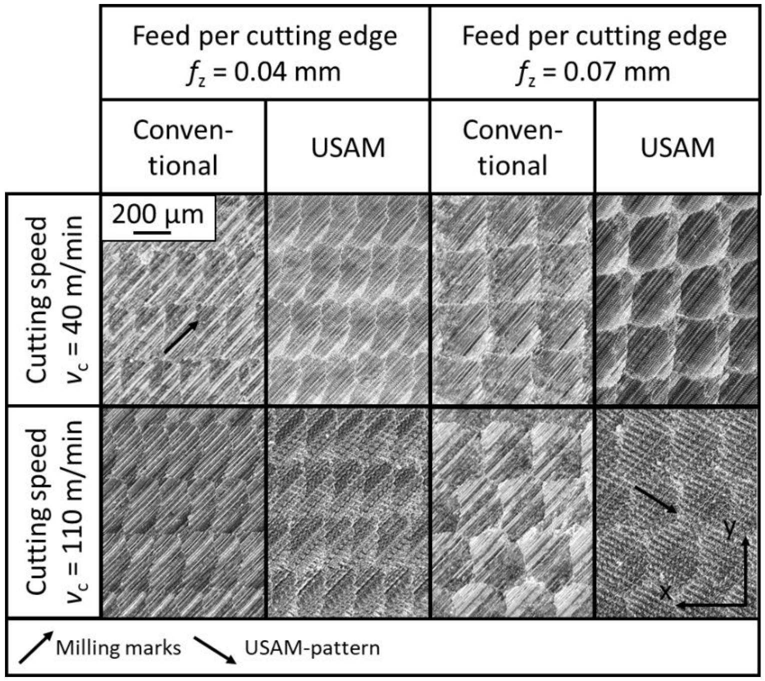

Figure 109: LOM of milled surfaces with different milling parameters of CoCrNi-MEA; cutting speed v_c = 40–110 m/min; feed per cutting edge f_z = 0.04–0.07 mm; conventional and ultrasonic assisted milling (USAM)

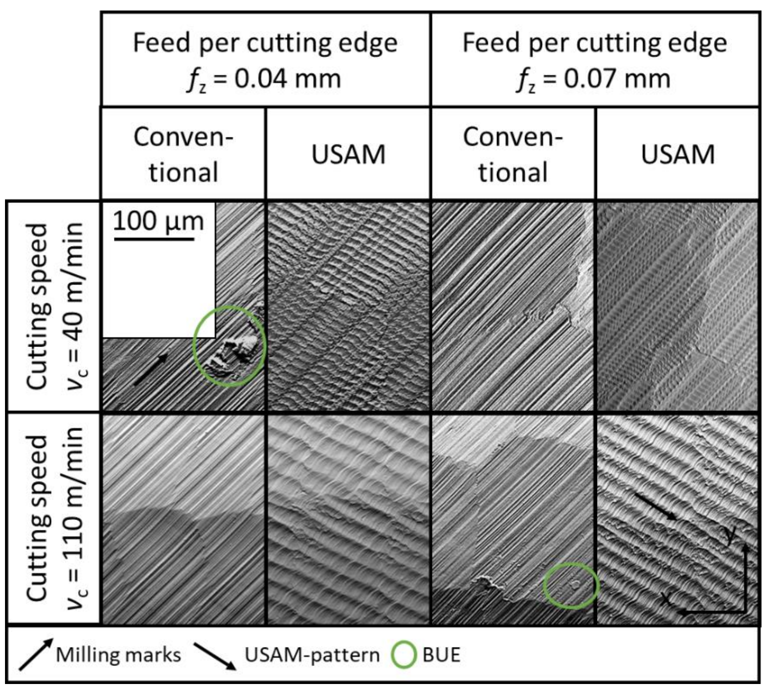

Figure 110: SEM investigations of milled surfaces with different milling parameters of CoCrNi-MEA; cutting speed v_c = 40–110 m/min; feed per cutting edge f_z = 0.04–0.07 mm; conventional and ultrasonic-assisted milling (USAM)

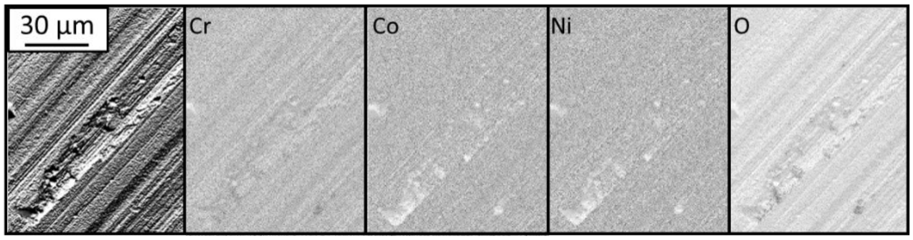

Figure 111: EDX measurement of a tear defect on milled CoCrNi-MEA surface

In the following, the surface topography of the finish-milled HEA and MEA surfaces is quantitatively described using tactile roughness measurements. The influence of the varied parameters f_z and v_c will be discussed before the characterization of the USAM effect.

A quantitative description of the milled surface topography of the CoCrFeMnNi-HEA is shown in Figure 112. Contour plots of the arithmetical mean roughness R_a of the roughness profile in the x-direction (Figure 112a) and y-direction (Figure 112b) and the mean roughness depth R_z in the x-direction (Figure 112c) and y-direction (Figure 112d) are given for different sets of milling parameters f_z and v_c. These Figures show a proportional relationship between the resulting roughness parameters R_a and R_z.

As expected, the feed per cutting edge f_z has a significant effect on the roughness values in the x-direction (Figure 112a and c), i.e. the roughness decreases continuously with decreasing f_z. In the y-direction, f_z has no significant effect on roughness (Figure 112b and d). It can be concluded that lower f_z values on average lead to lower roughness, but since the chip thickness cannot become infinitely small, a too small f_z would lead to an unstable process. This result correlates with the cutting force results (see Section 10.1.1). Lower f_z values result in lower roughness and tool load, which reduces productivity (material removal per time). Compared to the theoretical roughness R_{zth} calculated according to Equation 12, the measured R_{zy} values (4-5 µm) in the y-direction are slightly larger (R_{zth} = 3.75 µm for a_e = 0.3 mm). In the x-direction, the measured R_{zx} values (2.2-4.6 µm) are significantly higher than the calculated R_{zth} value (0.07 µm for f_z = 0.04 mm and 0.20 µm for f_z = 0.07 mm). The reason for the significant deviations is the large difference in the parameters f_z and a_e, which causes the roughness to influence each other in different directions. This means the roughness in x cannot be much smaller than the roughness in y. In addition, Nespor et al. [212] showed that the deviation of the theoretical roughness from the actual roughness depends on the spindle retraction since it can lead to an angular offset between two cutting paths.

The cutting speed v_c reveals almost no effect on surface roughness R_{zx}, as shown in Figure 112a and c. Small variations in roughness are observed in both directions, with slightly higher values at higher cutting speeds. This could be due to different occurring vibrations (frequency and amplitude) of the tool and the specimens at different cutting speeds [286] or the mentioned offset between the cutting paths [212]. However, further experiments, e.g., in a larger parameter range, would be necessary for a final clarification of this small effect.

The minimum average roughness for both directions is observed at v_c = 50–70 m/min, which does not correspond to the minimum of cutting forces, cf. section 10. Since higher cutting speeds v_c lead to lower forces and higher productivity, a compromise between tool load, productivity, and surface finish has to be found in industrial practice.

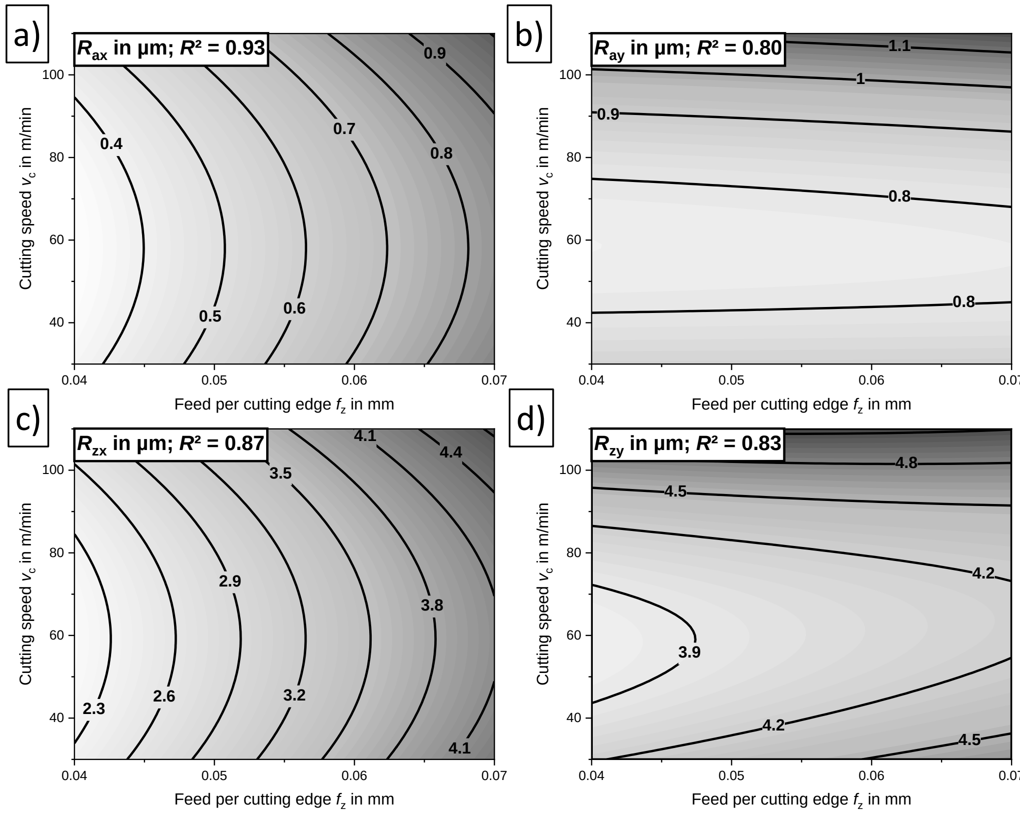

Regression models

a)	R_{ax}=-0.160+17.25*f_z-7.4*10^{-3}*v_c+6.41*10^{-5}*v_c^2
b)	R_{ay}=1.206-0.015*v_c+1.256*10^{-4}*v_c^2+1.464*10^{-3}*f_z^2*v_c^2
c)	R_{zx}=0.466+64.667*f_z-0.31*v_c+2.625*10^{-4}*v_c^2
d)	R_{zy}=4.737+17.7*f_z-0.057*v_c+5.122*10^{-4}*v_c^2-0.0138*f_z^2*v_c^2

Figure 112: Linear regression of surface roughness by milling parameters cutting speed v_c and feed per cutting edge f_z for CoCrFeMnNi-HEA: (a) arithmetical average roughness R_a in x-direction; (b) arithmetical average roughness R_a in y-direction; (c) meaning roughness depth R_z in x-direction; (d) meaning roughness depth R_z in y-direction (parts c and d are published in [207])

For the machined MEA surfaces the linear regression models of the roughness parameters R_a and R_z are shown in Figure 113 in x- (a and c) and y- (b and d) direction as a function of f_z and v_c. As for the HEA, a proportional relationship of the characteristic values R_a (Figure 113a and b) and R_z (Figure 113c and d) is shown. In the x-direction, R_a (Figure 113a) and R_z (Figure 113c) increase with increasing f_z, analogous to the HEA, which is the result of the correlation of the cutting engagement parameters, the primary tool geometry, and the resulting surface morphology. Therefore, f_z (feed in x-direction) has only a minor influence in the y-direction (Figure 113b and d). The influence of v_c is negligible in the x-direction (Figure 113a and c) and the y-direction (Figure 113b and d), as found for HEA. The comparison of the measured R_z values with the theoretical R_{zth} (Equation 12) is according to the machined HEA surfaces. The values are almost similar in the y direction (R_{zy} = 3.3–4.6 µm, R_{zth} = 3.75 µm for a_e = 0.3 mm) and in the x-direction (R_{zx} = 2.3–4.3 µm and R_{zth} = 0.07 – 0.20 µm for f_z = 0.04–0.07 mm) due to the large difference in f_z and a_e

which influence the roughness in both directions but are not considered interacting in the calculation. The lowest roughness derived from the models is shown at low cutting speed v_c = 40 m/min and in the x-direction at low feed per cutting edge f_z of 0.04 mm. In the y-direction, the values are lowest in the range between f_z 0.05 and 0.06 mm. Low f_z and v_c lead to longer manufacturing time and thus reduced productivity.

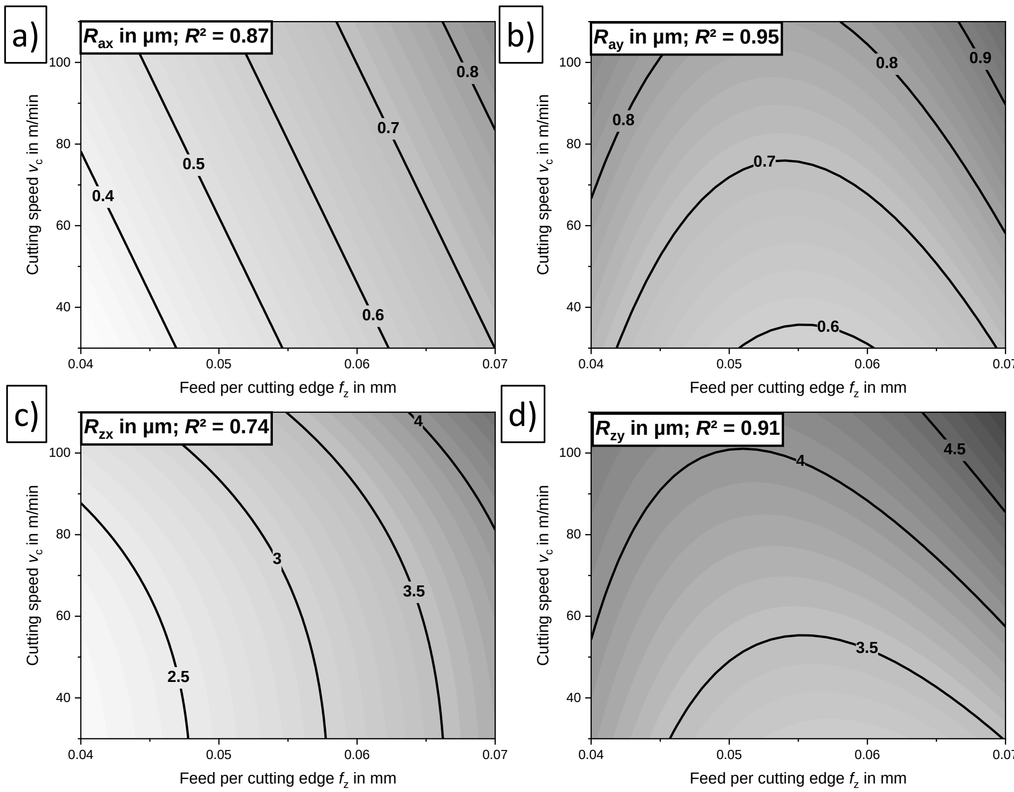

Regression models

a)	R_{ax}=-0.266+13.008*f_z-1.866*10^{-3}*v_c
b)	R_{ay}=2.454-68.61*f_z+6.25*10-6*v_c+605*f_z^2+0.04437*f_z*v_c
c)	R_{zx}=1.4+475.9*f_z^2+5.012*10^{-7}*v_c^3
d)	R_{zy}=10.684-260.638*f_z-0.0108*v_c+2150*f_z^2+0.410*f_z*v_c

Figure 113: Linear regression of surface roughness by milling parameters cutting speed v_c and feed per cutting edge f_z for CoCrNi-MEA: (a) arithmetical average roughness R_a in x-direction; (b) arithmetical average roughness R_a in y-direction; (c) meaning roughness depth R_z in x-direction; (d) meaning roughness depth R_z in y-direction

When comparing the roughness values of surfaces of both MPEA, the minimum values in the x-direction R_a~0.4 µm and R_z ~2.3 µm and in the y-direction (R_a~ 0.6 µm; R_z ~ 2.3 µm) are in accordance. The maximum values of HEA (in x R_a~ 1.0 µm; R_z ~ 4.7 µm and in y R_a~ 1.2 µm; R_z ~ 5.1 µm) are slightly higher than those of MEA (in x R_a~ 0.8 µm; R_z ~ 4.4 µm and in y R_a~ 0.9 µm; R_z ~ 4.7 µm), with the higher proportion of the surface defects on HEA surfaces, described previously.

In Figure 114 (HEA) and Figure 115 (MEA), effect diagrams are given for the influence of v_c (a and b) and f_z (c and d) in x- (a and c) and y- (b and d) direction on the arithmetical average roughness R_a. The influence of USAM compared to the conventional process will be described. For all cases investigated, the ultrasonic assistance has no significant influence on the roughness R_a, since for all cases of HEA (Figure 114) and MEA (Figure 115) the values are within the scatter bands. Increased roughness could be expected from the US patterns (Figure 107 and Figure 110). The reduced defect density due to USAM and the low waviness amplitude of the US patterns result in similar roughness. It can be concluded that ultrasonic assistance has no significant influence on the surface roughness and therefore does not have to be considered to comply with application-related roughness values.

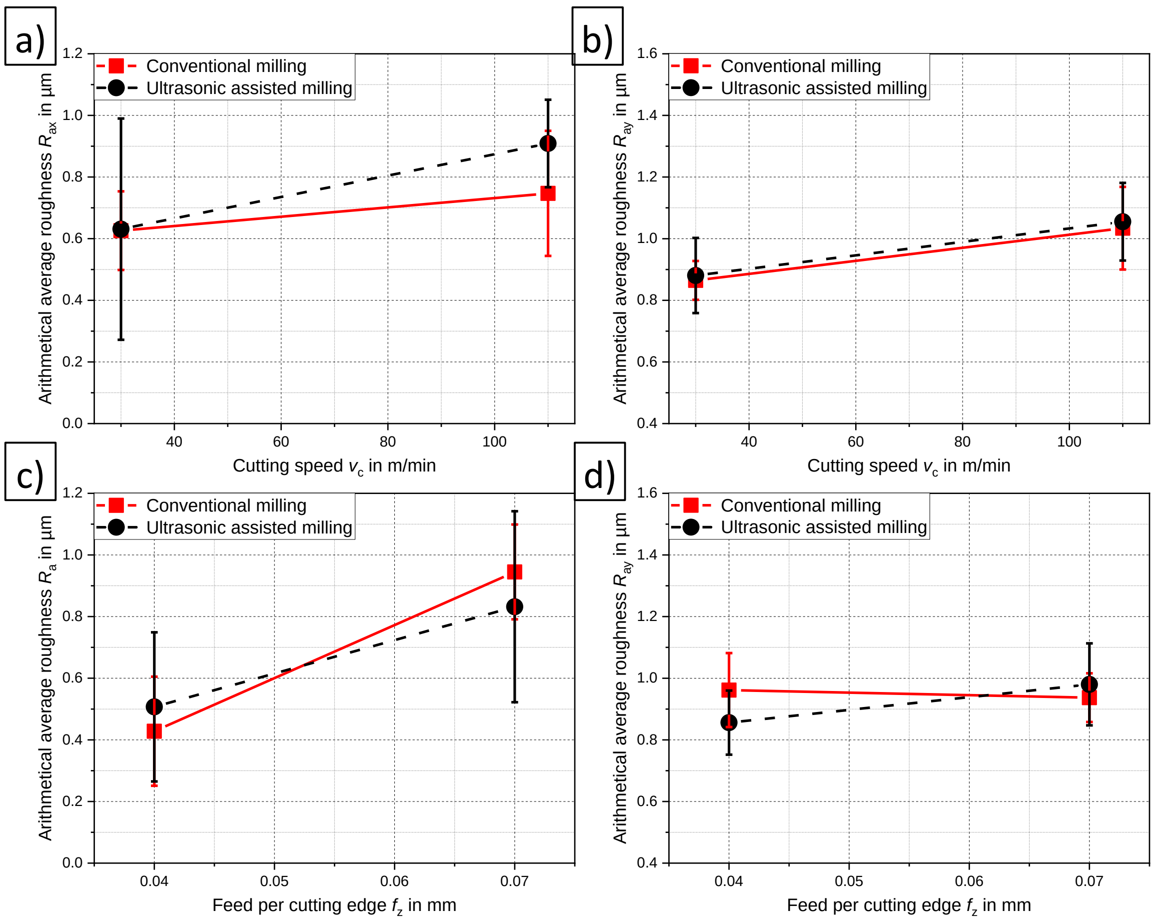

Figure 114: Influence of cutting speed v_c (a, b) and feed per cutting edge f_z (c, d) on the arithmetical average roughness R_a on the milled CoCrFeMnNi-HEA surface in x- (a, c) and y- direction (b, d)

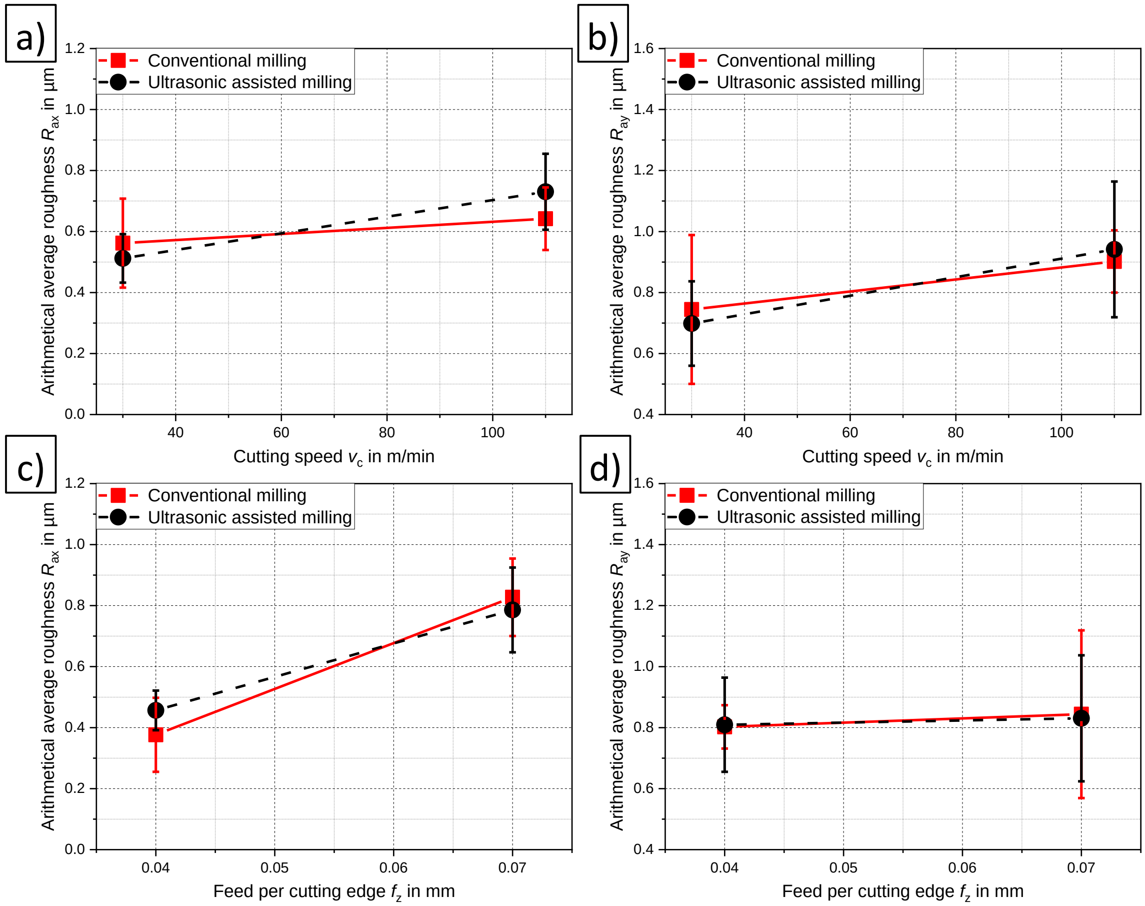

Figure 115: Influence of cutting speed v_c (a, b) and feed per cutting edge f_z (c, d) on the arithmetical average roughness R_a on the milled CoCrNi-MEA surface in x- (a, c) and y- direction (b, d)

10.2.2 Mechanical influence on surfaces

The mechanical influence of milling is mainly related to the development of residual stresses at and below the surface as described in Section 2.3.1. The maximum principal residual stresses at the milled surface were characterized by XRD, see Figure 116 for the CoCrFeMnNi-HEA. Independent of the milling parameters f_z (Figure 116a) and v_c (Figure 116b) and whether ultrasonic assistance was applied, the maximum principal residual stresses are tensile stresses ranging from 300 to 350 MPa. The tensile residual stresses were caused by plastic deformation and a local temperature gradient during machining [163]. Since the residual stresses after plastic deformation are in the range of the YS of the material ($R_{p0.2}$ = 240 MPa for HT-HEA), there are no significant differences at the surface. The highest tensile residual stresses occur at the highest cutting speed. The reason for this could be higher temperatures during machining due to high friction and heat input, which result in plasticization and a temperature gradient (surface to BM) [155]. The high temperature gradient can be caused by the low thermal conductivity of the HEA. Since tensile residual stresses are likely to be of thermal origin, machining with coolant could further reduce them or even lead to mechanically induced compressive residual stresses, as has been observed in NiCr alloys [154]. Tensile residual stresses are detrimental because they reduce resistance to crack initiation and propagation [160] and thus surface integrity.

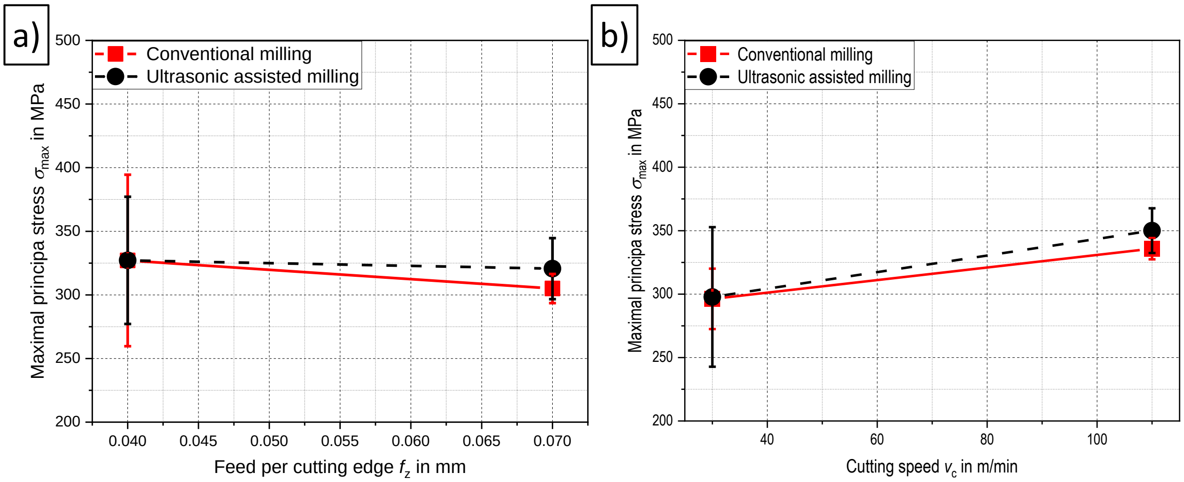

Figure 116: Influence of milling parameters on the maximum principal residual stresses σ_{max} on the milled CoCrFeMnNi-HEA surface: (a) feed per cutting edge f_z and (b) cutting speed v_c (published in [207])

The residual stresses profile in depth (z-) direction is shown in Figure 117a and the residual stresses in x- and y-directions in Figure 117b, for the center point tests with (Test No. 11) and without (Test No. 6) ultrasonic support. Figure 117 shows that the tensile residual stresses at the surface caused by machining decrease with increasing distance (i.e. depth) from the surface *z.* As the thermal and mechanical load is reduced in depth, the plasticization decreases. The surface tensile stresses have to be balanced by compressive stresses in the depth direction, resulting in a typical residual stress profile for machined surfaces of NiCr alloys [154]. Without USAM, the principal tensile residual stresses decrease from 310 to 150 MPa in the first 10 µm below the surface and remain approx. constant above 100 MPa. In contrast, with USAM, tensile residual stresses decrease stronger from approx. 300 to approx. 0 MPa between 0 and 15 µm below the surface. Then residual stresses decrease linearly and turn into compressive residual stresses at approx. 25 µm depth. Figure b shows that USAM has no significant effect on residual stresses in the y-direction compared to conventional milling. In the x-direction, however, USAM shows consistently lower residual stresses, so it can be assumed that USAM primarily affects residual stresses in the x-direction.

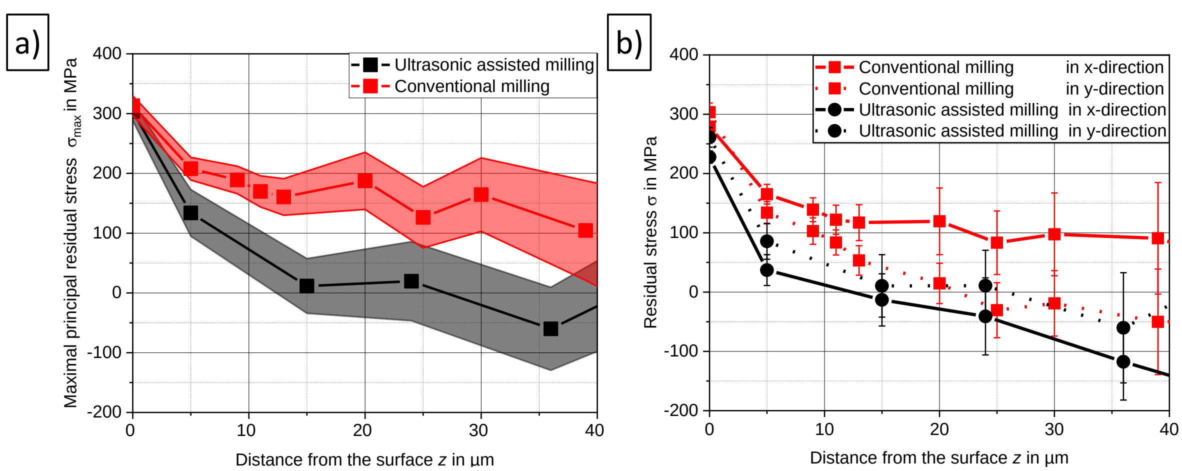

Figure 117: Comparison of subsurface residual stress condition for conventional and ultrasonic assisted milling with the central point test parameters (Test No. 6 and 11; f_z = 0.055 mm; v_c = 70 m/min) with the CoCrFeMnNi-HEA; (a) maximal principal residual stresses σ_{max} and (b) residual stresses σ in x- and y-direction (a published in [287] and b published in[207])

USAM significantly improves the tensile residual stresses condition below the surface, which has also been reported for NiCr alloys [154]. The reasons given in the literature for this behavior are a reduced tool-workpiece contact ratio with altered fracture dynamics [281]. In addition, USAM generates lower temperatures in machining MPEAs [187], resulting in a lower temperature gradient and consequently reduced tensile stresses.

For the CoCrNi-MEA the maximum principal residual stresses on the milled surface are shown as effect diagrams as a function of f_z and v_c in Figure 118. The maximum principal residual stresses are tensile in the range of 250 to 450 MPa and thus in the range of the YS of the MEA ($R_{p0.2}$ = 254 MPa).

The feed per cutting edge f_z in Figure 118 does not show a significant influence on the principal residual stresses due to the large scatter of the results. Nevertheless, a trend can be derived, with the tensile principal residual stresses increasing with higher f_z, i.e., a reduced f_z improves the surface residual stress condition. Cutting speed v_c shown in Figure 118b, indicates a reducing influence on tensile residual stresses with decreasing v_c. Where at reduced v_c of 40 m/min, residual stresses are decreased with USAM vs. conventional process. Even if this is not a significant influence, it shows a trend in favor of using USAM at low v_c, similar to results for Ni-base [288]. For all other f_z and v_c conditions in Figure 118, no effect of ultrasonic assistance on residual stresses is apparent.

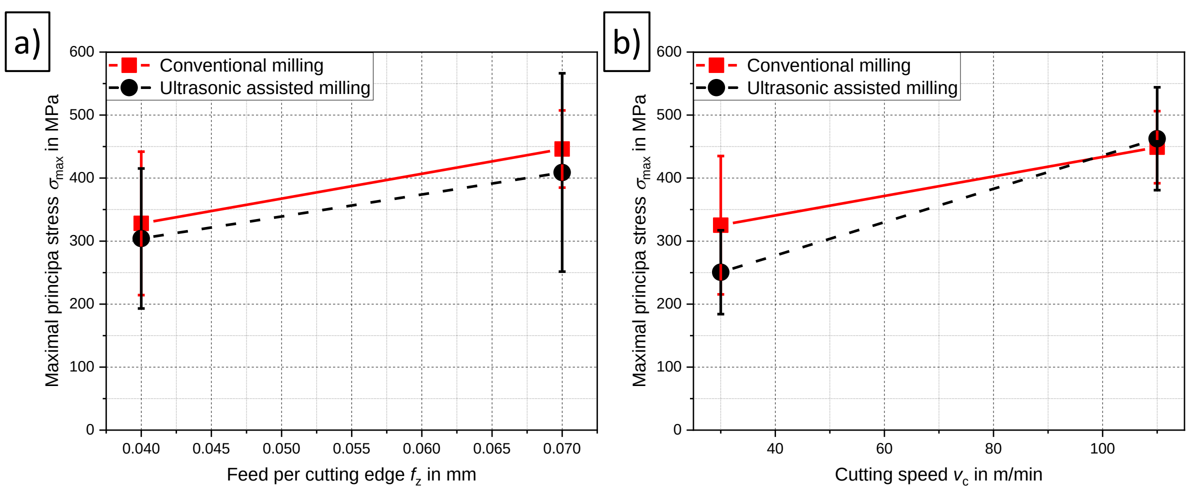

Figure 118: Influence of milling parameters on the maximal principal residual stresses σ_{max} on the milled CoCrNi-EA surface: (a) feed per cutting edge f_z and (b) cutting speed v_c

The residual stresses in-depth profiles are shown in Figure 119a and the residual stresses in the x- and y-directions in Figure 119b for the central point tests with (Test No. 11) and without (Test No. 6) ultrasonic assistance. Similar to HEA, the tensile residual stresses at the surface caused by machining decrease with increasing depth. However, unlike HEA, it shows a plateau in tensile residual stresses in the first 10 µm. The maximum can be seen especially in the x- and y-direction in Figure 119b regardless of the process. Below 10 µm depth the residual stresses decrease. In the first approx. 10 µm, the principal tensile residual stresses are lower by up to 150 MPa for the USAM (Figure 119a). After the 10 µm, the main residual stresses decrease. The influence of the ultrasonic support on the maximum principal residual stresses with the MEA is limited to the first 10 µm.

With USAM, residual stresses in the x- and y-directions are nearly identical, diverging slightly only after the initial 10 µm. In contrast, the conventional process exhibits consistently higher residual stresses in the y direction, ranging from 50 MPa to 150 MPa compared to those in the x-direction. This highlights a distinct directional dependency of tensile residual stresses in the subsurface region of the MEA processed conventionally.

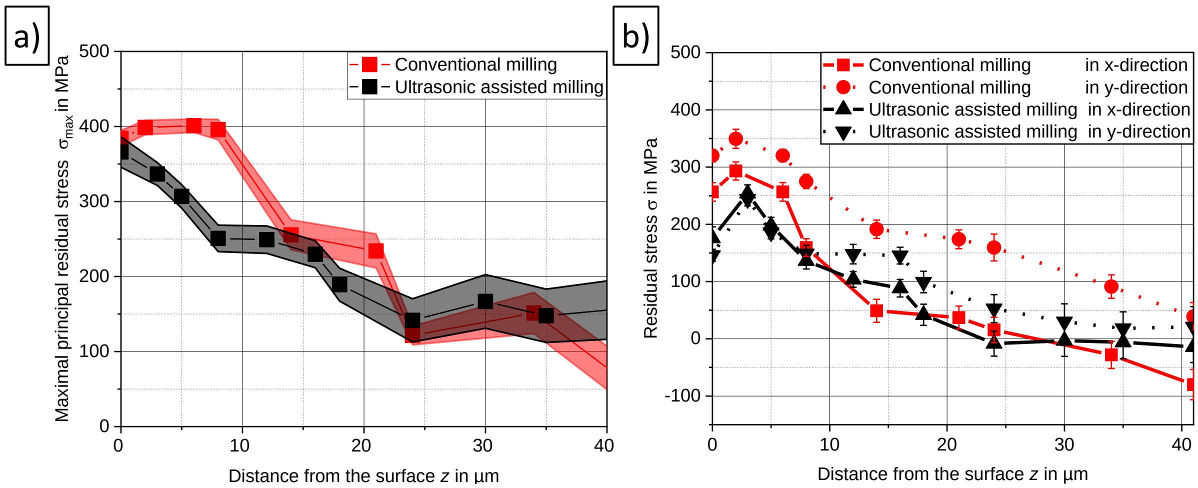

Figure 119: Comparison of subsurface residual stress condition for conventional and ultrasonic assisted milling with the central point test parameters (Test No. 6 and 11; f_z = 0.055 mm; v_c = 70 m/min) with the CoCrNi-MEA: (a) maximum principal residual stresses σ_{max} and (b) residual stresses σ in x- and y-direction

These results are of paramount importance for component design as they provide general guidelines for matching the machining direction with the resulting directional residual stresses to an applied load spectrum to ensure the integrity of the component during its operation. This should be considered when designing components and adapted to the expected load spectrum to optimize the surface integrity.

10.2.3 Metallurgical influence in the subsurface region

To characterize the microstructural degradation in the subsurface regions of the milled specimens of CoCrFeMnNi-HEA, crystallographic orientation maps obtained by EBSD on metallographic cross-sections perpendicular to the y-direction are shown in Figure 120. The colors in these images show the crystallographic orientations that are parallel to the x-direction (see Figure 120d for color decoding). No Kikuchi patterns (which means no usable EBSD signal) could be detected on the milled surface (black areas), which can be attributed to severe plastic deformation leading to the formation of a nanocrystalline or even amorphous microstructure [28]. Similar features are also referred to as "white layers" or "featureless structures" in the literature [165, 289, 290]. The milling process should be optimized to minimize or even avoid these features, which are detrimental to the surface integrity and durability of the finished surfaces. Directly under this 1 µm thin and " featureless" layer, Kikuchi patterns could be indexed, and orientation maps showed a 2 to 5 µm thick layer with submicron grains and local texture changes, depending on the milling conditions. Underneath, shear bands were observed extending from 9 to 15 µm. The extent of the shear bands was found to be affected by ultrasonic assistance. USAM reduces the deformation-affected zone by approx. 35 % compared to conventional milling (see Figure 120b, d for conventional milling with shear bands extending 15 µm and Figure 120a, c for USAM with shear bands extending 9 µm). Simulations of ultrasonic-assisted cutting [291] suggest that this reduction may be attributed to decreased hydrostatic and shear stresses in the subsurface region and increased stresses in the chip. It is also found that the extent of the shear bands scales with the milling parameters f_z and v_c, i.e., their extent increases with higher f_z and lower v_c, compare Figure 120c,d with Figure 120a,b, indicating higher cutting forces. Liu et al. [292] attributed the same subsurface effect to increased f_z and decreased v_c values due to increased frictional forces in Ti-6Al-4V alloy. The smallest deformation-affected zone is shown in Figure 120c, where USAM was used in combination with optimized milling parameters. The lowest microstructural degradation occurs at low f_z and high v_c values using USAM (test no. 10) which agrees well with the results presented in Section 10.1 for the cutting forces (lowest F_r in test no. 10).

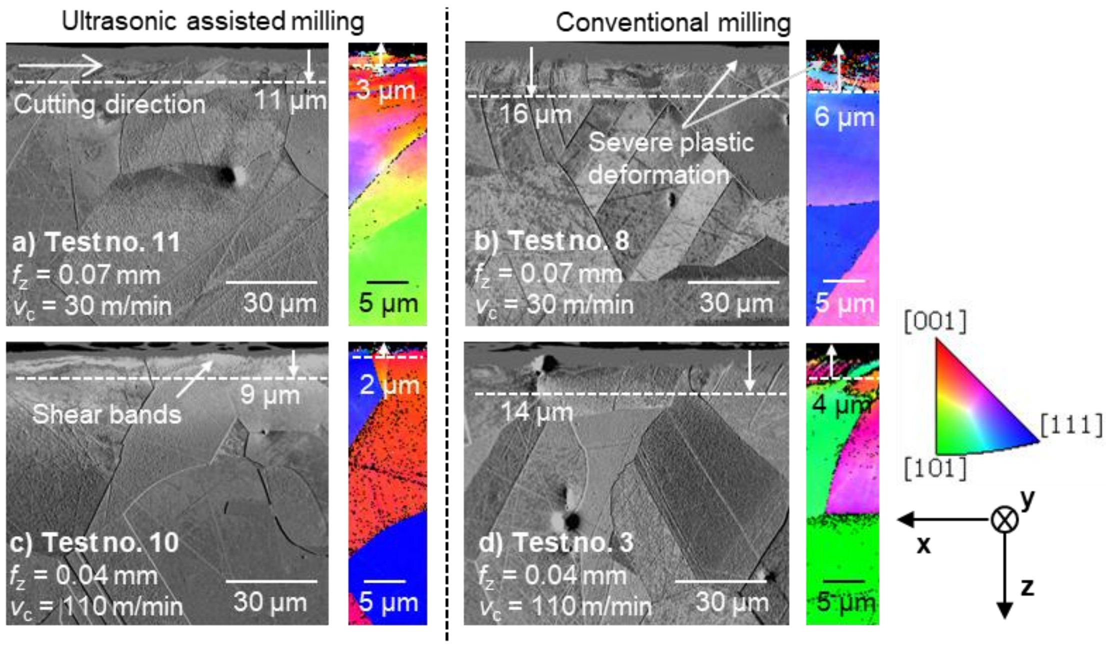

Figure 120: SEM and EBSD images of cross-sections of the CoCrFeMnNi alloy after machining and showing the microstructure below the milled surface. Effect of ultrasonic assistance on microstructures. Compare (a) test no. 11 with ultrasonic assistance and (b) no. 8 without ultrasonic assistance for v_c = 30 m/min and f_z = 0.07 mm, and (c) test no. 10 with ultrasonic assistance and (d) no. 3 without ultrasonic assistance for v_c = 110 m/min and f_z = 0.04 mm (published in [207])

11. Summary and outlook

In the following section, the results presented and discussed in Section 5 are summarized once again and the main statements are highlighted. Starting with the results for **TIG-welding of CoCrFeMnNi-HEA and CoCrNi-MEA**:

- Surface preparation significantly impacts welding test outcomes, as discussed in Section 5.1. Cracks in the HAZ occur during TIG welding of HEA and MEA with eroded surfaces but can be prevented by surface grinding prior to welding. TIG bead-on-plate welds for MPEA could be achieved without imperfections. Hence, TIG welding confirms the process-related weldability of the investigated HEA and MEA.

- Microstructure analysis in Section 5.2 reveals an epitaxially oriented dendritic microstructure in the WM of the respective MPEA. In HEA, dendritic regions are enriched in Co, Cr, and Fe, while interdendritic areas are rich in Mn and Ni. In MEA, dendrites are rich in Ni and Co, with interdendritic regions rich in Cr. Both MPEAs exhibit similar HAZ formation, primarily influenced by the initial material conditions. Although no notable effect on grain size and shape is evident in the HT HEA and MEA, the CR MPEAs show grain growth in the HAZ, with decreasing grain size from the FL towards the BM. For HEA, the formation of a FQZ in the HAZ is reported for the first time.

- For the first time, welding residual stresses were determined for TIG-welded HEA and MEA. Findings reveal that residual stresses in the WM cannot be completely assessed via XRD due to large and directional grains. Moreover, both types of MPEAs, under varying initial conditions, exhibit tensile residual stresses extending up to the YS.

- Mechanical-technological properties of MPEA TIG welds were studied to assess material-related weldability. Microhardness mappings revealed slight hardening in the WM for welds with HT-BM. Conversely, welds from initial CR conditions displayed softening in the HAZ, resulting in a hardness gradient due to varying grain sizes. Hardness increased from approximately 200 HV0.1 at the FL to around 600 to 650 HV0.1. Tensile tests showed HEA and MEA welds reaching strengths (YS and UTS) comparable to the HT BM, yet all welds failed in the WM, indicating it as a weak point. Moreover, welds exhibited reduced fracture strain compared to the HT BM, but still in the ductile range (HT-BM: $\varepsilon > 30$ % and CR-BM: $\varepsilon > 10$ %). Fracture surface analysis revealed ductile morphology with prominent dimple formation in all TIG-welded MPEAs. However, since the mechanical strength of the HT-BM is achieved with sufficient fracture strain (ductility), the results indicate that the MPEAs have good material-related weldability.

- For the first time, the local strain states of MPEA TIG welds were described in the tensile test by means of DIC. The local strains of the welds consistently showed a maximum local strain in the WM. Local strains of over 100 % for the HEA and over 90 % for the MEA were measured. In addition, no local strain was measured in the BM of the CR-BMs until failure. This shows that in the TIG-WMs, large local deformability and thus elongation reserves are present.

In summary, both CoCrFeMnNi HEA and CoCrNi MEA can be qualified as having good weldability using TIG. This is expressed by the welds without weld imperfections and mechanical properties (hardness, YS, and UTS) in the range of the HT BM.

This work shows for the first-time comprehensive investigations regarding the **TIG-DMW weldability of CoCrFeMnNi-HEA with austenitic stainless steel AISI 304** which can be summarized as follows:

- The TIG-DMWs show no weld imperfections in both the radiographic test and the cross-section. Only the DMW with HT-HEA exhibits a small offset of the plates to each other. Hence, TIG welding confirms the process-related weldability of the investigated TIG-DMW with HEA and austenitic steel.

- Microstructural analysis reveals a shoulder on the steel side in both TIG-DMWs, with dendritic structures observed in the WM. Near the FL on the HEA side, a black seam is evident in both welds HAZ. SEM examinations of the HEA-HAZ reveal partially melted zones and pronounced pitting, attributed to etching during sample preparation. HAZ formations resemble those of pure HEA welds and are contingent upon the initial condition. EBSD investigations also indicate an FQZ in the HEA-HAZ. SEM and EDX examinations depict a dendritic WM with Fe enrichment in dendrites and Ni and Mn enrichment in interdendritic areas. Additionally, unmolten steel particles are present in the WM, while EDX line scans reveal significant chemical composition heterogeneity within the WM.

- For the first time, welding residual stresses were determined for TIG-DMW of HEA and austenitic steels. Residual stresses in the WM remain incompletely measurable via XRD due to large directional grains. The most significant tensile residual stresses are observed in the WM and the HAZ, particularly notable for CR-HEA, where values of up to 400 MPa have been measured in both longitudinal and transverse directions, resulting in local reduced stress reserves.

- The hardness mappings show a slight hardening (up to 300 HV0.1) of the WM compared to the HT-HEA. In contrast, the WM with the CR-HEA is softer with approximately 150 HV0.1. The HAZ of the HT-HEA shows no influence on the hardness. With the CR-HEA, the HEA shows a softening in the HAZ with a hardness gradient between the WM and the BM. The steel shows a slight softening just in the shoulder area. The tensile tests show strengths for both TIG-DMWs in the range of the HT-HEA. Nevertheless, all tensile specimens failed in the WM, so this should be considered a weak point. Both welds also show a significant reduction in fracture strain compared to the BMs of the HT-HEA and steel. In TIG-DMW with CR-HEA, the HEA shows no elongation and the steel (ε_{loc}~13 %) shows very little local elongation. The highest local strain of approximately 90 % is measured in the WM near the FL of the HEA side. The morphology of the fracture surfaces of both TIG-DMWs shows a ductile failure due to a clear dimple formation.

- To evaluate the material-related weldability, mechanical-technological properties of TIG-DMWs were investigated. Hardness mappings reveal slight WM hardening (up to 300 HV0.1) compared to HT-HEA-BM, while WM with CR-HEA is softer, approx. 150 HV0.1. The HT-HEA HAZ exhibits no hardness influence, whereas CR-HEA shows HAZ softening with a hardness gradient between WM and BM. Steel experiences slight softening in the shoulder area. Tensile tests demonstrate strengths (YS and UTS) within the HT-HEA range for both TIG-DMWs; however, all specimens fail in WM, indicating its weakness. Both welds exhibit fracture strain > 10 % indicating elongation reserves after welding. Fracture surface morphology displays ductile failure characterized by clear dimple formation in both TIG-DMWs. These findings suggest excellent material-related weldability, further extending to potential component applications. Consequently, TIG-DMW with HEA and austenitic steel can be certified for proficient constructive weldability, particularly in butt joint configurations.

- For the first time, DIC investigations on TIG-DMW with HEA and austenitic steel are presented in this work. The HT-HEA material has more local elongation compared to the austenitic steel. The largest local strain of up to 70 % is present in the WM near the FL of the HEA side. CR-HEA TIG-DMWs show no HEA elongation and minimal local steel elongation (ε_{loc} = approx. 13 %). The highest local strain (approx. 90 %) is measured in WM near the FL on the HEA side.

In summary, TIG-DMWs of CoCrFeMnNi-HEA with the austenitic stainless steel AISI 304 can be certified as having good weldability based on the present results. This is due to the welds without weld defects and UTS in the range of the HT-HEA-BM.

The comprehensive results of the **CoCrFeMnNi-HEA and CoCrNi-MEA FSW butt joints** are presented in detail in Section 7. They can be summarized as follows:

- HT-MPEAs exhibit uniform weld surfaces, with radiation test imaging confirming defect-free weld joints, except for the expected run-in area of the FSW. This reaffirms excellent process-related weldability for HT-MPEAs. Conversely, the FSW of CR-HEA displays notable chip formation and surface inhomogeneity. Moreover, both CR-MPEA FSWs demonstrate insufficient weld penetration at the weld center. Consequently, based on current findings, CR-MPEAs cannot be certified for satisfactory process-related weldability.

- Microstructural analysis of all four FSWs reveals a process-related segmentation into SZ, TMAZ, and BM. SEM and EDX examinations highlight a fine-grained microstructure in the SZ attributed to dynamic recrystallization. Moreover, the weld nugget features regions enriched in W, commonly known as the "white band," containing wear particles from the tool, predominantly lamellar in structure. The TMAZ also exhibits a gradient in grain size.

- This work investigated the residual stress state of MPEA-FSW for the first time. XRD analysis shows the highest tensile residual stresses are present in the WM on the AS. These are tensile residual stresses in the range of the BMs YS (approx. 200 MPa) in longitudinal and transversal directions. Therefore, this area has hardly any further stress reserves before plastic deformation and can be considered a weak point under mechanical load.

- Mechanical-technological properties of FSW butt joints were analyzed to assess material-related weldability. Microhardness mappings indicate hardening in the white band region across all welds. FSW joints with HT-BM exhibit slight hardening in the SZ and TMAZ due to grain refinement. Conversely, CR conditions reveal an additional HAZ, particularly pronounced on the AS. Tensile tests of HT-HEA FSW (failure in the BM) exhibit strengths (YS and UTS) comparable to HT-BM, with minimal reduced fracture strain, suggesting no weakness in the WM. However, CR-HEA displays incomplete weld penetration, resulting in lower

YS and UTS, and minimal fracture strain (~3%). MEA FSW tensile results show slightly reduced UTS and significantly reduced fracture strain, indicating WM weakness. Fracture morphology of MEA FSW reveals a tripartite division, with upper regions displaying mixed brittle-ductile fracture and lower areas showing ductile failure with variable dimple sizes. Material-related weldability varies based on BM condition; HT-MPEAs demonstrate good material-related weldability. CR-MPEAs exhibit poor mechanical-technological properties resulting in poor material-related weldability. Notably, the potential exists for CR joints with optimization of process parameters, although results are based on preliminary tests.

- This study presents preliminary examinations into local strain ratios during tensile testing of MPEA-FSW butt joints. DIC analysis reveals maximum local strains (approx. 100%) on the AS of the HT-HEA BM. In the case of MEA FSW, non-uniform strain distribution in the WM suggests bulging due to heterogeneous microstructure, inducing a multiaxial stress condition leading to WM failure.

The findings underscore the dependency of FSW weldability on the condition of the MPEA-BM. HT-MPEAs exhibit excellent weldability, devoid of imperfections, and boast strong mechanical-technological properties. Conversely, CR-MEA demonstrates conditional weldability; while imperfections are present, satisfactory strengths are attained. CR-HEA is certified by poor weldability, due to weld imperfections leading to miserable mechanical properties. Moreover, there exists significant potential for process optimization with these materials.

The comprehensive results of **FSW-DMW for the CoCrFeMnNi-HEA and austenitic stainless steel AISI 304** are presented in detail in Section 8. They can be summarized as follows:

- Radiographic inspection and cross-sectional analysis by LOM reveal a lack of weld penetration in both DMWs. Moreover, the DMW involving HT-HEA exhibits incomplete weld overlap and a tunnel defect. The placement of the higher melting point weld partner (steel) on the RS in the HT-HEA DMW hinders sufficient temperature input, leading to inadequate plasticization and the formation of tunnel and surface defects. Consequently, due to these welding imperfections, certification of HEA steel FSW-DMW is only possible as having poor process-related weldability.

- Microstructural characterization reveals grain refinement and a lamellar structure in the SZ of both DMWs. Additionally, chemical mixing of the BMs is observed in the weld nugget, alongside the presence of tungsten W abrasion particles from the tool and a "white band".

- This work presents initial investigations into the residual stress state of FSW-DMW comprising HEA and austenitic steel. Both DMWs exhibit the highest tensile stresses in the WM. However, while the DMW with CR-HEA reaches approx. 100 MPa in both directions, the DMW with HT-HEA demonstrates significantly higher tensile residual stresses, exceeding 300 MPa in the longitudinal direction.

- The mechanical properties of the FSW-DMW were determined to conclude on the corresponding material- and constructive-related weldability. On the CR-HEA side, reduced hardness in the HAZ and TMAZ was evident due to tempering processes compared to the BM. Conversely, for the DMW with HT-HEA, no discernible HAZ was identified, but a TMAZ was observed. No HAZ was detected on the steel side based on hardness measurements.

Additionally, both DMWs exhibited hardening in the white band region within the SZ. Both joints displayed YS slightly above and UTS slightly below that of HT-HEA, with low fracture strain. Insufficient weld penetration resulted in premature partial fracture during tensile testing, indicated by specimen bulging ("shear effect") and mixed fracture patterns. The failure occurred within the weld region in both joints. The results show a conditional material-related weldability.

- This study marks the initial inquiry into local strain states during tensile testing of FSW-DMW consisting of HEA and steel. DIC analysis reveals approx. 40 % local strain at the weld center prior to failure for both DMWs. While the DMW with HT-HEA exhibits strains of up to 12 % in the HEA-BM before failure, no measured strain is observed until failure for the CR-HEA DMW.

The findings from FSW-DMWs involving CoCrFeMnNi-HEA and austenitic stainless steel AISI 304 indicate conditional weldability at best. Existing weld imperfections notably degrade mechanical properties in tensile tests. Incorporating steel on the AS resulted in a substantial reduction in weld imperfections, suggesting that further process optimization could yield welds without such imperfections.

In conclusion, the following initial process instructions can be derived for welding MPEA and HEA steel DMWs using TIG or FSW:

- MPEAs are recommended to be welded in the HT condition, as superior mechanical-technological properties (YS, UTS, fracture strain) are consistently achieved compared to the CR condition, irrespective of the welding process (TIG or FSW).
- MPEAs in the CR condition are advised to undergo TIG welding to mitigate weld seam imperfections.
- DMWs involving HEA and austenitic steels are best suited for TIG welding, exhibiting significantly fewer weld imperfections and enhanced mechanical properties compared to FSW.
- Implementation of distortion-reducing techniques is recommended for TIG welding of HEA-austenitic steel DMWs.
- With FSW-DMW made of HEA and steel, the steel should be on the AS.

Outlook

Lastly, a forward-looking perspective will be provided on essential areas for further investigation to enhance the understanding of the weldability of HEAs and HEA-DMWs. These will be categorized into the distinct factors of weldability as outlined in Figure 5:

- Further investigations are warranted to explore the impact of welding parameters on HEA and HEA-DMWs to assess process-related weldability. Priority in FSW should be given to strategies aimed at minimizing welding imperfections.
- Further exploration into the impact of varying sheet thicknesses and weld seam geometries is essential for constructive-related weldability. These factors can significantly affect the residual stress state and distortion of components. Additionally, different weld seam geometries may necessitate distinct welding procedures, such as preheating and compliance with interpass temperatures.

- To assess material-related weldability comprehensively, it's crucial to extend the findings of this study to other MPEAs with varying crystal structures (FCC, BCC, or multiphase). Additionally, exploring the weldability of DMW with other alloys, such as ferritic steel, aluminum alloys for lightweight construction, or nickel-based alloys for high-temperature applications, holds particular significance.

Machinability

The following summarizes the results of **conventional and ultrasonic-assisted milling of the CoCrFeMnNi-HEA and CoCrNi-MEA**:

- The cutting force results demonstrate that established theories, such as the theory of undeformed chips, apply to both MPEAs. Here, lower feed rates per cutting edge result in decreased cutting forces. Moreover, the MEA, with greater hardness, exhibits higher cutting forces compared to the HEA. Introducing ultrasonic assistance leads to approx. 5 % reduction in cutting forces for HEA and a 4 % increase for MEA.

- Topography characterization reveals significant differences between conventional and ultrasonic-assisted milling processes, with USAM inducing a distinct pattern. Additionally, USAM yields a more uniform surface morphology with lower defect density. Conventional milling of HEA surfaces exhibits oxide grooves and tear defects due to Cr and Mn oxides from the manufacturing process, whereas MEA surfaces display BUE defects. Quantitative analysis of roughness indicates that f_z influences roughness differently depending on the direction, with increased f_z leading to higher roughness in the x direction. Ultrasonic assistance does not significantly affect roughness.

- Mechanical effects on surfaces are analyzed through residual stress states. Machined surfaces reveal that neither f_z, v_c, nor US significantly affect maximum principal residual stresses. Surface principal residual stresses exceed YS in the tensile range for both MPEAs. Subsurface residual stresses indicate that the US reduces detrimental tensile residual stresses more than conventional milling.

- The impact on the HEA microstructure in the subsurface zone varies with cutting parameters. Shear bands penetrate 2 µm deeper with high f_z and low v_c compared to low f_z and high v_c. Additionally, the US narrows the shear band range by approx. 5 µm.

Overall, both alloys demonstrated good machinability, with tools remaining intact and surfaces exhibiting minimal defects. Ultrasonic assistance notably improves surface integrity by reducing both the frequency and severity of defects. Moreover, USAM facilitates the reduction of residual stresses and the size of the subsurface deformation-affected zone.

Outlook

The results indicate excellent machinability of MPEAs featuring a pure FCC microstructure, renowned for their softness and ease of shaping. It is intriguing to explore how these findings can be extrapolated to other MPEAs with differing phases, whether pure BCC or multi-phase, like

AlxCoCrFeNi. Moreover, MPEAs exhibit potential for specialized applications rather than conventional construction materials, underscoring the importance of researching machining techniques for functional surfaces on MPEA coatings.

In summary, MPEAs exhibit favorable characteristics for both welding and milling, albeit requiring specific procedural considerations. This study offers invaluable new insights into the processing and machining of MPEAs, significantly expanding existing literature (as shown in Sections 2.2.4, 2.2.5, and 2.3.3) in terms of microstructural changes and resultant properties. These findings serve as a foundational basis for future explorations in this field.

Authors publications

M Rhode, T. Richter, P. Mayr, A. Nitsche, T. Mente, T. Böllinghaus, Hydrogen diffusion in creep-resistant 9 % Cr P91 multi-layer weld metal, Welding in the World, 64, 267-281, 2020; DOI: 10.1007/s40194-019-00828-8

T. Richter, D. Schröpfer, M. Rhode, A. Börner, Influence of modern machining processes on the surface integrity of high-entropy alloys, IOP Conference Series Materials Science and Engineering, 882:012016, 2020; DOI: 10.1088/1757-899X/882/1/012016

M. Rhode, A. Wentzel, O. Özcan, J. Nietzke, T. Richter, D. Schröpfer, Hydrogen diffusion and local Volta potential in high- and medium-entropy alloys, IOP Conference Series Materials Science and Engineering, 882:012015, 2020; DOI: 10.1088/1757-899X/882/1/012015

T. Richter, D Schröpfer, M Rhode, A Börner, Rührreibschweißen von Hoch- und Mittelentropie-Legierungen, 4. Niedersächsisches Symposium Materialtechnik Clausthal, Band 10, 502-511, 2021

M Rhode, T. Richter, D Schröpfer, A.M. Manzoni, M. Schneider, G. Laplanche, Welding of high-entropy alloys and compositionally complex alloys – An overview, Welding in the World, 65/8: 1645-1659, 2021, DOI: 10.1007/s40194-021-01110-6

M. Rhode, A. Wentzel, O. Özcan, J. Nietzke, T. Richter, D. Schröpfer, Corrigendum: Hydrogen diffusion and local Volta potential in high- and medium-entropy alloys, IOP Conference Series Materials Science and Engineering, 882:012027, 2021; DOI:10.1088/1757-899X/882/1/012027

T. Richter, D. Schröpfer, M. Rhode, A. Börner, R. S. Neumann, M. Schneider, G. Laplanche, Influence of machining on the surface integrity of high- and medium-entropy alloys, Materials Chemistry and Physics, 275:125271, 2022, DOI: 10.1016/j.matchemphys.2021.125271

M. Rhode, T. Richter, T. Mente, P. Mayer, A. Nitsche, Thickness and microstructure effect on hydrogen diffusion in creep-resistant 9% Cr P92 steel and P91 weld metal, angenommener Beitrag für IIW-Annual Assembly 2021; Welding in the World. (2021) DOI: 10.1007/s40194-021-01218-9

T. Richter, M. Giese, M. Rhode, D. Schroepfer, T. Michael, T. Fritsch, Influence of Surface Preparation on Cracking Phenomena in TIG-Welded High and Medium Entropy Alloys, Beitrag zur “2nd International Conference on advanced joining Processes”, Journal of Manufacturing and Materials Processing (2021), DOI: 10.3390/jmmp6010005

M. Rhode, J. Nietzke, T. Mente, T. Richter, E. Wilhelm, T. Kannengießer, Characterization of Hydrogen Diffusion for Cracking Avoidance in a Thick-walled Submerged Arc Multi-Layer Weld Joint of an Offshore Steel Grade S420G2+M Beitrag zur “EUROMAT 2021, Commission C12-Joining”, (2022), DOI: 10.1007/s11665-022-06679-7

T. Richter, D. Schröpfer, M. Rhode, Residual Stresses in a High- and a Medium-Entropy Alloy due to TIG and Friction Stir Welding, Journal of Manufacturing and Materials Processing, DOI: 10.3390/jmmp6060147

T. Richter, D. Delgado, A. Börner, D. Schröpfer, M. Rhode, T. Lindner, M Löbel, B. Preuß, T. Lampke, Ultrasonic assisted milling of a CoCrFeNi medium entropy alloy, Procedia CIRP 108(6), DOI: 10.1016/j.procir.2022.05.203

T. Richter, D. Schröpfer, M. Rhode, Innovative Multielement-Legierungen: Aktuelle Ergebnisse zur Schweißbarkeit und An-wendungseigenschaften, 75 DVS Kongress, Tagungsband

M. Rhode, J. Nietzke, T. Mente, T. Richter, P. Mayr, A Nitsche, Hydrogen effect on mechanical properties and cracking of creep-resistant 9% Cr P92 steel and P91 weld metal, Welding in the World (2022), DOI: 10.1007/s40194-022-01410-5

D. Delgado, T. Richter, A. Börner, D. Schröpfer, M. Rhode, T. Lindner, M Löbel, B. Preuß, T. Lampke, Influence of milling conditions on AlxCoCrFeNiMoy Multi-Principal Element Alloys, MDPI Coating (23), DOI: https://doi.org/10.3390/coatings13030662

R. Henrique Buzolin, T. Richter, F. Pixner, M. Rhode, D. Schroepfer, N. Enzinger, Microstructure characterisation of multi-principal element alloys welds produced by electron beam welding, Materials & Design (2023) DOI: https://doi.org/10.1016/j.matdes.2023.111609.

Ricardo Henrique Buzolin, Tim Richter, Florian Pixner, Michael Rhode, Dirk Schroepfer, Norbert Enzinger, Microstructure and texture characterisation of friction stir welded CoCrNi and CoCrFeMnNi multi-principle element alloys, Materials Today Communications (2023), DOI: https://doi.org/10.1016/j.mtcomm.2023.105870.

T. Richter, K. Erxleben, M. Rhode, D. Schroepfer, T. Michael, A. Boerner, Microstructure characterization of dissimilar metal welds of innovative high- and medium-entropy alloys to austenitic stainless steels joint by tungsten inert gas and friction stir welding, Welding in the world (2023), DOI: 10.1007/s40194-023-01618-z

M. Rhode, T. Richter, K. Erxleben, D. Schroepfer, T. Mente, T. Michael, Local mechanical properties of dissimilar metal TIG welded joints of CoCrFeMnNi high entropy alloy and AISI 304 austenitic steel, Welding in the World (2024), DOI: 10.1007/s40194-024-01718-4

References

[1] J.W. Yeh, S.K. Chen, S.J. Lin, J.Y. Gan, T.S. Chin, T.T. Shun, C.H. Tsau, S.Y. Chang, N*anostructured high-entropy alloys with multiple principal elements: Novel alloy design concepts and outcomes*, Advanced Engineering Materials **6**(5) (2004) 299-303.

[2] B. Cantor, I.T.H. Chang, P. Knight, A.J.B. Vincent, *Microstructural development in equiatomic multicomponent alloys*, Materials Science and Engineering: A **375-377** (2004) 213-218.

[3] J.-W. Yeh, S.-J. Lin, T.-S. Chin, J.-Y. Gan, S.-K. Chen, T.-T. Shun, C.H. Tsau, S. Chou, *Formation of simple crystal structures in Cu-Co-Ni-Cr-Al-Fe-Ti-V alloys with multiprincipal metallic elements*, Metallurgical and Materials Transactions A **35** (2004) 2533-2536.

[4] D.B. Miracle, O.N. Senkov, *A critical review of high entropy alloys and related concepts*, Acta Materialia **122** (2017) 448-511.

[5] J.-W. Yeh, *Recent progress in high-entropy alloys*, Annales de Chimie Science des Matériaux **31**(6) (2006) 633-648.

[6] B. Heinz-Deuerling, https://www.sppccahea.uni-bayreuth.de/en/general-information/index.html, 2016. (Accessed 11.05. 2023).

[7] Y. Zhang, T.T. Zuo, Z. Tang, M.C. Gao, K.A. Dahmen, P.K. Liaw, Z.P. Lu, *Microstructures and properties of high-entropy alloys*, Progress in Materials Science **61** (2014) 1-93.

[8] M.C. Gao, J.-W. Yeh, P.K. Liaw, Y. Zhang, *High-Entropy Alloys Fundamentals and Applications*, Springer International, Switzerland, 2016.

[9] Y.F. Ye, Q. Wang, J. Lu, C.T. Liu, Y. Yang, *High-entropy alloy: challenges and prospects*, Materials Today **19**(6) (2016) 349-362.

[10] B.S. Mutrty, J.W. Yeh, s. Ranganathan, *High Entropy Alloys*, Butterworth-Heinemann, 2014.

[11] K.Y. Tsai, M.H. Tsai, J.W. Yeh, *Sluggish diffusion in Co–Cr–Fe–Mn–Ni high-entropy alloys,* Acta Materialia **61**(13) (2013) 4887-4897.

[12] A. Durand, L. Peng, G. Laplanche, J.R. Morris, E.P. George, G. Eggeler, Interdiffusion in Cr–Fe–Co–Ni medium-entropy alloys, Intermetallics 122 (2020).

[13] G. Laplanche, U.F. Volkert, G. Eggeler, E.P. George, *Oxidation Behavior of the CrMnFeCoNi High-Entropy Alloy*, Oxidation of Metals **85**(5-6) (2016) 629-645.

[14] G. Laplanche, S. Berglund, C. Reinhart, A. Kostka, F. Fox, E.P. George, *Phase stability and kinetics of σ-phase precipitation in CrMnFeCoNi high-entropy alloys*, Acta Materialia **161** (2018) 338-351.

[15] G. Laplanche, *Growth kinetics of σ-phase precipitates and underlying diffusion processes in CrMnFeCoNi high-entropy alloys*, Acta Materialia **199** (2020) 193-208.

[16] O.N. Senkov, G.B. Wilks, J.M. Scott, D.B. Miracle, *Mechanical properties of Nb25Mo25Ta25W25 and V20Nb20Mo20Ta20W20 refractory high entropy alloys*, Intermetallics **19**(5) (2011) 698-706.

[17] J.Y. He, W.H. Liu, H. Wang, Y. Wu, X.J. Liu, T.G. Nieh, Z.P. Lu, *Effects of Al addition on structural evolution and tensile properties of the FeCoNiCrMn high-entropy alloy system*, Acta Materialia **62** (2014) 105-113.

[18] E.J. Pickering, N.G. Jones, *High-entropy alloys: a critical assessment of their founding principles and future prospects*, International Materials Reviews **61**(3) (2016) 183-202.

[19] J.-W. Yeh, *Alloy Design Strategies and Future Trends in High-Entropy Alloys*, JOM **65**(12) (2013) 1759-1771.

[20] M. Schneider, *Zum Einfluss von Rekristallisations- und Verformungszwillingen auf die mechanischen Eigenschaften kompositionell komplexer Mischkristalle*, Fakultät für Maschinenbau, Ruhr-Universität Bochum, 2021.

[21] A.M. Manzoni, U. Glatzel, *High-Entropy Alloys: Balancing Strength and Ductility at Room Temperature*, Encyclopedia of Materials: Metals and Alloys 2022, pp. 441-453.

[22] G. Laplanche, P. Gadaud, C. Bärsch, K. Demtröder, C. Reinhart, J. Schreuer, E.P. George, *Elastic moduli and thermal expansion coefficients of medium-entropy subsystems of the CrMnFeCoNi high-entropy alloy*, Journal of Alloys and Compounds **746** (2018) 244-255.

[23] G. Laplanche, A. Kostka, C. Reinhart, J. Hunfeld, G. Eggeler, E.P. George, R*easons for the superior mechanical properties of medium-entropy CrCoNi compared to high-entropy CrMnFeCoNi*, Acta Materialia **128** (2017) 292-303.

[24] J. Rackwitz, Q. Yu, Y. Yang, G. Laplanche, E.P. George, A.M. Minor, R.O. Ritchie, E*ffects of cryogenic temperature and grain size on fatigue-crack propagation in the medium-entropy CrCoNi alloy*, Acta Materialia **200** (2020) 351-365.

[25] F. Otto, A. Dlouhý, C. Somsen, H. Bei, G. Eggeler, E.P. George, *The influences of temperature and microstructure on the tensile properties of a CoCrFeMnNi high-entropy alloy*, Acta Materialia **61**(15) (2013) 5743-5755.

[26] D.Y. Kovalev, A.S. Rogachev, N.A. Kochetov, S.G. Vadchenko, *Evolution of the Phase Composition of the Cantor CoCrFeNiMn Alloy during Prolonged Annealing*, Physics of Metals and Metallography **123**(11) (2023) 1161-1170.

[27] D. Xu, M. Wang, T. Li, X. Wei, Y. Lu, *A critical review of the mechanical properties of CoCrNi-based medium-entropy alloys*, Microstructures (2022).

[28] H. Wang, D. Chen, X. An, Y. Zhang, S. Sun, Y. Tian, Z. Zhang, A. Wang, J. Liu, M. Song, S.P. Ringer, T. Zhu, X. Liao, *Deformation-induced crystalline-to-amorphous phase transformation in a CrMnFeCoNi high-entropy alloy*, Sci Adv **7**(14) (2021).

[29] C.-C. Hsieh, W. Wu, *Overview of Intermetallic Sigma (σ) Phase Precipitation in Stainless Steels*, ISRN Metallurgy **2012** (2012) 1-16.

[30] Y. Shi, B. Yang, P. Liaw, *Corrosion-Resistant High-Entropy Alloys: A Review*, Metals **7**(2) (2017).

[31] A. Wetzel, M. von der Au, P.M. Dietrich, J. Radnik, O. Ozcan, J. Witt, *The comparison of the corrosion behavior of the CrCoNi medium entropy alloy and CrMnFeCoNi high entropy alloy*, Applied Surface Science **601** (2022).

[32] S. Pathak, N. Kumar, R.S. Mishra, P.S. De, *Aqueous Corrosion Behavior of Cast CoCrFeMnNi Alloy*, Journal of Materials Engineering and Performance **28**(10) (2019) 5970-5977.

[33] C. Stephan-Scherb, W. Schulz, M. Schneider, S. Karafiludis, G. Laplanche, *High-Temperature Oxidation in Dry and Humid Atmospheres of the Equiatomic CrMnFeCoNi and CrCoNi High- and Medium-Entropy Alloys*, Oxidation of Metals **95**(1-2) (2020) 105-133.

[34] N.D. Stepanov, D.G. Shaysultanov, N.Y. Yurchenko, S.V. Zherebtsov, A.N. Ladygin, G.A. Salishchev, M.A. Tikhonovsky, *High temperature deformation behavior and dynamic recrystallization in CoCrFeNiMn high entropy alloy*, Materials Science and Engineering: A **636** (2015) 188-195.

[35] K.V.S. Thurston, B. Gludovatz, A. Hohenwarter, G. Laplanche, E.P. George, R.O. Ritchie, E*ffect of temperature on the fatigue-crack growth behavior of the high-entropy alloy CrMnFeCoNi*, Intermetallics **88** (2017) 65-72.

[36] Y. Zhao, D.-H. Lee, M.-Y. Seok, J.-A. Lee, M.P. Phaniraj, J.-Y. Suh, H.-Y. Ha, J.-Y. Kim, U. Ramamurty, J.-i. Jang, *Resistance of CoCrFeMnNi high-entropy alloy to gaseous hydrogen embrittlement*, Scripta Materialia **135** (2017) 54-58.

[37] M. Koyama, K. Ichii, K. Tsuzaki, *Grain refinement effect on hydrogen embrittlement resistance of an equiatomic CoCrFeMnNi high-entropy alloy*, International Journal of Hydrogen Energy **44**(31) (2019) 17163-17167.

[38] G. Yang, Y. Zhao, D.-H. Lee, J.-M. Park, M.-Y. Seok, J.-Y. Suh, U. Ramamurty, J.-i. Jang, *Influence of hydrogen on incipient plasticity in CoCrFeMnNi high-entropy alloy*, Scripta Materialia **161** (2019) 23-27.

[39] M. Rhode, A. Wetzel, O. Ozcan, J. Nietzke, T. Richter, D. Schroepfer, *Hydrogen diffusion and local Volta potential in high- and medium-entropy alloys*, IOP Conference Series: Materials Science and Engineering **882**(1) (2020).

[40] J.S. Belo, S.C. Marques, A.V. Castilho, L.M. de Oliveira, R.A. Simão, D.S. dos Santos, *Hydrogen diffusivity and interaction with Fe20Mn20Ni20Co20Cr20 and Fe22Mn40Ni30Co6Cr2 high-entropy alloys*, Journal of Alloys and Compounds **815** (2020).

[41] K. Jin, B.C. Sales, G.M. Stocks, G.D. Samolyuk, M. Daene, W.J. Weber, Y. Zhang, H. Bei, *Tailoring the physical properties of Ni-based single-phase equiatomic alloys by modifying the chemical complexity*, Sci Rep **6** (2016) 20159.

[42] G. Laplanche, P. Gadaud, O. Horst, F. Otto, G. Eggeler, E.P. George, T*emperature dependencies of the elastic moduli and thermal expansion coefficient of an equiatomic, single-phase CoCrFeMnNi high-entropy alloy*, Journal of Alloys and Compounds **623** (2015) 348-353.

[43] Y. Lei, S.P. Hu, T.L. Yang, X.G. Song, Y. Luo, G.D. Wang, *Vacuum diffusion bonding of high-entropy Al0.85CoCrFeNi alloy to TiAl intermetallic*, Journal of Materials Processing Technology **278** (2020).

[44] B.R. Chen, A.C. Yeh, J.W. Yeh, *Effect of one-step recrystallization on the grain boundary evolution of CoCrFeMnNi high entropy alloy and its subsystems*, Sci Rep **6** (2016) 22306.

[45] Z. Wu, H. Bei, F. Otto, G.M. Pharr, E.P. George, *Recovery, recrystallization, grain growth and phase stability of a family of FCC-structured multi-component equiatomic solid solution alloys*, Intermetallics **46** (2014) 131-140.

[46] C.J. Smithells, W.F. Gale, T.C. Totemeier, *Smithells metals reference book*, 8th ed., Elsevier Butterworth-Heinemann, Amsterdam; Boston, 2004.

[47] R. Oriani, *Hydrogen embrittlement of steels*, Annual review of materials science **8**(1) (1978) 327-357.

[48] I.M. Robertson, P. Sofronis, A. Nagao, M.L. Martin, S. Wang, D.W. Gross, K.E. Nygren, H*ydrogen Embrittlement Understood*, Metallurgical and Materials Transactions B **46**(3) (2015) 1085-1103.

[49] Y.-K. Kim, J.-Y. Suh, K.-A. Lee, *Effect of gaseous hydrogen embrittlement on the mechanical properties of additively manufactured CrMnFeCoNi high-entropy alloy strengthened by in-situ formed oxide*, Materials Science and Engineering: A **796** (2020) 140039.

[50] Y. Zhao, J.-M. Park, D.-H. Lee, E.J. Song, J.-Y. Suh, U. Ramamurty, J.-i. Jang, *Influences of hydrogen charging method on the hydrogen distribution and nanomechanical properties of face-centered cubic high-entropy alloy: A comparative study*, Scripta Materialia **168** (2019) 76-80.

[51] L. Junghoon, P. Cheolho, P. Hanji, K. Namhyun, *Effective hydrogen diffusion coefficient for CoCrFeMnNi high-entropy alloy and microstructural behaviors after hydrogen permeation*, International Journal of Hydrogen Energy **45**(16) (2020) 10227-10232.

[52] H. Luo, Z. Li, D. Raabe, *Hydrogen enhances strength and ductility of an equiatomic high-entropy alloy*, Sci Rep **7**(1) (2017) 9892.

[53] S.K. Dewangan, A. Mangish, S. Kumar, A. Sharma, B. Ahn, V. Kumar, *A review on High-Temperature Applicability: A milestone for high entropy alloys*, Engineering Science and Technology, an International Journal **35** (2022).

[54] A.M. Manzoni, S. Haas, H. Daoud, U. Glatzel, C. Forster, N. Wanderka, *Tensile Behavior and Evolution of the Phases in the Al(10)Co(25)Cr(8)Fe(15)Ni(36)Ti(6) Compositionally Complex/High Entropy Alloy*, Entropy **20**(9) (2018).

[55] T.M. Smith, C.A. Kantzos, N.A. Zarkevich, B.J. Harder, M. Heczko, P.R. Gradl, A.C. Thompson, M.J. Mills, T.P. Gabb, J.W. Lawson, *A 3D printable alloy designed for extreme environments*, Nature **617** (2023) 513-518.

[56] B.-l. Pang, M. Wang, Y.-g. Shen, X.-l. Xi, Z.-r. Nie, *Improvement in oxidation resistance of Cantor alloy through microstructure tailoring*, China Foundry **19**(6) (2022) 503-510.

[57] M.L. Bürckner, L. Mengis, E.M.H. White, M.C. Galetz, I*nfluence of copper and aluminum substitution on high‐temperature oxidation of the FeCoCrNiMn "Cantor" alloy*, Materials and Corrosion **74**(1) (2022) 79-90.

[58] DIN-Fachbericht ISO/TR 581:2007-04; *Schweißbarkeit - Metallische Werkstoffe - Allgemeine Grundlagen*, Beuth publishing DIN, Berlin, 2007.

[59] U. Dilthey, *Schweißtechnische Fertigungsverfahren 2: Verhalten der Werkstoffe beim Schweißen*, Springer-Verlag, Berlin, Germany, 2005.

[60] H.J. Fahrenwaldt, V. Schuler, *Praxiswissen Schweißtechnik: Werkstoffe, Prozesse, Fertigung*, GWV Fachverlage GmbH, Wiesbaden, Germany, 2009.

[61] U. Dilthey, *Schweißtechnische Fertigungsverfahren 1: Schweiß- und Schneidtechnologien*, Springer-Verlag, Berlin, Germany, 2006.

[62] C. Huang, S. Kou, P*artially melted zone in aluminum welds - Liquation mechanism and directional solidification*, Welding Journal **79**(5) (2000) 113s-120s.

[63] R.S. Mishra, Z.Y. Ma, *Friction stir welding and processing*, Materials Science and Engineering: R: Reports **50**(1-2) (2005) 1-78.

[64] A. Heidarzadeh, S. Mironov, R. Kaibyshev, G. Çam, A. Simar, A. Gerlich, F. Khodabakhshi, A. Mostafaei, D.P. Field, J.D. Robson, A. Deschamps, P.J. Withers, *Friction stir welding/processing of metals and alloys: A comprehensive review on microstructural evolution*, Progress in Materials Science **117** (2021).

[65] A. Arora, R. Nandan, A.P. Reynolds, T. DebRoy, *Torque, power requirement and stir zone geometry in friction stir welding through modeling and experiments*, Scripta Materialia **60**(1) (2009) 13-16.

[66] P. Upadhyay, A.P. Reynolds, *Effects of thermal boundary conditions in friction stir welded AA7050-T7 sheets*, Materials Science and Engineering: A **527**(6) (2010) 1537-1543.

[67] P. Kah, R. Rajan, J. Martikainen, R. Suoranta, *Investigation of weld defects in friction-stir welding and fusion welding of aluminium alloys*, International Journal of Mechanical and Materials Engineering **10**(1) (2015).

[68] A.I. Albannai, Review: The Common Defects In Friction Stir Welding, International Journal of Scientific & Technology Research **9**(11) (2020) 318-329.

[69] A.P. Reynolds, W. Tang, T. Gnaupel-Herold, H. Prask, *Structure, properties, and residual stress of 304L stainless steel friction stir welds*, Scripta Materialia **48**(9) (2003) 1289-1294.

[70] M.-G. Jo, H.-J. Kim, M. Kang, P.P. Madakashira, E.S. Park, J.-Y. Suh, D.-I. Kim, S.-T. Hong, H.N. Han, *Microstructure and mechanical properties of friction stir welded and laser welded high entropy alloy CrMnFeCoNi*, Metals and Materials International **24**(1) (2018) 73-83.

[71] R.H. Buzolin, T. Richter, F. Pixner, M. Rhode, D. Schroepfer, N. Enzinger, *Microstructure and texture characterisation of friction stir welded CoCrNi and CoCrFeMnNi multi-principle element alloys*, Materials Today Communications **35** (2023).

[72] F.J. Humphreys, M. Hatherly, *Recrystallization and Related Annealing Phenomena*, Elsevier Ltd. 2004.

[73] P. Cavaliere, E. Cerri, A. Squillace, *Mechanical response of 2024-7075 aluminium alloys joined by Friction Stir Welding*, Journal of Materials Science **40**(14) (2005) 3669-3676.

[74] R. Nandan, T. Debroy, H. Bhadeshia, *Recent advances in friction-stir welding – Process*, *weldment structure and properties*, Progress in Materials Science **53**(6) (2008) 980-1023.

[75] T. Sakai, A. Belyakov, R. Kaibyshev, H. Miura, J.J. Jonas, *Dynamic and post-dynamic recrystallization under hot, cold and severe plastic deformation conditions*, Progress in Materials Science **60** (2014) 130-207.

[76] S. Mironov, Y.S. Sato, H. Kokawa, *Microstructural evolution during friction stir-processing of pure iron*, Acta Materialia 56(11) (2008) 2602-2614.

[77] S. Mironov, Y.S. Sato, H. Kokawa, *Development of grain structure during friction stir welding of pure titanium*, Acta Materialia **57**(15) (2009) 4519-4528.

[78] M. Tikhonova, R. Kaibyshev, A. Belyakov, *Microstructure and Mechanical Properties of Austenitic Stainless Steels after Dynamic and Post-Dynamic Recrystallization Treatment*, Advanced Engineering Materials **20**(7) (2018).

[79] N. Dudova, A. Belyakov, T. Sakai, R. Kaibyshev, *Dynamic recrystallization mechanisms operating in a Ni–20%Cr alloy under hot-to-warm working*, Acta Materialia **58**(10) (2010) 3624-3632.

[80] H.-J. Bargel, G. Schulze, *Werkstoffkunde*, Springer-Verlag2008.

[81] G. Schulze, D*ie Metallurgie des Schweißens: Eisenwerkstoffe - Nichteisenmetallische Werkstoffe*, Springer Verlag, Heidelberg, Deutschland, 2012.

[82] H.İ. Kurt, R. Samur, *Study on Microstructure, Tensile Test and Hardness 304 Stainless Steel Jointed by TIG Welding*, International Journal of Science and Technology **2**(2) (2013) 163-168.

[83] P. Sathiya, S. Aravindan, A. Noorul Haq, *Mechanical and metallurgical properties of friction welded AISI 304 austenitic stainless steel*, The International Journal of Advanced Manufacturing Technology **26**(5-6) (2004) 505-511.

[84] M. Sahin, D. Pullen, *An investigation into joining of austenitic-stainless steels (AISI 304) with friction welding*, Assembly Automation **25**(2) (2005) 140-145.

[85] A. Lingerfelter,*Welding of Inconel Alloy 718: A Historical Overview*, Superalloy 718-Metallurgy and Applications The Minerals, Metals & Materials Society, (1989) 673-683.

[86] J.N. DuPont, J.C. Lippold, S.D. Kiser, *Welding metallurgy and weldability of nickel base alloys*, John Wiley & Sons Inc., Hoboken, New Jersey., 2009.

[87] J.T. Tharappel, J. Babu, *Welding processes for Inconel 718- A brief review*, IOP Conference Series: Materials Science and Engineering **330** (2018).

[88] F. Carolin, *Ductility Dip Cracking beim Schweißen von Nickel-Basislegierungen – Phänomenologische und experimentelle Betrachtungen*, Shaker Verlag, 2016.

[89] B. Hemsworth, T. Boniszewski, N.F. Eaton, *Classification and Definition of High Temperature Welding Cracks in Alloys*, Met Constr-Brit Weld **1**(2) (1969) 5-16.

[90] C. Fink, M. Zinke, S. Jüttner, *An investigation of ductility-dip cracking in the base metal heat-affected zone of wrought nickel base alloys—part II: correlation of PVR and STF results*, Welding in the World **60**(5) (2016) 951-961.

[91] R. Killing, *Angewandte Schweissmetallurgie*, DVS Media GmbH, Düsseldorf, Germany, 1996.

[92] S. Kou, W*elding metallurgy*, John Wiley & Sons Inc., Hoboken, New Jersey, 2003.

[93] J.C. Lippold, *Welding Metallurgy and Weldability*, John Wiley & Sons Inc., Hoboken, New Jersey, 2015.

[94] M. Rappaz, J.M. Drezet, M. Gremaud, *A new hot-tearing criterion*, Metallurgical and Materials Transactions A **30**(2) (1999) 449-455.

[95] T. Böllinghaus, C.E. Cross, H. Herold, J.C. Lippold, *Hot Cracking Phenomena in Welds II*, Springer-Verlag, Berlin-Heidelberg, Germany, 2008.

[96] J.E. Norkett, M.D. Dickey, V.M. Miller, *A Review of Liquid Metal Embrittlement: Cracking Open the Disparate Mechanisms*, Metallurgical and Materials Transactions A **52**(6) (2021) 2158-2172.

[97] S.P. Murugan, J.B. Jeon, C. Ji, Y.-D. Park, *Liquid zinc penetration induced intergranular brittle cracking in resistance spot welding of galvannealed advanced high strength steel*, Welding in the World **64**(11) (2020) 1957-1969.

[98] W.F. Savage, E.P. Nippes, M.C. Mushala, *Copper-Contamination Cracking in the Weld Heat-Affected Zone*, Welding Research Supplement (1978) 145-152.

[99] W.F. Savage, E.F. Nippes, M.C. Mushala, *Liquid-Metal Embrittlement of Heat-Affected Zone by Copper Contamination*, Welding Journal **57**(8) (1978) S237-S245.

[100] L. Cui, B. Ma, S.Q. Feng, X.L. Wang, *Microstructure and Mechanical Properties of High-Entropy Alloys CoCrFeNiAl by Welding*, Advanced Materials Research **936** (2014) 1635-1640.

[101] T. Sonar, M. Ivanov, E. Trofimov, A. Tingaev, I. Suleymanova, *A Comprehensive Review on Fusion Welding of High Entropy Alloys – Processing, Microstructural Evolution and Mechanical Properties of Joints*, International Journal of Lightweight Materials and Manufacture **7** (2024) 122-183.

[102] F.C. Garcia Filho, S.N. Monteiro, *Welding Joints in High Entropy Alloys: A Short-Review on Recent Trends*, Materials (Basel) **13**(6) (2020).

[103] J. Guo, C. Tang, G. Rothwell, L. Li, Y.-C. Wang, Q. Yang, X. Ren, *Welding of High Entropy Alloys—A Review*, Entropy **21**(4) (2019).

[104] M. John, O. Diaz, A. Esparza, A. Fliegler, D. Ocenosak, C. Van Dorn, K.U. Bhat, P.L. Menezes, *Welding Techniques for High Entropy Alloys: Processes, Properties, Characterization, and Challenges*, Materials (Basel) **15**(6) (2022).

[105] J.G. Lopes, J.P. Oliveira, *A Short Review on Welding and Joining of High Entropy Alloys*, Metals **10**(2) (2020).

[106] M. Rhode, T. Richter, D. Schroepfer, A.M. Manzoni, M. Schneider, G. Laplanche, *Welding of high-entropy alloys and compositionally complex alloys—an overview*, Welding in the World **65**(8) (2021) 1645-1659.

[107] E. Scutelnicu, G. Simion, C.C. Rusu, M.C. Gheonea, I. Voiculescu, V. Geanta, *High Entropy Alloys Behaviour During Welding*, Revista de Chimie **71**(3) (2020) 219-233.

[108] H. Nam, C. Park, C. Kim, H. Kim, N. Kang, *Effect of post weld heat treatment on weldability of high entropy alloy welds*, Science and Technology of Welding and Joining **23**(5) (2017) 420-427.

[109] H. Nam, S. Park, E.-J. Chun, H. Kim, Y. Na, N. Kang, *Laser dissimilar weldability of cast and rolled CoCrFeMnNi high-entropy alloys for cryogenic applications*, Science and Technology of Welding and Joining **25**(2) (2019) 127-134.

[110] C. Park, T. Hwang, G.-D. Kim, H. Nam, N. Kang, E*ffect of the Initial Grain Size on Laser Beam Weldability for High-Entropy Alloys*, Crystals **13**(1) (2022).

[111] J.P. Oliveira, T.M. Curado, Z. Zeng, J.G. Lopes, E. Rossinyol, J.M. Park, N. Schell, F.M. Braz Fernandes, H.S. Kim, *Gas tungsten arc welding of as-rolled CrMnFeCoNi high entropy alloy*, Materials & Design **189** (2020).

[112] R.H. Buzolin, T. Richter, F. Pixner, M. Rhode, D. Schroepfer, N. Enzinger, *Microstructure characterisation of multi-principal element alloys welds produced by electron beam welding*, Materials & Design **225** (2023).

[113] Z. Wu, S.A. David, D.N. Leonard, Z. Feng, H. Bei, M*icrostructures and mechanical properties of a welded CoCrFeMnNi high-entropy alloy*, Science and Technology of Welding and Joining **23**(7) (2018) 585-595.

[114] H. Nam, S. Park, N. Park, Y. Na, H. Kim, S.-J. Yoo, Y.-H. Moon, N. Kang, *Weldability of cast CoCrFeMnNi high-entropy alloys using various filler metals for cryogenic applications*, Journal of Alloys and Compounds **819** (2020).

[115] Z. Chen, B. Wang, B. Duan, X. Zhang, *Mechanical properties and microstructure of laser welded FeCoNiCrMn high-entropy alloy*, Materials Letters **262** (2020).

[116] J.G. Lopes, P. Rocha, D.A. Santana, J. Shen, E. Maawad, N. Schell, F.G. Coury, J.P. Oliveira, *Impact of arc‐based welding on the microstructure evolution and mechanical properties in newly developed Cr29.7Co29.7Ni35.4Al4Ti1.2 multi‐principal element alloy*, Advanced Engineering Materials **25**(13) (2023).

[117] I. Cazic, J. Zollinger, S. Mathieu, M. El Kandaoui, P. Plapper, B. Appolaire, *New insights into the origin of fine equiaxed microstructures in additively manufactured Inconel 718*, Scripta Materialia **195** (2021).

[118] O.G. Rivera, P.G. Allison, J.B. Jordon, O.L. Rodriguez, L.N. Brewer, Z. McClelland, W.R. Whittington, D. Francis, J. Su, R.L. Martens, N. Hardwick, *Microstructures and mechanical behavior of Inconel 625 fabricated by solid-state additive manufacturing*, Materials Science and Engineering: A **694** (2017) 1-9.

[119] Y. Hu, S. Wu, Y. Guo, Z. Shen, A.M. Korsunsky, Y. Yu, X. Zhang, Y. Fu, Z. Che, T. Xiao, S. Lozano-Perez, Q. Yuan, X. Zhong, X. Zeng, G. Kang, P.J. Withers, *Inhibiting weld cracking in high-strength aluminium alloys*, Nat Commun **13**(1) (2022) 5816.

[120] S. Shah, J. Wittig, G. Hahn, *Microstructural analysis of a high strength Al-Cu-Li (Weldalite 049) alloy weld*, Proceedings of the 3rd International Conference on Trends in Welding Research, 1992.

[121] A. Kostrivas, J.C. Lippold, *Weldability of Li-bearing aluminium alloys*, International Materials Reviews **44**(6) (1999) 217-237.

[122] A. Kostrivas, J.C. Lippold, *Fusion Boundary Microstructure Evolution in Aluminium Alloys*, Welding in the World **50** (2006) 24-34.

[123] M. Nahmany, Z. Hooper, A. Stern, V. Geanta, I. Voiculescu, *AlxCrFeCoNi High-Entropy Alloys: Surface Modification by Electron Beam Bead-on-Plate Melting*, Metallography, Microstructure, and Analysis **5**(3) (2016) 229-240.

[124] A. Asabre, A. Kostka, O. Stryzhyboroda, J. Pfetzing-Micklich, U. Hecht, G. Laplanche, *Effect of Al, Ti and C additions on Widmanstätten microstructures and mechanical properties of cast Al0.6CoCrFeNi compositionally complex alloys*, Materials & Design **184** (2019).

[125] A.C. Martin, C. Fink, *Initial weldability study on Al0.5CrCoCu0.1FeNi high-entropy alloy*, Welding in the World **63**(3) (2019) 739-750.

[126] A.C. Martin, J.P. Oliveira, C. Fink, *Elemental Effects on Weld Cracking Susceptibility in AlxCoCrCuyFeNi High-Entropy Alloy*, Metallurgical and Materials Transactions A **51**(2) (2019) 778-787.

[127] P. Li, H. Sun, S. Wang, X. Hao, H. Dong, *Rotary friction welding of AlCoCrFeNi2.1 eutectic high entropy alloy*, Journal of Alloys and Compounds **814** (2020).

[128] L. Zuo, K. Zhang, T. Zhang, *Direct drive friction welding of a multi-phase Al13Cr23.5Fe20Co20Ni23.5 high-entropy alloy*, Science and Technology of Welding and Joining **26**(7) (2021) 513-520.

[129] H. Gao, G. He, Q. Li, Y. Li, W. Hu, S. Zhou, F. Liu, J. Yi, Y. Zhang, Z. Cai, S. Ogata, L. Qiao, L. Gao, *Diffusion bonding of high entropy alloy and stainless steel at a relative lower temperature via surface nano-crystallization treatment*, Journal of Materials Research and Technology **24** (2023) 475-487.

[130] D.G. Shaysultanov, N.D. Stepanov, I.V. Vysotskiy, S.V. Zherebtsov, *Effect of friction stir welding on the structure and mechanical properties of the CoCrFeNiMn-0.9%C alloy*, Proceedings of the International Conference on Advanced Materials with Hierarchical Structure for New Technologies and Reliable Structures 2019, 2019.

[131] S. Park, H. Nam, Y. Na, H. Kim, Y. Moon, N. Kang, *Effect of Initial Grain Size on Friction Stir Weldability for Rolled and Cast CoCrFeMnNi High-Entropy Alloys*, Metals and Materials International **26** (2020) 641-649.

[132] Z.G. Zhu, Y.F. Sun, M.H. Goh, F.L. Ng, Q.B. Nguyen, H. Fujii, S.M.L. Nai, J. Wei, C.H. Shek, *Friction stir welding of a CoCrFeNiAl0.3 high entropy alloy*, Materials Letters **205** (2017) 142-144.

[133] T. Wang, S. Shukla, M. Komarasamy, K. Liu, R.S. Mishra, *Towards heterogeneous AlxCoCrFeNi high entropy alloy via friction stir processing*, Materials Letters **236** (2019) 472-475.

[134] X. Qin, Y. Xu, Y. Sun, H. Fujii, Z. Zhu, C.H. Shek, *Effect of process parameters on microstructure and mechanical properties of friction stir welded CoCrFeNi high entropy alloy*, Materials Science and Engineering: A **782** (2020).

[135] S. Park, C. Park, Y. Na, H.-S. Kim, N. Kang, *Effects of (W, Cr) carbide on grain refinement and mechanical properties for CoCrFeMnNi high entropy alloys*, Journal of Alloys and Compounds **770** (2019) 222-228.

[136] S. Zherebtsov, N. Stepanov, D. Shaysultanov, S. Malopheyev, I. Vysotskiy, V. Sanin, N. Kashaev, R. Kaibyshev, *Use of Novel Welding Technologies for High-Entropy Alloys Joining*, Materials Science Forum **941** (2018) 919-924.

[137] Z.G. Zhu, Y.F. Sun, F.L. Ng, M.H. Goh, P.K. Liaw, H. Fujii, Q.B. Nguyen, Y. Xu, C.H. Shek, S.M.L. Nai, J. Wei, *Friction-stir welding of a ductile high entropy alloy: microstructural evolution and weld strength*, Materials Science and Engineering: A **711** (2018) 524-532.

[138] D. Shaysultanov, N. Stepanov, S. Malopheyev, I. Vysotskiy, V. Sanin, S. Mironov, R. Kaibyshev, G. Salishchev, S. Zherebtsov, *Friction stir welding of a carbon-doped CoCrFeNiMn high-entropy alloy*, Materials Characterization **145** (2018) 353-361.

[139] H. Moghanni, K. Dehghani, A. Shafiei, *Effects of process parameters on microstructure and mechanical properties of Al0.5CoCrFeNi high entropy alloy thin sheets using pinless friction stir welding*, Journal of Materials Research and Technology **16** (2022) 1069-1089.

[140] Y. Fang, X. Jiang, D. Mo, D. Zhu, Z. Luo, *A review on dissimilar metals' welding methods and mechanisms with interlayer*, The International Journal of Advanced Manufacturing Technology **102**(9-12) (2019) 2845-2863.

[141] J.P. Oliveira, A. Shamsolhodaei, J. Shen, J.G. Lopes, R.M. Gonçalves, M. de Brito Ferraz, L. Piçarra, Z. Zeng, N. Schell, N. Zhou, H. Seop Kim, *Improving the ductility in laser welded joints of CoCrFeMnNi high entropy alloy to 316 stainless steel*, Materials & Design **219** (2022).

[142] A. Simar, M.-N. Avettand-Fènoël, *State of the art about dissimilar metal friction stir welding*, Science and Technology of Welding and Joining **22**(5) (2016) 389-403.

[143] P. Carlone, A. Astarita, *Dissimilar Metal Welding*, Metals **9**(11) (2019).

[144] J. Shen, R. Gonçalves, Y.T. Choi, J.G. Lopes, J. Yang, N. Schell, H.S. Kim, J.P. Oliveira, *Microstructure and mechanical properties of gas metal arc welded CoCrFeMnNi joints using a 308 stainless steel filler metal*, Scripta Materialia **222** (2023).

[145] J.P. Oliveira, J. Shen, Z. Zeng, J.M. Park, Y.T. Choi, N. Schell, E. Maawad, N. Zhou, H.S. Kim, *Dissimilar laser welding of a CoCrFeMnNi high entropy alloy to 316 stainless steel*, Scripta Materialia **206** (2022).

[146] M. Samiuddin, J. Li, M. Muzamil, S. Khan, J. Xiong, *Parametric Optimization of Diffusion Welding Process in Joining of CoCrNi Medium-Entropy Alloys (MEA) and SUS 304 Stainless Steel Using Full Factorial Design*, JOM **74**(11) (2022) 4280-4293.

[147] *Fertigungsverfahren – Begriffe, Einteilung DIN 8580 2022-12*, Beuth Verlag GmbH, Berlin, 2022.

[148] F. Klocke, W. Köning, *Fertigungsverfahren 1*, Springer - Verlag, Heidelberg, 2008.

[149] S. Kalpakjian, S.R. Schmid, *Manufacturing Engineering and Technology*, Pearson, USA, 2010.

[150] J. Kundrák, C. Felhő, *Investigation of the Topography of Face Milled Surfaces*, Materials Science Forum **919** (2018) 78-83.

[151] J. Kundrák, B. Karpuschewski, Z. Pálmai, C. Felhő, T. Makkai, D. Borysenko, T*he energetic characteristics of milling with changing cross-section in the definition of specific cutting force by FEM method*, CIRP Journal of Manufacturing Science and Technology **32** (2021) 61-69.

[152] D. Nespor, *Randzonenbeeinflussung durch die Rekonturierung komplexer Investitionsgüter aus Ti-6Al-4V*, Fakultät für Maschienenbau, Gottfired Wilhelm Leibnitz Universität Hannover, 2015.

[153] S. Yan, D. Zhu, K. Zhuang, X. Zhang, H. Ding, M*odeling and analysis of coated tool temperature variation in dry milling of Inconel 718 turbine blade considering flank wear effect*, Journal of Materials Processing Technology **214** (2014) 2985-3001.

[154] D. Schroepfer, K. Treutler, A. Boerner, R. Gustus, T. Kannengiesser, V. Wesling, W. Maus-Friedrichs, *Surface finishing of hard-to-machine cladding alloys for highly stressed components*, The International Journal of Advanced Manufacturing Technology **114**(5-6) (2021) 1427-1442.

[155] R. M'Saoubi, J.C. Outeiro, H. Chandrasekaran, O.W.D. Jr., I.S. Jawahir, *A review of surface integrity in machining and its impact on functional performance and life of machined products*, Int. J. Sustainable Manufacturing **1** (2008) 203-236.

[156] D. Ulutan, T. Ozel, *Machining induced surface integrity in titanium and nickel alloys: A review*, International Journal of Machine Tools and Manufacture **51**(3) (2011) 250-280.

[157] G.K. Dosbaeva, S.C. Veldhuis, A. Elfizy, G. Fox-Rabinovich, T. Wagg, *Microscopic Observations on the Origin of Defects During Machining of Direct Aged (DA) Inconel 718 Superalloy*, Journal of Materials Engineering and Performance **19**(8) (2010) 1193-1198.

[158] J.M. Zhou, V. Bushlya, J.E. Stahl, *An investigation of surface damage in the high speed turning of Inconel 718 with use of whisker reinforced ceramic tools*, Journal of Materials Processing Technology **212**(2) (2012) 372-384.

[159] C. Liu, C. Ren, G. Wang, Y. Yang, L. Zhang, *Study on surface defects in milling Inconel 718 super alloy*, Journal of Mechanical Science and Technology **29**(4) (2015) 1723-1730.

[160] P.J. Withers, *Residual stress and its role in failure*, Reports on Progress in Physics **70**(12) (2007) 2211-2264.

[161] B. Scholtes, *Residual stresses introduced by machining*, Advances in Surface Treatments. Technology--Applications--Effects **4** (1987) 59-72.

[162] Y. Li, W. Gan, W. Zhou, D. Li, *Review on residual stress and its effects on manufacturing of aluminium alloy structural panels with typical multi-processes*, Chinese Journal of Aeronautics **36**(5) (2023) 96-124.

[163] V. Sharma, P.M. Pandey, *Optimization of machining and vibration parameters for residual stresses minimization in ultrasonic assisted turning of 4340 hardened steel*, Ultrasonics **70** (2016) 172-82.

[164] D. Novovic, R.C. Dewes, D.K. Aspinwall, W. Voice, P. Bowen, *The effect of machined topography and integrity on fatigue life*, International Journal of Machine Tools and Manufacture **44**(2-3) (2004) 125-134.

[165] D. Umbrello, *Analysis of the white layers formed during machining of hardened AISI 52100 steel under dry and cryogenic cooling conditions*, The International Journal of Advanced Manufacturing Technology **64**(5-8) (2012) 633-642.

[166] L. Engelking, D. Schroepfer, T. Kannengiesser, A. Eissel, K. Treutler, V. Wesling, *Alloy modification for additive manufactured Ni alloy components Part II: Effect on subsequent machining properties*, Welding in the World **67**(4) (2022) 1059-1066.

[167] Engelking L, Eissel A, Schroepfer D, reutler K, Kannengiesser T, W. V, *Untersuchungsmethoden beim Fräsen additiv gefertigter schwer spanbarer Kobalt-Chrom-Legierungen*. Tagung Werkstoffprüfung 2021, Krupp U (eds) Stahlinstitut VDEh, Online, 2021, pp. 93-98.

[168] P.M. Rinck, A. Gueray, R. Kleinwort, M.F. Zaeh, *Experimental investigations on longitudinal-torsional vibration-assisted milling of Ti-6Al-4V*, The International Journal of Advanced Manufacturing Technology **108**(11-12) (2020) 3607-3618.

[169] Z. Yao, G.-Y. Kim, Z. Wang, L. Faidley, Q. Zou, D. Mei, Z. Chen, *Acoustic softening and residual hardening in aluminum: Modeling and experiments*, International Journal of Plasticity **39** (2012) 75-87.

[170] Z. Yao, G.-Y. Kim, L. Faidley, Q. Zou, D. Mei, Z. Chen, *Acoustic Softening and Hardening of Aluminum in High-Frequency Vibration-Assisted Micro/Meso Forming*, Materials and Manufacturing Processes **28**(5) (2013) 584-588.

[171] G.C. Verma, P.M. Pandey, U.S. Dixit, *Modeling of static machining force in axial ultrasonic-vibration assisted milling considering acoustic softening*, International Journal of Mechanical Sciences **136** (2018) 1-16.

[172] G.C. Verma, P.M. Pandey, *Machining forces in ultrasonic-vibration assisted end milling*, Ultrasonics **94** (2019) 350-363.

[173] M.N. Kumar, S.K. Subbu, P.V. Krishna, A. Venugopal, *Vibration Assisted Conventional and Advanced Machining: A Review*, Procedia Engineering **97** (2014) 1577-1586.

[174] B. Azarhoushang, J. Akbari, *Ultrasonic-assisted drilling of Inconel 738-LC*, International Journal of Machine Tools and Manufacture **47**(7-8) (2007) 1027-1033.

[175] M.G. Nik, M.R. Movahhedy, J. Akbari, U*ltrasonic-Assisted Grinding of Ti6Al4V Alloy*, Procedia CIRP **1** (2012) 353-358.

[176] M.R. Razfar, P. Sarvi, M.M.A. Zarchi, *Experimental investigation of the surface roughness in ultrasonic-assisted milling*, Proceedings of the Institution of Mechanical Engineers, Part B: Journal of Engineering Manufacture **225**(9) (2011) 1615-1620.

[177] M.M. Abootorabi Zarchi, M.R. Razfar, A. Abdullah, *Investigation of the effect of cutting speed and vibration amplitude on cutting forces in ultrasonic-assisted milling*, Proceedings of the Institution of Mechanical Engineers, Part B: Journal of Engineering Manufacture **226**(7) (2012) 1185-1191.

[178] W. Chen, D. Huo, Y. Shi, J.M. Hale, S*tate-of-the-art review on vibration-assisted milling: principle, system design, and application*, The International Journal of Advanced Manufacturing Technology **97**(5-8) (2018) 2033-2049.

[179] N. Ahmed, A.V. Mitrofanov, V.I. Babitsky, V.V. Silberschmidt, *Analysis of material response to ultrasonic vibration loading in turning Inconel 718*, Materials Science and Engineering: A **424**(1-2) (2006) 318-325.

[180] A. Suárez, F. Veiga, L.N.L. de Lacalle, R. Polvorosa, S. Lutze, A. Wretland, *Effects of Ultrasonics-Assisted Face Milling on Surface Integrity and Fatigue Life of Ni-Alloy 718*, Journal of Materials Engineering and Performance **25**(11) (2016) 5076-5086.

[181] B. Fang, Z. Yuan, D. Li, L. Gao, *Effect of ultrasonic vibration on finished quality in ultrasonic vibration assisted micromilling of Inconel718*, Chinese Journal of Aeronautics **34**(6) (2021) 209-219.

[182] A. Eissel, L. Engelking, K. Treutler, V. Wesling, D. Schröpfer, T. Kannengießer, *Modification of Co–Cr alloys to optimize additively welded microstructures and subsequent surface finishing*, Welding in the World **66**(11) (2022) 2245-2257.

[183] J. Witte, D. Schroepfer, M. Hamacher, H. Michels, C. Hamm, M. Appelt, A. Boerner, T. Kannengiesser, *Tool development for hybrid finishing milling of iron aluminides*, Procedia CIRP **108** (2022) 793-798.

[184] J. Guo, M. Goh, Z. Zhu, X. Lee, M.L.S. Nai, J. Wei, *On the machining of selective laser melting CoCrFeMnNi high-entropy alloy*, Materials & Design **153** (2018) 211-220.

[185] P. Litwa, E. Hernandez-Nava, D. Guan, R. Goodall, K.K. Wika, *The additive manufacture processing and machinability of CrMnFeCoNi high entropy alloy*, Materials & Design **198** (2021).

[186] N. Kaushik, A. Meena, H.S. Mali, *Flat-end mill machining analysis of processed CrMnFeCoNi high-entropy alloys*, Materials and Manufacturing Processes **38**(6) (2022) 755-769.

[187] D. Delgado Arroyo, T. Richter, D. Schroepfer, A. Boerner, M. Rhode, T. Lindner, B. Preuß, T. Lampke, *Influence of Milling Conditions on AlxCoCrFeNiMoy Multi-Principal-Element Alloys*, Coatings **13**(3) (2023).

[188] G. Constantin, E. Balan, I. Voiculescu, V. Geanta, V. Craciun, *Cutting Behavior of Al(0.6)CoCrFeNi High Entropy Alloy*, Materials (Basel) **13**(18) (2020).

[189] B. Clauß, H. Liborius, T. Lindner, M. Löbel, A. Schubert, T. Lampke, *Influence of the cutting parameters on the surface properties in turning of a thermally sprayed AlCoCrFeNiTi coating*, Procedia CIRP **87** (2020) 19-24.

[190] H. Liborius, T. Uhlig, B. Clauß, A. Nestler, T. Lindner, A. Schubert, G. Wagner, T. Lampke, *Influence of the cutting material on tool wear, surface roughness, and force components for different cutting speeds in face turning of CoCrFeNi high-entropy alloys*, IOP Conference Series: Materials Science and Engineering **1147**(1) (2021).

[191] M. Schneider, F. Werner, D. Langenkämper, C. Reinhart, G. Laplanche, *Effect of Temperature and Texture on Hall–Petch Strengthening by Grain and Annealing Twin Boundaries in the MnFeNi Medium-Entropy Alloy*, Metals **9**(1) (2019).

[192] M. Schneider, E.P. George, T.J. Manescau, T. Záležák, J. Hunfeld, A. Dlouhý, G. Eggeler, G. Laplanche, *Analysis of strengthening due to grain boundaries and annealing twin boundaries in the CrCoNi medium-entropy alloy*, International Journal of Plasticity **124** (2020) 155-169.

[193] DIN EN 10088-3:2014-12, *Nichtrostende Stähle - Teil 3: Technische Lieferbedingungen für Halbzeug, Stäbe, Walzdraht, gezogenen Draht, Profile und Blankstahlerzeugnisse aus korrosionsbeständigen Stählen für allgemeine Verwendung*, Beuth GmbH, Berlin Germany, 2014.

[194] DIN EN ISO 14175:2008, *Schweißzusätze - Gase und Mischgase für das Lichtbogenschweißen und verwandte Prozesse*, Beuth GmbH, Berlin Germany, 2008.

[195] DIN EN ISO 6848:2015, Lichtbogenschweißen und -schneiden - Wolframelektrode - Einteilung, Beuth GmbH, Berlin Germany 2015.

[196] M. Giese, Experimentelle Charakterisierung der WIG-Schweißeignung einer Hoch- und Mittelentropie-Legierung, Bundesanstalt für Materialforschung und -prüfung (BAM), Otto-von-Guericke Universität Magdeburg, 2021.

[197] DIN 50159-1: *Metallische Werkstoffe –Härteprüfung nach dem UCI-Verfahren –Teil 1: Prüfverfahren*, Beuth Verlag GmbH, Berlin, Germany, 2015-01.

[198] I.C. Noyan, J.B. Cohen., *Residual stress – measurement by diffraction and interpretation.* Springer Series on Materials Research and Engineering, Springer-Verlag, New York-Berlin-Heidelberg-London-Paris-Tokyo, 1987.

[199] P.J. Withers, M. Turski, L. Edwards, P.J. Bouchard, D.J. Buttle, R*ecent advances in residual stress measurement*, International Journal of Pressure Vessels and Piping **85**(3) (2008) 118-127.

[200] A.J. Zaddach, C. Niu, C.C. Koch, D.L. Irving, *Mechanical Properties and Stacking Fault Energies of NiFeCrCoMn High-Entropy Alloy*, JOM **65**(12) (2013) 1780-1789.

[201] S. Lamb, *CASTI handbook of stainless steels and nickel alloys. 2. ed*., CASTI Publishing Inc., Alberta (Canada), 2002.

[202] DIN EN ISO 17636-1: *Zerstörungsfreie Prüfung von Schweißverbindungen - Durchstrahlungsprüfung - Teil 1: Röntgen- und Gammastrahlungstechniken mit Filmen*, Beuth GmbH, Berlin, Germany, 2013.

[203] DIN EN ISO 6892-1:*Metallische Werkstoffe - Zugversuch - Teil 1: Prüfverfahren bei Raumtemperatur*, Beuth Verlag GmbH, Berlin, Germany, 2020.

[204] K. Erxleben, Schweißbarkeit bei Mischverbindungen aus Hoch- und Mediumentropielegierungen mit hochlegierten, konventionellen Werkstoffen, Bundesanstalt für Materialforschung und -prüfung (BAM), Technische Universität Berlin, 2023.

[205] C.Z.G.M. GmbH, https://www.gom.com/de-de/produkte/zeiss-quality-suite/gom-correlate-pro, 2023. (Accessed 25.04. 2023).

[206] M. Rhode, K. Erxleben, T. Richter, D. Schroepfer, T. Mente, T. Michael, *Local mechanical properties of dissimilar metal TIG welded joints of CoCrFeMnNi high entropy alloy and AISI 304 austenitic steel*, Welding in the World (2024).

[207] T. Richter, D. Schroepfer, M. Rhode, A. Boerner, R.S. Neumann, M. Schneider, G. Laplanche, *Influence of machining on the surface integrity of high- and medium-entropy alloys*, Materials Chemistry and Physics **275** (2022).

[208] M.G.G.C. KG, https://schnittdaten.meusburger.com/effektiver-fraesdurchmesser/. 2023. (Accessed 25.04. 2023).

[209] DIN-6527L: *Vollhartmetall-Schaftfräser mit abgesetztem Zylinderschaft-Maße*, Beuth publishing DIN, Berlin, Germany, 2002.

[210] P. Yang, C. Yao, S. Xie, D. Zhang, D.X. Tang, *Effect of Tool Orientation on Surface Integrity During Ball End Milling of Titanium Alloy TC17*, Procedia CIRP **56** (2016) 143-148.

[211] DIN EN ISO 4287: *Geometrische Produktspezifikation (GPS) - Oberflächenbeschaffenheit: Tastschnittverfahren - Benennungen, Definitionen und Kenngrößen der Oberflächenbeschaffenheit*, Beuth publishing DIN, Berlin, Germany, 2010.

[212] D. Nespor, B. Denkena, T. Grove, O. Pape, *Surface topography after re-contouring of welded Ti-6Al-4V parts by means of 5-axis ball nose end milling*, The International Journal of Advanced Manufacturing Technology **85**(5-8) (2015) 1585-1602.

[213] K.-H. Grote, H. Hefazi, *Springer Handbook of Mechanical Engineering, 2nd ed.*, Springer Nature Switzerland AG, Cham, Switzerland, 2021.

[214] T. Richter, M. Giese, M. Rhode, D. Schroepfer, T. Michael, T. Fritsch, *Influence of Surface Preparation on Cracking Phenomena in TIG-Welded High and Medium Entropy Alloys*, Journal of Manufacturing and Materials Processing **6**(1) (2021).

[215] Y.G. Kim, I.J. Kim, J.S. Kim, Y.I. Chung, D.Y. Choi, *Evaluation of Surface Crack in Resistance Spot Welds of Zn-Coated Steel*, Materials Transactions **55**(1) (2014) 171-175.

[216] C.K. Soundararajan, H. Luo, D. Raabe, Z. Li, *Hydrogen resistance of a 1 GPa strong equiatomic CoCrNi medium entropy alloy*, Corrosion Science **167** (2020) 108510.

[217] E. Hornbogen, H. Warlimont, B. Skotzki, *Metalle: Struktur und Eigenschaften der Metalle und Legierungen*, Springer-Verlag GmbH, Berlin, Germany, 2019.

[218] G. Schulze, H. Krafka, P. Neuman, *Schweisstechnik Wekstoffe - Konstruieren - Prüfen*, VDI-Verlag GmbH, 1992.

[219] W.F. Savage, E.F. Nippes, K. Agusa, *Effect of Arc Force on Defect Formation in Gta Welding*, Welding Journal **58**(7) (1979) S212-S224.

[220] H. Inoue, T. Koseki, S. Okita, M. Fuji, *Epitaxial growth and phase formation of austenitic stainless steel weld metals near fusion boundaries: Study of solidification and transformation of Cr-Ni stainless steel weld metals (3rd Report)*, Welding International **12**(3) (2010) 195-206.

[221] S.A. David, J.M. Vitek, *Correlation between solidification parameters and weld microstructures*, International Materials Reviews **34**(1) (1989) 213-245.

[222] P.P. Bhattacharjee, G.D. Sathiaraj, M. Zaid, J.R. Gatti, C. Lee, C.-W. Tsai, J.-W. Yeh, *Microstructure and texture evolution during annealing of equiatomic CoCrFeMnNi high-entropy alloy*, Journal of Alloys and Compounds **587** (2014) 544-552.

[223] M.-H. Tsai, J.-W. Yeh, *High-Entropy Alloys: A Critical Review*, Materials Research Letters **2**(3) (2014) 107-123.

[224] M. Laurent-Brocq, A. Akhatova, L. Perrière, S. Chebini, X. Sauvage, E. Leroy, Y. Champion, *Insights into the phase diagram of the CrMnFeCoNi high entropy alloy*, Acta Materialia **88** (2015) 355-365.

[225] D. Field, L. Bradford, M. Nowell, T. Lillo, T*he role of annealing twins during recrystallization of Cu*, Acta Materialia **55**(12) (2007) 4233-4241.

[226] S. Mahajan, C.S. Pande, M.A. Imam, B.B. Rath, *Formation of annealing twins in f.c.c. crystals*, Acta Materialia **45**(6) (1997) 2633-2638.

[227] Z. Wu, S.A. David, Z. Feng, H. Bei, *Weldability of a high entropy CrMnFeCoNi alloy*, Scripta Materialia **124** (2016) 81-85.

[228] N. Kashaev, V. Ventzke, N. Stepanov, D. Shaysultanov, V. Sanin, S. Zherebtsov, *Laser beam welding of a CoCrFeNiMn-type high entropy alloy produced by self-propagating high-temperature synthesis*, Intermetallics **96** (2018) 63-71.

[229] T. Zheng, J. Lv, Y. Wu, H.-H. Wu, S. Liu, J. Tang, M. Zhou, H. Wang, X. Liu, S. Jiang, Z. Lu, *Effects of stacking fault energy on the deformation behavior of CoNiCrFeMn high-entropy alloys: A molecular dynamics study*, Applied Physics Letters **119**(20) (2021).

[230] D. Oliveros, A. Fraczkiewicz, A. Dlouhy, C. Zhang, H. Song, S. Sandfeld, M. Legros, *Orientation-related twinning and dislocation glide in a cantor high entropy alloy at room and cryogenic temperature studied by in situ TEM straining*, Materials Chemistry and Physics **272** (2021).

[231] Y.N. Hu, S.C. Wu, L. Chen, *Review on failure behaviors of fusion welded high-strength Al alloys due to fine equiaxed zone*, Engineering Fracture Mechanics **208** (2019) 45-71.

[232] T. Richter, D. Schroepfer, M. Rhode, *Residual Stresses in a High- and a Medium-Entropy Alloy due to TIG and Friction Stir Welding*, Journal of Manufacturing and Materials Processing **6**(6) (2022).

[233] T. Nitschke-Pagel, H. Wohlfahrt, *Residual Stresses in Welded Joints – Sources and Consequences*, Materials Science Forum 404-407 (2002) 215-226.

[234] U. Zerbst, *Application of fracture mechanics to welds with crack origin at the weld toe—a review. Part 2: welding residual stresses. Residual and total life assessment*, Welding in the World **64**(1) (2019) 151-169.

[235] Z. Zhou, F. Zhang, J. Wu, J. Pi, F. Chen, *Laser Beam Welding of Feconicrmn High-Entropy Alloys with Preplaced Powders*, Metals **10**(11) (2020).

[236] R. Darolia, W.S. Walston, *Effect of specimen surface preparation on room temperature tensile ductility of an Fe-containing NiAl single crystal alloy*, Intermetallics **4**(7) (1996) 505-516.

[237] Y.H. Wang, J.H. Jiang, C. Wanintrudal, C. Du, D. Zhou, L.M. Smith, L.X. Yang, *Whole Field Sheet-Metal Tensile Test Using Digital Image Correlation*, Experimental Techniques **34**(2) (2010) 54-59.

[238] G. Ben Salem, E. Héripré, P. Bompard, S. Chapuliot, A. Blouin, C. Jacquemoud, *Mechanical Behavior Characterization of a Stainless Steel Dissimilar Metal Weld Interface : In-situ Micro-Tensile Testing on Carburized Martensite and Austenite*, Experimental Mechanics **60**(8) (2020) 1037-1053.

[239] B. Gludovatz, E.P. George, R.O. Ritchie, *Processing, Microstructure and Mechanical Properties of the CrMnFeCoNi High-Entropy Alloy*, JOM **67**(10) (2015) 2262-2270.

[240] N.S.M. Nasir, M.K.A.A. Razab, S. Mamat, M.I. Ahmad, *Review on Welding Residual Stress*, ARPN Journal of Engineering and Applied Sciences **11**(9) (2016) 6166-6175.

[241] C.-W. Tsai, Y.-L. Chen, M.-H. Tsai, J.-W. Yeh, T.-T. Shun, S.-K. Chen, *Deformation and annealing behaviors of high-entropy alloy Al0.5CoCrCuFeNi*, Journal of Alloys and Compounds **486**(1-2) (2009) 427-435.

[242] A. Reynolds, F. Duval, *Digital image correlation for determination of weld and base metal constitutive behavior*, Weld J **78** (1999) 355-360.

[243] K. Pasewald, *Erscheinungsformen von Rissen und Brüchen metallischer Werkstoffe*, Verein Deutscher Eisenhüttenleute, Verlag Stahleisen, Düsseldorf, Deutschland, 1996.

[244] R.H.V. Stone, T.B. Cox, J.R. Low, J.A. Psioda, *Microstructural aspects of fracture by dimpled rupture*, International Metals Reviews **30**(1) (1985) 157-180.

[245] M. Büttner, *Versagensverhalten rissbehafteter Mischschweißnähte – theoretische und experimentelle Untersuchungen*, Fakultät Energie-, Verfahrens- und Biotechnik, Universität Stuttgart, 2011.

[246] A. du Plessis, I. Yadroitsev, I. Yadroitsava, S.G. Le Roux, *X-Ray Microcomputed Tomography in Additive Manufacturing: A Review of the Current Technology and Applications*, 3D Printing and Additive Manufacturing **5**(3) (2018) 227-247.

[247] T. Richter, K. Erxleben, M. Rhode, D. Schroepfer, T. Michael, A. Boerner, M*icrostructure characterization of dissimilar metal welds of innovative high- and medium-entropy alloys to austenitic stainless steels joint by tungsten inert gas and friction stir welding*, Welding in the World **68** (2024) 557-565.

[248] J. Yang, J. Wu, C.Y. Zhang, S.D. Zhang, B.J. Yang, W. Emori, J.Q. Wang, E*ffects of Mn on the electrochemical corrosion and passivation behavior of CoFeNiMnCr high-entropy alloy system in H2SO4 solution*, Journal of Alloys and Compounds **819** (2020).

[249] R. Sokkalingam, V. Muthupandi, K. Sivaprasad, K.G. Prashanth, *Dissimilar welding of Al0.1CoCrFeNi high-entropy alloy and AISI304 stainless steel*, Journal of Materials Research **34**(15) (2019) 2683-2694.

[250] S. Saha, M. Mukherjee, T.K. Pal, *Microstructure, Texture, and Mechanical Property Analysis of Gas Metal Arc Welded AISI 304 Austenitic Stainless Steel*, Journal of Materials Engineering and Performance **24**(3) (2014) 1125-1139.

[251] F.-x. Huang, X.-h. Wang, J.-m. Zhang, C.-x. Ji, Y. Fang, Y. Yu, *In Situ Observation of Solidification Process of AISI 304 Austenitic Stainless Steel*, Journal of Iron and Steel Research International **15**(6) (2008) 78-82.

[252] G. Laplanche, O. Horst, F. Otto, G. Eggeler, E.P. George, *Microstructural evolution of a CoCrFeMnNi high-entropy alloy after swaging and annealing*, Journal of Alloys and Compounds **647** (2015) 548-557.

[253] T.M. Angeliu, E.L. Hall, J. Sutliff, S. Sitzmen, P.L. Andresen, *Strain and Microstructure Characterization of Austenitic Stainless Steel Weld HAZs*, CORROSION 2000, 26-31 March 2000, Orlando, USA 2000.

[254] R.D. Adams, V. Mallick, *A Method for the Stress Analysis of Lap Joints*, The Journal of Adhesion **38**(3-4) (1992) 199-217.

[255] A.C.F. Silva, J. De Backer, G. Bolmsjö, *Temperature measurements during friction stir welding*, The International Journal of Advanced Manufacturing Technology **88**(9-12) (2016) 2899-2908.

[256] J. De Backer, G. Bolmsjö, A.-K. Christiansson, *Temperature control of robotic friction stir welding using the thermoelectric effect*, The International Journal of Advanced Manufacturing Technology **70**(1-4) (2013) 375-383.

[257] R. Rai, A. De, H.K.D.H. Bhadeshia, T. DebRoy, *Review: friction stir welding tools*, Science and Technology of Welding and Joining **16**(4) (2013) 325-342.

[258] F. Lambiase, A. Paoletti, A. Di Ilio, *Forces and temperature variation during friction stir welding of aluminum alloy AA6082-T6*, The International Journal of Advanced Manufacturing Technology **99**(1-4) (2018) 337-346.

[259] M. Hossfeld, *Experimentelle, analytische und numerische Untersuchungen des Rührreib-schweißprozesses*, Fakultät Energie-, Verfahrens- und Biotechnik, Universität Stuttgart, 2016.

[260] A. Yazdipour, A. Shafiei M, K. Dehghani, *Modeling the microstructural evolution and effect of cooling rate on the nanograins formed during the friction stir processing of Al5083*, Materials Science and Engineering: A *527*(1-2) (2009) 192-197.

[261] H. Niedrig, P*hysical background of electron backscattering*, Scanning **1**(1) (1978) 17-34.

[262] A. Tongne, C. Desrayaud, M. Jahazi, E. Feulvarch, *On material flow in Friction Stir Welded Al alloys*, Journal of Materials Processing Technology **239** (2017) 284-296.

[263] R.L. Fullman, J.C. Fisher, *Formation of Annealing Twins During Grain Growth*, Journal of Applied Physics **22**(11) (1951) 1350-1355.

[264] W. Ding, L. Zhang, Z. Li, Y. Zhu, H. Su, J. Xu, *Review on grinding-induced residual stresses in metallic materials*, The International Journal of Advanced Manufacturing Technology **88**(9-12) (2016) 2939-2968.

[265] Y.C. Lin, D.-X. Wen, M.-S. Chen, X.-M. Chen, *A novel unified dislocation density-based model for hot deformation behavior of a nickel-based superalloy under dynamic recrystallization conditions*, Applied Physics A **122**(9) (2016).

[266] H.A. Derazkola, H.J. Aval, M. Elyasi, *Analysis of process parameters effects on dissimilar friction stir welding of AA1100 and A441 AISI steel*, Science and Technology of Welding and Joining **20**(7) (2015) 553-562.

[267] L. Zhou, M. Yu, H. Zhao, Z. Jiang, F. Guo, X. Song, *Dissimilar friction stir welding of AA6061 and Ti6Al4V alloys: A study on microstructure and mechanical properties*, Journal of Manufacturing Processes **48** (2019) 119-126.

[268] P. Xue, B.L. Xiao, D.R. Ni, Z.Y. Ma, *Enhanced mechanical properties of friction stir welded dissimilar Al–Cu joint by intermetallic compounds*, Materials Science and Engineering: A **527**(21-22) (2010) 5723-5727.

[269] C.W. Tan, Z.G. Jiang, L.Q. Li, Y.B. Chen, X.Y. Chen, *Microstructural evolution and mechanical properties of dissimilar Al–Cu joints produced by friction stir welding*, Materials & Design **51** (2013) 466-473.

[270] V. Firouzdor, S. Kou, *Al-to-Mg Friction Stir Welding: Effect of Material Position, Travel Speed, and Rotation Speed*, Metallurgical and Materials Transactions A **41**(11) (2010) 2914-2935.

[271] B. Fu, G. Qin, F. Li, X. Meng, J. Zhang, C. Wu, *Friction stir welding process of dissimilar metals of 6061-T6 aluminum alloy to AZ31B magnesium alloy*, Journal of Materials Processing Technology **218** (2015) 38-47.

[272] P. Po drazaj, B. Jerman, D. Klobcar, *Welding Defects at Friction Stri Welding*, Metalurgija **54** (2015) 387-389.

[273] H. Taheri, M. Kilpatrick, M. Norvalls, W.J. Harper, L.W. Koester, T. Bigelow, L.J. Bond, I*nvestigation of Nondestructive Testing Methods for Friction Stir Welding*, Metals **9**(6) (2019).

[274] J.Y. Choi, W. Jin, *Strain induced martensite formation and its effect on strain hardening behavior in the cold drawn 304 austenitic stainless steels*, Scripta Materialia **36**(1) (1997) 99-104.

[275] S.H. Joo, H. Kato, M.J. Jang, J. Moon, C.W. Tsai, J.W. Yeh, H.S. Kim, *Tensile deformation behavior and deformation twinning of an equimolar CoCrFeMnNi high-entropy alloy*, Materials Science and Engineering: A **689** (2017) 122-133.

[276] E.J. Pavlina, C.J. Van Tyne, *Correlation of Yield Strength and Tensile Strength with Hardness for Steels*, Journal of Materials Engineering and Performance **17**(6) (2008) 888-893.

[277] J.A. Nugroho, D.E. Jodi, N. Park, S. Kim, U. Lee, E.R. Baek, Effects of Tungsten-Carbide Particle Addition on Friction-Stir-Processed Fe50(CoCrMnNi)50 Medium-Entropy Alloy, Jom 71(10) (2019) 3452-3459.

[278] E. Tschegg, *Erscheinungsformen von Brüchen Metallischer Werkstoffe*, in: H.-P. Rossmanith (Ed.), Grundlagen der Bruchmechanik, Springer Vienna, Vienna, 1982, pp. 136-151.

[279] V.D. Kalyankar, P. Shah, *A review on methodologies to reduce welding distortion*, Materials Today: Proceedings **5**(11) (2018) 24741-24749.

[280] V. Gaikhe, J. Sahu, R. Pawade, *Optimization of Cutting Parameters for Cutting Force Minimization in Helical Ball End Milling of Inconel 718 by Using Genetic Algorithm*, Procedia CIRP **77** (2018) 477-480.

[281] C. Nath, M. Rahman, *Evaluation of ultrasonic vibration cutting while machining Inconel 718*, International Journal of Precision Engineering and Manufacturing **9**(2) (2008) 63-68.

[282] A. Sharman, R.C. Dewes, D.K. Aspinwall, *Tool life when high speed ball nose end milling Inconel 718*, Journal of Materials Processing Technology **118**(1-3) (2001) 29-35.

[283] W. Grzesik, *A revised model for predicting surface roughness in turning*, Wear **194**(1-2) (1996) 143-148.

[284] A. Turnbull, K. Mingard, J.D. Lord, B. Roebuck, D.R. Tice, K.J. Mottershead, N.D. Fairweather, A.K. Bradbury, *Sensitivity of stress corrosion cracking of stainless steel to surface machining and grinding procedure*, Corrosion Science **53**(10) (2011) 3398-3415.

[285] P.R. Roberge, *Handbook of Corrosion Engineering*, McGraw Hill, Library of Congress Cataloging-in-Publication Data 2000.

[286] B.A. Khidhir, B. Mohamed, *Study of cutting speed on surface roughness and chip formation when machining nickel-based alloy*, Journal of Mechanical Science and Technology **24**(5) (2010) 1053-1059.

[287] T. Richter, D. Schröpfer, M. Rhode, A. Börner, Influence of modern machining processes on the surface integrity of high-entropy alloys, IOP Conference Series: Materials Science and Engineering 882(1) (2020).

[288] L. Engelking, *Herstellung beanspruchungsgerechter Oberflächen durch Kombination innovativer additiver und abtragender Fertigungsschritte an hochbelasteten Komponenten*, Sitzung des DVS Fachausschusses 01 „Schweißmetallurgie und Werkstoffverhalten“, not published, Online, 2022.

[289] M.S. Dargusch, M.X. Zhang, S. Palanisamy, A.J.M. Buddery, D.H. StJohn, *Subsurface Deformation After Dry Machining of Grade 2 Titanium*, Advanced Engineering Materials **10**(1-2) (2008) 85-88.

[290] D. Jin, Z. Liu, *Damage of the machined surface and subsurface in orthogonal milling of FGH95 superalloy*, The International Journal of Advanced Manufacturing Technology **68**(5-8) (2013) 1573-1581.

[291] H. Dai, J. Chen, G. Liu, *A numerical study on subsurface quality and material removal during ultrasonic vibration assisted cutting of monocrystalline silicon by molecular dynamics simulation*, Materials Research Express **6**(6) (2019).

[292] J. Liu, X. Jiang, X. Han, Z. Gao, D. Zhang, *Effects of rotary ultrasonic elliptical machining for side milling on the surface integrity of Ti-6Al-4V*, The International Journal of Advanced Manufacturing Technology **101**(5-8) (2018) 1451-1465.

List of Figures

List of Tables

Abbreviations

AS	Advancing side
BCC	Body centered cubic
BM	Base metal
BUE	Built-up edge
CCA	Compositionally complex alloys
CGHAZ	Coarse grain heat affected zone
CR	Cold rolled
DAS	Dendrite arm spacing
DDC	Ductility dip cracks
DIC	Digital image correlation
DMW	Dissimilar metal weld
DoE	Design of experiments
DT	Destructive testing
EB	Electron beam
EBSD	Electron backscatter diffraction
EDM	Electrical discharge machining
FCC	Face centered cubic
FGHAZ	Fine grain heat affected zone
FL	Fusion line
FQZ	Fine equiaxed zone
FSW	Friction stir welding
HEA	High entropy alloy
HAZ	Heat affected zone
HT	Heat treated
LB	Laser beam
LME	Liquid metal embrittlement
LOM	Light optical microscopy
MEA	Medium entropy alloys
MPEA	Multi principal element alloys
NDT	Non-destructive testing
OPS	Oxide polishing suspension
PWHT	Post weld heat-treatment
RS	Retreating side
RT	Room temperature
SEM	Scanning electron microscope

SZ	Stir zone
TIG	Tungsten inert gas welding
TMAZ	Thermomechanical affected zone
UCI	Ultrasonic contact impedance
UTS	Ultimate tensile strength
WM	Weld metal
XRD	X-ray diffraction
YS	Yield strength

Unit Symbols

a_e	Stepover	mm
a_p	Depth of cut	mm
c_p	Specific heat capacity	J/(kg*K)
F	Force	N
F_s	Shear force	N
F_c	Cutting force	N
F_n	Normal shear force	N
F_t	Thrust force	N
F_f	Friction force	N
F_r	Resulting cutting force	N
F_{res}	Resulting cutting force	N
F_x	Force in x-direction	N
F_y	Force in y-direction	N
F_z	Force in z-direction	N
f_z	Feed per cutting edge	mm
G	Gibbs free enthalpy	J
G_{mix}	Gibbs free enthalpy of mixing	J
H_{mix}	Enthalpy of mixing	J
L	Length	mm
L_0	Initial length	mm
N	Normal force	N
n	Rotation speed	
R	Universal gas constant	8.314 J/mol*K
R_M	Ultimate tensile strength	MPa
$R_{p0.2}$	Yield strength	MPa
S	Entropy	J/K
S_{conf}	Configuration entropy	J/K
S_{mix}	Mixing entropy	J/K
S_0	Initial cross-section	mm²
T	Temperature	K or °C
T_s	Melting temperature	K or °C
V_c	Material removal	mm³
v_c	Cutting speed	m/min
x_i	Molar fraction of component *i*	-

α	Thermal expansion coefficient	10^{-6}/K
α	Clearance angle	°
β	Friction angle	°
β	Resulting angle	°
ε	Strain	%
ε_{loc}	Local strain	%
γ	Rake angle	°
λ	Thermal conductivity	W/mK
λ	Feed angle	°
φ	Shear angle	°
σ	Stress	MPa
τ	Normal feed angle	°